Fakultät für Physik
Technische Universität München

Λ and K^0_S Production in Pion-Nucleus Reactions at 1.7 GeV/c

Steffen Maurus

FAKULTÄT FÜR PHYSIK

DER TECHNISCHEN UNIVERSITÄT MÜNCHEN

FACHBEREICH: DENSE AND STRANGE HADRONIC MATTER (E62)

Λ and K^0_S Production in Pion-Nucleus Reactions at 1.7 GeV/c

Steffen Maurus

Vollständiger Abdruck der von der Fakultät für Physik der Technischen Universität München zur Erlangung des akademischen Grades eines

Doktors der Naturwissenschaften (Dr. rer. nat.)

genehmigten Dissertation.

Vorsitzender:		apl. Prof. Dr. Norbert Kaiser
Prüfer der Dissertation:	1.	Prof. Dr. Laura Fabbietti
	2.	Prof. Dr. Stefan Schönert

Die Dissertation wurde am 04.09.2019 an der Technischen Universität München eingereicht und durch die Fakultät für Physik am 27.09.2019 angenommen.

Zusammenfassung

Diese Arbeit untersucht die Produktion und Eigenschaften von Λ (Σ^0) und K^0_S in kalter Kernmaterie, die in pion-induzierten Reaktionen bei einem einfallenden Strahlimpuls von $p_{\pi^-} = 1,7$ GeV/c, der auf Kohlenstoff (C) und Wolfram (W) trifft, gemessen wurden. Die Daten wurden mit dem HADES-Experiment, das sich bei der Gesellschaft für Schwerionenforschung (GSI) in Darmstadt (Deutschland) befindet, gemessen.
Um die Effizienzkorrekturen von HADES zu validieren, die zur Extraktion unverzerrter Spektren von Hyperonen und Mesonen erforderlich sind, wurde eine rein datengestützte Studie durchgeführt. Zu diesem Zweck wurde die elastische Streuung in einer experimentellen Kampagne mit negativ geladenen Pionen bei einem einfallenden Pionstrahlimpuls von $p_{\pi^-} = 690$ MeV/c, der auf ein Polyethylen (C_2H_4) Ziel trifft, untersucht. Aus dem Vergleich der elastischen Streuung von Pionen (π^-) und Protonen (p) in den experimentellen Daten und der Simulation ist ein systematischer Offset von $\Delta\epsilon = 3\%$ ermittelt worden. Diese Differenz wurde als systematische Unsicherheit für die weiteren Analysen berücksichtigt.
Für die (Doppel-)Differentielle Analyse von Λ und K^0_S wurden beide Hadronen über ihre dominanten schwachen geladenen Zerfallskanäle rekonstruiert, $\Lambda \rightarrow p + \pi^-$ (BR = 63.9±0.5% [1]) und $K^0_S \rightarrow \pi^+ + \pi^-$ (BR = 69.2±0.05% [1]). Aufgrund des dominanten Σ^0 Zerfallskanals von $\Sigma^0 \rightarrow \Lambda + \gamma$ (BR ≈ 100% [1]) trägt das Σ^0 zum beobachteten Λ Ertrag bei. Die absolut normierten, inklusiven Spektren konnten für Λ und K^0_S in beiden Kollisionssystemen innerhalb der HADES-Akzeptanz extrahiert werden. Somit konnten die Rapiditätsverteilungen dN/dy bestimmt werden, die starke Streueffekte für beide Hadronen im schwereren Ziel (W) zeigen, da die Verteilungen im Vergleich zum leichteren Ziel (C) nach hinten verschoben sind. Der integrierte differenzielle Wirkungsquerschnitt der innerhalb der HADES-Akzeptanz für Λ ($0 \leq y < 1.05$) und K^0_S ($0 \leq y < 1.6$) in $\pi^- + \mathrm{C}$ extrahiert wurde beläuft sich auf $\Delta\sigma^{\Lambda}_{\mathrm{C}} = 4347 \pm 19(\mathrm{stat}) \pm^{+129}_{-131} (\mathrm{sys})^{+188}_{-154}(\mathrm{norm})\,\mu$b und $\Delta\sigma^{K^0_S}_{\mathrm{C}} = 2080 \pm 14(\mathrm{stat})^{+83}_{-83}(\mathrm{sys}) \pm^{+84}_{-68} (\mathrm{norm})\,\mu$b und in $\pi^- + \mathrm{W}$ Reaktionen auf $\Delta\sigma^{\Lambda}_{\mathrm{W}} = 29712 \pm 127(\mathrm{stat}) \pm^{+677}_{-1114} (\mathrm{sys})^{+1416}_{-1159}(\mathrm{norm})\,\mu$b und $\Delta\sigma^{K^0_S}_{\mathrm{W}} = 12797 \pm 68(\mathrm{stat}) \pm^{+302}_{-277} (\mathrm{sys})^{+559}_{-457}(\mathrm{norm})\,\mu$b. Darüber hinaus wurden inklusive kinematischer Spektren mit den anerkannten Transportmodellen UrQMD [2] [3], GiBUU [4] und SMASH [5] verglichen. Die Modifikation von K^0_S innerhalb der Kern-

materie wurde anhand des Verhältnisses des Wirkunsquerschnittes von $R(\sigma_W^K/\sigma_C^K)$ bestimmt und zu GiBUU-Vorhersagen verglichen. Diese wurden mit und ohne einem chiralen (χ-EFT) KN-Potenzial simuliert. Es lässt sich dabei ein Trend zu einem abstossendem χ-EFT KN-Potenzial beobachten.
Für eine detaillierte Untersuchung der Λ (Σ^0) und K_S^0 Interaktion mit (normaler) Kernmaterie wurde der (halb-)exklusive Kanal $\pi^- + A \rightarrow \Lambda + K_S^0 + X$ untersucht. Aufgrund der eng verknüpften Produktion von Λ und K_S^0 wurde im Gegensatz zur weit verbreiteten Einzeluntersuchung der Hadron-Eigenschaften eine gleichzeitige Analyse der Modifikation innerhalb der Kernmaterie durchgeführt. Auf der Grundlage der GiBUU-Vorhersagen wurden verschiedene Szenarien getestet, die unterschiedliche Hyperon-Nukleon und Kaon-Nukleon-Interaktionen berücksichtigen. Auf diese Weise wurde erstmals eine attraktive Λ zusammen mit einer abstoßenden Σ^0 Interaktion untersucht, wie sie auch durch χ-EFT vorhergesagt wird. Ein globaler Fit an alle kinematischen Verteilungen (p_t, y, p, Θ) beider Teilchen (Λ, K_S^0) wurde durchgeführt. Im Gegensatz zu theoretischen Vorhersagen favorisieren die Daten eine attraktive ΛN und $\Sigma^0 N$ Interaktion, die auf der Grundlage einer χ^2/NDF-Analyse bewertet wurde. Die Übereinstimmung zwischen experimentellen Daten und Simulation verbesserte sich mit einem χ-EFT KN-Potenzial und deutet daher auf das Vorhandensein einer abstoßenden KN-Interaktion hin. Zusätzlich wurde das Verhältnis Λ/Σ^0 mit den bestehenden Erkenntnissen verglichen. Auch hier wurde die abstoßende $\Sigma^0 N$-Interaktion, die durch die χ-EFT Theorie vorhergesagt wird, weitestgehend ausgeschlossen.

Abstract

This work investigates the production and properties of Λ (Σ^0) and K^0_S within cold nuclear matter generated in pion-induced reactions at an incident beam momentum of $p_{\pi^-} = 1.7$ GeV/c impinging on carbon (C) and tungsten (W) targets. The data was collected with the HADES experiment at the Gesellschaft für Schwerionenforschung (GSI) in Darmstadt (Germany).
In order to validate the efficiency correction of HADES, which is required to extract undistorted spectra of hyperons and mesons, a purely data driven study was performed. For this purpose, the elastic scattering in a subsequent experimental campaign with negatively charged pions at an incident pion beam momentum of $p_{\pi^-} = 690$ MeV/c impinging on a polyethylene (C_2H_4) target was investigated. From the comparison of elastic scattered pions (π^-) and protons (p) in the experimental data and simulation a systematic offset of the efficiency correction procedure of $\Delta\epsilon = 3\%$ was extracted. This retrieved difference was considered as correction uncertainty contributing to the systematic uncertainty in further analyses.
For the inclusive (double-)differential analysis of Λ and K^0_S, both hadrons were reconstructed via their dominant weak charged decay channels, $\Lambda \rightarrow p + \pi^-$ (BR $= 63.9 \pm 0.5\%$ [1]) and $K^0_S \rightarrow \pi^+ + \pi^-$ (BR $= 69.2 \pm 0.05\%$ [1]). Due to the dominant Σ^0 decay channel of $\Sigma^0 \rightarrow \Lambda + \gamma$ (BR $\approx 100\%$ [1]), the Σ^0 contributes to the observed Λ yield. The absolute normalised inclusive kinematic spectra were extracted for the Λ and K^0_S in both collision systems within the HADES acceptance. Hence, the rapidity density distributions dN/dy were retrieved, and these show strong scattering effects for both hadrons in the heavier target (W) as the distributions are shifted to backward rapidity with respect to the ones in the lighter target (C). The integrated differential production cross-section within the HADES acceptance for Λ ($0 \leq y < 1.05$) and K^0_S ($0 \leq y < 1.6$) in $\pi^- + $C reactions are found to be equal to $\Delta\sigma^{\Lambda}_{\mathrm{C}} = 4347 \pm 19(\mathrm{stat}) \pm^{+129}_{-131} (\mathrm{sys})^{+188}_{-154}(\mathrm{norm})\mu$b and $\Delta\sigma^{K^0_S}_{\mathrm{C}} = 2080 \pm 14(\mathrm{stat})^{+83}_{-83}(\mathrm{sys}) \pm^{+84}_{-68} (\mathrm{norm})\mu$b and in $\pi^- + $W reactions equal to $\Delta\sigma^{\Lambda}_{\mathrm{W}} = 29712 \pm 127(\mathrm{stat}) \pm^{+677}_{-1114} (\mathrm{sys})^{+1416}_{-1159}(\mathrm{norm})\mu$b and $\Delta\sigma^{K^0_S}_{\mathrm{W}} = 12797 \pm 68(\mathrm{stat}) \pm^{+302}_{-277} (\mathrm{sys})^{+559}_{-457}(\mathrm{norm})\mu$b. Moreover, inclusive kinematic spectra were compared with the state-of-the-art transport models, UrQMD [2] [3], GiBUU [4] and SMASH [5]. The in-medium modification of K^0_S is discussed on the basis of the cross-section ratio of $R(\sigma^K_W/\sigma^K_C)$ in comparison to GiBUU predictions

with and without a chiral-effective theory (χ-EFT) KN potential. Here a trend towards the repulsive in-medium χ-EFT KN potential is observed.
For a detailed investigation of Λ (Σ^0) and K_S^0 interaction with (normal) nuclear matter, the (semi-)exclusive channel $\pi^- + A \rightarrow \Lambda + K_S^0 + X$ was studied. Due to the associated production of the Λ and K_S^0, a simultaneous analysis of the in-medium effects was conducted. Different scenarios on the basis of GiBUU predictions, which consider different hyperon-nucleon and kaon-nucleon interactions, were tested. In this way, for the first time an attractive Λ together with a repulsive Σ^0 interaction, which are predicted by χ-EFT, was examined. A global fit to all kinematic distributions (p_t, y, p, Θ) of both particles (Λ, K_S^0) was performed. Contrary to theoretical predictions, the data favours an attractive ΛN and $\Sigma^0 N$ interaction, evaluated on the basis of a χ^2/NDF analysis. The agreement between experimental data and simulation improved with a χ-EFT KN potential and therefore hints to the presence of a repulsive KN interaction. In addition the Λ/Σ^0 ratio was compared to world data. Here, again the repulsive $\Sigma^0 N$ interaction predicted by χ-effective theory is disfavoured.

“If no one comes from the future to stop you from doing it then how bad of a decision can it really be. ”

Author unknown

Contents

1 Introduction

1.1 Standard Model of Particle Physics

Since the discovery of the electron by J.J. Thomson in 1897, nearly 200 years of research in particle physics have passed by. With the discovery of the nucleus by Ernest Rutherford in 1911 and the discovery of the neutron by James Chadwick in 1932, everyday matter could be understood. With technological progress and the increasing available energy of particle accelerator and statistics, more exotic states of matter could be studied. This led to the discovery of an entire zoo of particles. To explain everything with a single theory, the Standard Model (SM) of particle physics was formulated in the 1970s.
As shown in Fig. 1.1, the SM consists of spin 1/2 fermions that obey the Fermi-Dirac statistics and spin 1 and spin 0 bosons which obey the Bose-Einstein statistics. These spin 1/2 particles are divided into 6 leptons (+6 anti-leptons), as shown in Fig. 1.1 in green. These are assumed to be point-like without any inner structure and can exist freely. Beside, six more fundamental fermions are included in the SM, the so called quarks (+6 anti-quarks) indicated in blue. These are the constituents which form the hadrons. These quarks can never be observed as single quarks, but only in combination of three, the so-called baryons or of a quark anti-quark pair, the so-called mesons. More recent results also point to more exotic combinations of five quarks [6]. These fermions are divided into three generations. The first generation consists of the electron, the electron neutrino, the up-quark and the-down quark, which build normal nuclear matter. The generations II and III are more exotic. As the

generation increases, so do the masses, ranging from 2.2 MeV/c^2 from up-quark to 173.0 GeV/c^2 to the top-quark. The only known stable particles consist of generation I fermions and are the electron, the proton and the neutron, where the latter has to be bound in a nucleus to be stable. All other matter can be considered as an excited state that decays in the end. In addition, the interactions between the particles in the SM are also taken into account.

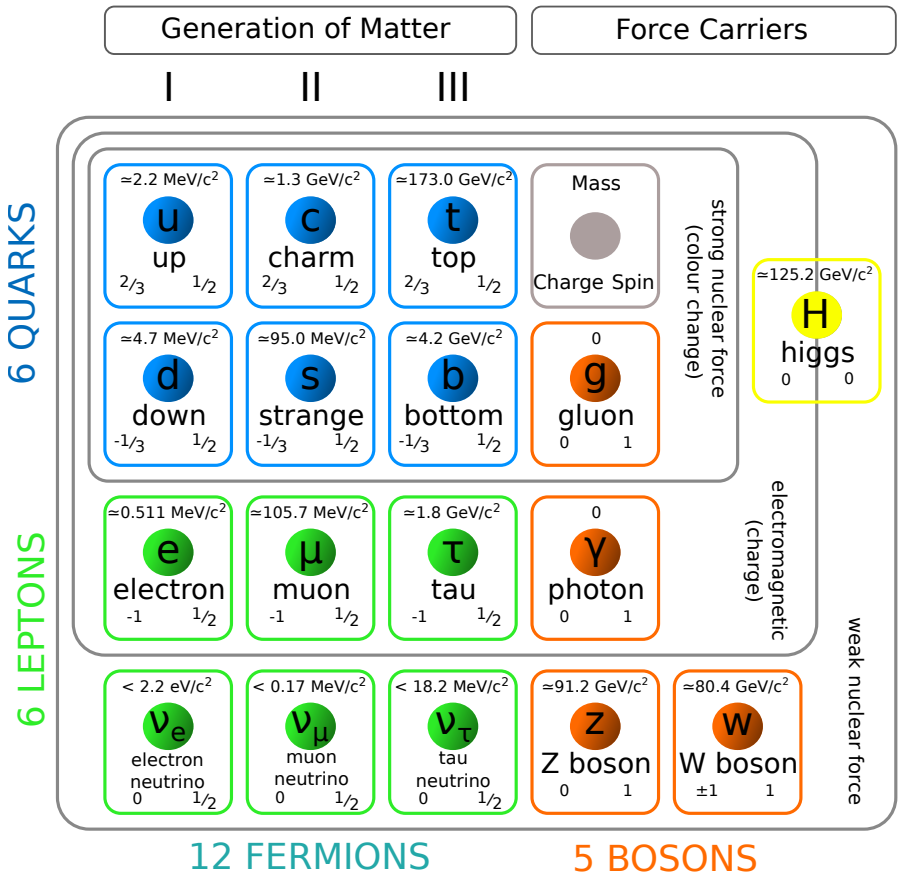

Figure 1.1: Illustration of the standard-model of particle physics. See text for details.

Three of the four fundamental forces are considered in the SM: the weak, electromagnetic and strong force. It is assumed that the forces are mediated by the exchange of gauge bosons. Due to the negligible strength of gravity at the microscopic level, it is not part of the SM. It is assumed that the hypothetical graviton is the exchange boson of gravitational force, but has not been observed until now. For the strong force, the gluon is the exchange particle, where only quarks participate in the interaction. This force is responsible for the binding of the quarks and thus for the formation of hadrons. For electromagnetic interaction, the photon is the exchange particle in which the hadrons (charged combination) and the charged

leptons are involved. The weak force is mediated by the neutral Z boson and the charged W boson, which are quite heavy. This force is known e.g. for the relatively slow processes of a nuclear β-decay. The image of the SM was recently completed with the discovery of the long-predicted Higgs boson [7, 8]. This boson is responsible for generating the mass of the fundamental constituents of the SM [9]. Although the predictions have been validated in numerous experimental approaches, some of the important questions cannot yet be answered by the SM. Why are there exactly three generations of quarks and leptons and why are their masses so different? Also the nature of dark matter and dark energy cannot be explained by the SM or what happened to antimatter after the Big Bang?
New approaches are trying to fill this gap, but so far the SM has proven that it provides the best description and understanding of matter and its interaction.

1.2 Strong Interaction

The strong interaction with the gluon as exchange particle is responsible for the binding of quarks and thus for the formation of hadrons. It is called strong interaction, because at scales of 1 fm it is about 137 stronger than the electromagnetic force, 10^6 stronger than the weak force and 10^{38} stronger than the gravitational force. The strong interaction is described in the theoretical framework of **q**uantum **c**hromo**d**ynamics (QCD), a non-abelian gauge theory based on SU(3) symmetry. Similar to **q**uantum **e**lectro**d**ynamics (QED), a charge is introduced. As the name chromo implies, colours are introduced as the charge of strong interaction. A quark can carry one of the three colours (red, green, blue), while anti-quarks carry the anti-colours (anti-red, anti-green, anti-blue). Thus, a total of three colour types are the internal degrees of freedom in QCD. In contrast to the QED, where the exchange particle, the photon, does not carry any charge, the gluon does. This means that the gluons can also couple to themselves and self-interact. This leads to effects of such asymptotic freedom and colour confinement contained in the QCD potential $V_s(r)$:

$$V_s(r) = -\frac{4}{3}\frac{\alpha_s(r)}{r} + kr \tag{1.1}$$

where

α_s: strong coupling constant
r: distance between quarks
$k \approx 1$ GeV/fm

The linear term kr is responsible for the confinement and dominates at long distances ($\sim r$) and thus low energy scales. With increasing distance the potential also increases and couples the quarks strong to each other. The potential energy reaches the rest mass of a $q\bar{q}$-pair at some point, whereby the creation of a $q\bar{q}$-pair is energetically favourable. Therefore, a single quark can never be observed directly. The first term of Eq. (1.1) becomes relevant for small distances ($\sim \frac{1}{r}$) or very high transmitted momenta (q^2). The energy dependent running coupling α_s decreases with increasing q^2 [10]. Therefore, the interaction strength between the quarks in this energy range becomes weak. Thus, the quarks in this asymptotic boundary can be considered almost free. This makes it possible to treat the QCD Lagrangian perturbatively, where the quarks are the degrees of freedom [11].

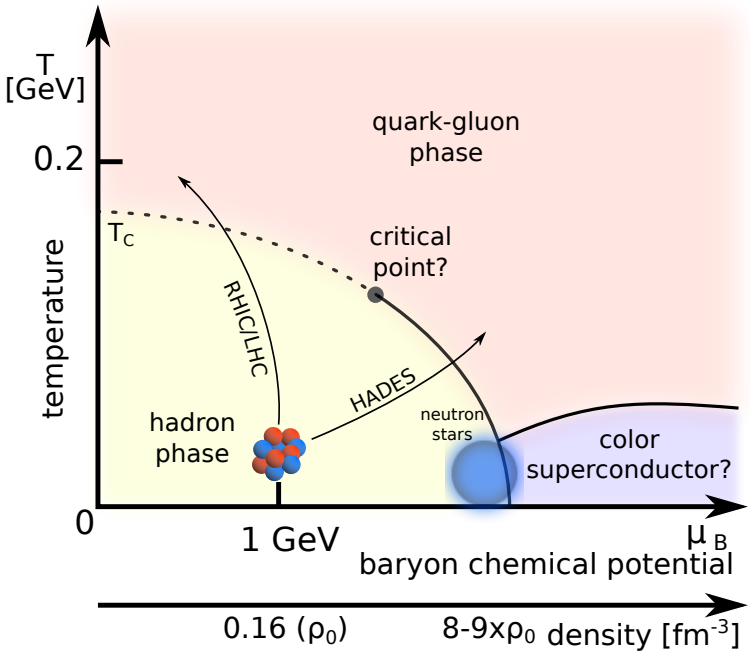

Figure 1.2: QCD phase diagram for temperature vs. baryon-chemical potential. The yellow shaded area corresponds to the hadronic phase, the red area to the quark-gluon plasma and blue to the hypothetical colour superconducting phase. $T_C \approx 155$ MeV reads the critical temperatures of second order transition, for higher densities depicted with the dashed line. See text for details.

At very high temperatures or densities, a transition from the hadron regime to a deconfined plasma, known as **q**uark **g**luon **p**lasma (QGP), is also predicted. Here the hadrons melt and no longer exist, but the quarks and gluons can move freely in a plasma and become the new degrees of freedom.
These different energy-dependent phases of the strongly interacting matter can

be summarised in a QCD phase diagram, which is depicted in Fig. 1.2. Here the temperature is represented as a function of the chemical potential of the baryon. The chemical potential of the baryon can be related to the baryonic net density, which is indicated by the double x-axis. The confined phase, in which hadrons are the degrees of freedom, is at low temperatures and rather moderate baryonic densities, indicated by the yellow shaded area. Here hadrons are the suitable degrees of freedom and their interaction can be studied by means of e.g. χ-effective theory (χ-EFT). In this phase also the normal nuclear matter is located around 1 GeV ($\rho_0 = 0.16$ fm^{-3}). At moderate temperatures ($T \sim 1$ MeV) but very high densities (up to 8-9 ρ_0) neutron stars are located, where the structure of the inner core is still under debate. A phase transition from hadrons to deconfined quarks and gluons is predicted, when at such low temperature nuclear matter reaches very high densities. The order of this phase transition and the exact position in the (T,μ_b) plane of the so-called critical point are strongly model dependent and affected by the underlying symmetries included in the theoretical description of the system. Currently there are no experimental evidences able to pin down the nature of such transition and the location of the critical point. This critical point determines the beginning of the so-called crossover transition from confined hadrons to QGP that takes place at higher temperatures and almost zero density. Lattice QCD calculations [12, 13] show that this smooth transition occurs at temperatures around $T \sim 155$ MeV.

High-energy particle accelerators such as LHC/RHIC probe the high-temperature ranges at low nuclear densities, while HADES and the future accelerator facility FAIR will probe higher densities and lower temperatures.
Cold nuclear experiments such as the pion-induced reactions presented here are close to normal nuclear saturation densities at moderate temperatures.

1.3 Equation of State

The representation of the phase diagram in the Fig. 1.2 is the result of the equation of state (EoS), which connects temperature, pressure p and baryon density: p(ρ,T). These equations include the fundamental interactions predicted by QCD. These interactions can then be used as input to describe stellar objects such as supernovae or neutron stars. Especially neutron stars, where the mass of 1-2 solar masses is compressed in a sphere with a radius of $r \approx 15$ km are very dense objects full of questions. While the outer layers are partially understood, the interior remains a subject of intense discussion. To shed light on the inner structure of such a dense object, which can reach up to eight times nuclear saturation density, the fundamental interactions can be used to predict the mass of the stellar object. But to go from a description of the interaction between hadrons to a predicted mass of a stellar object such as a neutron star, where the difference in scale are of the order of 10^{16} (QCD ~ 1 fm

- radius NS $\sim$ 10 km) the Tolman, Oppenheimer and Volkoff (TOV) equation can be used [14, 15]. The TOV equation assumes a hydrostatic equilibrium, therefore to be constant in time and an isotropic mass distribution. This implies that the gravitational pressure is counterbalanced by the matter properties and interaction. The TOV equation reads:

$$\frac{dp}{dr} = -\frac{G\epsilon(r)m(r)}{c^2 r^2}\left(1+\frac{p(r)}{\epsilon(r)}\right)\left(1+\frac{4\pi r^3 p(r)}{m(r)c^2}\right)\left(1-\frac{2Gm(r)}{c^2 r}\right)^{-1} \tag{1.2}$$

where

$p(r)$: pressure
$\epsilon(r)$: energy density
$m(r)$: mass with $\frac{dm}{dr} = 4\pi r^2 \epsilon(r)$

This is a coupled differential equation with the three unknowns: $p(r), m(r), \epsilon(r)$. This equation can be solved exactly by inserting the EoS $p(\epsilon)$, which is derived from the interaction of the fundamental particles and translated into a mass-radius relation. The derivation of EoS is anything but trivial and there are a variety of models with different assumptions available. A compilation of different equations of states connecting pressure to density is depicted in the left panel of Fig. 1.3, taken from [16]. In the right panel the corresponding mass-radius relation is shown in the same figure. In the upper right corner there are non-physical areas in which e.g. causality is violated. All these criteria contradict the assumption of an equilibrium between gravitational compression and the pressure of matter and thus a stable stellar object. By comparing the left and right panels of Fig. 1.3 the influence of the microscopic description on the final mass radius predictions is visible. The predicted EoS and thus the resulting radii and the maximum achievable masses are very different.

From astrophysical observations we know that the neutron stars PSR J0348+0432 and PSRJ1614-2230 [17, 18] both reached a mass of two solar masses. To illustrate the influence of the fundamental interaction on the final mass, we focus on a special case, the hyperon star. As matter becomes more and more compressed during the formation of a neutron star, the baryochemical potential increases. At some point it reaches the mass of the hyperon. Instead of further increasing the potential, it is therefore energetically advantageous to produce hyperons. The first prediction of strangeness inside a neutron star was formulated 1960 by [19]. Since Λ is the lightest hyperon ($M_\Lambda = 1115.683$ MeV/c^2 [1]), it should appear first. Now the hyperons act like a new degree of freedom. This softens the EoS, not allowing to reach the two solar mass limit. But the exact onset of the production of hyperons can be shifted by

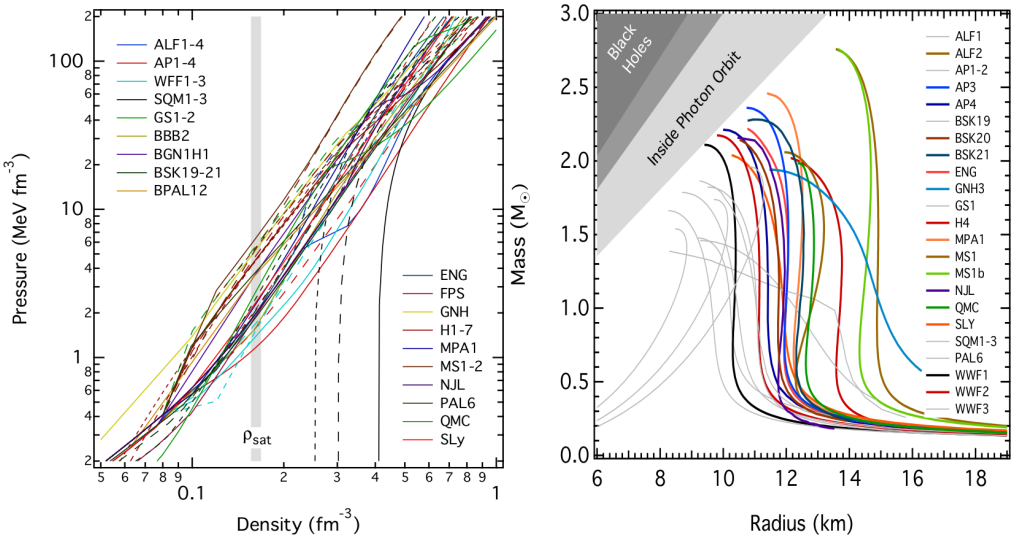

Figure 1.3: Left panel: pressure vs. density for a compilation of different EoS. Right panel: corresponding mass vs. radius relation taken from [16].

nucleon-hyperon interactions. If the interaction is attractive, it softens the EoS and the hyperon should appear earlier, which result in lower reachable mass-limits. For a repulsive interaction the EoS stiffens, where higher masses can be reached. The influence on the final mass vs. radius is shown in Fig. 1.4, where Quantum-Monte-Carlo simulations were performed [20]. In this approach, two body interactions and three body interactions are considered. Again the unphysical region is in the upper left corner where no stable stellar object can exist. Since masses up to two solar masses have been measured, each EoS must reach or exceed this limit. Let us first consider a simpler case where only neutrons are the components of the neutron star, represented by the green line in Fig. 1.4. We see that here the condition to reach two solar masses is fulfilled. If we now consider an attractive ΛN two-body interaction, which is shown in red, the prediction changes enormously. Now the EoS becomes very soft and therefore cannot reach the masses of the measurements. However, if we consider phenomenologically repulsive three-body interactions that were constraint to hypernuclei data, two different predictions can be made. For both predictions the EoS stiffens and thus higher masses can be achieved.

In the first case, however, the observation still cannot be reproduced, while in the second case the repulsive three-body interaction shifts the appearance of hyperons to a density too large to be compatible with NS.
In addition also χ-EFT calculations performed by [21] are included.
To complicate this picture, other particles (Σ, Ξ) can also be produced and, depending on the interaction, soften or stiffen the EoS. In order to understand the formation and structure of very heavy neutron stars and stellar objects on a large scale, it is therefore

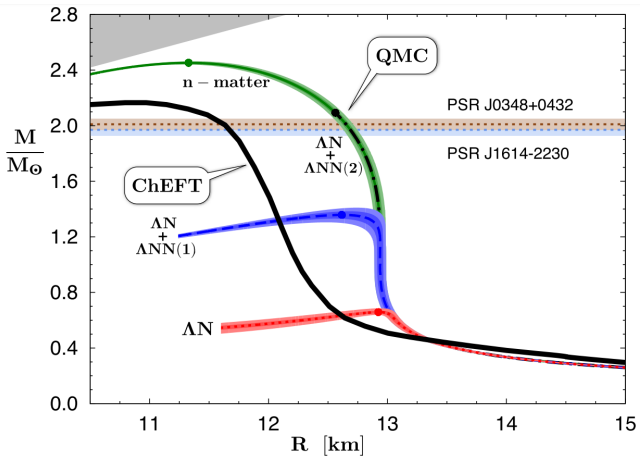

Figure 1.4: Mass vs. radius relation calculated with Quantum-Monte-Carlo taken from [20] and χ-EFT from [21]. The green curve indicates pure neutron matter, while the red curve included two-body ΛN interaction. The dashed and blue line include two different version of three-body interactions. The solid Black line depicts the χ-EFT calculations. Figure taken from [22].

crucial to understand the fundamental interactions of particles in the vicinity of normal nuclear matter at the microscopic level.

1.4 Hadron Masses

Protons, the lightest stable particles, consist of uud quarks with a rest mass of $M_p = 938.27$ MeV/c^2. They are part of the baryon octett, which is illustrated in the left panel of Fig. 1.5. If one compares the rest mass of the proton to the sum of the masses of the single constituents, which results in $M \approx 11.6$ MeV/c^2, it becomes clear that the total mass of the baryon is not only the sum of its components. One must consider that the mass of all quarks, fermions and the gauge bosons W^+, W^- and Z^0 is generated by the coupling to the Higgs boson in the Higgs mechanism [9]. But this mechanism cannot be held responsible for the entire observed mass.
The missing gap can be closed by introducing the spontaneous breaking of chiral symmetry, widely studied within the framework of χ-EFT. χ-EFT is an effective theory where, depending on the energy scale, hadrons or quarks are the degrees of freedom. For the description of the hadron mass, quarks are used as the degrees of freedom. The SU(3)$_{colour}$ colour symmetry and the U(1)-symmetry, which preserves the baryon number are conserved within χ-EFT [11]. However the $SU(3)_L x SU(3)_R$ symmetry, in the chiral limit where the quarks mass goes to zero, is the basic symmetry of chiral pertubative. This symmetry preserves the chirality of left- and right-handed

hardrons in strong interaction processes. However if one considers the ground state, the vacuum, this changes. The symmetry is broken by the non-vanishing expectation value of the ground state $<0|\bar{q}q|0>$, in which dynamically quark-anti-quark pairs are generated and destroyed. The non-vanishing expectation value of the ground state is called quark condensate.
By the interaction of a quark with this quark-anti-quark pair the chirality can be changed e.g. from q_r to q_l by the annihilation of q_r with the anti-quark of $<0|\bar{q}_r q_l|0>$, whereby the symmetry is broken. This spontaneous breaking of chiral symmetry produces additional mass of the hadrons in addition to the sum of the quark masses. This spontaneous breaking also predicts the eight Goldstone bosons ($\pi K \eta$), illustrated in Fig. 1.5 right. In contrast to the nuclear saturation density of $\rho_0 = 0.16$ fm^{-3} the density of the quark condensate is $|<\bar{u}u+\bar{d}d>| \approx 3$ fm^{-3}.

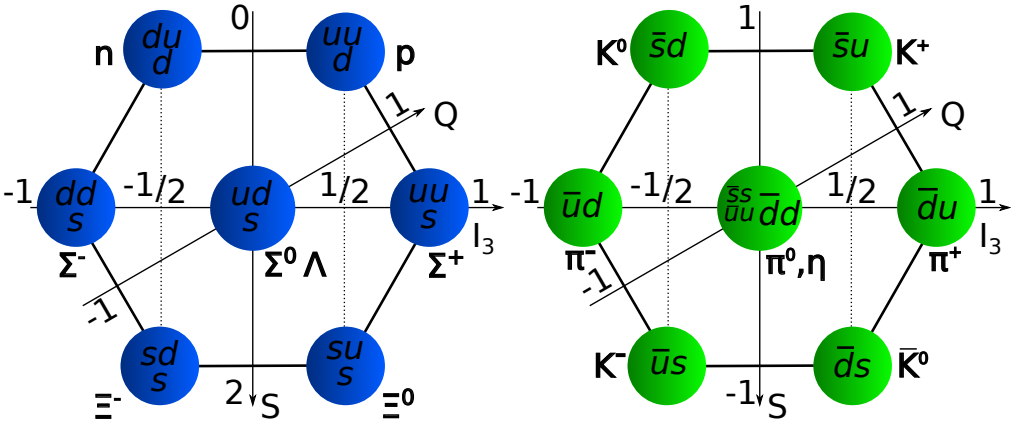

Figure 1.5: The baryon octet with $J^P = 1/2^+$ (left) and pseudoscalar meson octet $J^P = 0^-$ (right).

The π mass ($m_\pi \approx 140$ MeV/c^2) is described by the Gell-Mann-Oakes-Renner (GOR) relation [23, 24]:

$$m_\pi^2 f_\pi^2 = -\frac{m_u + m_d}{2} <0|\bar{u}u+\bar{d}d|0> \tag{1.3}$$

where

f_π: pion decay constant
m_u, m_d: first generation quark masses
$<0|\bar{u}u+\bar{d}d|0>$: expectation value of the ground state

The mass thus consists of an explicit part implied by the quark masses and the spontaneous part implied by the non vanishing vacuum expectation value. The

nucleon mass can also be calculated in a similar way using the so-called linear σ model [23]. Here the mass M_N follows the expression:

$$\begin{aligned} M_N &= g_\pi v_0 + \Sigma_{\pi N} \\ \text{where } \Sigma_{\pi N} &= \frac{m_u + m_d}{2} < N|\bar{u}u + \bar{d}d|N > \end{aligned} \tag{1.4}$$

Also here we distinguish the explicit symmetry breaking by the pion-nucleon $\Sigma_{\pi N}$ term and the spontaneous symmetry breaking is determined by the term $g_\pi v_0$

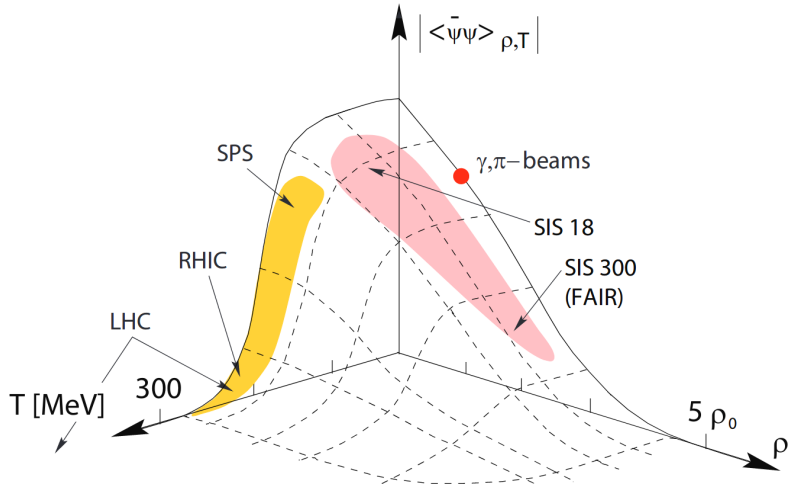

Figure 1.6: Expectation values of the chiral condensate as a function of the temperature and the nuclear density calculated with the Nambu-Jona-Lasinio model [25]. Indicated are the experimental accessible regions. HADES is located at the SIS18 point. Figure taken from [26].

By going further away from the vacuum by increased temperature and finite densities, the expectation value should decrease or even disappear completely. This would mean that the chiral symmetry is partially restored. Calculations for the chiral condensate $< \bar{q}q >$, predicted by the Nambu-Jona-Lasinio model [25] are shown in Fig. 1.6 taken from [26]. The expectation value is represented as a function of temperature T and nuclear density ρ_0. We see that with increasing temperatures and densities the expectation values decrease. In yellow the high energy experiments are shown. These probe high temperatures but low densities. The SIS18 (HADES) and the future facility FAIR/SIS 300 are shown in red. If we now look at Eq. (1.3) and Eq. (1.4), it is expected that the mass spectrum of hadrons in the vicinity of matter or temperature increase will change. To search for evidence of chiral restoration, HADES began to study the decay of vector mesons (e.g., ρ and ω) in the decay channel of di-electron pairs [27, 28]. Even though the branching ratios are quite

small, di-electrons do not participate in the strong interaction and thus act as an undisturbed probe. But if the change in the mass spectrum is a clear sign for the chiral restoration is part of discussions [29].
In the following, the in-medium modification of K^0, Λ and Σ^0 will be of particular interest as these particles are discussed in this thesis.

1.4.1 Kaons in Matter

The Goldstone boson (anti-)kaon has a rest mass of around $m_K \approx 500$ MeV/c^2. As explained above, their mass is the result of the chiral-symmetry breaking, partly explicit and spontaneous. The difference between kaon and its counterpart is their strangeness content where kaons have S = 1 and anti-kaons S = -1. The kaon can split into K^+ ($\bar{s}\,u$) and K^0 ($\bar{s}\,d$) and the anti-kaon into K^-($\bar{u}\,s$) and $\bar{K^0}$ ($\bar{d}\,s$). Therefore they can be completely distinguished by their charge, isospin and mass [30]. As in the later analysis only K^0_S are discussed, all other kaons are not treated in this chapter. But it has to be noted that due to isospin symmetry the behaviour of the K^+ and K^0 according to the strong interaction is identical. The interaction of the kaon with nuclear matter can be described within the χ-EFT framework, where the baryon octet of Fig. 1.5 are the new degrees of freedom. The first calculations of the interaction of kaons with matter was performed by Kaplan and Nelson [31, 32]. For the study of this interaction a chiral kaon-nucleon effective Lagrangian was used [30]:

$$\mathscr{L} = \underbrace{\bar{N}(i\gamma^\mu\partial_\mu - m_N)N}_{\text{nuc. inter.}} + \underbrace{\partial^\mu\bar{K}\partial_\mu K}_{\text{kin. term}} - \underbrace{\left(m_K^2 - \frac{\Sigma_{KN}}{f_\pi^2}\bar{N}N\right)\bar{K}K}_{\text{Kaplan-Nelson}} - \underbrace{\frac{3i}{8f_\pi^2}\bar{N}\gamma^\mu N\bar{K}\overleftrightarrow{\partial^\mu}K}_{\text{Weinberg-Tomozawa}} \quad (1.5)$$

with

$N(\bar{N})$ and $K(\bar{K})$: nucleon and kaon field
$N = \begin{pmatrix} p \\ n \end{pmatrix}$ $\bar{N} = \begin{pmatrix} \bar{p} & \bar{n} \end{pmatrix}$, $K = \begin{pmatrix} K^+ \\ K^0 \end{pmatrix}$ $\bar{K} = \begin{pmatrix} K^- & \bar{K^0} \end{pmatrix}$
m_n and m_K: nucleon and kaon mass
Σ_{KN}: kaon-nucleon sigma term
f_π: pion decay constant

Besides the nuclear interaction term and the kinetic term, two special terms are included in the Lagrangian. The Kaplan-Nelson term predicts an attractive kaon-nucleon interaction based on the scalar interaction, both for kaons and anti-kaons. This interaction is proportional to $\Sigma_K N$ term, that is related to the content of

the strange quark in the nucleus. This value is poorly constraint and ranges from $\Sigma_K N = 270-450$ GeV/fm depending on the model [33]. The Weinberg-Tomozawa term describes the vector-nucleon interaction, which is repulsive for kaons (attractive for anti-kaons). In the mean-field approximation the kaon dispersion relation in matter can be deduced:

$$\omega^2(\vec{k},\rho_N) = m_K^2 + \vec{k}^2 - \frac{\Sigma_{KN}\rho_S}{f_\pi^2} \pm \frac{3}{4}\frac{\omega}{f_\pi^2}\rho_N \tag{1.6}$$

with

m_K : mass of the kaon
$\vec{k}$: three-momentum vector of the kaon
Σ_{KN} : kaon-nucleon sigma term
f_π : pion decay constant
ρ_S and ρ_N : scalar and nuclear density

All terms beside the mass and the three momenta are summarised in a so-called self-energy $\Pi(\omega,\vec{k},\rho_N)$, which includes all treated interactions within nuclear matter. This can be translated to the kaon in-medium energy given by:

$$E(\vec{k},\rho_N) = \left[m_K^2 + \vec{k}^2 - \frac{\Sigma_{KN}\rho_S}{f_\pi^2} + \left(\frac{3}{8}\frac{\rho_N}{f_\pi^2}\right)^2 \right]^{1/2} \pm \frac{3}{8}\frac{\rho_N}{f_\pi^2} \tag{1.7}$$

The last term is called Weinberg-Tomozawa and the sign is positive for kaons and negative for antikaons. Hence for kaons, the effective in-medium energy and therefore the effective mass is increased with increasing density. This can have a huge impact on the production of the K^0 as depicted in Fig. 1.7.

Here the measured K^0 cross-section by FOPI [34] in pion induced reactions at an incident momentum of $p_{\pi^-} = 1.15$ GeV/c on a lead target was normalised to carbon as a function of momentum and is depicted by the blue squares. For the K^+, similar measurements have been performed by ANKE [35], with proton induced reactions on gold with a beam energy of $E_p = 2.3$ GeV, depicted by the pink circles, also normalised to carbon. These predictions have been compared to the HSD model [36] for different potentials. For both experimental data sets a steep drop of the ratio is visible for lower momenta with a maximum around $p = 200$ MeV/c. In both cases the ratio gets rather flat for higher momenta above $p = 500$ MeV/c. If we compare these distributions to the HSD predictions, we see that the prediction without a repulsive in-medium potential for the kaons presents a rise of the ratio at lower momenta. This is completely in contradiction to the experimental observations. If a

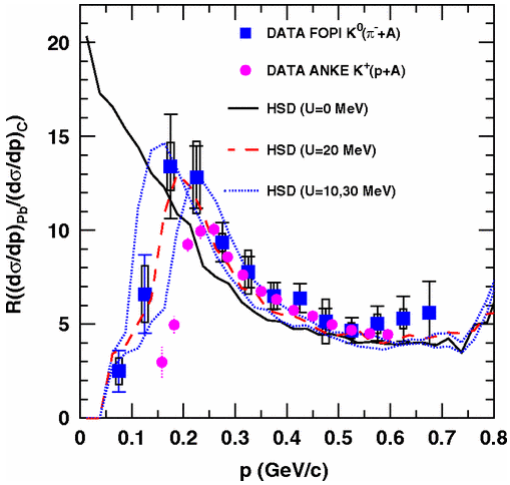

Figure 1.7: Ratio of K^0 cross section of lead normalised to carbon as a function of momentum in pion induced reaction measured by FOPI [34], illustrated by the blue squares. The circles show the K^+ cross-section of gold normalised to carbon in proton induced reactions by ANKE [35]. These results are compared to the HSD model [36] for different potentials. Figure taken from [34].

repulsive potential between 10 and 30 MeV is included in the calculations, the trend of the experimental data is reproduced, even though the exact potential strength is difficult to determine.
The systematic study of the kaon in-medium modification was also studied by the HADES collaboration [37].

The measured ratio of kaons emitted between $10° < \Theta < 20°$ and $20° < \Theta < 30°$ is depicted in Fig. 1.8. Here the GiBUU [4] model was used, including a repulsive KN potential computed within the χ-EFT framework. The dependence of the repulsive potential upon the kaon momentum and baryon density is shown in Fig. 1.9. The blue curve in Fig. 1.8 corresponds to the predictions without the potential, while the cyan curve show the prediction with the potential. Again a clear signature of the repulsive kaon interaction can be seen. A potential of $U \approx 35$ MeV was extracted from this analysis.

1.4.2 Λ in Matter

The first Λp scattering experiments in vacuum were carried out in 1968. They were measured with the 81-cm Saclay hydrogen bubble chamber by [38] and [39] at CERN. In total around 600 elastic events were observed, for both experiments combined. To produce the Λ hyperon a K^--beam was employed that was produced with a momentum of $p_{K^-} = 800$ MeV/c and then slowed down in a 20 cm copper absorber

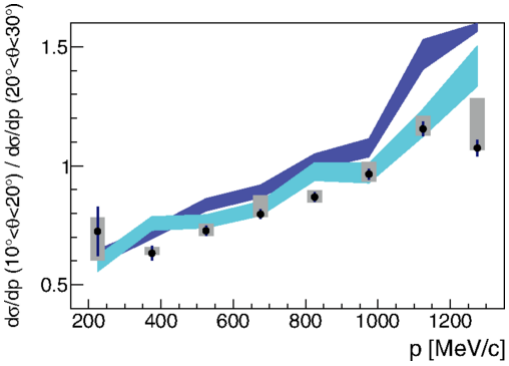

Figure 1.8: Ratio of K^0 cross-section for different angle intervals as a function of the momentum in p+Nb reactions at 3.5 AGeV [37]. For the predictions the GiBUU [4] code was used where a fully χ-EFT potential is implemented as illustrated in Fig. 1.9. Depicted by the black points are the experimental data, the blue curve show the predictions of GiBUU without the potential and cyan with the potential. See text for details.

to a final momentum of $p_{K^-} = 230$ MeV/c. These K^- entered the hydrogen bubble chamber and came to rest, where it eventually reacted inelastically with a proton and produce a Λ. The following production channels have been considered:

1. $K^- + p \rightarrow \Lambda\pi^0$
2. $K^- + p \rightarrow \Sigma^0\pi^0, \Sigma^0 \rightarrow \Lambda + \gamma$
3. $K^- + p \rightarrow \Sigma^-\pi^+, \Sigma^- + p \rightarrow \Lambda + n$
4. $K^- + p \rightarrow \Sigma^-\pi^+, \Sigma^- + p \rightarrow \Sigma^0 + n, \Sigma^0 \rightarrow \Lambda + \gamma$

Channel 2) was identified as the primary production channel with an overall occurrence of 70% [38]. Due to the different production channels in vacuum, these channels populate different regions in the momentum phase space. The dominant channel is in the range of $90 < p_\Lambda < 250$ MeV/c. For low momenta Λ reaching the production threshold, channel 4) populates the spectra in the range of $0 < p_\Lambda < 130$ MeV/c.

The final state Λ can then eventually scatter with another proton. In total around 100k Λ have been measured, but only 336 recorded events fulfilled the criteria for elastic scattering. Still six momentum bins have been chosen to extract the cross-section. The elastic cross-section of Λ with a proton as a function of the hyperon momentum taken from [40] is depicted in Fig. 1.10. The black filled circles illustrate the results from [38].

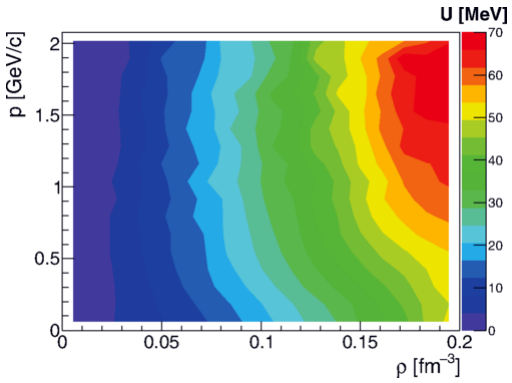

Figure 1.9: Implemented kaon-nucleon potential as a function of the momentum and density of [37] in the GiBUU [4] code.

Also other experiments contributed to world data, where the open squares correspond to [39] and the open circles to [41]. These cross-sections have been compared to calculation using χ-EFT from [40]. Here the green band in Fig. 1.10 corresponds to **l**eading **o**rder (LO) and the red band to **n**ext-to-**l**eading **o**rder (NLO) calculations. For the low momenta and the momentum range of $300 < p_\Lambda < 600$ MeV/c the NLO calculation fits better to the data. However no scattering data are available in the low momentum part below 100 MeV/c. To reach this low part femtoscopy can be used, which shows very promising results [42].

Still these data were recorded in vacuum and not at finite densities. Information on the interaction of the Λ hyperon close to ρ_0 are available from hypernuclei. Here hyperons are bound in the nucleus. If such a hypernuclei exists, this implies that for low momenta, the interaction for this specific hyperon must be attractive. But the determination of such binding energies are still model dependent and performed at saturation density. Various hypernuclei have been measured for the Λ, which is depicted in the upper panel of Fig. 1.11. Indeed a whole chart of hypernuclei could be deduced.
The binding energy for the hypernuclei in different reactions are depicted in the lower panel, same figure taken from [43] based on [44]. The binding energies itself have been extracted employing a 3-parameter Woods-Saxon potential [45]. Also more exotic hypernuclei could be produced like double Λ Helium [46] or double Λ Beryllium [47, 48]. Here also the Λ Λ interaction could be studied, which suggest a slight attractive interaction. In addition also a Σ helium hypernuclei could be produced [49]. Even for the double-strange Ξ data is available [50, 51, 52]. But besides these measurements no conclusive picture could be derived at finite densities and momenta, where the hyperons traverse the medium.

However, predictions of the in-medium modification of Λ and Σ^0 can be calculated within the framework of χ-EFT.

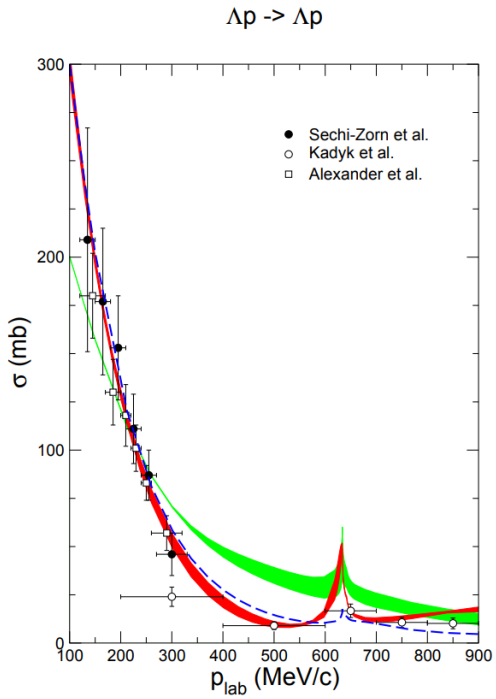

Figure 1.10: Cross-section of elastic Λp scattering taken from [40]. Black filled circles correspond to data from [38], open circles from [41] and open squares from [39]. Green band corresponds to χ-EFT LO calculations and red bands to NLO performed by [40].

The real part of the single particle potential is illustrated in the left panel of Fig. 1.12 as a function of momentum for symmetric nuclear matter [54]. The green solid curve corresponds to a Fermi-momenta of $k_F = 1.00$ fm^{-1} ($\rho = 0.4\ \rho_0$ [fm^{3}])[1], the red dotted line to $k_F = 1.35$ fm^{-1} ($\rho = 1.0\ \rho_0$ [fm^{3}]) and the blue dotted line to $k_F = 1.53$ fm^{-1} ($\rho = 1.5\ \rho_0$ [fm^{3}]), with the nuclear saturation density $\rho_0 = 0.16$ fm^{3}. It is apparent that for low momenta the single particle potential of the Λ is attractive, while the absolute depth of the potential depends on the nuclear density. This is crucial as various experiments confirmed the existence of hypernuclei [53], where a attractive interaction at low momenta becomes necessary. For higher momenta a repulsive interaction is predicted. The onset of this repulsive part starts for higher densities at lower momenta.
The real part of the single particle potential of the Σ^0 is depicted in the right panel of Fig. 1.12, with the same densities and colour codes as for the Λ. It is apparent that the in-medium behaviour of the Σ^0 significantly deviates from that of the Λ. Here only for the lowest density a shallow attractive interaction is predicted at low

[1] $\rho_{symmetric} = \rho_n + \rho_p, \rho_n = \rho_p = \frac{(k_F)^3}{3\pi^2}$

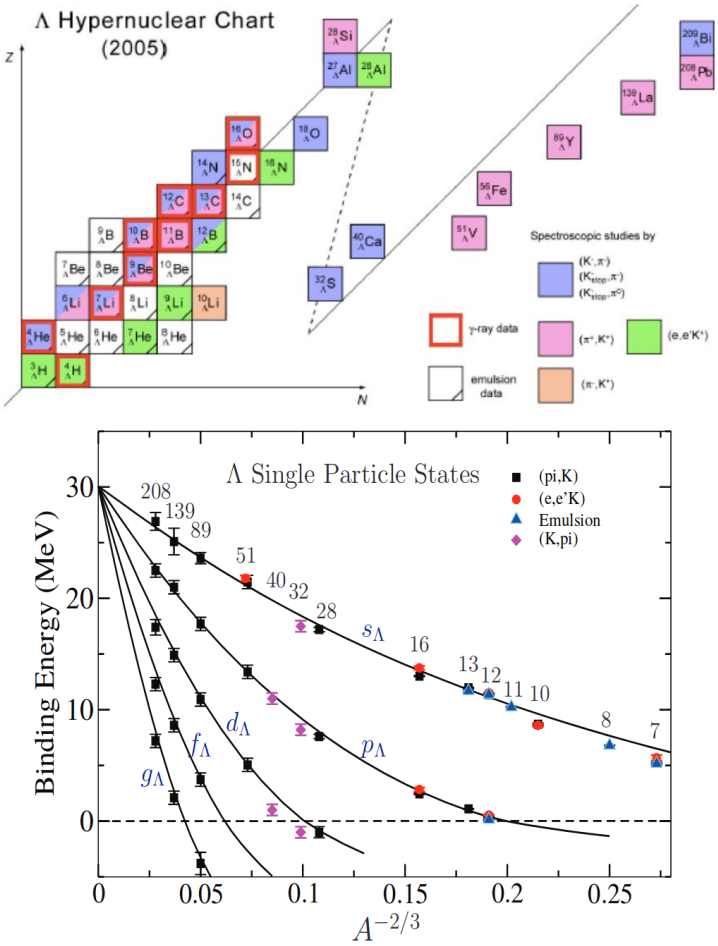

Figure 1.11: Upper: Chart of confirmed Λ hypernuclei taken from [53]. Lower: compilation of Λ binding energies taken from [43], based on [44] from different reactions. The energies have been calculated using a 3-parameter Woods-Saxon potential [45].

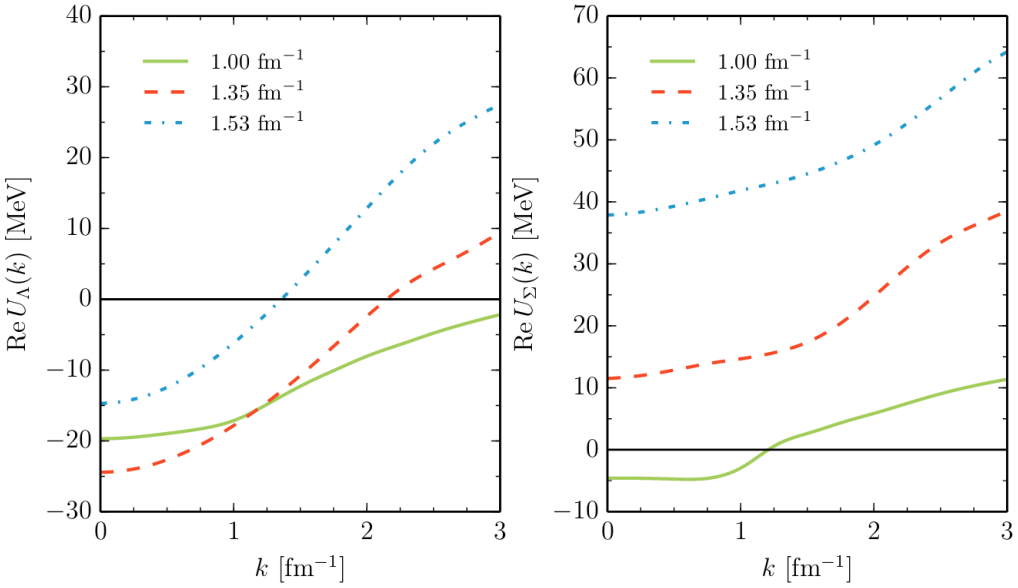

Figure 1.12: Real part of the χ-EFT single particle potential take from [54]. On the left predictions for the Λ and on the right for the Σ^0 are shown. The different line colours correspond to different Fermi momenta of $k_F = 1.00$ fm^{-1} (solid green, $\rho = 0.4\ \rho_0$), $k_F = 1.35$ fm^{-1} (dotted red, $\rho = 1.0\ \rho_0$) and $k_F = 1.53$ fm^{-1} (dotted blue, $\rho = 1.5\ \rho_0$).

momenta. With increasing density and momentum the interaction is predicted to be predominantly repulsive.
To test experimentally these predictions based on χ-EFT for the in-medium behaviour of hyperons at finite momenta, the hyperon must traverse a nuclear medium. This can either be realised by photon, proton or π induced reactions with a nucleus where the hyperon is surrounded by the remaining nucleons or nucleus-nucleus collisions, where also higher densities are accessible.
Often these data are combined with predictions from transport codes, where different interactions can be implemented and compared to the data. Such an approach is part of this thesis in Chapter 6, where the in-medium behaviour of the Λ and Σ^0 was studied to contribute to the scarce available in-medium data.

2
Pion Beams at HADES

2.1 Pion Beam Facility

Many different accelerators in different energy regimes are available all over the world, most of them have in common that they accelerate particles like protons, nuclei or electrons.
By improving accelerator technology, this has become day-to-day business, but also more exotic beams became available.
One example is the GSI fragment separator (FRS), where rare unstable isotopes are produced in spallation processes and selected with the FRS [55]. Such experiments are not feasible in a normal laboratory environment or with standard accelerators.
If we consider μ, π, K, $\bar{p}$ or generally antiparticles, similarly to the rare unstable isotopes, the hadrons have to be produced in nuclear reactions and then selected by the beam optics. A so-called secondary beam facility is required to produce, identify, select and transport the desired particle species.
The first step is to use a primary beam (protons or ions) and hit it on a fixed target, where nuclear reactions produce a large mixture of fragments/nucleons, but also π, K among other hadrons. By adjusting the accelerated particle, the beam energy and target nucleus, the admixture and momentum of the particles of interest can be tuned to some extend, as depicted in Fig. 2.1 for a secondary π-beam.

Due to momentum conservation these fragments follow the direction of the beam in a cone with a non-monochromatic momentum distribution. To guide the beam along the beam line to the experimental setup and to select the desired mo-

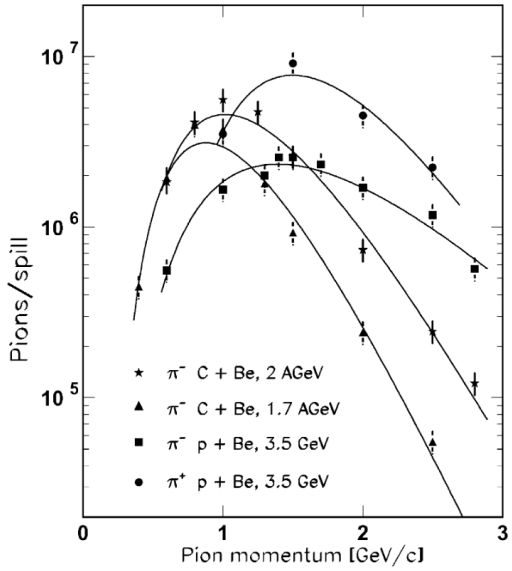

Figure 2.1: Pions/spill as a function of the π momentum at the HADES target position. The secondary π momentum distribution is shown for different primary beams (proton, carbon), impinging on Beryllium for different primary beam-momenta, taken from [56].

mentum and polarity of the particles, quadrupole and dipole magnets are used. As these particles are decaying in flight, there is a correlation between the desired beam-momentum, which is selected by the dipoles in combination with the length of the beam-line and the achievable particle flux.
Experimental data used in the framework of this thesis were recorded in the year 2014 with the **H**igh **A**cceptance **D**i-**E**lectron **S**pectrometer (HADES) experiment using a secondary π^--beam. HADES is located at the Gesellschaft fuer Schwerionenforschung (GSI), Darmstadt. The **Uni**versal **L**inear **Ac**celerator (UNILAC) preaccelerates particles to a kinetic energy of E = 11.4 MeV/u, while the accelerator stage of the **S**chwer-**I**onen-**S**ynchrotron 18 (SIS18) accelerates the to their final energy. Here protons can reach a kinetic energy up to E = 4.5 GeV and heavy ions up to E = 2 AGev. A schematic overview of the GSI facility is illustrated in Fig. 2.2.

For the production of the secondary π^--beam a primary nitrogen (N) beam at a primary central energy of E = 2 AGeV with $\approx 10^{11}$ particles/spill (spill $\approx 4s$) was impinging on a 1.84 g/cm^2 dense Beryllium (Be) target. This configurations are based on studies by [56], depicted in Fig. 2.1, where it was found that fully stripped carbon or nitrogen ions, that where close to the SIS18 space charge limit of $\approx 10^{11}$ ions/s, at this primary beam energy lead to a maximum intensity of negative pions at the HADES target. Due to technical reasons a nitrogen beam was chosen.
Moreover the anticipated momentum range of 0.656 GeV/c $< p_\pi^- <$ 1.7 GeV/c for the

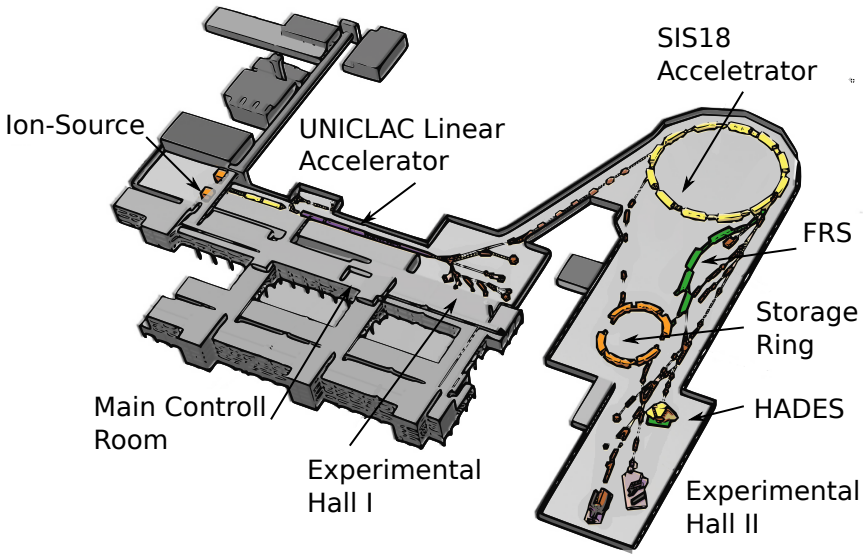

Figure 2.2: Illustrative overview of the GSI-SIS18 accelerator facility. Ions get pre-accelerated with the UNILAC and reach their final kinetic energy in the SIS18 synchrotron. Depending on the requirement the beam gets transported to different locations, e.g pion-beam chicane.

negative pion campaign with HADES could be covered by this configuration.

The fragments leaving the Be target, with a certain pion fraction, enter then the pion-chicane where they get selected with combinations of dipole and quadrupole magnets as depicted in Fig. 2.3.
As this selection procedure has a finite acceptance, the beam is not monochromatic ($\Delta p/p \approx 8\%$). For a detailed description of the pion-chicane see [57]. The remaining electron and muon contamination at the target position was found to be below 1% [56, 57]. In order the get the momenta of every individual π^- with a high precision ($\Delta p/p < 0.5\%$), the detector system CERBEROS developed at the TUM (see Section 2.2.1) has been successfully installed in the pion-beam chicane [57].
Finally a resulting intensity of around $\approx 3 \times 10^5$ π^-/s reaches the HADES target.

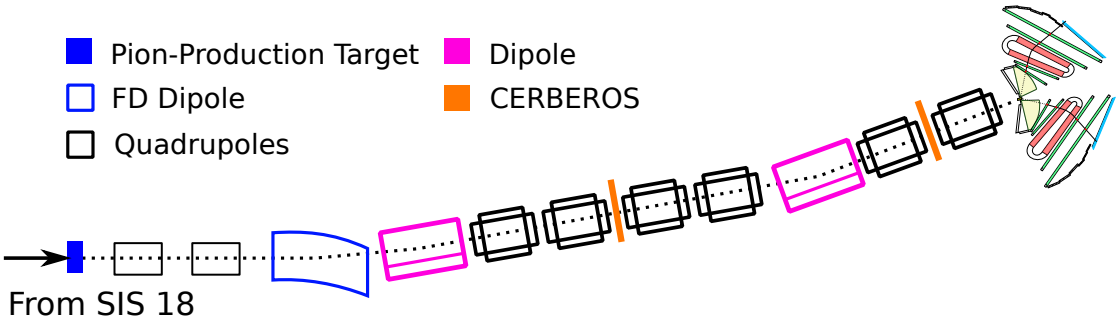

Figure 2.3: Schematic overview of the pion-beam chicane. The primary beam from the SIS18 hits the production target from the left and produces secondaries including pions. These get selected and transported via dipole and quadrupole magnets while their momentum is measured with the CERBEROS detector.

2.2 High Acceptance Di-Electron Spectrometer (HADES) Experiment

The following chapter gives an overview of HADES, concentrating on all important subdetector systems and explaining their technical basics.
HADES is a fixed target experiment at the GSI Helmholtzzentrum für Schwerionenforschung in Darmstadt, Germany. The beam is delivered by the SIS18 accelerator, which can deliver heavy ions with a kinetic energy in the range of 1-2 AGeV for heavy ions. Kinetic energies of up to 4.5 GeV are available for proton-induced reactions with a maximum intensity of 10^{11} ions per 4s extraction cycle.
HADES consists of six identical detector segments surrounding the beam guide. Each of these segments consists of the internal **R**ing **I**maging **Ch**erenkov (RICH) detector followed by a two **M**ini **W**ire Drift **C**hambers (MDC), MDC I and MDC II. For momentum identification a superconducting magnet after the inner MDCs is used, followed by the outer MDC III/IV. For the trigger decision the **M**ultiplicity and **E**lectron **T**rigger **A**rray (META) is employed at the end of each segment.
A schematic overview is shown in the Fig. 2.4.
This detector allow almost for an complete coverage of the azimuthal plane and a polar angle coverage of $18° < \Theta < 85°$ for single charged particles with an average momentum resolution of $\frac{\Delta p}{p} \approx 4\%$. A detailed description of the spectrometer can be found in [58].

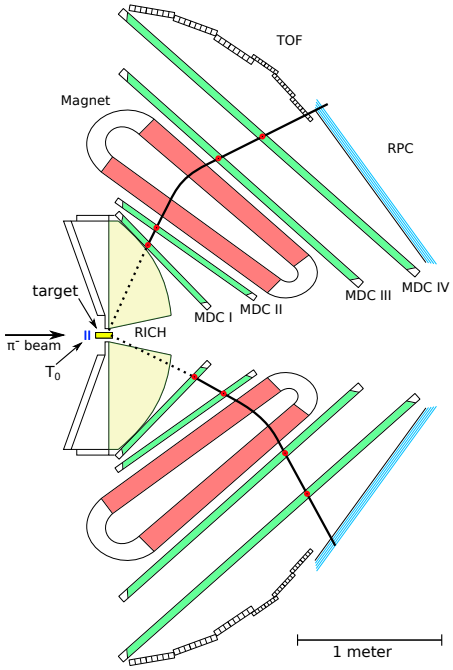

Figure 2.4: The HADES detector setup in a schematic cross-section with all its important detector components. The beam enters the detector from the left.

2.2.1 CERBEROS Detector

Since the momentum spectrum of the secondary π^- at the HADES target is wide ($\Delta p/p \approx 8\%$) a dedicated tracking system was developed. The pion-beam chicane has been equipped with the so called **Ce**ntr**r**al **Be**am T**r**acker for Pi**on**s (CERBEROS) tracker, consisting of two silicon tracking stations located at position C1 and C2 which is depicted in Fig. 2.3. Both tracking station consist of double sided p-type doped silicon strip detector for enhanced radiation hardness [57].
A detection area of 10x10 cm^2 with a corresponding detector thickness of 300 ± 10 μm has been chosen. The detector is double-side segmented with 128 parallel strips with a length of L = 97.22 mm, a width of W = 700 μm and a pitch of Δ = 760 μm. The strip orientation of the rear and the front are perpendicular to each other and therefore are a maximum binary position resolution of $\Delta/\sqrt{12} = 219$ μm can be reached. The momentum of each pion is then determined by the evaluation of the beam optic transport [57] and the hit position in the double sided-silicon detectors at the position C1 and C2.
To enhance the radiation hardness and reduced the electronic noise, both detectors are operated at temperatures around -5°C. A photograph of the fully assembled detector system without the top cover is presented in Fig. 2.5. The detectors are readout with the so called n-XYTER ASIC, which features a self-triggered readout

and local storage capabilities. For the later on performed event builder every registered pion-hit is assigned with a time-stamp for later on performed correlation with the other HADES sub-detectors. In total a readout rate of 32 MHz was achieved corresponding on average to 160 kHz per channel. The data is then transported through the TRB3-net (Section 2.2.8), which is the HADES data acquisition system. The timing signal of the CERBEROS ($\sigma = 8$ ns) coincident within a 400 ns window with respect to the T_0 target detector to suppress pile-up in the tracking stations. In the experiment the detector cope with a rate of 7 MHz at the first tracking position C1 and 800 kHz at the second tracking station C2. It was found that the detection efficiencies are $\epsilon = 92.5\%$ and $\epsilon = 93.2\%$ at C1 and C2, respectively. The overall resulting detection efficiencies was found to be 87.0%.
The detector system allows for an online beam monitoring with a rate capability up to $< 10^6$ particles, while maintaining a momentum resolution of $\Delta p/p <$ 0.5% for each single pion. The latter is mandatory for the analysis of reactions like $\pi^- + p \rightarrow n + e^+ + e^-$ where a disentanglement of the different resonance contributions demands a momentum reconstruction on a per-mil level.
A further key feature of the system is, that it can be fully integrated into the existing beam line, withing the vacuum environment, without any entrance windows.

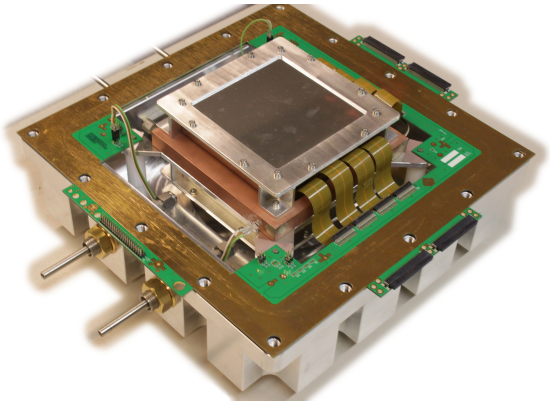

Figure 2.5: Top view of a single stage of the CERBEROS system without the top cover. Picture taken from [59].

2.2.2 Target T_0 Detector

For the optimisation of the beam profile and the generation of a fast T_0 timing signal, a T_0 detector is located 2 cm upstream to the HADES reaction target. The detector is based on a 300 μm mono-crystalline diamond produced by a **C**hemical **V**apour **D**eposition (CVD) process. The detector system consist of a 3x3 matrix of CVD diamond sensors with a fourfold segmented readout, which are mounted on two

subsequent PCBs containing 4 and 5 detectors as illustrated in Fig. 2.6. A typical signal-rise time (10%—90%) of $\tau_{rise} \approx 1.35$ ns with an corresponding timing precision of $\tau_{prec} < 250$ ps and a Signal/RMS noise ration of 30:1 has been achieved.

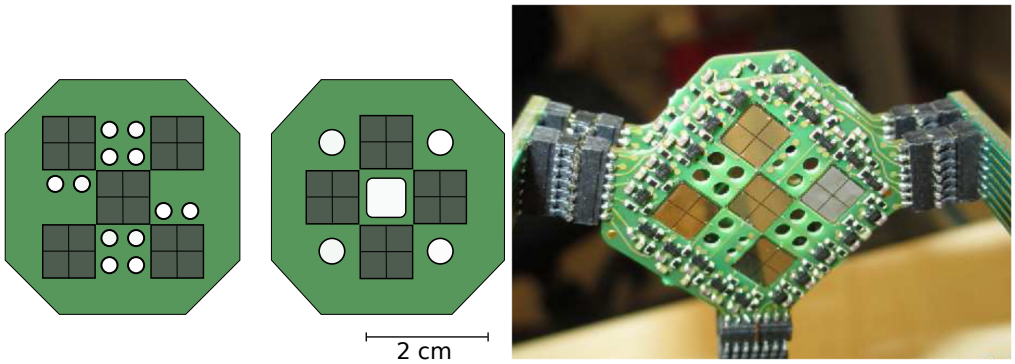

Figure 2.6: Schematic illustration of the subsequent mounted PCB with the fourfold CVD diamond detector structure on the left and a photograph of the ready detector on the right. Schematics adapted from [59] and picture taken from [56].

2.2.3 Target

The HADES target is located in the centre of detector (schematic drawing Fig. 2.4), 2 cm behind the T_0 detector. Due to the toroidal magnetic field (see Section 2.2.5), the area around the target is nearly free of any artificial magnetic fields.
A wide range of targets can be employed including liquid, e.g. liquid hydrogen and solid targets. Solid targets are either divided into several segments or consist of a single piece. The single segment length are depending on their density to reduce scattering and energy loss of the particles inside the target. The different targets of the experimental pion beam campaign are depicted in Fig. 2.7.
They are mounted and fastened with thin carbon structure. Listed in Table 2.1 is a summary of all important target properties.

2.2.4 RICH Detector

The **R**ing **I**maging **Ch**erenkov (RICH) detector is the closest detector to the target and used for the identification of e^+e^-- pairs in the momentum range of 0.1 GeV/c $< p_{e^\pm} <$1.5 GeV/c. A schematically cross-section of the radiator and gas filled detector is shown in Fig. 2.8, for details see [60].
All particles coming from the target have to traverse the detector gas volume of Perfluorobutane (C_4F_{10}), where the average length is 36-60 cm, depending on the incident angle.

Target	Diam.	Length	Dens. ρ [g/cm^3]	p_{π^-} [GeV/c]	Dist. Seg.
W	12	2.4	19.3	1.7	18
C	12	7.2	1.85	1.7	18
PE	12	46	0.97	0.69	-

Table 2.1: Material properties of the pion beam targets. All diameters, length and distances are in [mm]. The first two columns read the diameter and length of the segment. This is followed by the density and the momentum of the impinging pion beam. The last column reads the distance of two subsequent segments.

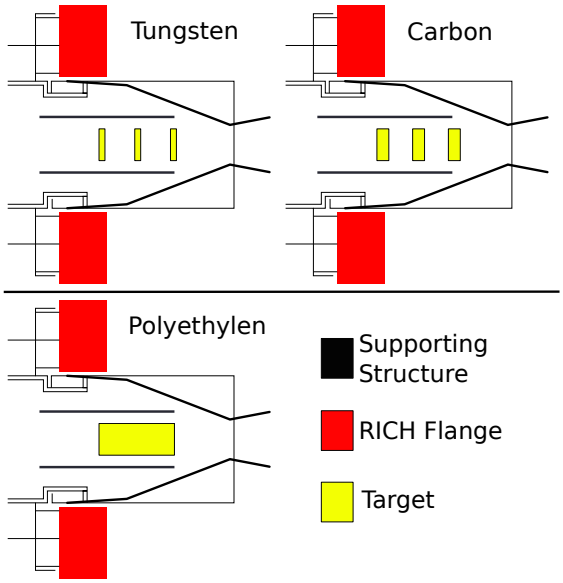

Figure 2.7: Schematically drawing of the three solid targets used in this thesis.

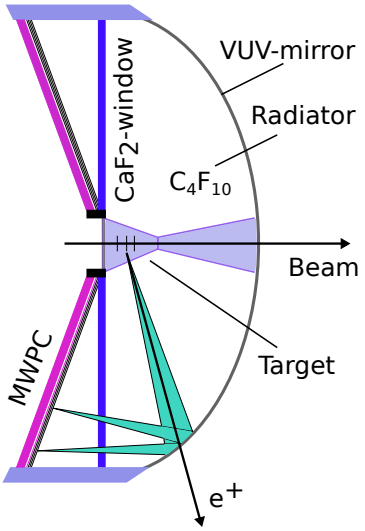

Figure 2.8: Schematic cross section of the RICH detector. The target is located in the middle of the detector, so every reaction particles have to pass this detector. Only Leptons overcome the threshold for the Cherenkov-radiation, producing a light cone, which gets detected on the back plane with MWPC after reflection. Schematic adapted from [59].

To create Cherenkov radiation the particle has to exceed the threshold in C_4F_{10} of $\gamma_{thr} \approx 18$ where $\beta = \sqrt{1-\frac{1}{\gamma^2}} = \frac{v}{c}$. This correspond to $\beta \approx 0.99$. While the electrons and positrons are nearly travelling at the speed of light, hadrons are in the range of $\beta < 0.95$ at SIS18 energies. The RICH is therefore hadron blind. Typically 100-200 Photons are produced by traversing e^+/e^- with an opening angle of $cos(\theta) = \frac{1}{\beta n}$, where n is the refractive index. These photons get reflected on the mirror plane and redirected through a calcium fluoride window (CaF_2) to the multi-wire proportional chambers. These have a thin caesium-cathode for the photon-electron conversion, with a total detector granularity of 28 000 Pads. Including the typical efficiency of the RICH ($\epsilon \approx 5\%$) 5-10 photons per electron can be reconstructed.

2.2.5 Magnet

The trajectory of every charged particle moving in a magnetic field is bent by the Lorentz force. By measuring their bending radius after the reconstruction of their path trough the detector (see Sec 2.2.6) and knowing their charged state, the momentum of a particle can be deduced. The key component is the super-conducting toroidal magnet ILSE [1], which consist of six identical coils, placed symmetrically

[1] **I**ron **L**ess **S**uperconducting **E**lectron Magnet

around the beam pipe, located between MDC chamber II and III. This design keeps the magnetic field in the surrounding detector components low ($B_{MDCI} \approx 0.08$ T) and reaches its maximum of $B_{Max} \approx 3.6$ T at the sector edge. In between two coils a magnetic field of $B_{Max} \approx 0.9$ T is reached.

2.2.6 Mini Wire Drift Chambers

For the reconstruction of charged particles traversing the HADES, it is equipped with 4 planes of **M**ini Wire **D**rift **C**hambers (MDC) (I - VI), two upstream and two downstream the magnetic coils (Fig. 2.4). Following the geometry of HADES, each MDC is divided into six identical chambers with trapezoidal shape. Each of this chamber consist of six planes, with different orientations to maximise spatial resolution. Depicted in Fig. 2.9 is an schematic of one of the chambers. The inner chambers are continuously flushed with Argon as a counting gas and CO_2 for quenching in the ratio 70:30. The outer chambers use a gas mixture of 84% Argon 16% Isobutane (C_4H_{10}). Every particle traversing these chambers ionising the gas on their way, leaving a track of electrons and ions. These electrons are multiplied in the electric field by avalanche effects and drift to sense wires, where they induce an electric signal which can be read-out. With this the hit position in every single MDC can be reconstructed. Due to the near field-free environment outside the magnet, straight trajectories of the particles are expected from MDC I to MDC II (inner track segment) and MDC III to MDC VI (outer track segment) with an inclination due to the magnetic field between planes II and III.
The resulting particle trajectory and momentum is then reconstructed numerically with a Runge-Kutta tracking algorithm including hits in the MDCs, the precisely known magnetic field map and eventually hits in the META system. With this procedure a momentum resolution of $\frac{\Delta p}{p} \approx 1-4\%$ is achieved.
As the principle of the MDCs is based on the ionisation and therefore the energy-loss of the traversing particles, also dE/dx can be retrieved. Since no **A**nalog **D**igital **C**onverter (ADC) was present, this is done by **T**ime-**o**ver-**T**hreshold (ToT), where the time over a pre-defined threshold is measured, which is proportional to the energy loss. However the calibration is rather complicated as the procedure depends on the local electric field, the geometry of the track and other effects. Finally an energy loss resolution $\frac{\Delta E}{E}_{MinIP} = 7\%$ for minimum ionising particles and $\frac{\Delta E}{E}_{MaxIP} = 4\%$ for strong ionising particles could be achieved. This feature can be used for the particle identification.

2.2.7 META System

The detector system of HADES for trigger information and measuring time-of-flight of each individual particle is the **M**ultiplicity and **E**lectron **T**rigger **A**rray (META),

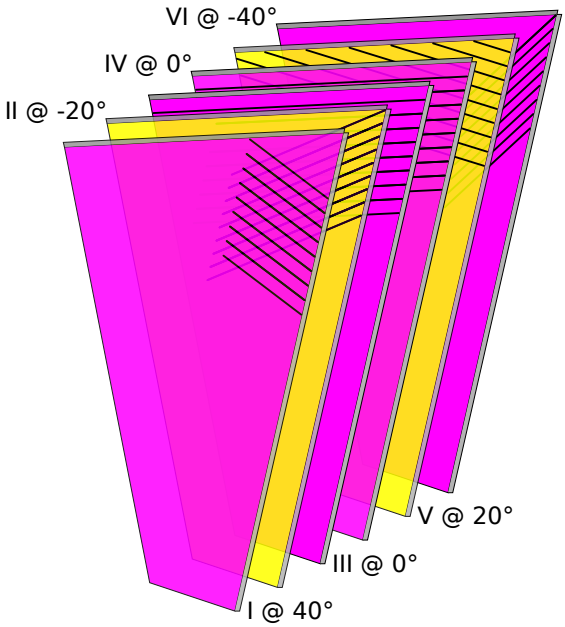

Figure 2.9: Schematic illustration of a MDC chamber. Each chamber consist of six planes, all with different orientation for enhanced position resolution.

which consist of two detector systems, different in technology and coverage.
In the low angle region of $12° < \theta < 45°$, time measurement is performed with **R**esitive **P**late **C**hambers (RPC) while the **T**ime **O**f **F**light (TOF) detector system cover the high polar angles of $44° < \theta < 88°$.

TOF Detector

The TOF detector consist out of 384 scintillator rods, arranged in eight planes with eight rods, maintaining the six folded HADES symmetry. The rod diameters D ranges from 20x20 mm^2 to 30x30 mm^2, while the length L varies from 1475 to 2365 mm. Traversing particles produce scintillating light insight the rods, converted into electrons and amplified by **P**hoto-**M**ultiplier-**T**ubes (PMT) at the end of both sides of each individual rod.
The arrival time of the particle can then be calculated by the arrival time of photons on the left and right PMT with $t_{TOF} = \frac{1}{2}(t_{right} + t_{left} - \frac{L}{v_M})$, where v_M donates the speed of light in medium. With this setup a time resolution of $\sigma_T < 150$ ps can be reached.

RPC Detector

The RPC system is build up by multiple small independent detector cells, retaining the six folded structure of HADES. A single cell is constructed with a multi-layer conductor-isolator-conductor pair, enclosed in an aluminium casing for cross-talk reduction, as depicted in the left panel of Fig. 2.10. A high potential is applied between these pairs, causing a short-circuit by minimum ionising due to traversing charged particles. This leads to a high detection efficiency. The potential drop is stopped by the insulating glass layer, setting the cell back to its initial state. To increase detection efficiency and acceptance, two layers of these cells are used. A single layer would have dead detector spots, introduced by the insensitive but necessary aluminium casing between neighbouring cells, as illustrated in Fig. 2.10 on the left.
These single cells are then combined to the complete detector, depicted on the right same figure. The key feature of the RPC are a single particle detection efficiency of $\epsilon > 0.95$, a timing resolution of $\sigma_T < 100$ ps and a rate capability up to 1 kHz.

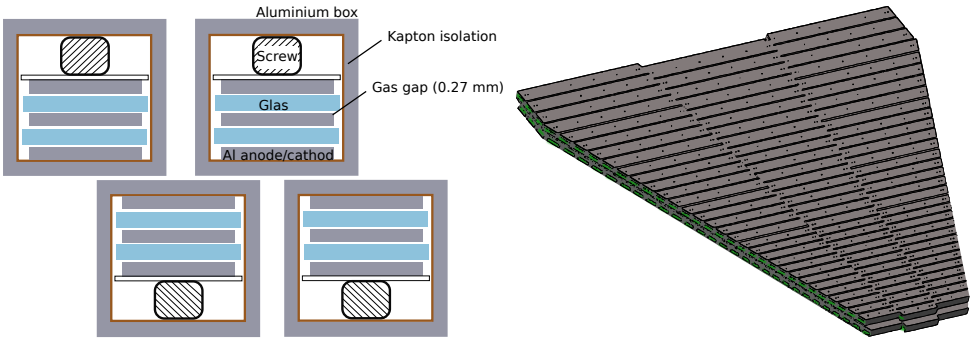

Figure 2.10: Left: schematic illustration of the RPC cross section. Each single cell consist of conductor-isolator pairs with an efficiency of $\epsilon \approx 0.95$ and a timing resolution of $\sigma_\tau < 100$ ps, adapted from [59]. Right: Final assembly of the single RPC cells.

2.2.8 Trigger and DAQ

A **f**irst **l**evel **t**rigger (LVL1) is employed to suppress the acquisition of empty events and thus to shorten the dead-time of the **D**ata **AQ**uisition (DAQ). The LVL1 trigger condition requires a valid signal in the T_0 detector (see Section 2.2.2) and at least two hits in the META (see Section 2.2.7). The readout of all sub-detector systems is then synchronised by the **C**entral **T**rigger **S**ystem (CTS), while the data itself is transported to the **E**vent **B**uilder (EB) by a dedicated network employing the TrbNet protocol [61].

The TRB3 board is used for the physical connection between all HADES sub-systems. It contains a triggered readout card with four FPGAs (Field Programmable Gate Arrays) [62]. These four FPGAs (Lattice ECP3) can process any type of detector readout with an FPGA **T**ime-to-**D**igital-**C**onverter (TDC) with an accuracy of $\tau_{timing} \approx 15$ ps (RMS) and binary signals. The DAQ Network is connected via fibre optic cable, while the data is transmitted via a Gigabit Ethernet connection. In the final step, all information are collected and combined in the EB and finally sent to a data storage.

3
Data and Event Selection

In this section the general event selection within the HADES acceptance is discussed together with the identification of the charged particles and reconstruction of neutral particles which can only be detected via their associated charged decay products. At the end of the chapter all used transport codes are introduced and the simulation of the detector response aside with the normalisation procedure for the extraction of cross sections.

3.1 Event Criteria

Not all recorded events stem from interactions of the π^--beam with the target. Even though the LVL1 trigger (see chapter 2.2.8) reduces the amount of false detector responses due to the high radiation inside the cave, empty or fake events can fulfil the LVL1 condition and pass this stage. Another effect that must be suppressed is pile-up, where multiple pions are registered in the T_0 detector withing the time window applied for the selection of single events. This makes it impossible to assign particle tracks to a single event or reconstruct the correct number of interactions that are necessary for the absolute normalisation. To cope with these five criteria (so-called flags) must be fulfilled for the post-analysis procedure:

- **GoodTrigger**: this criteria ensures that all events meet the **p**hysical **t**rigger condition of LVL**1** (PT1).
- **GoodStart**: a hit is registered in the target T_0 detector.

- **GoodVertexCluster**: at least one track in the inner MDC I/II is required, with an track reconstruction χ^2 larger than zero and a z-position of $z > -160$ mm.
- **NoPileUp**: a multiplicity of one is reconstructed in the target T_0 detector in the time window of -5 ns $< t_0 < 15$ ns to reject pile-up events.
- **Trigger**: charged particle multiplicity of $M \geq 2$ in the META (TOF + RPC).

In addition to these selection criteria an additional one was required, for every particle candidate. Due to the reconstruction of tracks based on MDC and META hits it can come to track splitting, where the track of a single particle is reconstructed as two independent ones. These tracks were identified and sorted according to their track reconstruction quality based on χ^2/NDF, where the track with the highest quality was marked. Only these particle candidates that were marked were considered for the later analysis and all others were rejected.

3.2 Particle Identification

In this section the **P**article **ID**entification (PID) is outlined where, depending on the analyses, two different approaches have been chosen for each analysis. One is based on a mass selection in the β-momentum plane, applied for the analysis of the experimental efficiency determinations in Chapter 4 and for the selection of the daughter particles of the inclusive Λ and K_S^0 analysis presented in Chapter 5.
The second one was considered for the exclusive analysis in Chapter 6 and is based on a method similar to a likelihood, combined with the particle species specific β, energy loss dE/dx in the active volume of the MDC drift chambers and momentum. The particles were reconstructed via their dominant weak decay into two charged particles $\Lambda \rightarrow p + \pi^-$ (BR $= 63.9 \pm 0.5\%$ [1]) and $K_S^0 \rightarrow \pi^+ + \pi^-$ (BR $= 69.2 \pm 0.05\%$ [1])).

3.2.1 Time of Flight Selection

In the first approach the particle specific relation of the time-of-flight (TOF) measurement, hence velocity, to momentum relation is exploited“

$$\frac{p}{E} = \frac{p}{\sqrt{p^2 + m_{PDG}^2}} = \beta = \frac{v}{c} \tag{3.1}$$

where

p: total momentum of the particle,
E: energy of the particle,
m_{PDG}: nominal mass of the different particles species,
β: velocity in terms of the speed of light c.

The momentum p of the particle was determined by the curvature of the track in the magnetic field between MDC II and MDC III and reconstructed by combining the hits inside the MDCs. The TOF was calculated by the time difference of the target T_0 detector just before the target and the hit of the charged particle in the META. Although the timing resolution of RPC and TOF are different, a combined PID was performed. To select a certain particle species a cut window of ±0.2 β_{theo} was applied:

$$\frac{p}{E} - 0.2 < \beta < \frac{p}{E} + 0.2 \tag{3.2}$$

This is only a pre-selection for the particles as later on topological cuts will further purify the sample. The experimental and simulated correlation between β and momentum is depicted in Fig. 3.1, where the shaded area corresponds to the applied cut and the blue line represents the calculated theoretical β value for the different particle species at a given momenta. For illustration purposes only the β-momentum plane for the PE target is shown, at an incident pion momentum of $p_{\pi^-} = 690$ MeV/c. In the same way the PID is performed for the daughter particles of Λ and K^0_S namely proton, π^- and π^+ with their respective nominal mass.

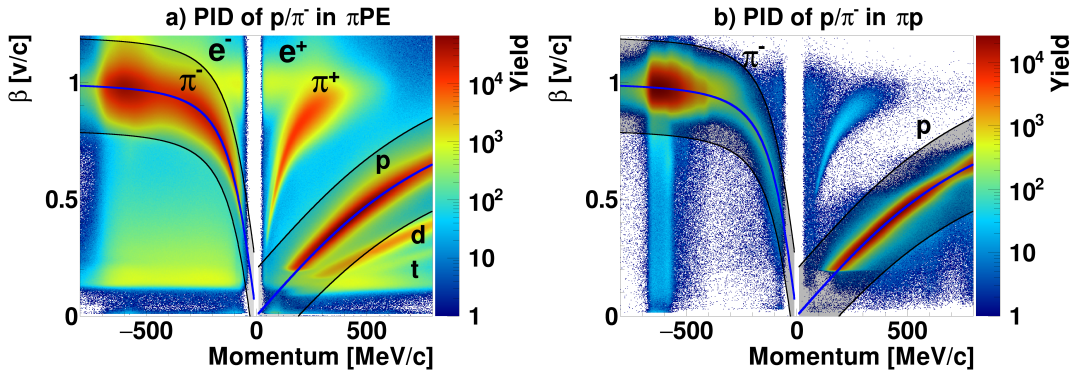

Figure 3.1: PID for protons and π^-: in panel (a) for the experiment and in panel (b) for simulated data. The shaded area corresponds to the applied cut of $p/E \pm 0.2 \gtrless \beta$ while the blue line corresponds to the theoretical value of a given momenta. In the simulated data only elastic scattered events have been considered.

In case of the simulated data only elastic scattered events $p + \pi^- \rightarrow p + \pi^-$ have been simulated with the PLUTO event generator (Section 3.5.1), dedicated for the efficiency determination procedure outline in Chapter 3. For the experiment also other charged particles are visible and can be clearly distinguished. The selection region of the protons suffer from deuteron contamination in the low β and momentum region, however deuterons were removed in a later stage due to kinematical

constrains of elastic scattering events introduced in Chapter 4. Thus, this stage performs a pre-selection of the particles.

3.2.2 Likelihood

The particle identification discussed in this subsection was developed for the exclusive analysis of $\pi^- + A \rightarrow \Lambda\,(p\pi^-) + K^0_S\,(\pi^-\pi^+) + X$ presented in Chapter 6. The procedure is outlined for tungsten, while the figures shown in this section for carbon can be found in Appendix A.1. Due to the limited acceptance of HADES together with the multiplicity of four charged particle in the final state, the statistics of the recorded data drops tremendously. This makes a PID necessary, with a minimal loss of signal while maintaining a high purity. For this a selection procedure was developed, which similar to a likelihood is based on minimisation. While the developed method is not a likelihood according to the mathematical definition, it is proportional to it. Therefore the term likelihood is used, even the mathematical definition is not fulfilled. In contrast to the strict PID selection introduced in the last subsection, the likelihood PID does not introduce a hard selection criteria. The applied likelihood method is based on the already introduced PID selection exploiting the correlation between β and momentum in combination with the specific energy loss dE/dx in the MDC in addition to the event topology of the final state of the exclusive channel $(\pi^-\pi^-\pi^+p)$. For the theoretical dE/dx calculation the fully relativistic description of the energy loss for particles with $m \gg m_e = 511$ keV by the Bethe-Bloch equation was used [1]:

$$-\left\langle \frac{dE}{dx} \right\rangle = 4\pi N_A r_e^2 m_e c^2 z^2 \frac{Z}{A}\frac{1}{\beta^2}\left[\frac{1}{2} ln\left(\frac{2m_e c^2\beta^2\gamma^2 T_{max}}{I^2}\right) - \beta^2 - \frac{\delta(\beta\gamma)}{2}\right] \quad (3.3)$$

where

z: charge of incident particle
A, Z: mass and atomic number of the traversed material
N_A: Avogadro constant
m_e: rest mass of the electron
r_e: Bohr electron radius
I: mean excitation potential of material
δ: density correction
T_{max}: maximum kinetic energy transfer

The energy loss depends on the charge z of the particle and through $\beta\gamma = p/m$ also on the particle specific ratio between the momentum and the mass, which make it possible to distinguish single particle species.
Due to the unambiguous abundance of the π^- in the final state, it was sufficient to meet the following criteria to identify the negative pions:

1. negative charge
2. $m_{\pi^-} > 80$ MeV/c^2

For the positive charged particles the situation changes, as the final state is populated by two different positive particle species. Here it was necessary to assign a particle candidate to either be a proton or a positive pion.
Motivated by the final state of interest, an approach was chosen, where the best matching candidate to be a proton was searched for. To determine which candidate was the best matching proton, difference spectra were needed, which were determined by calculating the theoretical values of the specific β and dE/dx for protons for a given momentum, subtracted by the measured value of all positive candidate:

$$\begin{aligned} \Delta\beta &= \beta_{cand} - \beta(p)_{theo} = \beta_{cand} - \frac{p}{\sqrt{p^2 + m_p^2}} \\ \Delta\left(\frac{dE}{dx}\right) &= \left(\frac{dE}{dx}\right)_{cand} - \left(\frac{dE}{dx}\right)(p)_{theo} \end{aligned} \tag{3.4}$$

The velocity β of all charged particle and specific energy loss as a function of the particle momenta are illustrated in Fig. 3.2. While in case of β a visible separation between all the particle species is visible, the situation for the energy loss is more entangled for positive particles at high momentum that are not well separated. In both cases the lines represent the theoretical values for the indicated particle species, while the red curves highlight the curves for proton and π^+.

The theoretical value for β_{theo} was calculated by the particles specific relation of momentum and energy, introduced in the subsection before, while β_{cand} was the reconstructed one.
The measured energy loss $\left(\frac{dE}{dx}\right)_{cand}$ in the experiment was measured by the deposited energy of the traversing charged particle in the MDC planes. Here the **t**ime **o**ver **t**hreshold (TOT) of the resulting electronic signal which exceeds a certain threshold was measured. This is proportional to the energy loss TOT $= f\left(\frac{dE}{dx}\right)$.
For the theoretical energy loss the Bethe-Bloch equation was used (Eq. (3.3)). With the theoretical input and the assumption that all particles are protons, the difference spectra was extracted and the resulting distributions are depicted in Fig. 3.3. In the

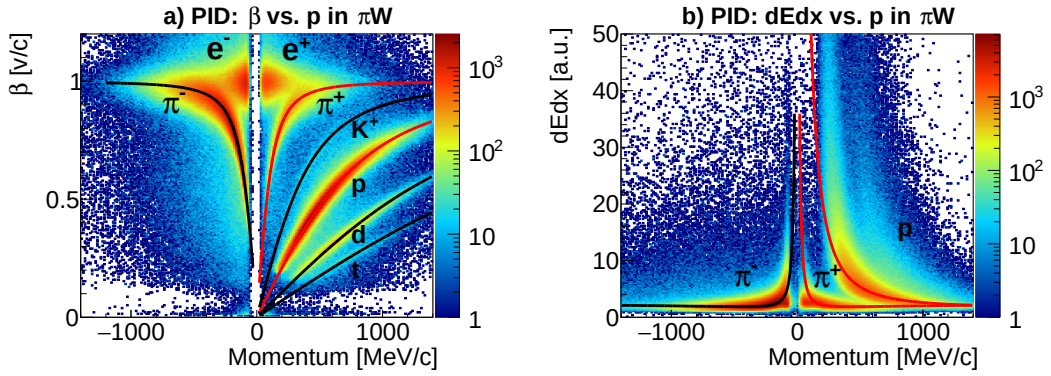

Figure 3.2: β and energy loss as a function of momentum in panel (a) and (b), respectively. In the β momentum-plane a visible separation between the particles species can be seen while the dEdx is more entangled. The lines represent the theoretical curves, indicated in red for p and π^+.

left panel $\Delta\beta$ is depicted and in the right panel the difference for the energy-loss $\Delta\left(\frac{dE}{dx}\right)$.

In both cases a clear peak around 0 is visible, which corresponds to protons as here the difference is expected to be the smallest. While in case of the $\Delta\beta$ distribution a clear Gaussian shaped peak was extracted, the difference spectra for the energy loss is more asymmetric. This can be explained by the difference of the theoretical description to the measured energy loss of the protons at smaller momenta.
A decision on the best matching candidate was determined on a event-by-event basis by the simultaneous selection on the distance of $\Delta\beta$ and $\Delta\left(\frac{dE}{dx}\right)$ to the origin, where an increased distance corresponds to a lower likelihood to be a proton. As the distribution of $\Delta\beta$ and $\Delta\left(\frac{dE}{dx}\right)$ are quite different, their widths (σ_β, $\sigma_{\frac{dE}{dx}}$) were extracted, by means of single Gaussian as shown in Fig. 3.3 with their corresponding widths indicated by the black lines and their numerical value.
Therefore the difference was normalised to the respective distribution width and the distance can be expressed in terms of σ. Then the overall likelihood was extracted by:

$$p_{like} = \left|\frac{\Delta\beta}{\sigma_\beta}\right| + \left|\frac{\Delta\left(\frac{dE}{dx}\right)}{\sigma_{\frac{dE}{dx}}}\right| \tag{3.5}$$

The candidate with the lowest value was then assigned to be a proton and the remaining one to be a π^+ with an additional mass selection:

1. $80 < M_{\pi^+} < 400$ MeV/c^2

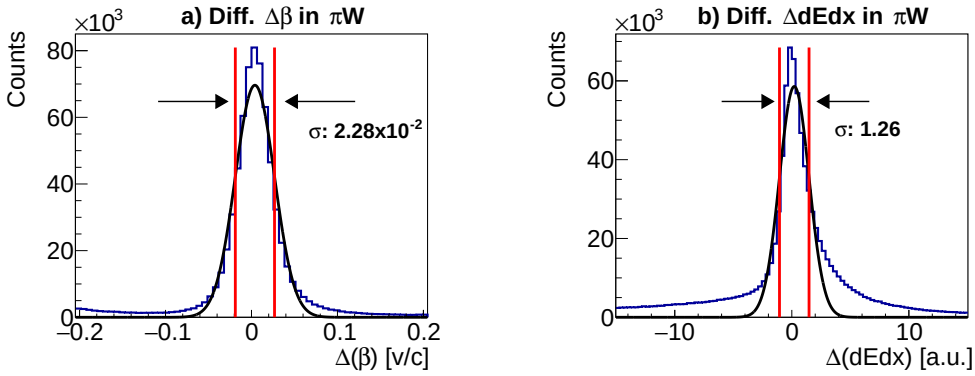

Figure 3.3: Difference spectra for the particle identification, for β in panel (a) and dEdx in panel (b) assuming theoretical values for a proton. The peak was fitted with a single Gaussian and the widths are indicated by the two lines with their corresponding value.

2. $750 < M_p < 1200\ \mathrm{MeV/c^2}$

By showing the p_{like} as a function of the reconstructed mass, as illustrated in Fig. 3.4, the separation power can be seen. The applied mass cut are indicated in black. Nearly all protons have very small values of p_{like} with a clear anti-correlation to the π^+ at lower masses and higher values of p_{like} illustrating the separation power of this particle identification.

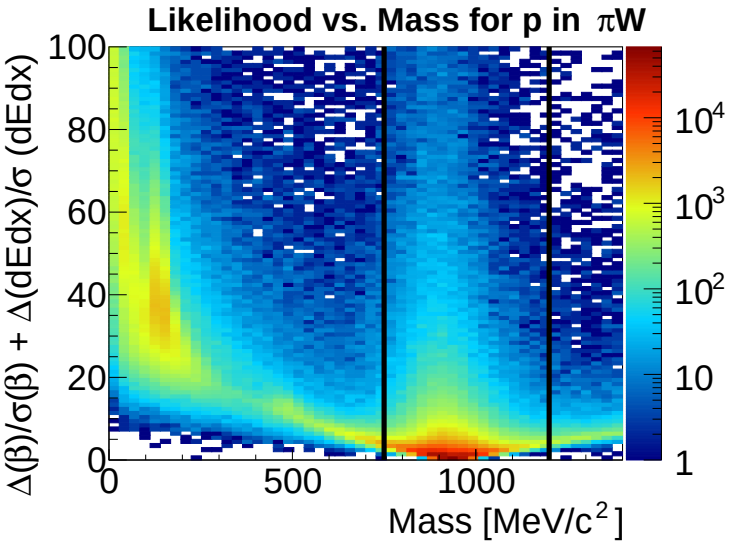

Figure 3.4: Likelihood value for a proton as a function of the momentum. All protons have very low values of p_{like} with an anti-correlation of the π^+, illustrating the separation power of the technique.

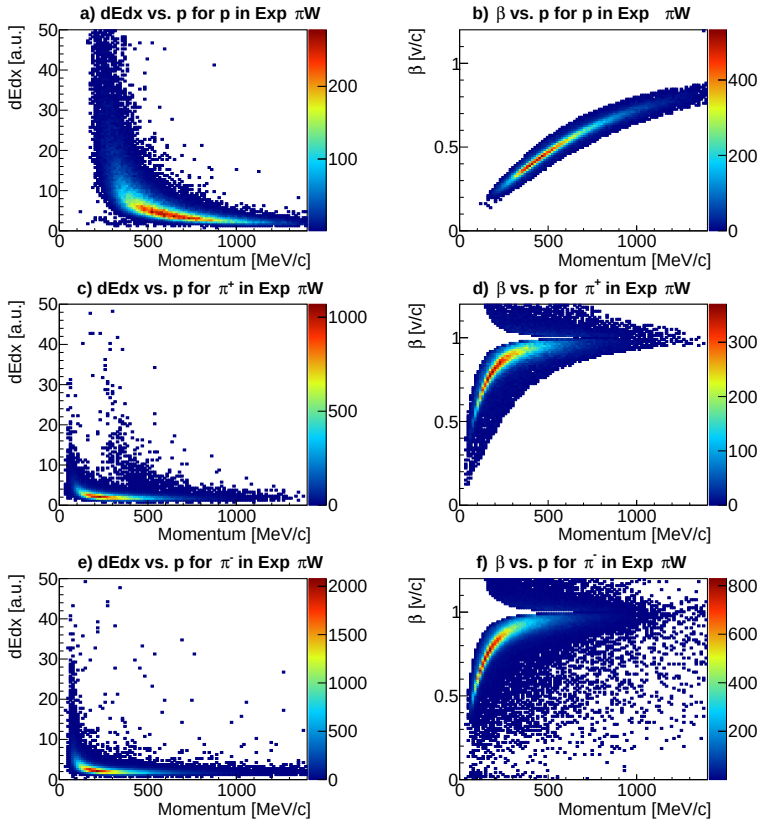

Figure 3.5: Particle distributions after the likelihood selection for dEdx/β vs. momentum for p in panel (a)/(b), π^+ in panel (c)/(d) and π^- in panel (e)/(f). For all three particles a clean identification can be seen, with a small proton contamination in the π^+ case.

The resulting particle distributions for p, π^+ and π^- are plotted in Fig. 3.5 from top to bottom for the and dEdx-momentum and β-momentum plane.
While for protons no contamination is visible, the π^+ still contain a very small contribution of protons. In addition the π^- show a very clean sample, with just a simple mass selection, caused by utilising the charged pattern of the final state.
With the help of all these steps a reliable and clean particles identification was performed without any strict cuts and a minimal loss of final state particles and therefore statistics.

3.3 Event Topology

To ensure that the pion beam interacted with the target and to discard events where the reaction took place outside this area, e.g. with the beam-pipe, a reconstruction and selection of the primary vertex becomes necessary. In addition, not all pairs of the expected decay products stem from the decay of the mother particle but some are rather originated from non-resonant contribution and combinatorial background. This background can be reduced by exploiting the characteristics of the off-vertex decay.
The here illustrated reconstruction procedure for the vertex and topology reconstruction is dedicated for particles with a weak charged decay channel, where all decay products have to be reconstructed withing the HADES acceptance.
For this purposes the reconstruction procedure is outlined only for the Λ in the heavy nuclear target tungsten, while the corresponding figures for carbon can be found in Appendix A.2.

3.3.1 Λ and K_S^0 Reconstruction

The K_S^0 and Λ were reconstructed via their dominant weak charged decay channel $\Lambda \rightarrow p + \pi^-$ (BR $= 63.9 \pm 0.5\%$ [1]), $K_S^0 \rightarrow \pi^+ + \pi^-$ (BR $= 69.2 \pm 0.05\%$ [1])). Therefore the first step was to identify the daughter particles. For this a rough PID selection was applied, based on time of flight or β vs. momentum outlined in Section 3.2.1. The reconstruction of the Λ or K_S^0 candidates was done later on by means of the invariant mass (Eq. (3.8)). Here topological cuts were employed to enhance the signal to background ratio, therefore a pre-selection of the daughter particles was sufficient.
After the identification of the daughter particles was performed the mother particle candidate could be reconstructed by employing the kinematical information of the two daughter tracks by:

$$\begin{aligned} \vec{B}_\Lambda &= \frac{1}{2} * \left(\vec{B}_p + \vec{B}_{\pi^-}\right) \\ \vec{D}_\Lambda &= \left(\vec{D}_p + \vec{D}_{\pi^-}\right) \end{aligned} \tag{3.6}$$

where $\vec{B}$ is the 3 dimensional coordinate basis vector of the Λ constructed on the basis vectors of the $p + \pi^-$ and $\vec{D}$ the normalised direction vector.
The standard format of the HADES data is in cylindrical coordinates and therefore

the mother candidate needs to be converted into Cartesian coordinates with:

$$\begin{pmatrix} B_x \\ B_y \\ B_z \end{pmatrix} = \begin{pmatrix} \rho * cos\left(\phi + \frac{\pi}{2}\right) \\ \rho * sin\left(\phi + \frac{\pi}{2}\right) \\ z \end{pmatrix} \qquad \begin{pmatrix} D_x \\ D_y \\ D_z \end{pmatrix} = \begin{pmatrix} sin(\theta) * cos\left(\phi\right) \\ sin(\theta) * sin\left(\phi\right) \\ cos(\theta) \end{pmatrix} \tag{3.7}$$

where ρ is the distance from the z axis, z the z coordinate, θ the polar angle and ϕ the azimuths angle. The additional factor of $\frac{\pi}{2}$ arises from a different angle convention inside HADES. This particle candidate was the basis for all later extracted topological values and cuts.

$$m_{inv} = \frac{1}{c^2}\sqrt{E^2 - \vec{p}^2 c^2} = \frac{1}{c^2}\sqrt{\left(\sum_{i=0}^{1} E_i\right)^2 - \left(\sum_{i=0}^{1} \vec{p}_i\right)^2 c^2} \tag{3.8}$$

where

m_{inv}: invariant mass of the mother particle candidate
E_i: total particle energy with nominal mass m_0
p_i: momentum vector

3.3.2 Vertex Selection

For an efficient event selection and reduction of non-resonant and combinatorial background the characteristics of the decay topology were exploited.
As described in the last chapter, the first step was the reconstruction of the potential mother particle by means of the daughter tracks of $p\pi^-$ inside HADES. With this all topological information could be reconstructed, started by the deduction of the point in space where the mother decayed, the so called secondary vertex (SV). For this the point of closest approach was calculated between the tracks of the daughter particles.
For the primary vertex, which is the point where the pion interacted with the target material, the vector of the mother candidate calculated with Eq. 3.7 was used. Here the point of closest approach was calculated between the vector of the mother and the beam axis. The latter was assumed to be the same as the z-axis. The z component of the reconstructed primary vertex distribution of Λ in the heavy collision system is shown in Fig. 3.6 for the experimental data indicated by the black curve aside with simulations based on GiBUU in red and UrQMD in blue. The black lines at z = -80 mm and z = 5 mm show the applied primary vertex cut in z-direction. All

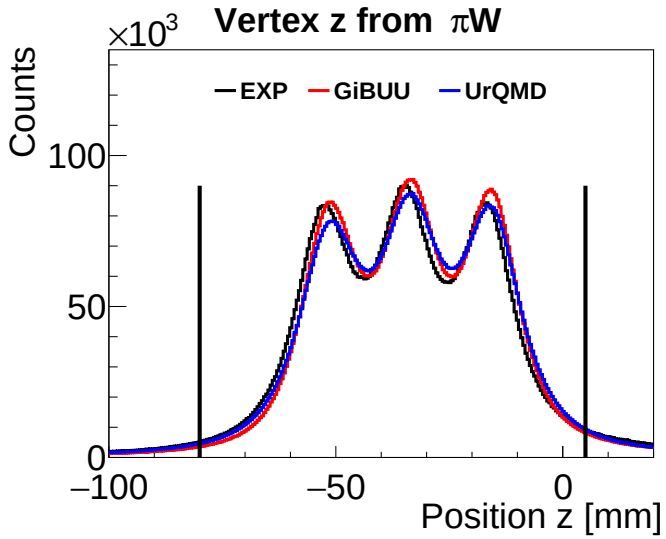

Figure 3.6: Z component of the primary vertex for experiment (black), GiBUU(red) and UrQMD (blue). The black lines indicated the applied cuts, while the three peaks correspond to the single segments of the target.

three vertex distributions are nicely in agreement, showing that the resolution in simulation can reproduce the experimental data.
Three peaks are visible, which are expected to be seen and corresponds to the three segments of the target (see Section 2.2.3).

To constrain the interaction point further, a cut in the x-y plane was applied. The corresponding primary vertex distribution in the x-y plane is depicted in Fig. 3.7. In panel (a) the position for the experimental data are shown, in panel (b) the GiBUU simulation and panel (c) the UrQMD transport code. The black circle corresponds to the applied cut of $R = \sqrt{x^2 + y^2} < 20$ mm.

Again all three distribution are in very good agreement. The six folded structure of the HADES can slightly been seen as the distribution has a slightly hexagonal structure.
The quantify each distribution and compare simulation and experiment the primary vertex distributions have been fitted. For the z-distributions a sum of three Gaussians for every segment was assumed with a parabola to describe the background. For the x-y distribution a double Gaussian has been employed. A overview of the extracted widths and target position are listed in Table 3.1.

With these cuts the pion-nucleus reaction can be selected, coming from the target region and suppressing off-target collisions.

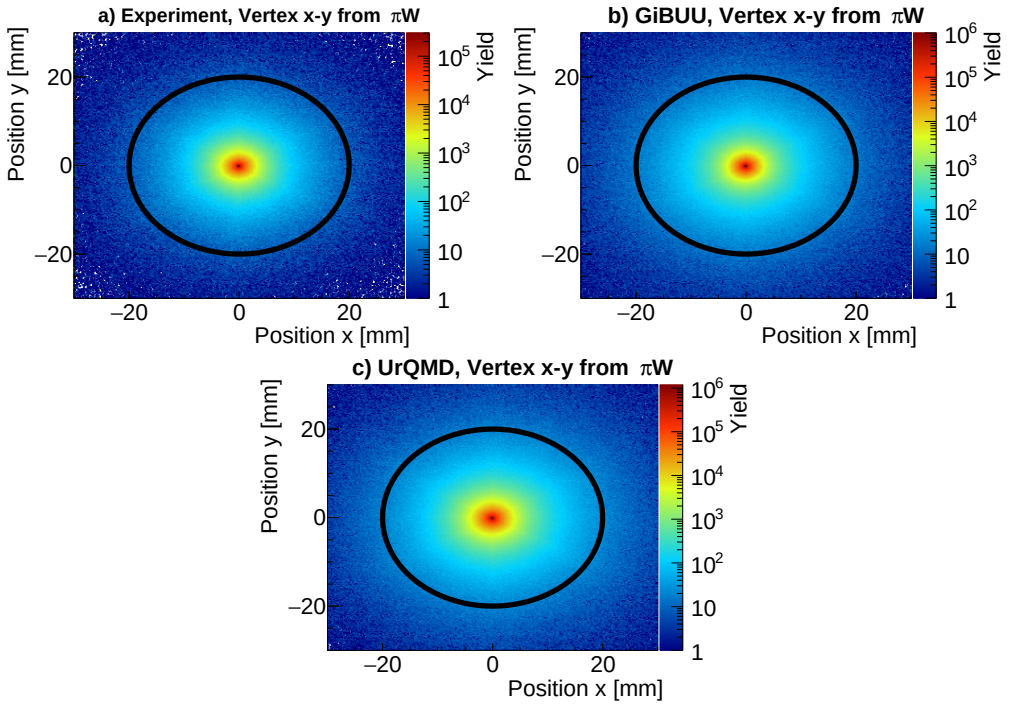

Figure 3.7: Reconstructed x-y coordinate of the primary vertex for experiment (panel (a)), GiBUU (panel (b)) and UrQMD (panel (c)). The black circle corresponds to the applied cut of $R < 20$ mm.

[mm]	σ_{z1}	σ_{z2}	σ_{z3}	μ_{z1}	μ_{z2}	μ_{z3}	σ_{xy}	μ_{xy}
W Experiment	6.46	5.19	6.15	-52.22	-34.65	-17.12	1.69	0.03
W GiBUU	6.36	5.26	6.15	-51.00	-33.53	-16.04	0.72	0.00
W UrQMD	7.02	5.24	6.79	-50.68	-33.51	-16.30	1.37	0.01
C Experiment	6.96	5.47	6.65	-52.76	-35.28	-18.02	1.58	0.08
C GiBUU	6.83	5.47	6.66	-51.35	-34.02	-16.66	1.09	0.00
C UrQMD	6.80	5.42	6.66	-51.33	-34.02	-16.64	1.35	0.00

Table 3.1: Target properties for experiment and simulation. σ_{zx} corresponds to the width of segment x with the corresponding mean value μ_{zx}. The same for the radial component in the x-y plane. See text for details.

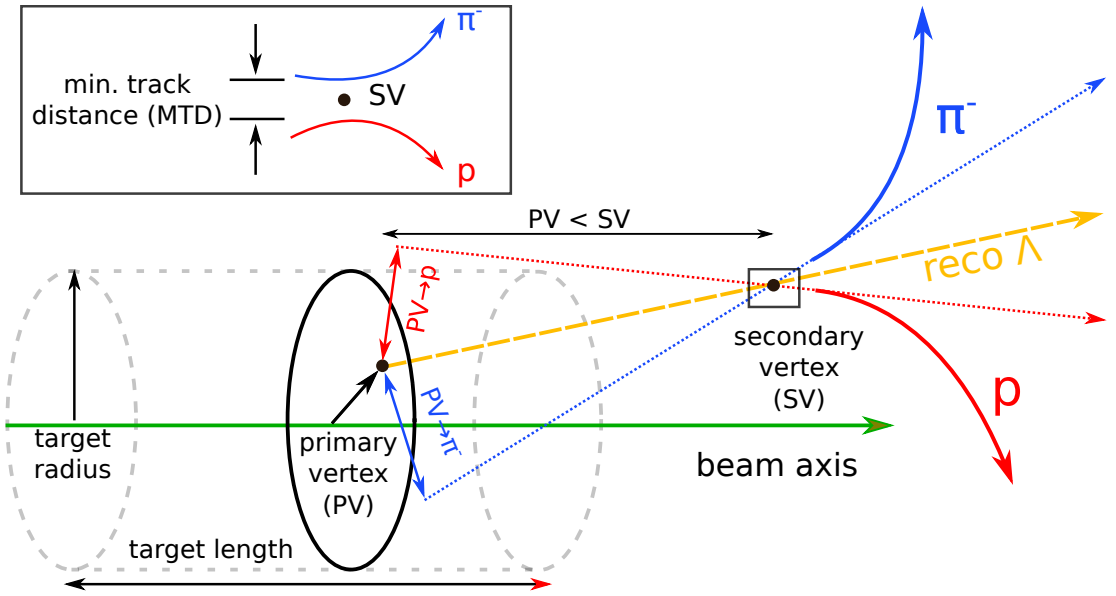

Figure 3.8: Decay topology of Λ with applied selections. The secondary vertex have to be downstream the beam axis compared to the primary vertex. In addition both decay particles have to be close enough ($|MTD|$) to each other to originate from the same production point. Moreover off-vertex ($|PV->\pi/p|$) was required to select particles decaying outside the target region (off-vertex)

3.3.3 Topological Cuts

At this stage of the analysis the mother candidates were reconstructed and events stemming from the target region were selected but still a large background contribution remained in the data.
To reduce the amount of the non-resonant contribution the unique topology of the event was used. After the creation of the Λ ($c\tau = 7.89$ cm [1]) or K^0_S ($c\tau = 2.67$ cm [1]) inside the target, both particles traverse the target and most likely decay outside. At this point two charged particles can be tracked inside HADES. Accordingly, an off-vertex from which two charged particles are originated should be present. The two daughter particle tracks should be close to each other in space and the mother particle should point to the target region and have a certain flight distance.
This results in three topological selections as illustrated in Fig. 3.8.

The first selection required that the z-coordinate of the secondary vertex (SV) was downstream in respect to the primary vertex (PV), in order to fulfil that the mother particle travelled a certain distance.
As both decay particles have to originate from the same point in space, a cut on

Cut	$K_S^0(\pi^+\pi^-)$	$\Lambda(p\pi^-)$
Target [mm]	$R < 20, -80 < z < 5$	$R < 20, -80 < z < 5$
$PV->SV$ [mm]	$PV < SV$	$PV < SV$
$\lvert MTD\rvert$ [mm]	$Dist \leqq 6.0$	$Dist \leqq 10.0$
$\lvert PV->\pi\rvert$ [mm]	$Dist \geq 4.5$	$Dist \geq 18.0$
$\lvert PV->p\rvert$ [mm]	-	$Dist \geq 5.0$
Inv. Mass [MeV/c^2]	$300 < M_{\pi^+\pi^-} < 600$	$1000 < M_{p\pi^-} < 1300$

Table 3.2: Topological cuts and mass range selection for Λ and K_S^0.

the minimum track distance (MTD) between the these tracks was applied. The last selection imposed a minimal track distance from the PV to the track of the daughter particles. If particles are directly created within the target zone, this is closer to zero, while it increases for the off-vertex decay. In case of the K_S^0 the off-vertex cut was the same for the $\pi^+\pi^-$ and for the Λ, the cut differs for p and π^-.
In summary, following criteria are applied:

- **PV < SV**:
  The z-coordinate of SV was downstream with respect to the z coordinate of the PV
- **Minimum Track Distance (MTD)**:
  The distance between the daughter tracks was required to be small
- **Minimum Track Distance to PV**:
  The minimum distance of $|PV \rightarrow \pi^-|$ and $|PV \rightarrow p|$ had to be large enough, to ensure off-vertex production

These cuts were optimised to maximise signal-to-background ratio. Hence to ensure high statistic and a stable signal extraction while reducing the non-resonant background. In addition, a rough selection around the expected invariant mass was applied to further purify and reduce the collected data.
The final cuts for K_S^0 and Λ are summarised in Table 3.2.

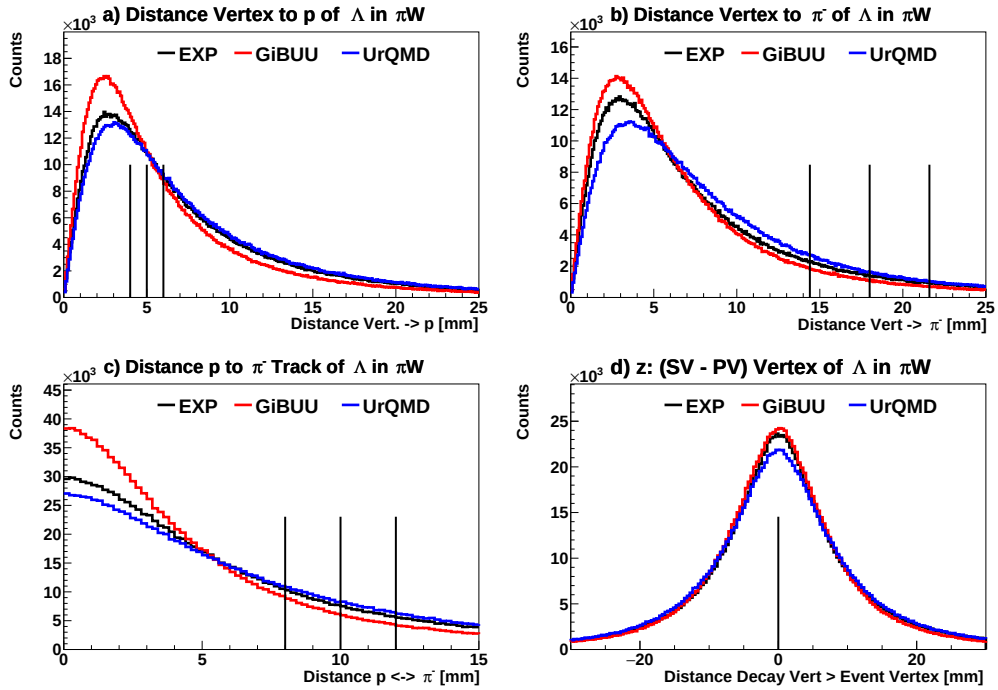

Figure 3.9: Topological distributions for Λ in $\pi^- W$ for experiment (black), GiBUU (red) and UrQMD (blue) panel (a) and panel (b) shows the distance to the PV for protons and π^-, respectively. Panel (c) the track distance between the daughter track and depicted in panel (d) z component of the SV minus the PV vertex. The black lines represent the applied topological cuts, where the line in the middle represents the nomial cut and the outer lines the systematic variation.

The distributions of the variables used for the topological cuts for Λ from $\pi^- W$ are depicted in Fig. 3.9 for experiment in black, GiBUU in red and UrQMD in blue. The black lines show the applied cut and the later on performed systematic variation, while the centred line represents the nominal cut and the outer lines the variation. In panel (a) the minimal distance of the proton track to the PV is depicted and in panel (b) for the π^-. The minimal distance between these tracks is depicted in panel (c), while panel (d) illustrates the z component of the SV subtracted by the z of the PV. The corresponding distributions for carbon and K^0_S can be found in Appendix A.2. Smaller deviations are visible between all three data sets, while experiment and UrQMD are more in agreement. This can be explained by different background contributions. A quantitative estimation of the error introduced by the topological cuts is discussed in Section 5.1.3.

3.4 Kinematic Observable and Extrapolation

The extraction of double-differential yields can shed light on the internal dynamics of the collision system as the final state of the measured particle is highly modified by the interaction with the surrounding nuclear matter. Since no model-dependence of the efficiency correction due to the underlying simulated initial distribution (Section 5.1.2) is introduced the extracted kinematics distributions can be extrapolated to phase space regions outside the HADES acceptance.
In this section the two sets of phase-space variables are presented aside with the description of the extrapolation procedure to uncovered regions. The z-axis is defined longitudinal to the beam. All variables are considered in the laboratory frame.

Momentum - Polar Angle ($P-\Theta$)

The first set of phase-space variables consist of the total momentum and polar angle of the measured charged particle:

$$\theta = \text{polar angle} \qquad p = \sqrt{p_x^2 + p_y^2 + p_z^2} \tag{3.9}$$

This set can be used for e.g. interpretation of detector effects as the angle can easily be addressed to a detector segment.

Transverse Momentum - Rapidity ($P_t - Y$)

The second set of kinematic variables are transverse momentum and rapidity ($p_t - y$).
In the initial collisions no transverse component of the momentum is present. The transverse momentum provides the information of the internal dynamics, as it is decoupled from the boost of the beam, hence the interactions of the particle (c=1):

$$y = \frac{1}{2} ln \frac{E + p_z}{E - p_z} = \frac{1}{2} ln \frac{1 + \beta cos\theta}{1 - \beta cos\theta} \qquad p_t = \sqrt{p_x^2 + p_y^2} \tag{3.10}$$

where

E: energy of the particle
p_z: longitudinal momentum
β: velocity of the particle
θ: polar angle

Concerning the rapidity three regions can be distinguished, forward or beam rapidity, backward or target rapidity and mid-rapidity in between.
The term backward rapidity is used for rapidities going to y = 0 and beam or forward rapidities for higher positive values. The target rapidity for the $\pi^- N$ system is at $y_{\pi^-} = 0.76$.
If not stated otherwise no differential analysis in terms of the azimuthal angle Φ is performed as HADES is symmetric around the beam axis.

Boltzmann Fit and Extrapolation

Independent by the choice of the phase-space variables and the detector systems, the complete phase space is never covered due to the limited acceptance of each detector. In regions outside the acceptance no efficiency correction can be applied since not a single particle can be detected and therefore no efficiency can be determined.
However in case of $p_t - y$ the differential corrected yield $\left(\frac{dN}{dp_t dy}\right)$ can be extrapolated to uncovered p_t regions employing a fit based on Boltzmann distribution:

$$\frac{dN}{dp_t} = A \cdot p_t \cdot \sqrt{p_t^2 + m_0^2} \cdot e^{-\frac{\sqrt{p_t^2+m_0^2}}{T_B}} \tag{3.11}$$

where

A: amplitude
p_t: transverse momentum
m_0: nominal mass
T_B: inverse slope parameter

This function has been successfully employed for the extrapolation of various collisions systems from proton-proton [63], proton-nucleus [64] to nucleus-nucleus [65] systems for a huge variety of particle species ranging from light pions to heavier particles containing strangeness.
Even though a priori no Boltzmann distribution is expected in a π^-+A reaction, studies from [59] showed that the Fermi motion present in every nucleus smear the p_t spectra such to assume a Boltzmann shape. Another way to write Eq. (3.11) is as a function of transverse mass, with $m_t = \sqrt{p_t^2 - m_0^2}$. Although is has not been used in the course of this analysis.
An extrapolation to uncovered rapidity is not always possible or only with a strong model dependence. Only in cases where the underlying distribution is symmetric, like proton-proton collisions, the extrapolation can be done in a rather model independent way.

3.5 Software Framework

All experimental information measured with a detector are time-integrated over the whole evolution of the collision system.
To get an insight of the individual dynamics and interactions of the particles or the nuclear system in general, transport models can be used. Their core component consist of a microscopic description, where the degrees of freedom change on the actual energy scale. At high energies the degrees of freedom are strings or quarks while at lower energies the degrees of freedom are hadrons. Different interactions can be implemented and the impact on the final state can be tested and compared to experimental results. As the name suggest particles are transported through e.g. a nucleus, where the interaction and their equation of motion is solved numerically. Here a full time evolution of the nuclear system is accessible, as illustrated in Fig. 3.10. All reaction cross-sections σ and decay widths are either constrained by available experimental data or theoretical predictions.

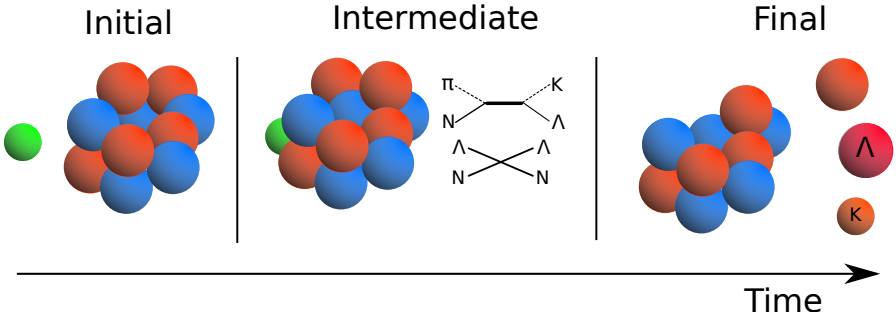

Figure 3.10: Illustrative representation of the time evolution of the transport code from the initial to the final state.

The main difference and also big advantage of such microscopic transport models is that the whole time-evolution is considered in contrast to e.g. thermodynamical statistical models like THERMUS [66] , which consider only the final state where the thermodynamical equilibrium is reached. The latter are widely successfully applied in predicting of the correct particle yields, however they can not provide kinematic distributions.
In the framework of this thesis, three different transport models were used, namely UrQMD [2] [3], GiBUU [4] and SMASH [5]. All are discussed in the Section 3.5.1. In addition the event generator PLUTO [67] was used, as here a large amount of statistic can be calculated in a short amount of time.
As mentioned already earlier, a transition from the hadronic regime to the string fragmentation takes place. This transition energy is depending on the model. Listed in Table 3.3 are the transition energies $\sqrt{s}$. The ± for the GiBUU indicates the transition

	baryon-baryon	meson-baryon
UrQMD	5 GeV	3 GeV
GiBUU	2.6 ± 0.2 GeV	2.2 ± 0.2 GeV

Table 3.3: Transition energies $\sqrt{s}$ between hadronic regime and string fragmentation

window where the models pass linear from the hadronic to the string fragmentation.

In order to compare the final state predicted by these transport models to the experimental data, all effects introduced by the detector and reconstruction have to be taken into account. This was done in two steps. The first step simulates the acceptance and interaction of the particles with the detector material which is done with the so called HGeant software package. The second step includes the detector response calculated with the **Sim**ulation **D**ata **S**ummary **T**able (SimDST). Both are presented in Section 3.5.2.

3.5.1 Event Generator

In this section the event generators are discussed with particular emphasis on transport models. As already mentioned these models transport the particles from the initial to the final state. In principle the transport theory can be divided into two parts. The first part considers only binary collision. A reaction takes place if the distance of two particles meets the following criteria:

$$b < b_{max} = \sqrt{\frac{\sigma_{tot}\left(\sqrt{s}\right)}{\pi}} \tag{3.12}$$

where $\sigma_{tot}\left(\sqrt{s}\right)$ is the momentum dependent total cross-section. The second part is the interaction of the particles with each other. The classical derivation for the theory of transport is based on the theorem of Liouville. This states that the phase space density is constant in time, e.g. a change in the momentum space must result in an equal change in the coordinate space. This can be written as:

$$df = \frac{\partial f}{\partial r} dr + \frac{\partial f}{\partial p} dp + \frac{\partial f}{\partial t} dt = 0 \tag{3.13}$$

where df is the total differential phase space density in time, momentum and

coordinate space. By dividing equation 3.13 with $\frac{1}{dt}$ is can be rewritten as:

$$\frac{df}{dt} = v\frac{\partial f}{\partial r} + F\frac{\partial f}{\partial p} + \frac{\partial f}{\partial t} = 0 \tag{3.14}$$

with the velocity $\frac{dr}{dt} = v$ and external force $\frac{dp}{dt} = F$. This force can also be written as the gradient of a potential $F = -\vec{\nabla}^{(r)}U(r)$, which results in the Vlasov equation:

$$\frac{df}{dt} = \underbrace{\frac{\partial f}{\partial t} + \frac{\vec{p}}{m}\vec{\nabla}^{(r)}f}_{\text{drift term}} - \vec{\nabla}^{(r)}U(r)\vec{\nabla}^{(p)}f = 0 \tag{3.15}$$

Here two different components can be distinguished: the drift term and the field which can cause an acceleration due a potential $U(r)$. However Eq. (3.15) does not take into account any collisions, like in the cascade approach from Eq. (3.12), which can alter the phase space.
By introducing the total collision term I_{coll} the non-relativistic Boltzmann-Uehling-Uhlenbeck (BUU) is derived:

$$\frac{df}{dt} = \left(\frac{\partial}{\partial t} + \vec{v}\vec{\nabla}^{(r)} + \frac{1}{m}\vec{F}\vec{\nabla}^{(v)}\right) f(\vec{x}, \vec{v}, t) = I_{coll} \tag{3.16}$$

This collision term considers not only elastic interaction, but also all inelastic reactions. Thus, all cross-sections are included taking into account the production as well as the absorption of particles. In addition, the Pauli-principle is taken into account, suppressing particles production or scattering to an already occupied phase-space cell.
The potentials are often not only dependent on the position $\vec{r}$, but also on the momentum $\vec{p}$.
This equation can only be solved analytically in very limited cases, thus they are mostly solved employing numerical techniques. Two of this approaches, the test particle ansatz (GiBUU) and the quantum molecular dynamic (UrQMD, SMASH) are outlined in the following sections.

GiBUU (Giessen BUU) [4]

The approach of GiBUU (version 2017) for solving the BUU equation (Eq. (3.16)) is the test particle ansatz, in combination with a **R**elativistic **M**ean-**F**ield (RMF) approach. Here the test particles replace the continuous phase space distribution $f(\vec{x}, \vec{v}, t)$

by a sum of test particles N_{TP} constructed out of δ-functions in momentum and coordinate space:

$$f\left(\vec{r},\vec{p},t\right)=\sum_{i=0}^{N_{TP}}\delta\left(\vec{r}-\vec{r}_i(t)\right)\delta\left(\vec{p}-\vec{p}_i(t)\right) \tag{3.17}$$

This approach is valid for most of the particles for which the spectral function is narrow.
All particles are assumed to be propagated within a mean-field. In this way no local numerical fluctuations are introduced as the field is averaged over all test-particles. Thus the number of test particles must be large enough, in the order of 500 particles or higher.
The strange particle production itself is modelled by the parametrisation of elementary reactions on the basis of the Tsushima resonance model [68, 69, 70]. In the framework of this model the π, η and ρ mesons are treated as exchange bosons, while the strange particles are produced by resonance decay $R \rightarrow Y+K$ as illustrated in Fig. 3.11.

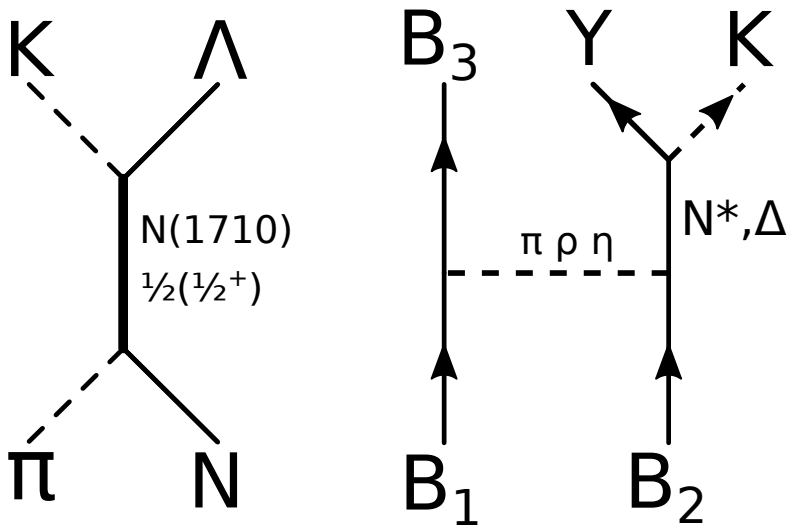

Figure 3.11: Examples of the implemented Tsushima model. Depending on the final state different parametrisation are used. See text for details.

The following cross-sections parameterisation are implemented into the GiBUU model:

$$\sigma(BB \to BYK) = a\left(\frac{s}{s_0}-1\right)^b \left(\frac{s}{s_0}\right)^c \tag{3.18}$$

$$\sigma(\pi B \to YK\pi) = a\left(\frac{s}{s_0}-1\right)^b \left(\frac{s}{s_0}\right)^{-c} \tag{3.19}$$

$$\sigma\left(\pi^- p \to \Lambda K^0\right) = \frac{0.007665\left(\sqrt{s}-1.613\right)^{0.1341}}{\left(\sqrt{s}-1.720\right)^2+0.007826} \tag{3.20}$$

while the last parametrisation of $\sigma\left(\pi^- + p \to \Lambda + K^0\right)$ is only an example for the 2-body final state. The parameters a, b and c are different for each of the parametrised channel. In total, up to 3 particle final state channels are implemented.
As already discussed in the introduction the particle properties can change tremendously inside of dense matter. These in-medium interaction can alter the production threshold and therefore change the yield and in addition the final state kinematics. Therefore they have to be considered for in a realistic transport model. For the description of the hyperon-nucleon interaction, GiBUU employs the RMF nucleon-nucleon interaction, multiplied by a pre-factor of 2/3 [71]. Note that a positive sign corresponds to an attractive interaction. However, by default the RMF is disabled.
For the kaons, a density and momentum dependent KN potential is implemented (see Fig. 1.9) in the transport model based on recent work of [37]. In this approach a fully χ-effective description of the kaon in-medium interaction is implemented.
In GiBUU several so called event types can be selected, changing the implemented dynamic of the nuclear reaction. In the framework of this thesis two different event types have been taken into account: elementary and hadron induced reactions. Besides, GiBUU offers the possibility to switch between pertubative and real mode. The elementary reaction can be used for the extraction of the implemented cross-sections, while the real and pertubative mode are used for pion-nucleus reactions. In the perturbation mode only particles are considered further, that participated in the first chance collision. All other particles are neglected in the subsequent transport. Hence, such calculations are very fast and a large statistic sample can be produced. The real mode is used for the comparison of the predicted particle yields to the experimental data. Here all particle interactions are considered during the whole time evolution.
In total 34 mesons and 90 baryons are considered in the code.
Reaching higher energies hadrons as degree of freedom are not sufficient any more to describe experimental data. Therefore, GiBUU switches to the string model PYTHIA [72, 73], where hadrons are replaced through quarks and gluons as the new degrees of freedom. This transition takes place at $\sqrt{s} = 2.2$ GeV for meson-baryon collisions and for baryon-baryon collisions at $\sqrt{s} = 2.6$ GeV with a transition window of $\Delta\sqrt{s} = 0.2$ GeV in the default settings.

UrQMD (Ultrarelativistic Quantum Molecular Dynamics) [2] [3]

UrQMD (version 3.4) uses the Quantum Molecular Dynamics (QMD) approach where the point like treatment of particles is replaced by a Gaussian wave package in the density distribution of the phase space (c=$\hbar$ =1):

$$\Phi_i\left(\vec{r},\vec{q}_i,\vec{p}_i,t\right)=\left(\frac{2}{L\pi}\right)^{\frac{3}{4}} exp\left[-\frac{2}{L}\left(\vec{r}-\vec{q}_i(t)\right)^2-i\vec{p}_i(t)\vec{r}\right] \tag{3.21}$$

with $\vec{q}_i, \vec{p}_i$, the three dimensional position and momentum and L the width of the wave package.
The whole nucleus is then modelled by the product of each single wave package:

$$\Phi=\prod_i \Phi_i\left(\vec{r},\vec{q}_i,\vec{p}_i,t\right) \tag{3.22}$$

With this ansatz different widths of the particles spectral function can be considered. The collision criteria is analogue to that of the cascade criteria of Eq. (3.12). In contrast to the direct particle production via the parametrisation, UrQMD mediates the particle production via the decay of resonances like N* or Δ.
In total, 32 mesons and 55 different baryons can be treated within the UrQMD software framework. Also here PYTHIA is employed at higher energies than $\sqrt{s} > 5$ GeV for baryon-baryon reactions and $\sqrt{s} > 3$ GeV for baryon-meson collisions.

SMASH (Simulating Many Accelerated Strongly Interacting Hadrons) [5]

SMASH (version 1.6) is a relatively new transport code written in C++. It is a combination of the already introduced transport models GiBUU and UrQMD.
The underlying transport equation which is solved numerically is the relativistic Boltzmann equation [5]:

$$p^\mu \partial_\mu f_i(r,p)+m_i F^\alpha \partial_\alpha^p f_i(r,p)=C^i_{coll} \tag{3.23}$$

where

C^i_{coll}: collision Term
F^α: force experienced by individual particles
m_i: particle mass

For high energy beams the force F^α vanishes and for low energies it is described by a mean-field potential with $F^\alpha = -\partial^\alpha U(x)$. In the same way as in GiBUU the test particle ansatz is employed.
In total 106 hadron species are implemented, where the creation mechanism for most of the particles is similar to UrQMD mediated by the decay of resonances. In addition to the resonance production also non-resonance channels are implemented based on parametrisation like in GiBUU. In the current version only 2-body collisions are considered.

Pluto [67]

The Pluto event generator is based on a Monte-Carlo approach and entirely based on the ROOT software package and can directly used with the build in C++ interpreter. It is designed to simulate hadronic interactions in the SIS/FAIR energy regime of ∼100 MeV up to several GeV per nucleon.
All events can either be generated in a single chain approach or as a combination of these single chains to a cocktail considering different production weights.
In the model the thermal particle production commonly assumed in heavy ion collisions can be simulated. Besides also user specific modifications can be implemented, like new particle species as well as resonances.
It is also possible to consider known angular distributions to obtain more realistic Monte Carlo based phase space distributions. The final state particle properties can then be stored in the widely used ROOT format.
Pluto is in contrast to the other presented model no transport code, where the whole time-evolution from the initial to the final state is considered.

3.5.2 HADES Acceptance and Efficiency

As already mentioned all particles simulated with the help of event generators, have to undergo the same effects as the experimental data introduced by the detector and measurement, for a one to one comparison or the extraction of an efficiency matrix. This is done in two steps, first the interaction with the detector material is simulated (HGeant) and then the response of the detector systems itself (SimDST) is taken into account.

HADES Acceptance (HGeant)

In order to simulate the interaction of the particles, which have been produced by one of the event generators, with the HADES, the HGeant framework is employed. This simulation framework is based on Geant3 [74] which has been developed at CERN. Here all active detector volumes and their mechanical holding structure are

realistically described with their different material properties. The Geant model of the HADES detector is adapted to reproduce the properties of each individual beam-time, to consider the different target geometries, associated densities and vertex distribution(see Section 2.2.3). The profile of the beam is assumed to be a Gaussian distribution in the x-y plane (perpendicular to the beam). Depending on the target in total a single (PE) or one Gaussian per segment (C,W) is assumed in z-direction.
This step of the simulation also includes effects like energy loss, elastic scattering, bending of the trajectory due to a magnetic field or eventually (Λ, K_S^0) decay into secondary particles according to their known branching ratios.

HADES Detector Response (SimDST)

Up to now the interaction of the particles with the detector material has been simulated. These interactions e.g. energy loss in the active volumes of the MDCs, serve as an input for the detector response and digitisation procedure.
Here all detector effects like detector resolution, noise and their inefficiencies are simulated to mimic the detector response and produce realistic hits in each subsystem.
These hits are then treated like experimental data and undergo the same reconstruction procedure.
Finally, all properties like momentum and time-of-flight "measured" inside HADES are available and stored in the SimDST. The data can now be treated in the same way as the experimental recorded data for further analysis.

HYDRA

To cope with the special data container structure of the HADES DSTs and to provide access to distinct detector or particle information the HYDRA framework has been developed. This framework is based on the CERN developed ROOT and provides not only information for high level analysis like particle momentum and energy loss but also very detailed detector specific information like fired hits in MDC.
Here also standard function are implemented like the calculation of the distance of closest approach or constants like the particle masses can be accessed.
In addition the so called track sorter is implemented. During the track reconstructions, the hits of all particles which traversed the HADES are combined to a track. There it can happen that the distribution of these hits lead to a ambiguous and two possible tracks are reconstructed. Dependent on the analysis different criteria can be chosen, e.g. that the track must have a signal in the RICH for di-electron analysis. In this framework the tracks are sorted according to their χ^2/NDF of the Runge-Kutta

reconstruction algorithm and that the track must be attributed to a hadron. The latter condition is fulfilled if the track has not been marked as a lepton, with a track in the RICH detector.

3.6 Absolute Normalisation

In this section the absolute normalisation of the experimental and simulated data is presented.

3.6.1 Experiment

In order to absolute normalise the extracted particle yields to cross-section the following formula is employed based on:

$$\sigma = \frac{N}{N_{beam}\,\rho/A\,N_A\,d_{target}} \tag{3.24}$$

where

N: particle yield
N_{beam}: number of incident pions
ρ: target density
d_{target}: target thickness
A: target nucleus mass number
N_A: Avogadro constant

The target properties are listed in Table 2.1 while the mass number of the employed target nuclei correspond to $A_W = 184$ and $A_C = 12$.
The number of pions N_{beam} reaching the target is deduced from the number of hits N_{T_0} registered in the target T_0 detector. This number needs to be corrected as the HADES DAQ has a dead-time t_{dead} and therefore is blind in this specific time interval for further events. The active area of the target T_0 detector is in addition larger than the diameter of the target, as depicted in Fig. 3.12. The reduction factor was extracted from dedicated simulations taken into account the π^--beam transport [57] with an systemic uncertainty of 10%. With this the number of π^- reaching the target can be calculated with the formula $N_{beam} = N_{T_0} \cdot (1 - t_{dead}) \cdot (0.81 \pm 0.10)$.
An additional uncertainty of 10% arises from investigation of quasi-elastic scattering of π^- from experimental data recorded with pion momenta of 656 MeV/c $< p_{\pi^-} <$ 800

MeV/c impinging on a polyethylene (C_2H_6) target [75]. In this analysis the ratio of N_{T_0}/N_{el}, where N_{el} is the number of quasi-elastic scattered events, was studied as a function of the recorded date. As this ratio should be constant in time, the difference reveal uncertainties for N_{T_0}. Summarised in Table 3.4 are the numbers for the different target runs.

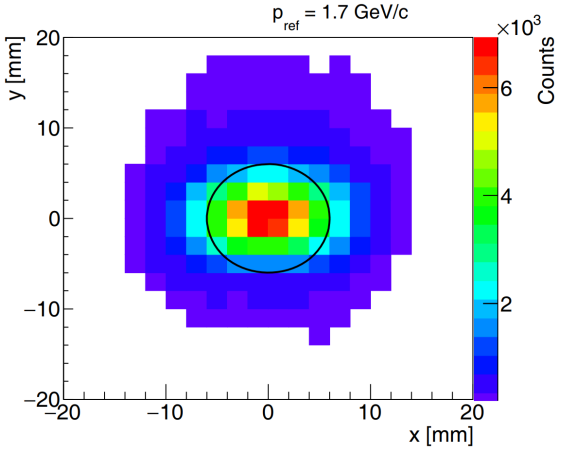

Figure 3.12: x-y distribution of beam transport simulations of the secondary π^- beam at an incident momentum of $p_{\pi^-} = 1.7$ GeV/c at the HADES target. The circle indicates the target area [57].

Target	N_{T_0}	N_{PT1}	N_{evt}	t_{dead}	σ [mb]
W	4.08×10^9	2.00×10^8	1.69×10^8	0.154	0.0077
C	4.31×10^9	1.58×10^8	1.33×10^8	0.156	0.0017

Table 3.4: Hits in T_0 detector N_{T_0}. Number that pass the PT1 trigger condition N_{PT1} and the number that pass the event criteria N_{evt} together with the dead-time t_{dead} and the normalisation factor σ in mb.

3.6.2 Normalisation of Simulated Data

Depending on the chosen transport model and the mode different normalisation procedures are applied. In general the absolute normalisation is based on the geometrical cross-section:

$$\sigma = \pi \cdot b_{max}^2 \tag{3.25}$$

where b_{max} is the maximum impact factor, which can be accessed in the simulated output.

GiBUU

Elementary:
The normalisation in the elementary mode is already provided by GiBUU itself and directly delivers absolute normalised σ. However each channel of interest must be implemented directly in the code.

Real:
For the real mode the following normalisation is applied:

$$\sigma = \frac{\sigma_{geom}}{10 * N_{run} N_{part}} \tag{3.26}$$

σ_{geom}: geometrical cross-section
N_{run}: number of simulated runs
N_{part}: number of particles per run
10: convert fm^2 to μb

where σ_{geom} is calculated with Eq. (3.25) and b_{max} was taken from the output.

UrQMD

The UrQMD output can be normalised by:

$$\sigma = \frac{\sigma_{geom}}{N_{run} N_{part}} \tag{3.27}$$

where

σ_{geom}: geometrical cross-section, provided by UrQMD output
N_{run}: number of simulated runs
N_{part}: number of particles per run

SMASH

For the absolute normalisation of SMASH also

$$\sigma = \frac{\sigma_{geom}}{10 * N_{run} N_{part}} \tag{3.28}$$

was used, while σ_{geom} was calculated with Eq. (3.25) and b_{max} was taken from the output.

4

Experimental Efficiency Determination

All data recorded with a detector suffer from a finite acceptance caused by the limitation of the detector itself or by indispensable supporting structures. But even the active areas, the detectors themselves, have an intrinsic efficiency lower than 100% caused by the design, manufacture, implementation of the detector and boundaries introduced by the physics of the applied technology. This leads to a distortion of the investigated particle spectra and thus to the interpretation of the underlying physics and makes it impossible to draw quantitative conclusions about the dynamics and interactions of the system.
In order to overcome these limitations, dedicated large-scale simulations are performed, which model the detector geometries as well as their independently and individually measured efficiencies and take into account as much as possible, e.g. the dead-regions of the apparatus. At the end an acceptance and efficiency matrix as a function of the kinematic variables of the particles can then be used to correct the recorded data for these effects and extract the undistorted particle spectra.
For a realistic digital model of the detector, the interaction of the particles with the detector material must be known with very high accuracy. Furthermore, the description of the efficiency of each sub detector and the response of the electronics is crucial for a reliable correction of the data. In addition during run-time electronic channels or detector parts can break, which also must be careful taken into account and be included into the digital model.
To test and verify the simulation and check the correct implementation of the efficiency of the HADES detector, elastic scattering was compared in experimental data and simulation. For this analysis, the experimental data recorded with the second

π^--beam at a central momentum of $p_{\pi^-} = 690$ MeV/c, impinging on a polyethylene (PE, see 2.2.3) target, was used.
In this chapter, the procedure of the experimental efficiency extraction based on elastic scattering is presented, followed by a comparison to the simulated data.

4.1 Analysis

In this section the procedure of the deduction of an experimental efficiency is outlined, separated into three major parts. First the basic method is introduced, then the method is applied to deduce the efficiency of the MDC and META sub-detector system, respectively.
The event selection and particle identification is based on a cut on the velocity β and momentum correlation, discussed in 3.2.1.

4.1.1 Procedure

Based on the kinematic constraints of elastic scattering (ES), $\pi^- + p \rightarrow \pi^- + p$, a correction matrix was derived in Φ, Θ and momentum. In this method, one of the two particles (π^- or p) was marked as the leading particle. By calculating the missing mass of this leading particle, it was possible to identify the second missing particle, which comes from an ES event. Taken the kinematic information of the leading particle, the expected properties of the missing particle can be calculated as follows:

$$\Phi_{miss} = \Phi_{ref} - 180° \tag{4.1}$$

$$\Theta_{miss} = \arctan\left(\frac{p_{ref} \cdot sin\left(\Theta_{ref}\right)}{p_{beam} - p_{ref} \cdot cos\left(\Theta_{ref}\right)}\right) \tag{4.2}$$

$$m_{miss} = \frac{1}{c^2}\sqrt{\left(E_{beam} + E_{target} - E_{ref}\right)^2 - \left(\vec{p}_{beam} - \vec{p}_{ref}\right)^2 c^2} \tag{4.3}$$

with

$\Theta_{miss}\Phi_{miss}$:angles of the missing particle
$\Theta_{ref}\Phi_{ref}$:angles of the leading particle
p_{ref} : momentum of the leading particle
p_{beam} : momentum of the beam measured with CERBEROS
E_{beam} : total energy of the beam
E_{ref} : total energy of leading particle with nominal mass
E_{target} :total energy of target: proton at rest

In this way, the expected yield for ES events can be determined in Φ, Θ and momentum. By applying 2σ cuts to the missing mass and to the kinematic properties of the ES system in $\Delta\Phi = \Phi_{miss} - \Phi_{measured}$ the missing particle can be traced (Fig. 4.2, Fig. 4.8, Appendix B) . This method is called **t**ag and **t**race **t**echnique (T^3). The developed method was applied to both experimental and simulated data.
In contrast to the simulated data set, which contains only elastically scattered events simulated with the PLUTO [67] event generator (Section 3.5.1), the experimental ones consist mainly of reactions with the proton (elastic) and the carbon nucleus (quasi-elastic, background) contained in the PE target material.
To validate the T^3 procedure, simulated single track efficiency was used as reference. Withing the scope of the simulated single track method, no M2 trigger in META was required (Section 3.1), as it was present at data taking. A particle was expected in the single track efficiency if its flying through the active detector area of the MDC drift chambers and traverses the META system on the HGeant level (see Section 3.5.2). Then the detector response was simulated and the reconstruction algorithm was applied. If now this particle can be reconstructed with a full track in MDC and at least one hit in META it was marked as measured and the single track efficiency could be extracted. Any larger differences or systematic offsets in the extracted single track efficiency to the simulated one extracted with T^3 hints to hidden biases or uncontrolled steps in the T^3 procedure.

4.1.2 MDC Efficiency

Method

A schematic sketch of the MDC efficiency reconstruction method is depicted in Fig. 4.1, which is divided into 4 major steps. In a first step, a leading particle was selected, for illustration purposes a proton, indicated in Fig. 4.1 at step 1). The proton track must have a hit in all MDC layers and at least one hit in the META system in RPC

or TOF and was selected by the post-analysis track sorter of HYDRA (Section 3.5.2). Based on the missing mass of this proton and the $\pi^- + p$ initial state as a function of the proton momentum the missing π^- can be selected employing Eq. 4.3.
To extract a cut specifically designed for selecting elastic scattered π^- in the proton missing mass, a dedicated subset of the available data was produced. This set only contains elastic events by applying a 2 σ cut on $\Delta\Phi_{MDC} = \Phi_{ExpectedPion} - \Phi_{MDC}$ in the expected π^- region, which is illustrated in Fig. 4.2 (a). This was biasing the data as only events were selected where the second particle was in the expected region of the MDC, but necessary to deduce a precises cut for elastic events.
The cut itself was extracted by projecting momentum slices of the missing mass vs. proton momentum distribution and fitting it with a asymmetric Gaussian and extract 2σ. This results in the distribution illustrated in Fig. 4.2 (a) where the 2σ of the individual momentum slices are indicated in green with their corresponding mean value μ coloured in red. These 2σ as a function of the proton momentum were fitted with a parabola to extract the final missing mass cut indicated in black in the same figure. The fit range has been tuned to exclude areas where huge fluctuations due to the lack of statistics occur.

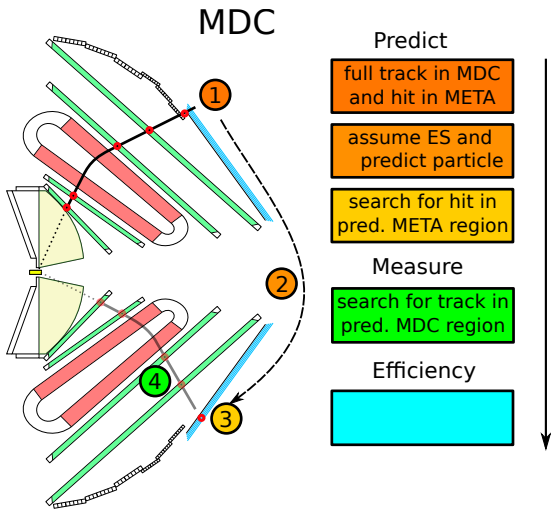

Figure 4.1: Schematically illustration of the T^3 for the extraction of the MDC efficiency. First a leading particle was selected which a full track in the MDC. Second, based on ES the missing particle was predicted with an additional cut in the predicted META region. As a last step these missing track was searched in the MDC.

This cut was then applied to the full data sample, illustrated in Fig. 4.2 (b), where no data bias was present.
Based on the kinematic boundary conditions of the ES system, the expected angle $\Phi_{ExpectedPion}$ of the π^- can be calculated and compared to the best matching angle

Φ_{META} reconstructed with the RPC/TOF detector system. A 2 σ cut on $\Delta\Phi_{META} = \Phi_{ExpectedPion} - \Phi_{META}$ applied with a Gaussian, as shown in Fig. 4.2 (c), ensures a clean sample of ES events and the reduction of carbon background.

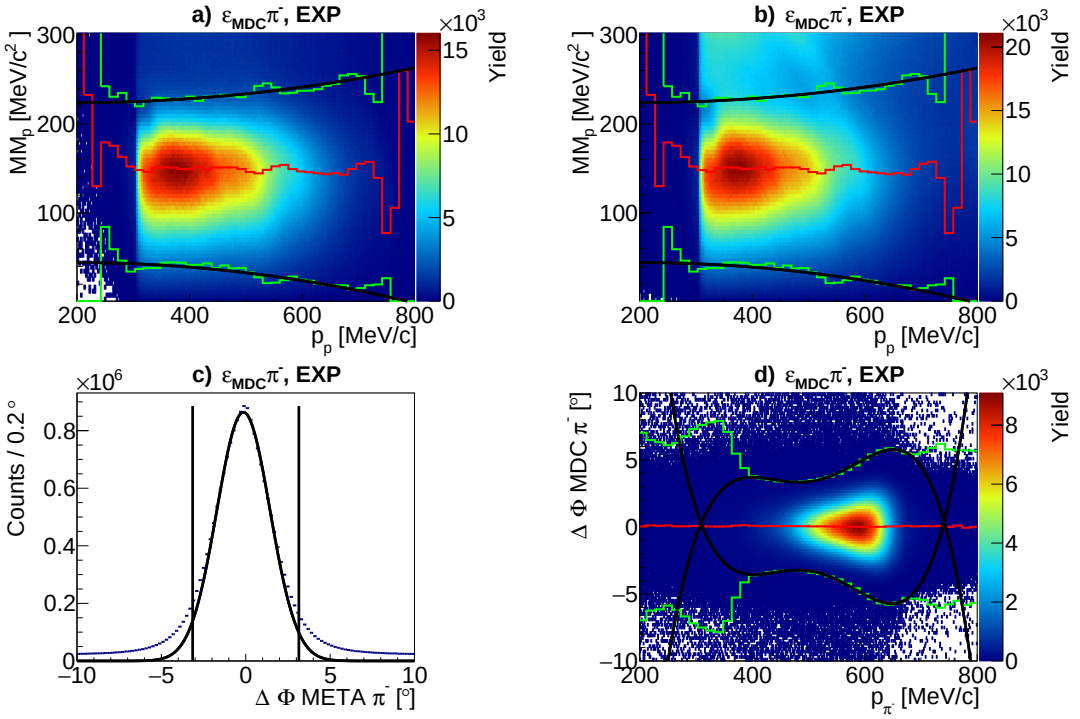

Figure 4.2: Cuts for the π^- MDC efficiency. First the missing mass cut for the missing particle (here π^-) of the leading particle (here proton) is constructed with an dedicated ES data sample in a) and then applied nominal data sample in b). Based on the ES constraints, the missing particle is predicted. A 2σ cut in this predicted region of the META further purifies the sample in c). As a last step a 3σ cut in the expected MDC regions selects the reconstructed π^- in d). See text for details.

Because of the statistical independence of the MDC and META detector systems, this cut does not introduce any bias to the outcome. Events passing this stage are expected to have a track of a π^- in the MDC in the expected region around $\Phi_{ExpectedPion}$, contributing to the expected yield in phase space. The last cut on $\Delta\Phi_{MDC} = \Phi_{ExpectedPion} - \Phi_{MDC}$ was applied with a 3σ Gaussian from the $\Delta\Phi_{MDC}$ vs. π^- momentum distribution, similar to the missing mass projecting momentum slices, but fitting with a 4th order polynomial to cope with the more complex shape of the extracted σ .
Also here the fit ranges were tuned to the momentum range where a stable and reliable width could be extracted. Events that go through this phase of the analysis were considered to be measured and contribute to the measured yield. The efficiency

was then simply derived by dividing these two yields bin wise.
To estimate the systematic error, the cut on $\Delta\Phi_{META}$ was varied withing $\pm 0.5\sigma$ and the cut on $\Delta\Phi_{MDC}$ was widened to 3.5σ. The difference of the efficiency to the nominal cut set was then taken as an systematic error. A comparison of the cuts for simulation and experiment aside with the cuts for the proton efficiency can be found in Appendix B.

Comparison to Simulations

The extracted MDC efficiencies with their corresponding θ and ϕ dependence are shown in Fig. 4.3 for the one dimensional efficiency and in Fig. 4.4, Fig. 4.5 double-differential. For ES there is a unambiguous relationship of the θ-angle of the particle to its momentum, indicated by the double x-axis label in the efficiency diagrams of the ϕ integrated efficiency of Fig. 4.3. This Fig. 4.3 depicts in the left panel the comparison of the experimental and simulated data with the T^3 procedure next to the single track for the π^- and on the right for the protons for the MDC detector.

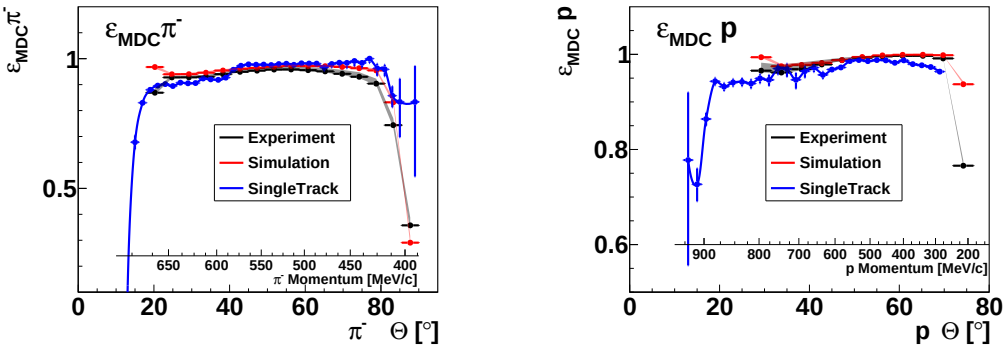

Figure 4.3: Efficiencies for the MDC detector system for pion and proton as a function of Θ and momentum. Indicated in black are the experimental, in red the simulated data aside with the single track efficiency in blue. Systematic uncertainties are indicated by the grey shaded area.

The different angle coverages between the developed method and the single track efficiency arises from the kinematic cut-off introduced by the elastic system, while the single track is unaffected by this cut-off. The pion efficiency shows a good agreement between the two data sets and the single track efficiency, although there are small deviations in the the higher angle range.
While both efficiencies deduced with the T^3 show the same trend with a small

systematic offset, the drop-off at $\Theta \approx 40°$ for the single track efficiency is not visible. In the case of proton efficiency, all efficiencies are very similar with respect to the covered angular range. Only slightly deviations can be found, again in the higher angle ranges.
The systematic error is indicated by the grey band while the other error bar represent the statistical error of the efficiency.
Differential efficiencies for the experimental (left) and simulated (right) approach can be seen in Fig. 4.4 and Fig. 4.5 for π^- and proton, respectively.
Both are in good agreement, while in both cases the simulated efficiency tend to predict slightly higher efficiencies.
Detector damages in the first sector causing lower efficiencies are reproduced for both particles, while in case of the π^- it is slightly overestimated.
To illustrate the overall agreement between these both approaches, the efficiency ratio is depicted in Fig. 4.6 in the left panel for protons and on the right for π^-. Larger deviations are only seen on the detector edges, where a stable extraction of the efficiency due to large fluctuations is not possible.

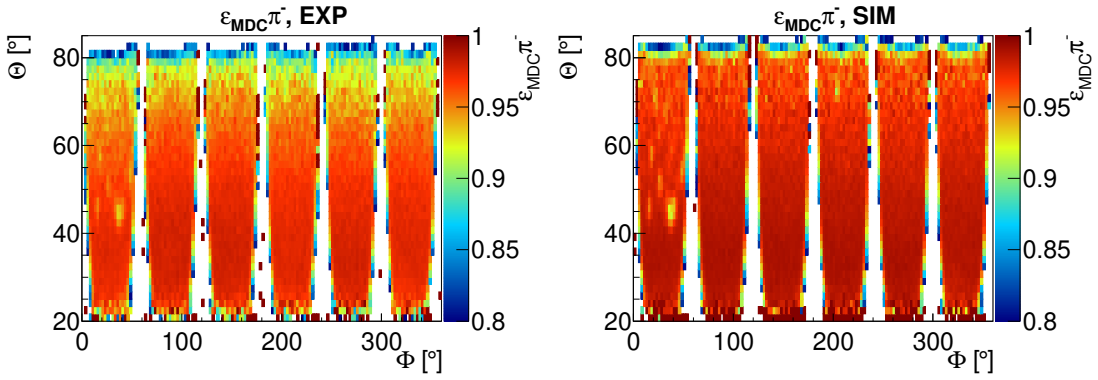

Figure 4.4: Two dimensional MDC efficiencies for π^- for experimental approach in the left panel and simulations in the right. Small deviations are visible by comparing the overall value of the efficiency, while dead detector spots in the first detector segment are well reproduced in the simulation.

4.1.3 META Efficiency

Method

Similar to the MDC efficiency method, the META procedure was also divided into four large steps, as shown in Fig. 4.7.
Again as a first step a leading particle (proton) was tagged. But in order to fulfil the M2-trigger condition which was applied during the data taking to avoid biasing the

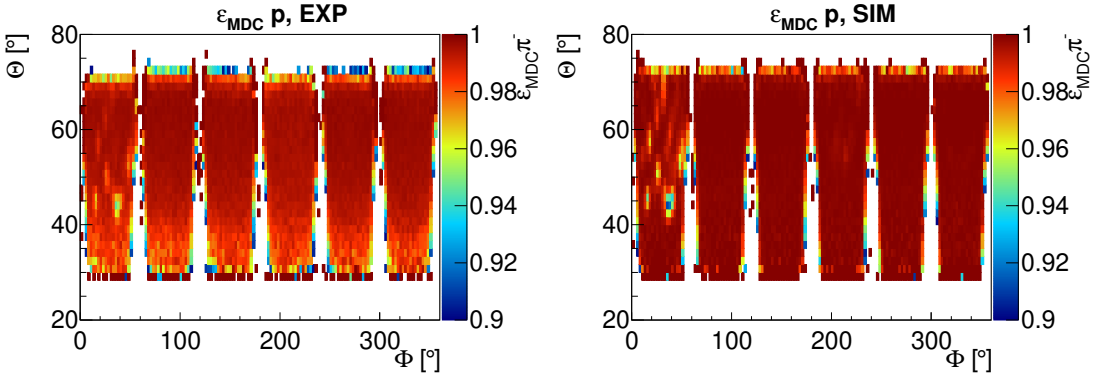

Figure 4.5: Two dimensional MDC efficiencies for p for experimental approach in the left panel and simulations in the right. Overall are both in good agreement while larger deviations are visible for lower Θ. Broken electronics in the first sector tend to be overestimated in the simulation.

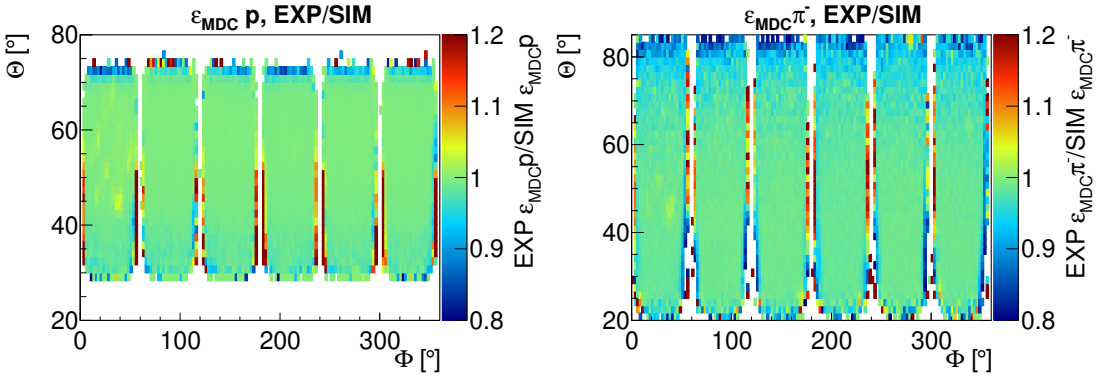

Figure 4.6: Two dimensional ratio of the experimental and simulations efficiencies for p and π^-. The overall detector response is well reproduced, while larger deviations are visible near the detector edges, where due to fluctuations no reliable efficiency can be extracted.

data, this particle alone needed a full track in all MDCs and in addition at least 2 hits (M2) in META, RPC and TOF. The response to this M2 trigger condition for a single particle in TOF and/or RPC is very diverse. In RPC it is much more likely to have 2 hits, with only a slight dependency on the position inside the detector, which can be explained by the double layer structure of the detector design (for details see Section 2.2.7, section RPC). However TOF shows a completely different behaviour. Here only two hits are matched to a track, if the particle is traversing the rods at the outer rim where two subsequent rods slightly overlap. As a consequence the statistic drops tremendously and also modifies the shape of the distribution as visible by comparing the missing mass of the proton in Fig. 4.8 (a) where the M2 criteria is not applied and the missing mass of panel (b) in the same figure where the M2 condition is applied. At about 550 MeV/c the system changes from RPC to TOF.

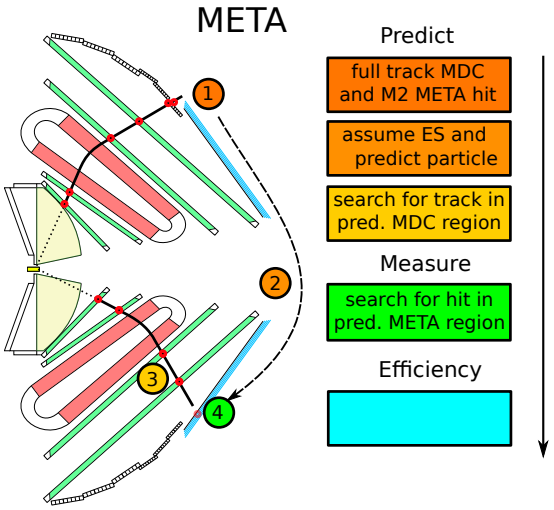

Figure 4.7: Schematically illustration of the T^3 for the extraction of the META efficiency. First a leading particle is selected which a full track in the MDC and in addition two hits in the META to avoid data bias. Second, based on ES the missing particle is predicted with an additional cut in the predicted MDC region. As a last step these missing track is searched in the META system.

In the same way as for the first step in the MDC efficiency procedure, a dedicated missing mass cut was constructed for the selection of elastic events as illustrated in Fig. 4.8 (a).
Also here a dedicated elastic data sample was produced by cutting on $\Delta\Phi_{MDC} = \Phi_{ExpectedPion} - \Phi_{MDC}$ in a 2σ window. Again the missing mass is projected in momentum slices and fitted with a asymmetric Gaussian to extract 2σ depicted in green and mean μ in red. The resulting distribution was fitted with a parabola for the final cut depicted in black and applied to the missing mass with the M2 condition in panel

(b). In this way elastic events can be selected coping with the complex structure introduced by the M2 trigger condition on the missing mass.
Since quasi-elastic reactions with the carbon in the PE also occur in the same missing mass range, the sample must be cleaned. This is performed by a 2σ symmetrical Gaussian on $\Delta\Phi_{MDC} = \Phi_{ExpectedPion} - \Phi_{MDC}$ with the same procedure as in the missing mass case and illustrated in Fig. 4.2 in panel (c). All events that passed this stage were expected events that contribute to the expected yield. The final step was comparing the expected $\Phi_{ExpectedPion}$ with all hits in the META system and cutting with a 3σ Gaussian $\Delta\Phi_{META} = \Phi_{ExpectedPion} - \Phi_{META}$ to extract the measured yield shown in the lower right panel of Fig. 4.8. The efficiency was then determined by dividing these yields. The systematics were calculated equally to the MDC efficiency, by vary the cut on $\Delta\Phi_{MDC}$ by $\pm 0.5\sigma$ and widen the cut on $\Delta\Phi_{META}$ to 3.5σ.

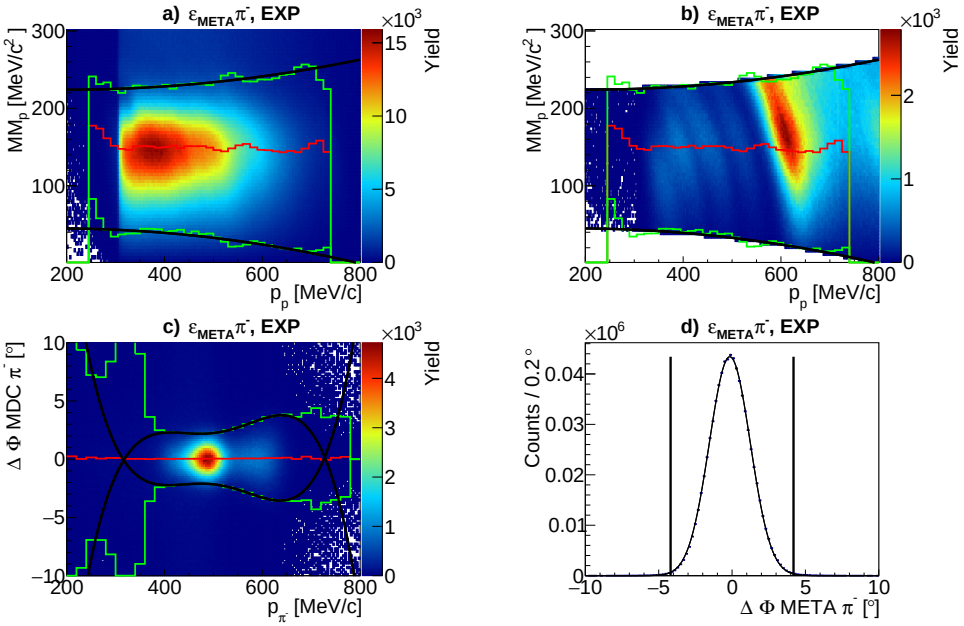

Figure 4.8: Applied cuts for the π^- META efficiency. First the proton missing mass cut was calculated by an ES data sample without the M2 condition in panel (a). This cut was then applied to the missing mass spectra of the full data set, with the additional M2 trigger condition for the proton in panel (b). The data sample was further purified by a 2σ cut in MDC in the predicted region depicted in panel (c). As a last step a 3σ cut in META was performed which selected the reconstructed π^- in panel (d). See text for details.

Comparison to Simulations

The subsection presents the extracted META efficiencies compared to its Θ, Φ and momentum dependence. Depicted in Fig. 4.9 are the extracted Φ integrated efficiencies for the META system with the T^3 approach and the single track efficiency for the META detector.
Again the different angle coverage is arising due to the elastic cut-off, not present for the single track efficiency. All efficiencies show a good agreement between the experimental, simulated and single-track efficiencies. Similar to the MDC the T^3 shows a slight offset to lower efficiencies for the experimental extracted efficiencies. In case of the META efficiencies the trend was reproduced for all three different efficiencies for the proton and π^-. This drop in efficiency for lower angles can be explained by the change of the system from TOF to RPC. Only in the case of the π^- in the lower Θ region a small deviation is visible, while in the proton case all three efficiencies show a perfect agreement.

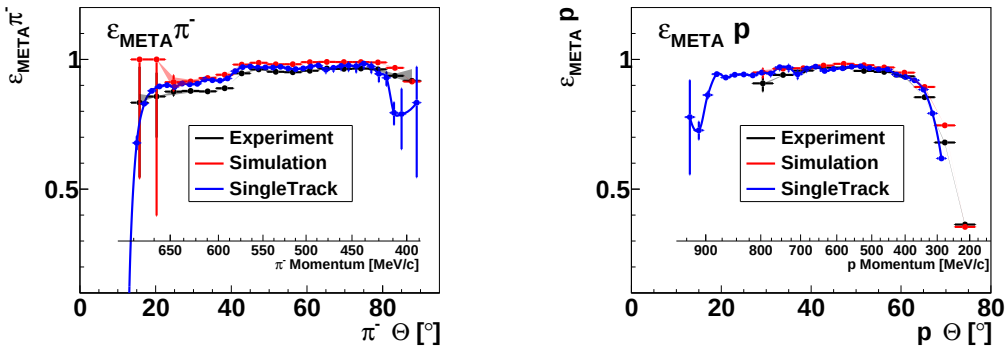

Figure 4.9: Efficiencies for the META detector system for proton and pion as a function of Θ and momentum. Indicated in black are the experimental, in red the simulated data aside with the single track efficiency in blue.

The different cut-off angles in the proton efficiencies by comparing MDC and META, result from protons that were stopped between the MDC and the META detector. In the case of the MDC, a META hit was required, so only events where protons reach META passing the event selection procedure through were selected. In the META case, however, only a MDC track was required, resulting that also protons that pass MDC and never reach the META system were expected, resulting in the difference of the cut-off. The two dimensional results for the proton efficiencies in the META system are illustrated in Fig. 4.11. Here the simulation and experiment are in perfect agreement, which also can be seen in the efficiency ratio of Fig. 4.12 on the right.

For the π^- the situation is slightly different, as the deviation between the simulated and experimental detector response is different, as depicted in Fig. 4.10. Here smaller detector effects are not perfectly modelled in the simulation.

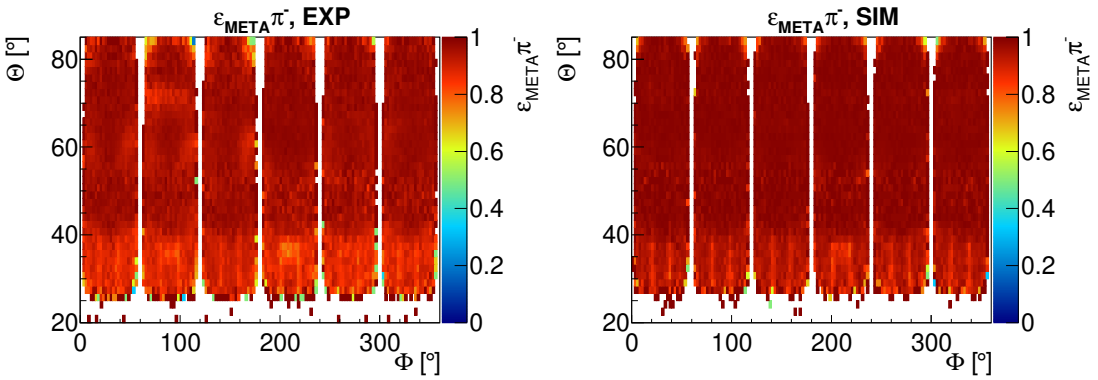

Figure 4.10: Two dimensional META efficiencies for π^- for experimental approach in the left panel and simulation in the right panel. The change of the META system from RPC to TOF at around $\Theta \approx 40°$ can easily be seen. Small deviations can be seen by an efficiency drop in the upper region of sector two, not seen in the simulation.

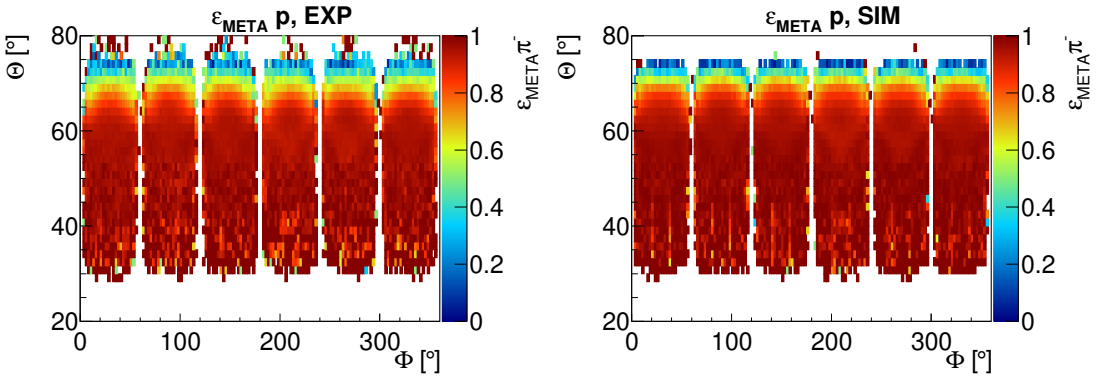

Figure 4.11: Two dimensional META efficiencies for protons for experimental approach in the left panel and simulation in the right panel. Both efficiencies show the same trend and the same magnitude.

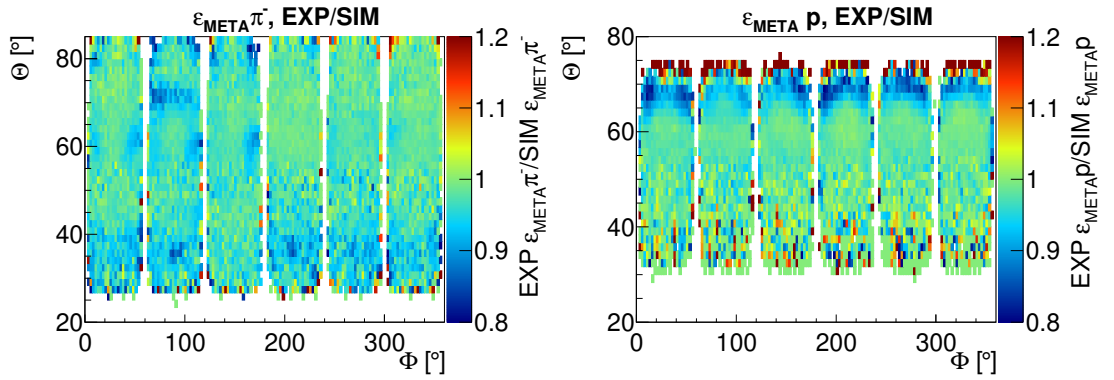

Figure 4.12: Two dimensional ratio of the experimental and simulations efficiencies for p and π^-. The overall detector response is well reproduced, while deviations are visible for the π^-.

4.2 Summary Experimental Efficiency Determination

In this section the tag and trace technique (T^3) was introduced, which allows for the derivative of a efficiency matrix for the MDC and META detector system based on experimental data, by exploiting the kinematic constraints of the elastic scattering $\pi^- + p \rightarrow \pi^- + p$ reaction. The experimental data was recorded with a secondary π^- beam impinging on a polyethylene target (Section 2.2.3). To suppress quasi-elastic scattering from the π^- on the carbon nucleus and isolate the elastic events, cuts were applied exploiting the kinematic characteristics of the ES system (Section 4.1.1).
This technique has been compared to simulations, where a pure elastic sample was simulated and the same procedure as for the experimental data was applied.
For the verification of this approach also the single track efficiency was calculated, where only the detector response of a single particle was considered.
By employing a slightly different approach for the META system in contrast to the MDC, where the track of the leading particle alone already fulfils the M2 trigger condition, any bias to the data could be avoided.
All extracted efficiencies employing the T^3 for the π^- and proton in MDC and META show consistency, both following the same trends for the Θ dependence. Only a small systematic offset to lower efficiencies for the experimental data can be seen, with and average offset in the MDC efficiency of $\Delta\epsilon_{MDC\pi^-} = -2.89$ % and $\Delta\epsilon_{MDCp} = -2.18$ % and in the META of $\Delta\epsilon_{META\pi^-} = -1.30$ % and $\Delta\epsilon_{METAp} = -0.29$ %. While in the case of the META system in addition all trends were reproduced, only the single track efficiency shows a drop-off for $\varepsilon_{MDC}\pi^-$ which is not reproduced by the T^3.
To give a conservative estimate on the difference of the simulated detector response to the real detector a systematic efficiency error of $\epsilon_{error} = 3\%$ is assumed for every charged particles and will be included in the systematic error evaluation.

The T^3 proves to give the possibility of testing and confirming the validity of simulated detector response by employing experimental data and comparing the extracted efficiency to simulations.

5

Inclusive Λ and K^0_S production in $\pi^- + A$ @ 1.7 GeV/c

In the following chapter the inclusive production of K^0_S and Λ in $\pi^- + A$ ($A = C, W$) reactions at a central beam momentum of $p_{\pi^-} = 1.7$ GeV/c is discussed. This inclusive analysis provide the cross-section for reactions of $\pi^- + A \rightarrow \Lambda(p\pi^-) + X$ and $\pi^- + A \rightarrow K^0_S(\pi^+\pi^-) + X$, respectively. To provide an overview on the kinematics of the lighter and heavier system, the double-differential analyses was carried out in $p_t - y$ and $p - \Theta$ bins. Experimental cross-sections were extracted this way and can be used in transport codes. The obtained double-differential kinematic spectra were then compared to three state-of-the-art transport codes, UrQMD [2] [3], GiBUU [4] and SMASH [5] (Section 3.5.1).
In the first part of this section the reconstruction of the K^0_S and Λ is outlined and the correction method for the detector effects is introduced. At the end of paragraph I the evaluation of the systematic uncertainties introduced by the analysis (Section 5.1) is presented. This is followed by the results section, which is divided into two subsections, one concentrating on the experiments data (Section 5.2.1) and the latter one on the comparison to transport predictions (Section 5.2.2). Here the basic inputs of the transport models, the elementary cross sections, were compared to the world data.
One aspect of the comparison to the transport models focuses on the extracted inclusive double-differential absolute normalised spectra with respect to the prediction of the three models.

At the end the kaon nuclear modification factor as a function of the momentum is deduced and compared to GiBUU simulations with and without a χ-EFT KN potential. The chapter is closed with a short summary on the inclusive analysis of K_S^0 and Λ.

5.1 Analysis Procedure

5.1.1 K_S^0 and Λ Reconstruction

Both particles were reconstructed via their dominant weak charged decay channel, namely $\Lambda \rightarrow p + \pi^-$ (BR = 63.9 ± 0.5% [1]) and $K_S^0 \rightarrow \pi^+ + \pi^-$ (BR = 69.2 ± 0.05% [1]). For the reconstruction of the mother particle, both charged daughter particles had to be measured with HADES.
In the first step, a suitable data sample was selected by applying event selections (Section 3.1) which suppresses pile-up and false triggered events caused by high radiation present in the experimental cave or detector channels with large noise contribution.
By applying the particle identification introduced in Section 3.2.1, which exploits the particle specific relation of velocity (β) to its momentum p, $p/\sqrt{p^2 + m_0^2} \pm 0.2 \gtrless \beta$, the daughter particles were identified. In a last step the mother particle was reconstructed by means of the invariant mass of the daughter particles, attributing the nominal mass m_0 to the selected daughter particles (p, π^-, π^+).
This procedure also introduced a combinatorial background arising from non-resonant particle production. To maximise the signal-to-background topological cuts were applied based on the characteristics of an off-vertex decay. In addition a broad cut on the invariant mass was selected. A summary of all cuts can be found in Table 5.1.

Cut	$K_S^0(\pi^+\pi^-)$	$\Lambda(p\pi^-)$
Target [mm]	$R < 20, -80 < z < 5$	$R < 20, -80 < z < 5$
$PV->SV$ [mm]	$PV < SV$	$PV < SV$
$\lvert MTD \rvert$ [mm]	$Dist \leqq 6.0$	$Dist \leqq 10.0$
$\lvert PV->\pi \rvert$ [mm]	$Dist \geq 4.5$	$Dist \geq 18.0$
$\lvert PV->p \rvert$ [mm]	-	$Dist \geq 5.0$
Inv. Mass [MeV/c^2]	$300 < M_{\pi^-\pi^+} < 600$	$1000 < M_{p\pi^-} < 1300$

Table 5.1: Summary of the applied vertex, invariant mass and topological cuts for Λ and K_S^0.

The selection on the primary vertex (PV, see Section 3.3.2) ensures that only

events were selected originating from the target region. As the neutral particles fly till they decay, the secondary or decay vertex (SV) must be downstream in respect to the PV, resulting in the condition $PV -> SV$.
Both daughter particles had to come from the same decay vertex, ensured by the cut on the minimum track distance $|MTD|$. In addition a minimum distance of the daughter particle track to the primary vertex was required to ensure off-vertex tracks ($|PV \rightarrow \pi/p|$).
For a detailed description of each single step concerning the reconstruction procedure, see Section 3.3.
The double differential inclusive analysis was carried out in the kinematics variables $p-\Theta$ and $p_t - y$. Table 5.2 lists the range of the kinematic variables for the two particles in the two different collision systems. Here the first column lists the nuclear system followed by the kinetic observable. The second and third column summarise the range, the bin width and the corresponding bin number for Λ and K^0_S, respectively.

	Λ			K^0_S		
Phase Space	Range	Bin Size	#Bins	Range	Bin Size	#Bins
C - Y	0-1.05	Δ(0.15)	7	0-1.6	Δ(0.2)	8
C - P_t [MeV/c]	100-900	Δ(100)	8	0-900	Δ(100)	9
W - Y	0-1.05	Δ(0.15)	7	0-1.6	Δ(0.2)	8
W - P_t [MeV/c]	100-900	Δ(100)	8	0-900	Δ(100)	9
C - Θ [°]	10-70	Δ(10)	6	0-80	Δ(10)	8
C - P [MeV/c]	320-1600	Δ(160)	8	150-1350	Δ(150)	8
W - Θ [°]	10-70	Δ(10)	6	0-80	Δ(10)	8
W - P [MeV/c]	320-1600	Δ(160)	8	150-1350	Δ(150)	8

Table 5.2: Range of the kinematic observables for the Λ and K^0_S in the different targets. The first column shows the total range, the second the bin size and the last column the corresponding number of bins.

As already mentioned the Λ and K^0_S were reconstructed by the invariant mass of their decayed particles over the covered phase-space. To extract the signal, fit functions were employed to these invariant mass distributions with $\Lambda(x, \mu_\Lambda, \sigma_1, \sigma_2, c)$ and $K^0_S(x, \mu_{K^0_S}, \sigma_{K^S_0})$. While the K^0_S was modelled by a single Gaussian, the Λ signal was described by two weighted ($0 < c < 1$) Gaussians. In the latter case the width was defined as the weighted σ of the individual Gaussians. In both cases the background

was modelled by a 3rd order polynomial:

$$\Lambda(x,\mu_\Lambda,\sigma_{\Lambda1},\sigma_{\Lambda2},c) = \underbrace{A\left[c\times e^{-\frac{1}{2}\left(\frac{(x-\mu_\Lambda)}{\sigma_{\Lambda1}}\right)^2} + (1-c)\times e^{-\frac{1}{2}\left(\frac{(x-\mu_\Lambda)}{\sigma_{\Lambda2}}\right)^2}\right]}_{\Lambda\text{ Signal}} \underbrace{+Pol(3)}_{\text{Background}}$$
$$K^0_S(x,\mu_{K^0_S},\sigma_{K^s_0}) = \underbrace{A\times e^{-\frac{1}{2}\left(\frac{(x-\mu_{K^0_S})}{\sigma_{K^0_S}}\right)^2}}_{K^0_S\text{ Signal}} \underbrace{+Pol(3)}_{\text{Background}} \tag{5.1}$$

where μ denotes the mean value or mass precision of the fit, σ the width or mass resolution and A the signal amplitude.
The yield and background were integrated within a $\pm 3\sigma$ window around the mean μ.
The fitting procedure was performed in an iterative way. First the background was fitted outside the signal region. Then the signal region was fitted with a Gaussian / double Gaussian, where the start values are the nominal mass for the mean μ and the approximate width ($\sigma_{K^0_S} = 6$ MeV/c^2, $\sigma_\Lambda = 2$ MeV/c^2).

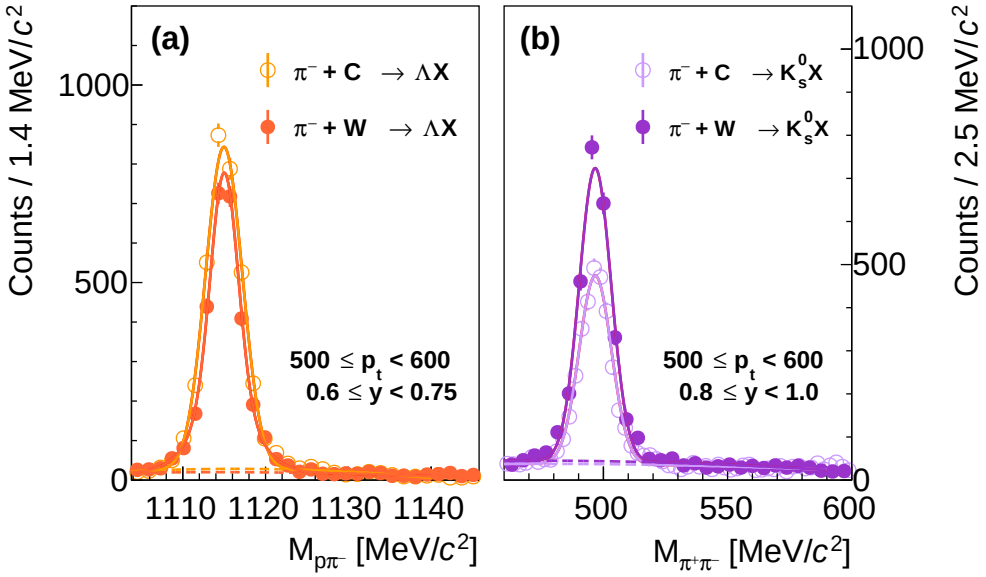

Figure 5.1: Reconstructed invariant mass of Λ in panel (a) and K^0_S in panel (b) candidates for an example bin in both nuclear system, together with their fitted function. The total fit is indicated with the solid line, while the background function is shown with the dashed lines.

C	Λ			K^0_S		
	Exp	GiBUU	UrQMD	Exp	GiBUU	UrQMD
σ	2.37	2.23	2.19	7.02	6.36	6.56
μ	1114.72	1114.77	1114.75	495.03	495.09	494.89
S/B	9.84	7.94	11.02	1.39	2.28	5.67
N_{reco}	6.64e+04	1.00e+05	5.09e+05	5.81e+04	3.14e+05	1.04e+06

W	Λ			K^0_S		
	Exp	GiBUU	UrQMD	Exp	GiBUU	UrQMD
σ	2.24	2.19	2.13	6.89	6.46	6.57
μ	1114.78	1114.73	1114.75	495.86	495.48	495.46
S/B	7.44	6.42	5.58	2.81	2.29	9.21
N_{reco}	7.76e+04	1.27e+05	1.98e+05	6.42e+04	4.39e+05	1.03e+06

Table 5.3: Average fit parameters for carbon (upper) and tungsten (lower) for Λ (left) and K^0_S (right) for experiment and simulation. σ donates the width, μ the mean value and S/B the signal-to-background ratio. N_{reco} corresponds to the total number of reconstructed Λ or K^0_S.

For the Λ a weighting factor of c = 0.5 was assumed as a start parameter. The resulting fit-parameters of the two pre-fits are then used a start values for the global fit.
A representative invariant mass distribution of the Λ candidates in both collision systems is shown in Fig. 5.1 (a), together with the total fit depicted by the solid lines and the background contribution by the dashed lines. The same is shown for the K^0_S Fig. 5.1 (b). In all cases a clear peak emerges from the background with an excellent signal to background (S/B) ratio, while in case of the K^0_S the background contribution is slightly higher. For details of the individual fit parameters see Table 5.3, where all average fit parameters are listed. The same fit function as for the reconstruction of the mother particle in the experiment were applied to the simulation and compared to the experimental one. Average values of the applied fits together with the extracted total number of mother particles are also summarised in Table 5.3 for carbon in the upper table and tungsten in the lower one for experimental data and the simulations based on GiBUU and UrQMD.

The reconstructed mass precision μ is in all cases reproduced by the simulation, with a global difference of $\Delta\mu < 0.40$ MeV/c^2. The distribution width σ of the invariant mass for the simulation tends to be slightly smaller than the experimental one, with a global difference of $\Delta\sigma < 0.66$ MeV/c^2. Still, one can state that the simulation is under control and all detector related effects observed in the experiment are re-

produced.
The S/B shows larger deviation, while in general GiBUU and experiment are in better agreement than compared to UrQMD. The differences can be explained by different underlying kinematic distributions and thus different implementation of cross-sections which influence the yield of the non-resonant background and therefore the extracted signal to background ratio.
The p_t dependence of these value is found to be negligible as shown Fig. 5.2 for the width σ of invariant mass , in Fig. 5.3 for the mass precision μ and in Fig. 5.4 for the S/B for Λ produced off the tungsten target. The experiment data are represent by black circles, GiBUU by the red and UrQMD by blue triangles.
The corresponding distributions for the lighter system (C) and for the K_S^0 can be found in Appendix C.1.

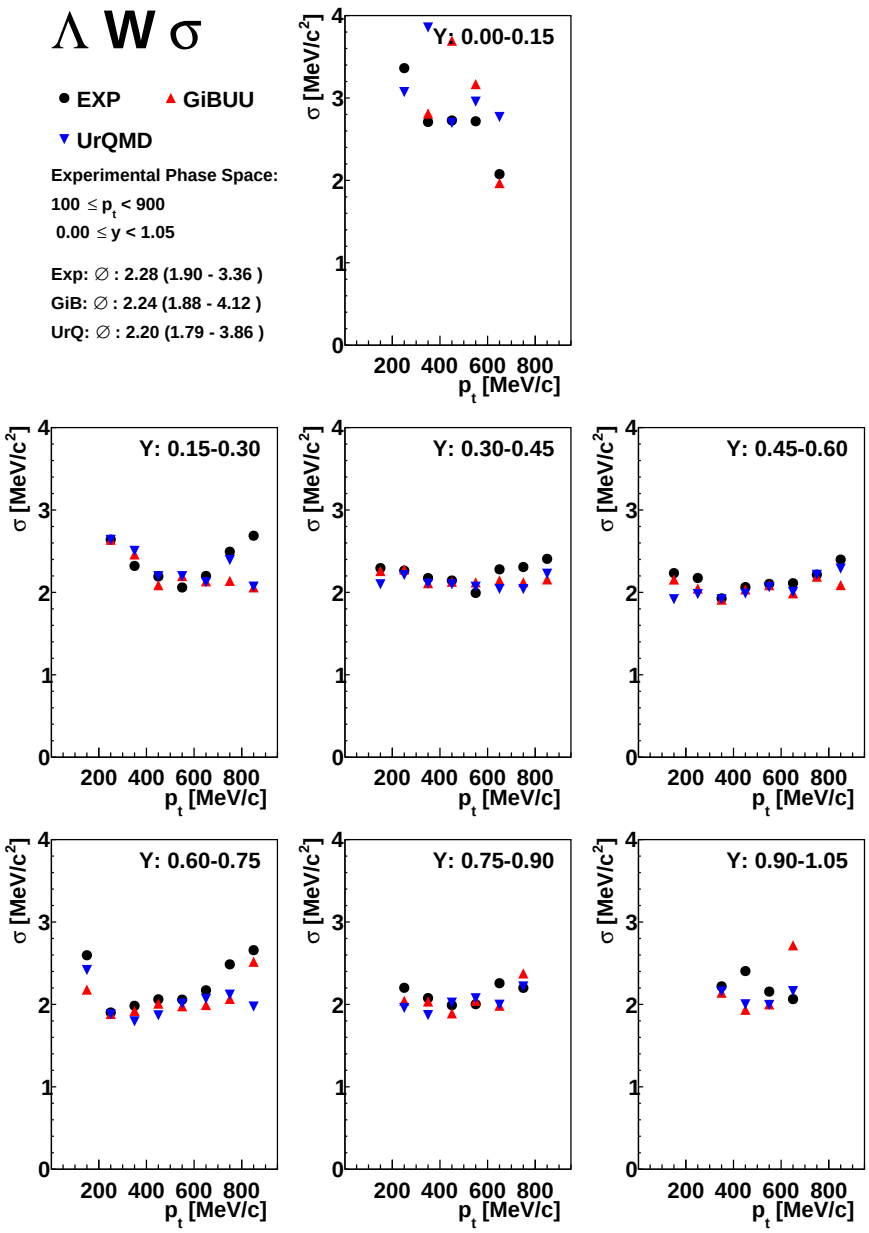

Figure 5.2: Mass resolution σ of the invariant mass distribution over the whole phase space for Λ in tungsten. The experiment data is coloured in black, GiBUU in red and UrQMD in blue.

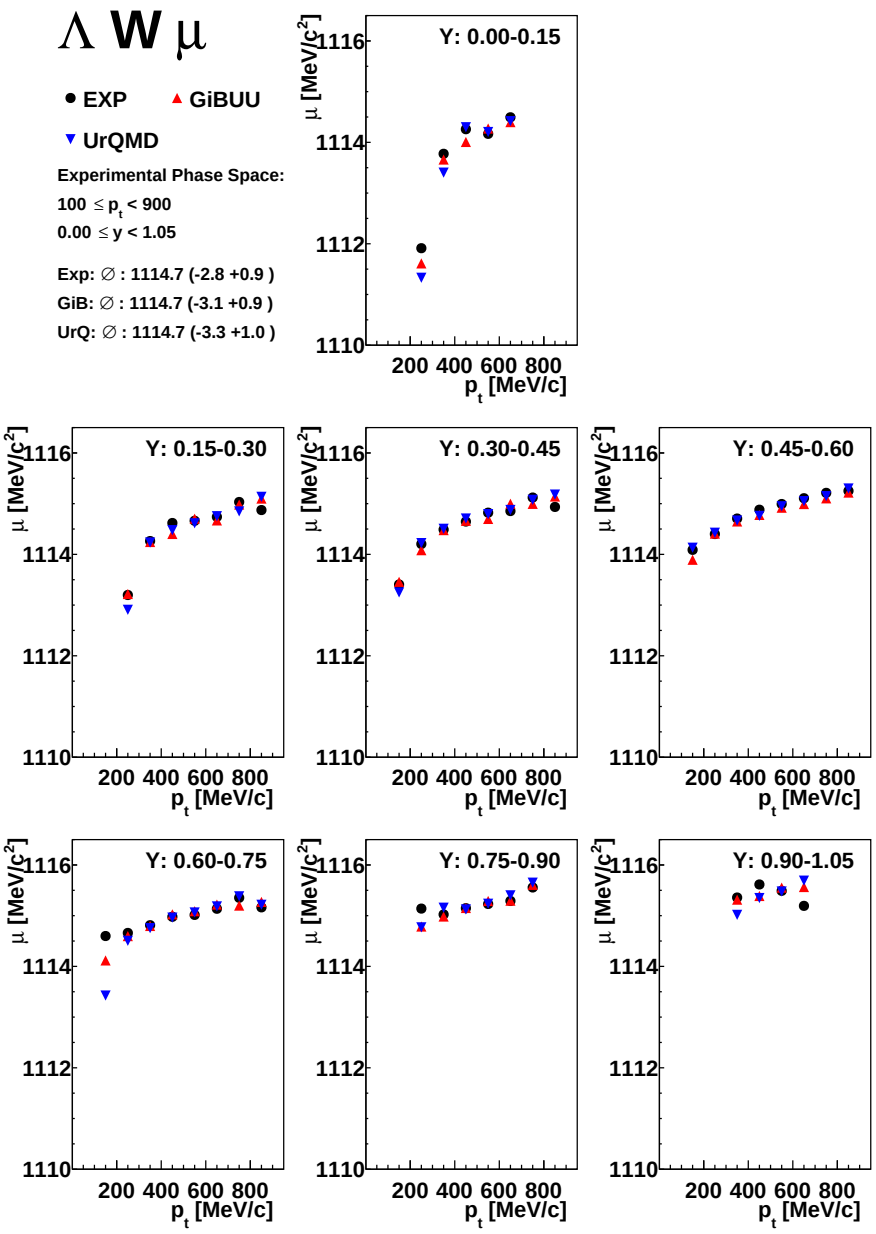

Figure 5.3: Mass precision μ of the invariant mass distribution over the whole phase space for Λ in tungsten. The experiment data is coloured in black, GiBUU in red and UrQMD in blue.

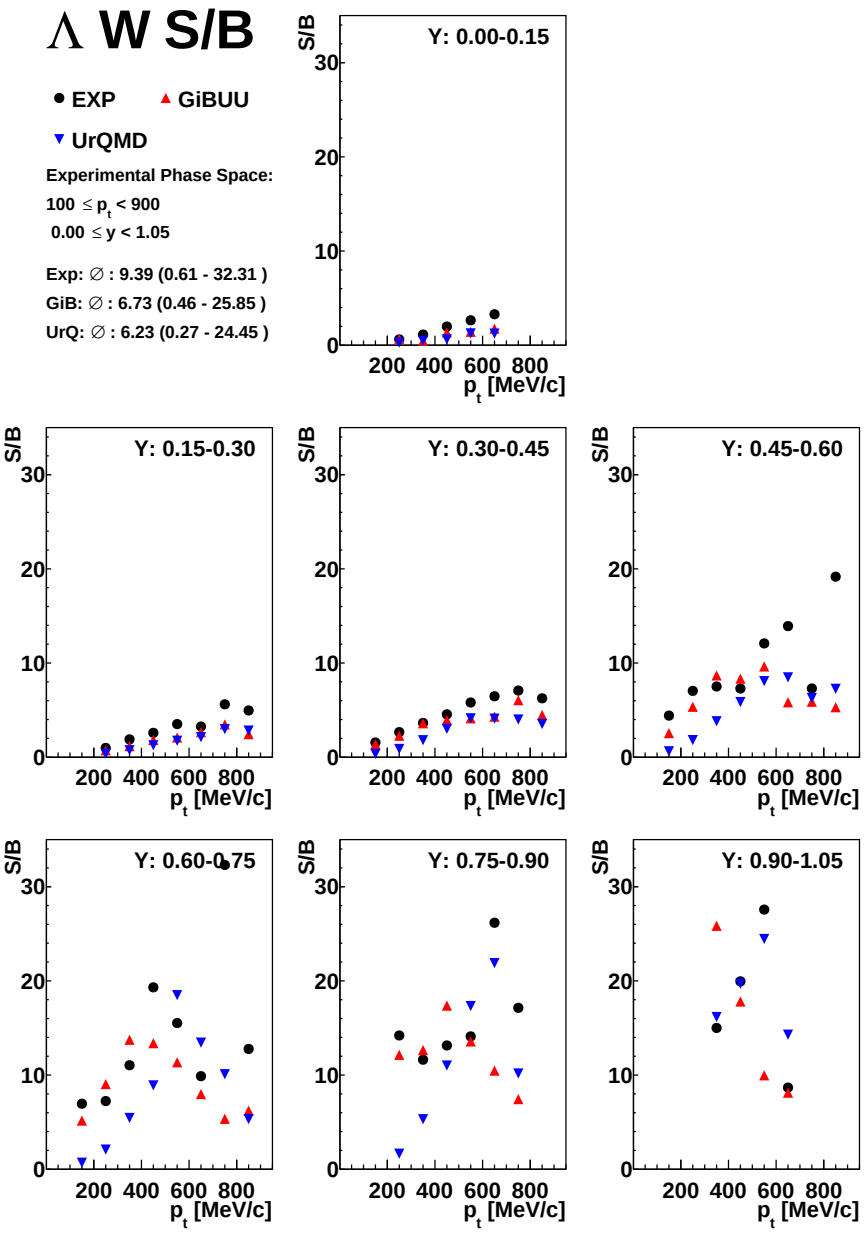

Figure 5.4: S/B of the invariant mass distribution over the whole phase space for Λ in tungsten. The experiment data is coloured in black, GiBUU in red and UrQMD in blue.

5.1.2 Acceptance and Efficiency Correction

Correction Procedure

All reconstructed particle distributions are altered by detector effects of HADES (Section 2.2). These effects include the finite geometrical coverage of the detector and the intrinsic efficiency of every sub-detector system, which was studied in Chapter 4 for META and MDC. The final detection efficiency depends e.g. on the particle species, its momentum and Θ angle and which sector of the HADES detector was traversed. Furthermore losses like scattering of the daughter particles inside the HADES detector material need to be taken into account. Also, effects introduced by the readout electronics have to be considered, the impact of the trigger decision or the inefficiency of the track reconstruction algorithm.
To cope with these effects and correct for them, dedicated full-scale simulations have been carried out employing specific simulations tools. Here every single step from the creation in the target to the signal registered in the detector and reconstruction of the particle is simulated and implemented to the highest known precision.
The simulation consists of a large data sample, ensuring small statistical errors, based on the GiBUU transport code (pertubative mode, Section 3.5.1) as a event generator covering the complete available phase space (4π).
To simulated the acceptance of the detector, these events where propagated through the HGeant framework, where a model of HADES is implemented including all detector systems and supporting structures. The response of the electronics and the conversion to the same data format as for experiment were treated by specific digitisation procedure for each subsystem within SimDST (for details see Section 3.5.2).
In addition, to consider all loses and effects introduced by the analysis procedure, like the particle identification, these SimDSTs were processed through the same analysis chain as the experimental data. This way a full-scale simulation was carried out, where the simulated 4π distribution undergoes the same losses and distortions as the experimental data. As the original undistorted phase-space distribution was known, an acceptance and efficiency matrix was obtained, by comparing the original distributions with the reconstructed ones.
The procedure was carried out in two sets of independent kinematic observable, $p_t - y$ and $p - \theta$, for the correction of the corresponding particle yield. The final efficiency correction matrix was calculated by:

$$\epsilon_{corr}(o1,o2) = \frac{D_{reco}(o1,o2)}{D_{4\pi}(o1,o2)} \tag{5.2}$$

where

$\epsilon_{corr}(o1, o2)$: efficiency matrix of kinematic variables o1 and o2

D_{reco}: distribution of the reconstructed full-scale simulation

$D_{4\pi}$: unfiltered event generator distribution

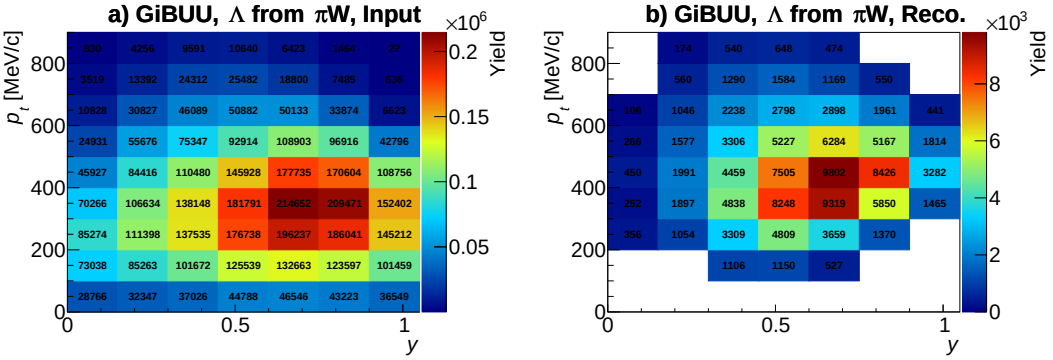

Figure 5.5: GiBUU input (a) and the reconstructed yield (b) inside the HADES acceptance for Λ in tungsten.

The phase-space distributions for the Λ hyperon in tungsten is illustrated in Fig. 5.5 is where the left panel (a) shows the undistorted spectra of GiBUU and the right panel (b) after the full-scale simulation. Equivalent figures for carbon and K_S^0 can be found in Appendix C.2

The bin size and ranges are the equivalent to the experimental data in the detector sensitive region (Table 5.2).

By comparing these distribution it is evident that a large effect is introduced by the detector, not only by a simple drop of statistic of the reconstructed particles but also by changing the shape. These effects can directly been observed in the acceptance and efficiency matrix, as an drop of efficiency to lower p_t and rapidity, illustrated in Fig. 5.6 for Λ in tungsten in panel (a), for carbon in panel (b) aside with the extracted maps for K_S^0 for tungsten in panel (c) and carbon in panel (d).

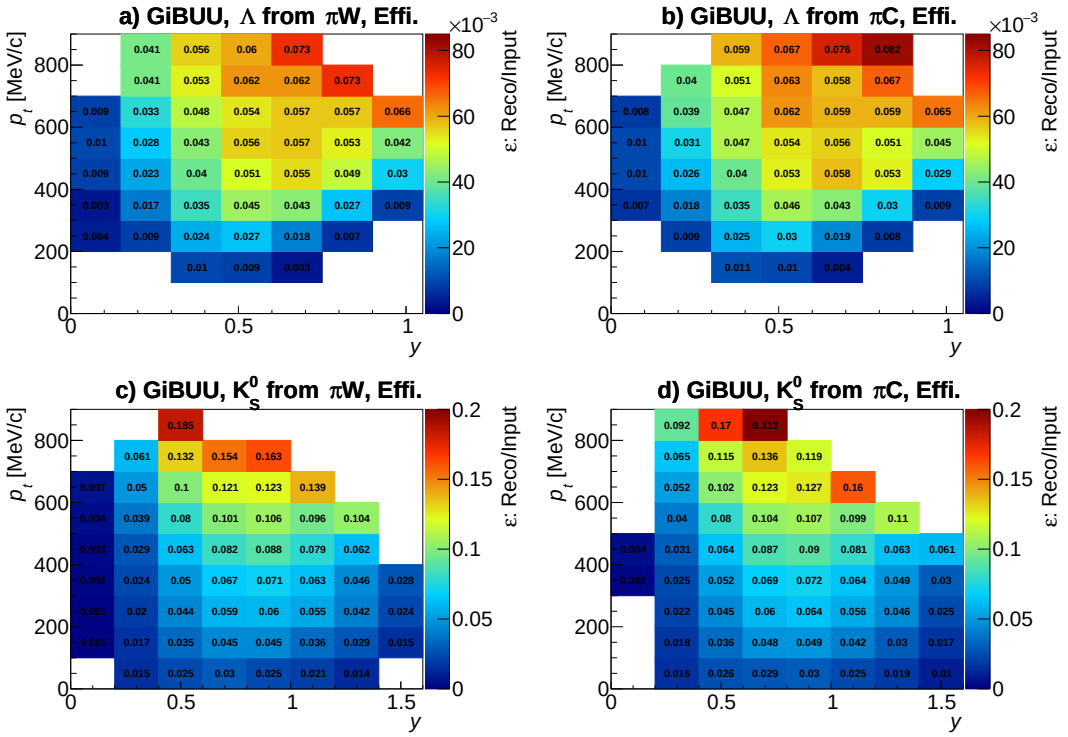

Figure 5.6: Efficiency correction matrices for Λ in carbon (a), Λ in tungsten (b), K^0_S in tungsten (c) and K^0_S in carbon (d).

For all particles the efficiency matrix is smooth over the entire phase space. The procedure was carried out for every particle species (K^0_S, Λ) and target (C,W) separately and the obtained correction values ($\epsilon_{corr}(p_t, y)$) and ($\epsilon_{corr}(p, \theta)$) are summarised in Table 5.4. The first number reads the average value and the second two numbers the interval from the lowest to the highest one.

Efficiency ϵ [%]		C	W
Λ	$P_t - Y$	3.98 (0.47 - 8.24)	3.71 (0.36 - 7.39)
K^0_S	$P_t - Y$	6.72 (0.28 - 31.34)	5.83 (0.14 - 18.55)
Λ	$P - \Theta$	3.96 (0.72 - 8.74)	3.80 (0.77 - 6.95)
K^0_S	$P - \Theta$	5.12 (0.09 - 12.67)	5.76 (0.51 - 18.78)

Table 5.4: Summary of the obtained correction efficiencies, $\epsilon_{corr}(p_t, y)$ and $\epsilon_{corr}(p, \theta)$ for K^0_S and Λ in both nuclear environments in %. The first number states the average value, while the interval reads the lowest and highest obtained efficiency.

The analysis of the comparison of elastic scattering $\pi^- + p \rightarrow \pi^- + p$ for experiment and simulation, presented in Chapter 4, revealed a systematic offset in the order

of 3%. This factor will be taken into account and added to the systematic error estimation discussed in Section 5.1.3.

Self-Consistency Check

To validate the independence of the acceptance and efficiency correction obtained from the GiBUU transport model, a self-consistency check was carried out. For this check another independent model was used, where also a full-scale simulation was performed in the same manner as for GiBUU. By correcting the yield of the GiBUU model, which is folded with the HADES acceptance and detector response, with this independent correction matrix based on another model, the initial distribution of GiBUU should be reconstructed.
For this purpose the UrQMD model was used as an event generator, which is based a completely different approach compared to the GiBUU model, as the particle production is only mediated by the decay of resonances (see Section 3.5.1).
For illustration purposes the procedure is outlined for the Λ in tungsten in $p_t - y$ phase-space, while all other self-consistency checks can be found in Appendix C.3. A double-differential analysis has been chosen with the same kinematic ranges and binning as for the inclusive spectra for every particle species and collision systems, respectively. Finally the efficiency matrix of UrQMD was applied to the GiBUU yield within HADES and compared to the initial distribution which is depicted in Fig. 5.7.

Both models are well in agreement, showing the independence of the efficiency correction method on the underlying initial distribution and thus the validity of the method. Only for small rapidities and p_t larger differences are observed that can be attributed to low statistics.
Additional smaller deviations are expected due to uncertainties of the signal extraction based on the fitting procedure (Section 5.1.1), which is affected by the different shapes of the background. Exemplary depicted in Fig. 5.8 for GiBUU on the left and UrQMD on the right. For UrQMD the background is more complex and can sometimes not be perfectly described causing these smaller deviations.

Overall the conclusion can be made that even though the underlying initial distributions of the models are quite different, they suffered the same efficiency losses and thus the correction method is model independent. Furthermore there is no need of a perfect description of the experimental data in order to perform the efficiency correction and no bias is introduced.

5.1.3 Systematic Uncertainties

Every analysis procedure and hence the obtained results are effected by systematic uncertainties. These effects are caused by a certain particle identification method, the applied topological selections or the fitting procedure.

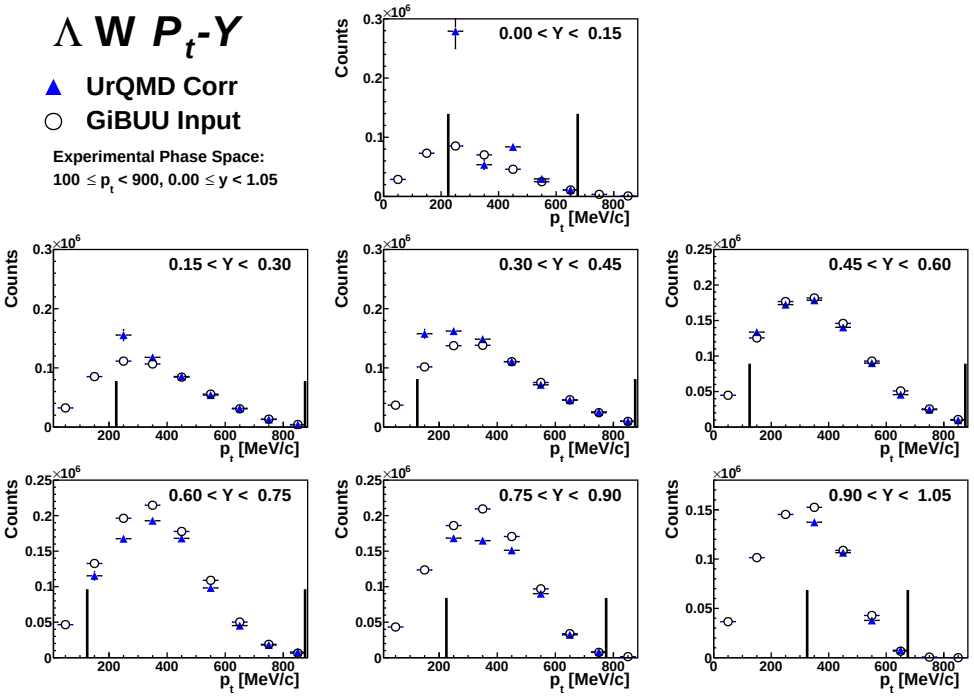

Figure 5.7: Self consistency check for Λ in tungsten. The reconstructed GiBUU yield, corrected with the UrQMD matrix is depicted in blue, while the open circle correspond to the undistorted GiBUU distribution. See text for details.

To estimate the systematic of each single step in the analysis procedure, these steps were systematically varied and the impact on the final corrected yield was determined. In the end all uncertainties were combined to a total systematic error.

PID

The first systematic check deals with the particle identification. For the inclusive analysis a simple β vs. momenta selection was applied (Section 3.2.1) for the identification of the charged daughter particles. Here the cut was varied from its nominal value of $\beta \pm 0.2$ to $\beta_{lower} \pm 0.16$ and $\beta_{upper} \pm 0.24$.
Due to the already wide open cut, no significant change of the yield was found ($< 0.2\%$).

Fitting Procedure

The extraction of the yield is highly dependent on the robustness of the fitting procedure. The systematic uncertainty was checked by varying the fit range and varying

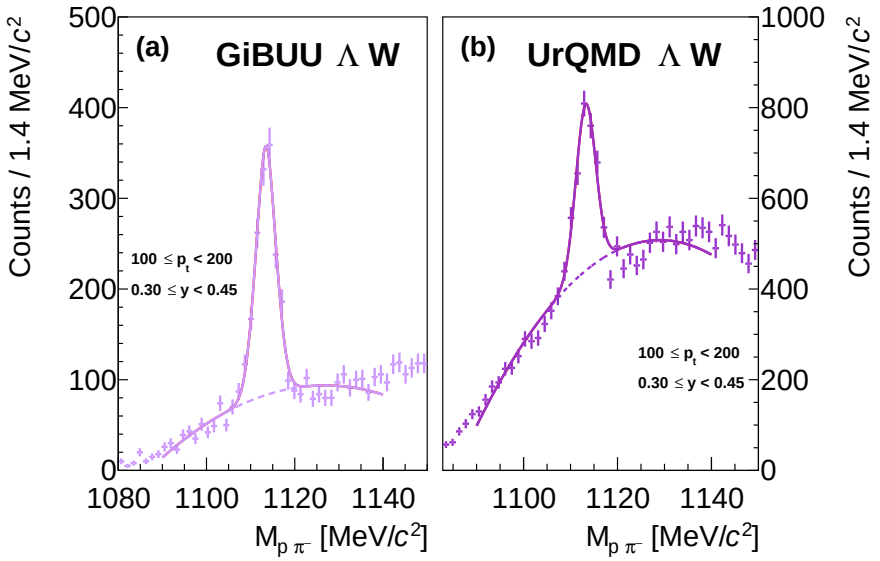

Figure 5.8: Invariant mass distribution based on GiBUU and UrQMD. In case of UrQMD the background is more complex, introducing small errors in the self-consistency.

the initial parameters of the signal and background function. Also here no significant variation of the extracted yield was found (< 0.32%).

Efficiency Correction

The correction uncertainty corresponds to 3% per particle and was evaluated from investigations of elastic scattering in a subsequent experimental campaign, as discussed in Chapter 4. As the K^0_S and the Λ were reconstructed via their dominant weak charged decay into two charged daughter particles, the total systematic uncertainty for the efficiency correction reads $\epsilon_{effi} = \sqrt{(3\%)^2 + (3\%)^2} = 4.24\%$

Topological Cuts

For the optimisation of signal-to-background ratio the kinematics of the decaying particles were used and four different topological cuts were employed. All have been introduced in Section 3.3. By varying independently the topological cuts (3x3x3 cut combinations) listed in Table 5.5 by ±20%, their impact on the final yield was determined.

With this check differences in the topological distributions between simulation and experiment were considered and taken into account in the systematic uncer-

Cut	$K^0_S(\pi^+\pi^-)$	$\Lambda(p\pi^-)$
$\|MTD\|$ [mm]	$Dist \leqq 6.0$	$Dist \leqq 10.0$
$\|PV->\pi\|$ [mm]	$Dist \geq 4.5$	$Dist \geq 18.0$
$\|PV->p\|$ [mm]	-	$Dist \geq 5.0$

Table 5.5: Topological cuts that were applied to the data, that have been varied within ±20%.

tainty. Due to the variation of the topological cuts, eventually different fraction of the signal in simulation and experiment are selected, which then result in a difference of the final corrected yield. This systematic error can be calculated double-differential for each single phase-space interval separately.
The systematic error is defined as:

$$\int_0^{x_{upper}} f(x)dx = 0.683 \cdot \int_0^{\infty} f(x)dx, \quad \int_{x_{lower}}^{0} f(x)dx = 0.683 \cdot \int_{-\infty}^{0} f(x)dx \tag{5.3}$$

where

x_{lower}: lower systematic error
x_{upper}: upper systematic error
$f(x)$: systematic error distribution

The confidence level is 68.3%, which corresponds to 1σ.
It was found that they are the main, non-negligible, contribution to the systematic uncertainty. The topological cuts are reducing/enhancing the signal in certain phase space intervals. Hence, this systematic errors also include and test the robustness of the fitting procedure. Therefore not only differences of the topological distributions are covered. A summary of the obtained average systematic errors with their range from the lowest to the highest value for all topological cuts can be found in Table 5.6.

5.1.4 Cross-Section Interpolation

In order to compare the inclusive particle production with the ones predicted by transport model a detailed investigation of the elementary cross-section included in the transport model to the known experimental cross sections was carried out.
For the experimental measured data no cross-sections has been measured at the

[%]		W	
Λ	$P_t - Y$	+ 3.3 (0.7 - 16.4)	- 4.3 (0.5 - 79.6)
K_S^0	$P_t - Y$	+ 1.5 (0.6 - 33.3)	- 1.7 (0.4 - 44.8)
Λ	$P - \Theta$	+ 3.1 (0.5 - 30.2)	- 2.5 (0.2 - 28.0)
K_S^0	$P - \Theta$	+ 1.0 (0.1 - 33.5)	- 1.2 (0.5 - 68.9)
[%]		C	
Λ	$P_t - Y$	+ 2.6 (1.9 - 39.8)	- 3.0 (1.8 - 28.3)
K_S^0	$P_t - Y$	+ 1.3 (0.2 - 45.3)	- 1.4 (0.3 - 45.2)
Λ	$P - \Theta$	+ 2.3 (0.1 - 36.5)	- 2.0 (0.5 - 29.4)
K_S^0	$P - \Theta$	+ 0.9 (0.3 - 50.6)	- 0.9 (0.2 - 20.7)

Table 5.6: Average systematics in percent with their lowest and highest value for all particles, nuclear systems and kinematics observables.

exact momentum of the incident pion beam ($p_{\pi^-} = 1.7$ GeV/c). Therefore a phase-space fit to the available data was performed to evaluated the cross-section at the following pion beam momenta of 1.7 GeV/c. The function was employed based on [76, 77]:

$$\sigma(s_0, s) = A * \left(1 - \frac{s_0}{s}\right)^B * \left(\frac{s_0}{s}\right)^C \tag{5.4}$$

with

$$s = m_{\pi^-}^2 + m_N^2 + 2\sqrt{x^2 + m_\pi^2} * m_N \tag{5.5}$$

$$s_0 = m_{\pi^-}^2 + m_N^2 + 2\sqrt{s_T^2 + m_\pi^2} * m_N \tag{5.6}$$

where $x = p_{\pi^-}$ momentum, s_T channel threshold m_{π^-} = pion mass, m_N = nucleon mass and A,B,C are the free fit parameters.
All experimental cross-sections presented in this chapter were exclusively taken from Landolt Bornstein [78]. For the GiBUU simulation the cross-section parametrisation was extracted directly from the code and also evaluated at the corresponding incident pion momentum.
Examples of the interpolation of the cross-section for the four different channels ΛK^0 in panel (a), $\Lambda K^0 \pi^0$ in panel (b), $\Sigma^0 K^0$ in panel (c) and $\Sigma^0 K^0 \pi^0$ in panel (d) are depicted in Fig. 5.9. The blue line shows the phase-space fit, whereas the green line shows the implemented parametrisation of GiBUU, while the black solid line marks the incident pion momentum of $p_{\pi^-} = 1.7$ GeV/c. The vertical lines represent the extracted cross-section for the phase-space and GiBUU implementation with their

value in the corresponding colour scheme.
Depending on the channel a large data set is available like for ΛK^0 in Fig. 5.9 (a) or $\Sigma^0 K^0$ in Fig. 5.9 (c). For some other channels like $\Lambda K^0 \pi^0$ only scarce data with large errors is present, depicted in Fig. 5.9 (b) or only a single measurement is existing as for $\Sigma^0 K^0 \pi^0$ shown in Fig. 5.9 (d).
All important channels with maximally three particles in the final state together with the corresponding cross section are summarised in Table 5.7. Production channels with four particles in the final state are not considered by the GiBUU framework. Anyhow, a phase-space extrapolation of the available data revealed that in the lower GeV range these channels can be neglected as their cross-section is $\sigma \leq 0.003$ mb.
While most of the cross-sections that are implemented in the GiBUU transport code are in a very good agreement to the phase-space extrapolated value within $\approx 10\%$, two significant channels show larger deviations: ΛK^0 and $\Sigma^- K^0$. While in case of ΛK^0, GiBUU undershoots by a factor of ≈ 3, the predicted cross-section in the latter channel is nearly one order of magnitude higher. But it has to be noted that only a single experimental point at $p_{\pi^-} = 5$ GeV/c has been measured, therefore no phase-space extrapolation can be made. For the GiBUU value the parametrisation of [69] is implemented. For SMASH the channels were extracted by dedicated simulations of $\pi^- + p$ and $\pi^- + n$ and normalised by the geometrical cross-section, for details see Section 3.6.2.

Channel $\pi^- + p$	p_{thr} [GeV/c]	σ_{fit} [mb]	σ_{GiBUU} [mb]	σ_{SMASH} [mb]	LB Channel
ΛK^0	0.896	0.177	0.067	0.163	52
$\Sigma^0 K^0$	1.031	0.146	0.132	0.105	81
$\Sigma^- K^+$	1.035	0.150	0.156	0.130	93
$\Lambda\pi^0 K^0$	1.140	0.118	0.110	0.074	45
$\Lambda\pi^- K^+$	1.144	0.079	0.091	0.149	48
$\Sigma^+\pi^- K^0$	1.290	0.014	0.015	0.005	72
$\Sigma^0\pi^0 K^0$	1.286	0.034	0.030	0.136	78
$\Sigma^0\pi^- K^+$	1.290	0.022	0.021	0.269	79
$\Sigma^-\pi^+ K^0$	1.305	0.037	0.030	0.201	88
$\Sigma^-\pi^0 K^+$	1.290	0.019	0.015	0.102	91
pK^0K^-	1.290	0.007	0.011	0.003	167
nK^+K^-	1.495	0.023	0.022	0.024	212
$n\phi$	1.559	0.027	0.020	-	200
$\Lambda\pi^+\pi^- K^0$	1.423	0.003	-	-	40
$\Lambda\pi^0\pi^- K^+$	1.407	0.002	-	-	44
$\Sigma^+\pi^0\pi^- K^0$	1.564	≈ 0	-	-	70
$\Sigma^+\pi^-\pi^- K^+$	1.568	≈ 0	-	-	74
$\Sigma^0\pi^-\pi^+ K^0$	1.580	≈ 0	-	-	76
$\Sigma^-\pi^+\pi^0 K^0$	1.580	≈ 0	-	-	86
$\Sigma^-\pi^+\pi^- K^+$	1.580	≈ 0	-	-	87
$\pi^- + n$					
$\Sigma^- K^0$	1.038	< 0.049	0.458	0.273	296
$\Sigma^-\pi^0 K^0$	1.296	< 0.042	0.036	0.505	294
$\Sigma^-\pi^- K^+$	1.290	< 0.070	0.025	1.035	295

Table 5.7: Production channel of Λ and K^0 in elementary $\pi^- N$ reactions together with the corresponding threshold momenta for the incident pion beam. The cross-section σ_{fit} at $p_{\pi^-} = 1.7$ GeV/c resembles the value obtained from a fit according to a parametrisations of [76, 77] to experimental data at several beam momenta. This is compared to σ_{GiBUU}, where the parametrisation were evaluated at the incident pion momenta and σ_{SMASH} where the cross-sections were extracted in elementary mode. The last column reads the channel number of Landolt Bornstein.

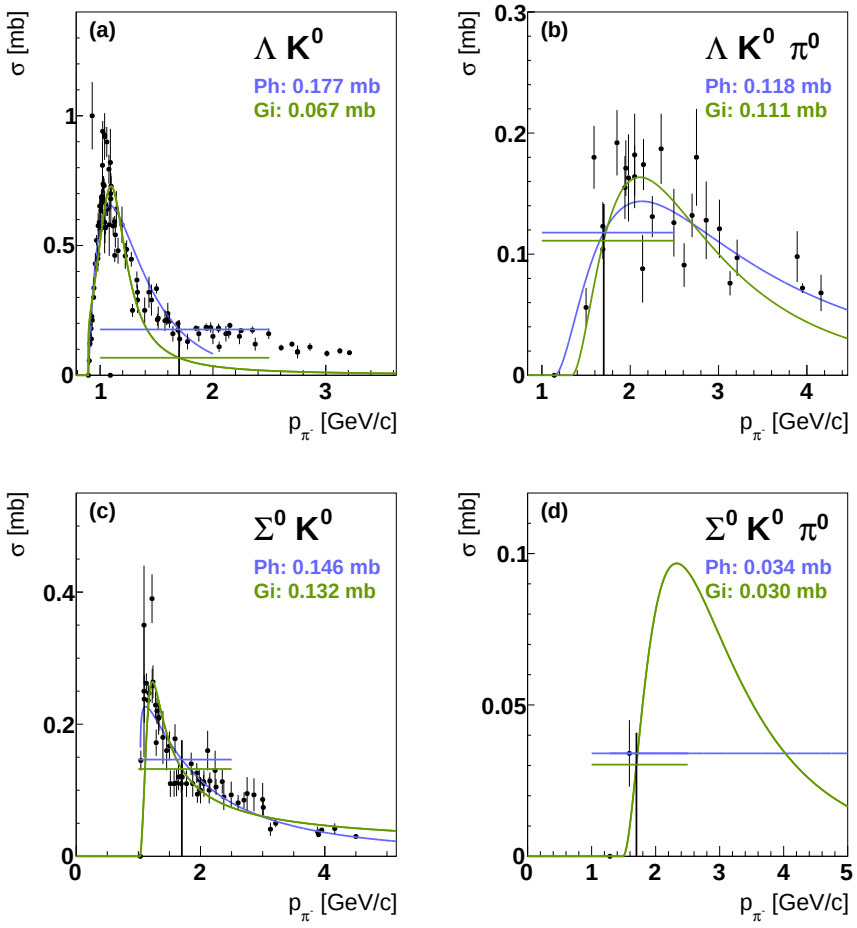

Figure 5.9: Examples for the interpolations of the cross-section with the phase-space fit in blue and the GiBUU parametrisation in green. The black solid lines corresponds to $p_{\pi^-} = 1.7$ GeV/c.

5.2 Results and Discussion

The following section deals with the study of the inclusive particle production of Λ and K_S^0 in tungsten and carbon.
Because of the large interaction cross section of the pion [78] with the nucleus, the production of the particles takes place near the upstream surface [34] . This leads on average to a longer path in the nuclear medium. In addition resonances can directly be excited and the dynamics are simpler (e.g. $\pi^- + N \rightarrow N^* \rightarrow \Lambda K_S^0$) with a two body final state, in contrast to proton-induced reactions (e.g. $p + N \rightarrow pN^* \rightarrow p\Lambda K_S^0$) where a three body final state occurs. Therefore pion induced reactions are superior for the study of resonances, particle production and the extraction of in-medium modification. These results can be used as constraints for transport codes and theoretical approaches and hence shed light on the involved physical dynamics.
The corrected yields are presented for the two sets of kinematic variables ($p-\theta$, $p_t - y$) and the extrapolation to obtain rapidity density distributions is outlined. At the end the comparison to the predictions of the employed transport codes GiBUU, UrQMD and SMASH is shown.

5.2.1 Kinematic Distributions

5.2.1.1 $P_t - Y$

The obtained particle yields extracted with the fitting procedure outlined in Section 5.1.1 have been corrected for the detector acceptance and efficiency applying the extracted efficiency matrices of Fig. 5.6. Hence undistorted spectra were extracted, which are presented in Fig. 5.10. In the upper panel the Λ distributions are shown for the heavy system in panel (a) and the lighter one in panel (b). The lower panel corresponds to the K_S^0. The dashed lines represent the conversion to $p-\Theta$ for constant angles of $\Theta = 30, 45, 85^\circ$ and total momenta of p = 200, 600, 1000 MeV/c.
If we focus on the Λ distribution in the upper panel (a) most of the yield is located at small rapidities and low p_t, in the region of the lowest efficiencies. (see Fig. 5.10, (a)). Hence most of the yield is shifted to backward rapidities and therefore outside of the HADES acceptance. By comparing the yield for the lighter system in panel (b) most of the yield is at mid-rapidity centred inside the acceptance with a rather symmetric distribution. Therefore backward scattering is the dominant effect in the heavier nucleus (W) as the number of nucleons is increasing compared to the lighter nucleus.

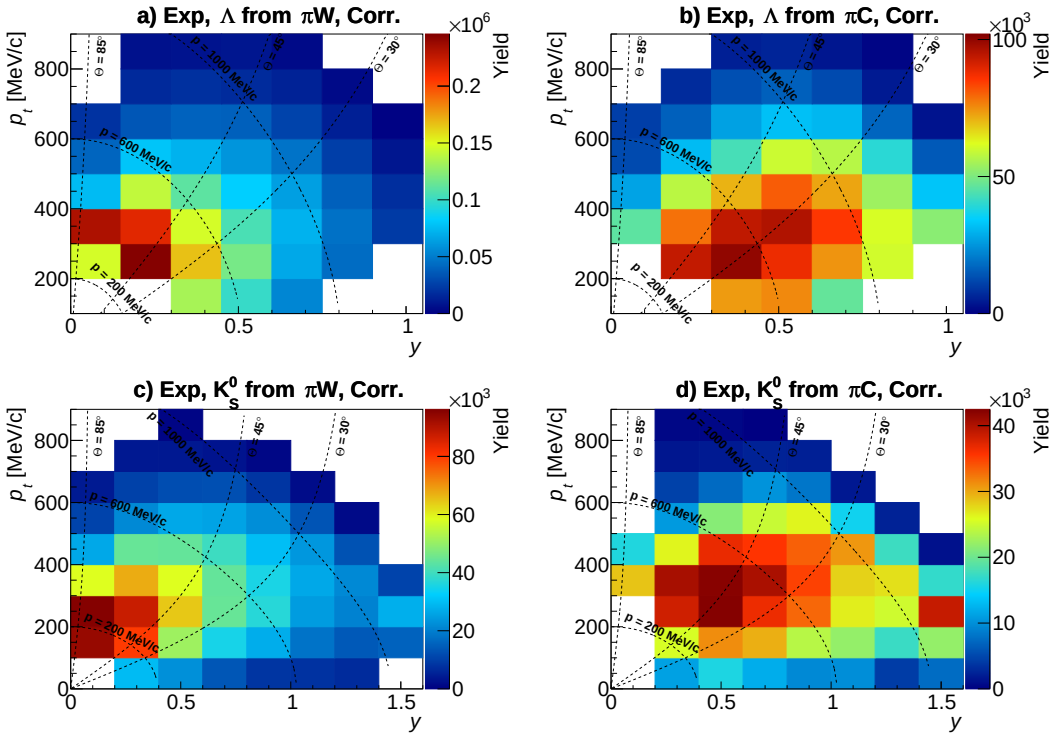

Figure 5.10: Corrected experimental $p_t - y$ yield for Λ and K^0_S in tungsten (a,c). The dashed lines represent constant vales of p = 200, 600, 1000 MeV/c and Θ = 30, 45, 85 °. For tungsten most of the yield is at low p_t and backward rapidity, while for carbon most of the yield is inside the acceptance with a rather symmetric distribution. See text for details.

The same behaviour is observed for the K^0_S comparing the corrected spectra for tungsten presented in panel (c) and carbon in panel (d). Also here backward-scattering to lower rapidities and out of the HADES acceptances can be seen.

Phase Space Extrapolation

As mentioned above, HADES does not cover the full-phase space and therefore also the extracted and corrected distributions are incomplete.
However, as discussed in Section 3.4 one can apply a Boltzmann fit to the p_t distributions obtained in different rapidity bins to extrapolate the total yield to uncovered regions transverse momentum regions with

$$\frac{dN}{dp_t} = A \cdot p_t \cdot \sqrt{p_t^2 + m_0^2} \cdot e^{-\frac{\sqrt{p_t^2+m_0^2}}{T_B}} \tag{5.7}$$

The extrapolation procedure is presented for the Λ in the tungsten (Fig. 5.11) and carbon target (Fig. 5.12) while the extrapolation for the K_S^0 can be found in Appendix C.4.

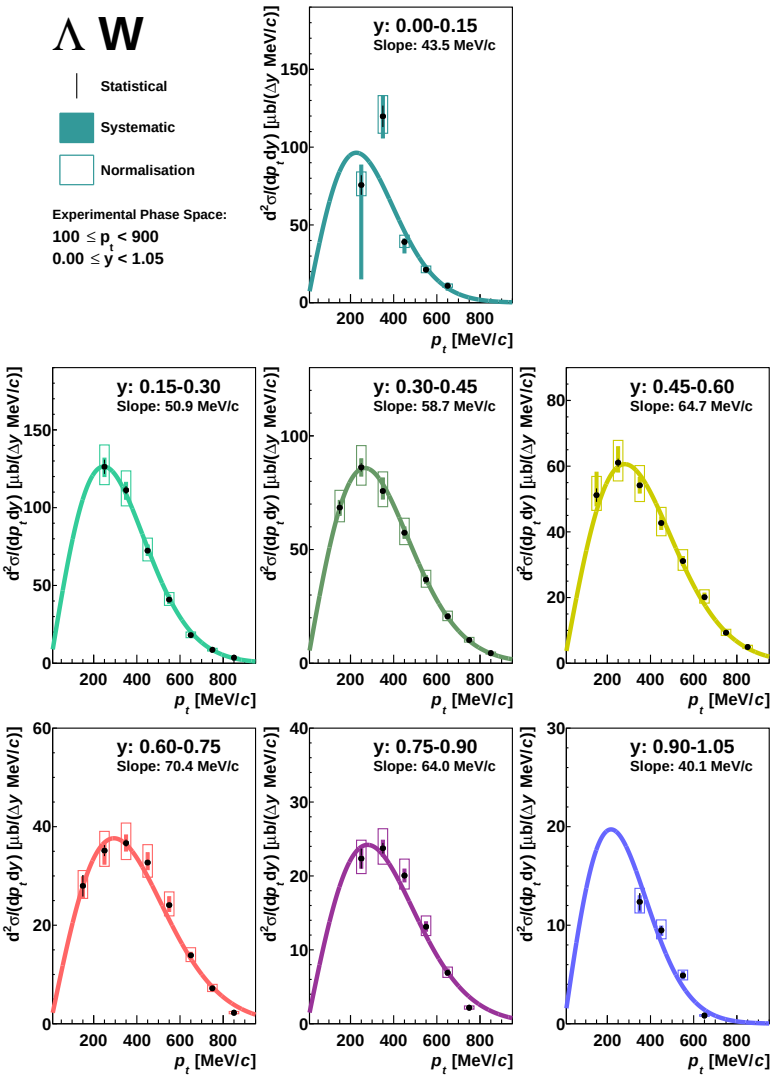

Figure 5.11: Cross-sections for Λ as a function of the transverse momentum in $\pi^- W$ reactions within HADES acceptance in different rapidity ranges (see legend). Statistical errors are indicated by the black line, systematic errors by the solid boxes and normalisation errors by the open boxes. The solid curve represent the applied Boltzmann fit. The slope parameter is indicated in every rapidity bin.

In both figures the same convention was chosen, where the statistical errors are indicated in black with the systematical errors shown by the solid boxes and the error

introduced by the normalisation procedure (Section 3.6.1) by the open boxes. The solid line represents the Boltzmann fit with the corresponding slope parameter for each rapidity slice in the upper right corner. For the fitting procedure a combined error of the statistic and systematical uncertainty was taken.

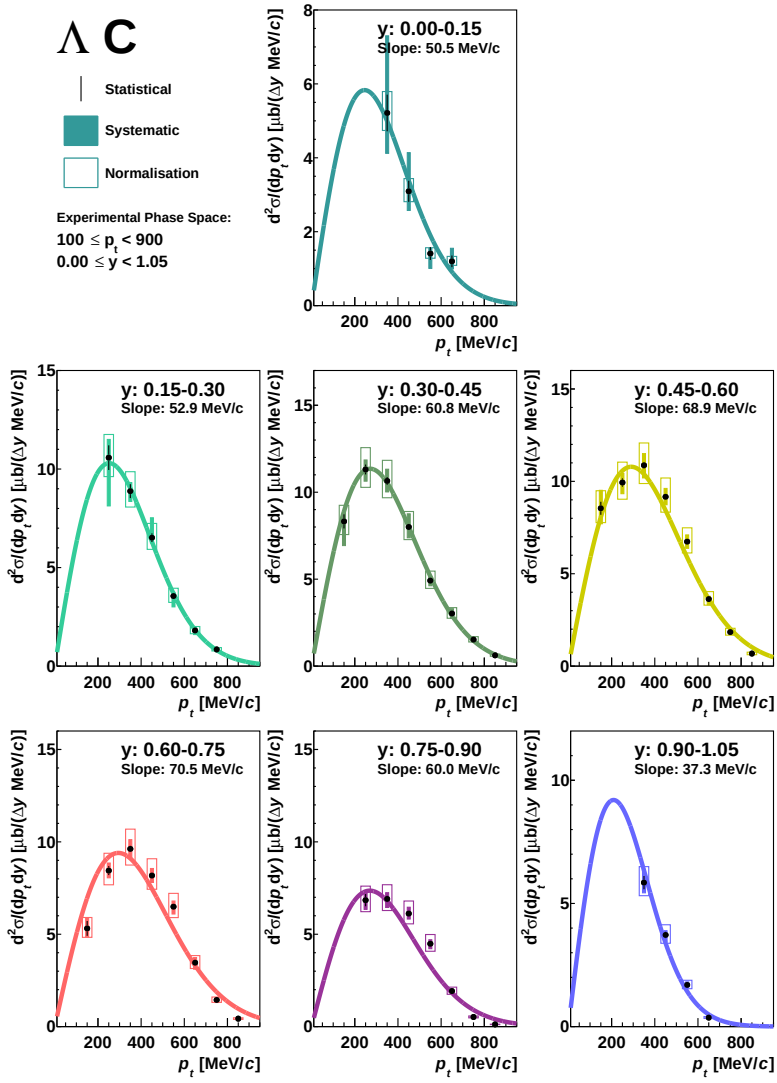

Figure 5.12: Cross-sections for Λ as a function of the transverse momentum in $\pi^- C$ reactions within HADES acceptance in different rapidity ranges (see legend). Statistical errors are indicated by the black line, systematic errors by the solid boxes and normalisation errors by the open boxes. The solid curve represent the applied Boltzmann fit. The slope parameter is indicated in every rapidity bin.

Over the whole phase-space and in both targets the fit describes the data very

well. Therefore the Boltzmann can be employed for the extraction of the yield in uncovered regions and extract a rapidity distribution.
For the extraction of the total yield in the rapidity bin all measured and corrected data points are summed up and the Boltzmann was integrated in the uncovered regions. To estimate the error of the extrapolated yield, the integral error from the fit was taken.
The extracted slope parameter for Λ and K^0_S for both targets is depicted in Fig. 5.13.

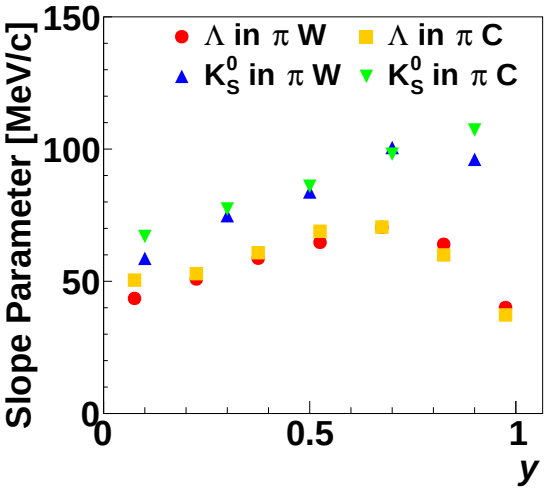

Figure 5.13: Slope parameters for Λ in tungsten (red circles) and carbon (yellow square) with K^0_S in tungsten (blue upward triangles) and carbon (green downward triangles).

5.2.1.2 Rapidity

By summing up all the corrected data points and integrate over the uncovered regions, the p_t extrapolated absolute normalised rapidity distribution $d\sigma/dy[\mu b/(\Delta y)]$ of Λ in panel (a), (b) and K^0_S in panel (c), (d) can be extracted as illustrated in Fig. 5.14. The statistical errors are indicated in black, the systematic errors including the error of the extrapolation are shown by the green shaded boxed and for the normalisation error by the red shaded boxes.

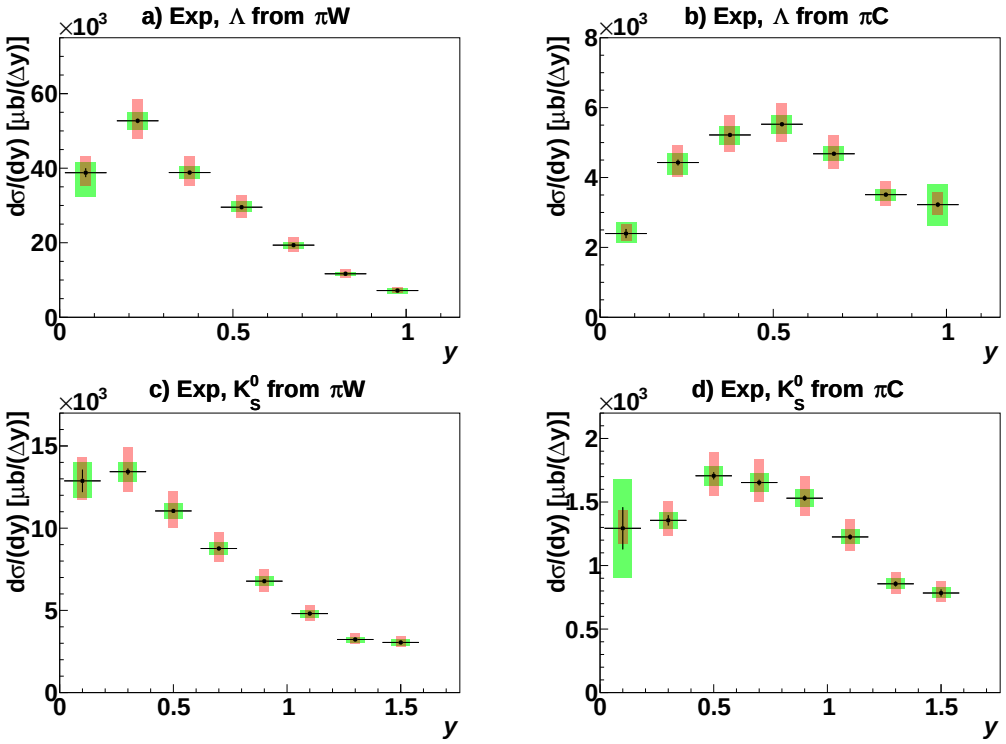

Figure 5.14: Rapidity distribution of Λ/K^0_S in $\pi^- W$ and $\pi^- C$ reactions. Statistical errors are indicated in black, systematical errors by the green shaded area and normalisation errors by the red shaded area.

By comparing the extrapolated rapidity distributions for both particles in the heavy target to the lighter one, the effect of backward scattering becomes evident. In case of tungsten for panel (a) and (c) the maximum is barely inside the HADES acceptance for both particles (Λ, K^0_S). For the carbon target in panel (b) and (d) most of the yield is inside acceptance with a rather symmetric distribution.
With this the total cross section $\Delta\sigma$ inside the HADES acceptance were extracted by summing up the rapidity distributions and are listed in Table 5.8. The first number represents the cross section $\Delta\sigma$ in μb, the statistical error followed by the upper and lower systematical error and the normalisation error.

5.2.2 Comparison to Transport Calculations

The inclusive production of the Λ and K^0_S could be studied over a large double-differential phase space in two different nuclear environments.
Thus the corrected data can be used for a comparison of the three state of the art transport models: GiBUU [4] , UrQMD [2] [3] and SMASH [5], of the shapes of the

Target	Particle	$\Delta\sigma$ [μb]
W	Λ	$29712 \pm 127^{+677\ +1416}_{-1114\ -1159}$
W	K^0_S	$12797 \pm 68^{+302\ +559}_{-277\ -457}$
C	Λ	$4347 \pm 19^{+129\ +188}_{-131\ -154}$
C	K^0_S	$2080 \pm 14^{+83\ +84}_{-83\ -68}$

Table 5.8: Target, particle species and cross-section inside the HADES acceptance (see text). Error values shown are statistic (first), systematic (second) and normalisation (third).

distributions and the absolute cross-section.
The production mechanism that is implemented in the transport codes differ strongly. In UrQMD and SMASH particle production is mediated via the decay of intermediate baryonic resonances (e.g. Δ, N*), while GiBUU uses parametrisations of the final states. Also the representation of the particles differs, while GiBUU and SMASH uses the test-particle approach with point like particles, UrQMD uses Gaussian wave-packages. For a detailed description of the transport models see Section 3.5.1.
In this way the here presented data can be used to either further constrain the parametrisation or the branching ratios of the resonance decays.
In the following the GiBUU model is presented by the solid line, the UrQMD model by the dashed line and SMASH by the dotted line. The first part presents the comparison of the transverse momentum distribution obtained for different rapidity bins followed by rapidity spectra. All figures are ordered in the following way: the upper panel shows the absolute normalised distributions for simulation and experiment, while the lower panel shows the difference (Sim - Exp)/Sim in percent.

5.2.2.1 $P_t - Y$

The Λ cross-section as a function of the transverse momentum in $\pi^- W$ reaction is shown in Fig. 5.15 and compared to the mentioned transport models. For the lower region of $y < 0.45$ all three models predict a quite similar shape, while the absolute cross-section deviates. Both GiBUU and SMASH, predict a similar cross-section, while UrQMD predicts a higher one. Here UrQMD shows a better prediction power in the shape and cross-section in compared to GiBUU and SMASH. Also for intermediate rapidities of $0.45 < y < 0.75$ SMASH and GiBUU predict comparable distributions, both undershooting the experimental extracted cross-sections. Although in case of SMASH a slightly double-peak structure begins to form. A similar behaviour can also been seen for UrQMD but with a much larger magnitude. These

structure with emerging peaks at higher transverse momentum can be explained by the decay of heavy resonances necessary to describe heavier particles like the Φ and Ξ^- [79]. For the Λ it was found that resonances N(2080) and N(2190) are dominating the production and shifting the transverse momentum to higher values.. The Σ^0 is mainly produced by the decay Δ(1950) and Δ(1930), whereas K^0_S are produced by all four of the given resonances. A detailed presentation of the single contributions of the resonances in UrQMD as a function of the transverse momentum in rapidity bins for Λ, Σ^0 and K^0_S can be found in Appendix C.5 This trend continues to the highest measured rapidities up to $y = 1.05$, while the prediction of the cross-section for SMASH and GiBUU gets better and UrQMD overpredicts the cross-section.

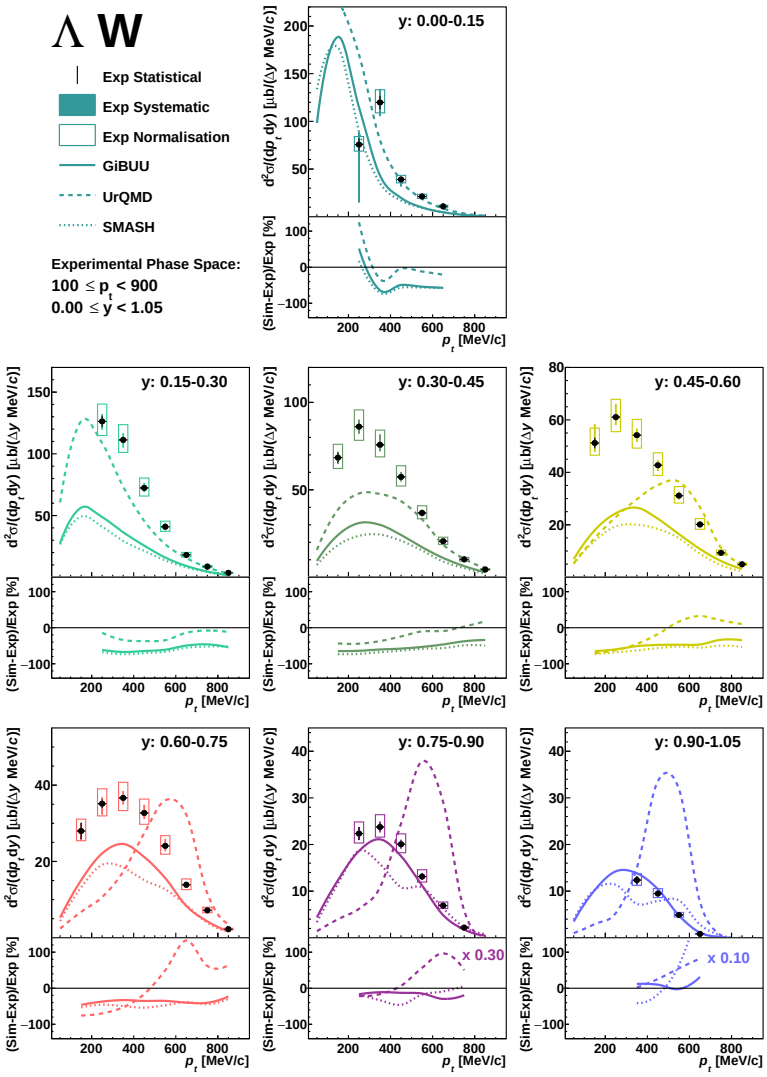

Figure 5.15: Comparison of the p_t distribution of absolute normalised transport codes GiBUU (solid curve), UrQMD (dashed curve) and SMASH (dotted curve) to the experimental Λ cross-section in tungsten for different rapidity bins. Experimental errors are indicated in black for the statistical, filled boxes for the systematic and open boxes for the normalisation error. In the upper panels the comparison of the transport models to the experimental data is shown, while the lower panel indicates the difference in percents. See text for details.

A similar trend can be observed for the absolute normalised cross-sections of Λ in carbon compared to the transport model shown in Fig. 5.16. In the lower rapidity $y < 0.45$ SMASH and GiBUU predict similar shapes and cross-section largely deviating from the experimental data. UrQMD again predicts a higher yield in this

region and hence is more in agreement with the experimental data. For the mid and high rapidity range again the double peak structure of SMASH evolves and the distribution for UrQMD gets shifted to higher transverse momenta. The deviation of the predicted cross-sections decreases for SMASH and GiBUU for higher rapidities in contrast to UrQMD. In comparison to tungsten, where these larger deviations started at $0.75 < y < 0.90$, in carbon they are already observed at lower rapidities $0.60 < y < 0.75$.

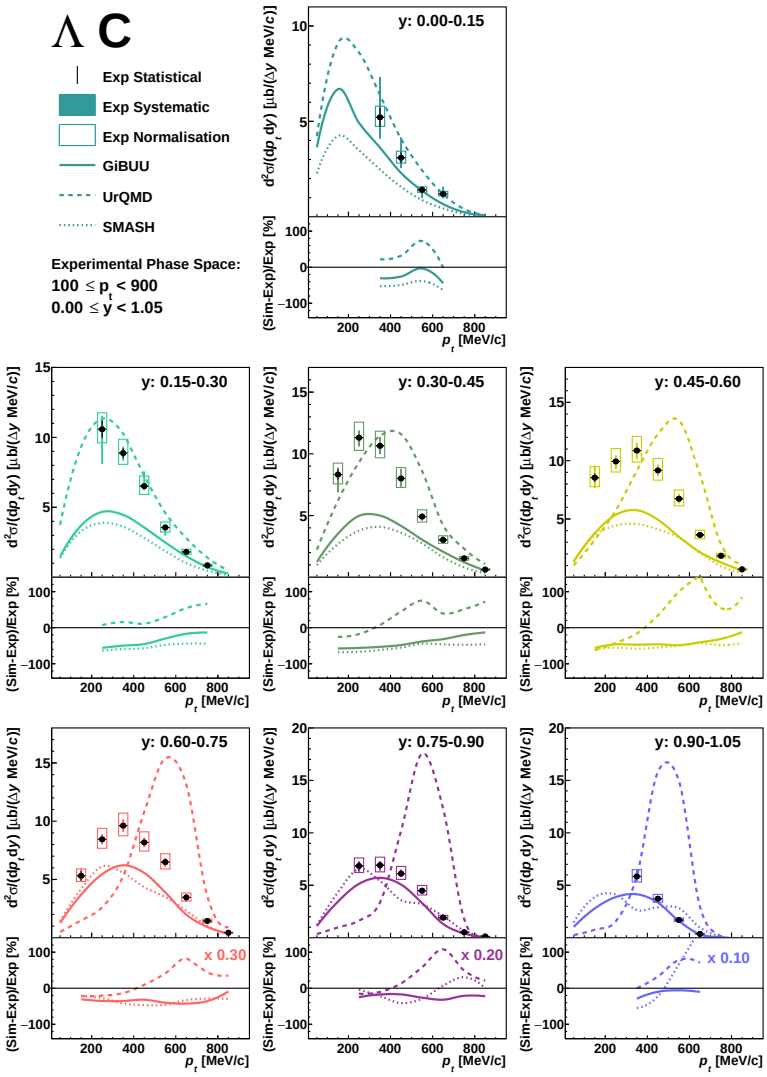

Figure 5.16: Comparison of absolute normalised transport codes GiBUU (solid curve), UrQMD (dashed curve) and SMASH (dotted curve) to the experimental Λ cross-section in carbon. The error representation is analogous to Fig. 5.15. See text for details.

In the same way we can compare the predictions for the K^0_S in the heavy system, depicted in Fig. 5.17.
If we first consider the UrQMD transport code a clear trend for the maximum to higher p_t is visible, similar to the Λ. The peak position is shifted to higher transverse momenta up to $0.8 < y < 1$ while the trend continues to the opposite direction for rapidities up to $y = 1.6$. The overestimation of the cross-section is more stringent for increasing rapidity.

SMASH in contrast predicts the correct shape of the experimental distributions up to $0.6 < y < 0.8$. Like in the Λ case, also here an evolving double peak structure towards higher rapidities is visible. The cross-section description is well in agreement for $0 < y < 0.4$, overpredicted in the mid-rapidity of $0.4 < y < 1.2$ and trends to underprediction up to the highest measured rapidities.
GiBUU is in very good agreement with the experimental data in term of the predicted shape and cross-section over the entire phase-space up to $1.2 < y < 1.4$, with smaller underprediction in the highest rapidity region. In the mid-rapidity of $0.6 < y < 1.2$ a shallow double-peak structure is visible, not seen in the experiment.

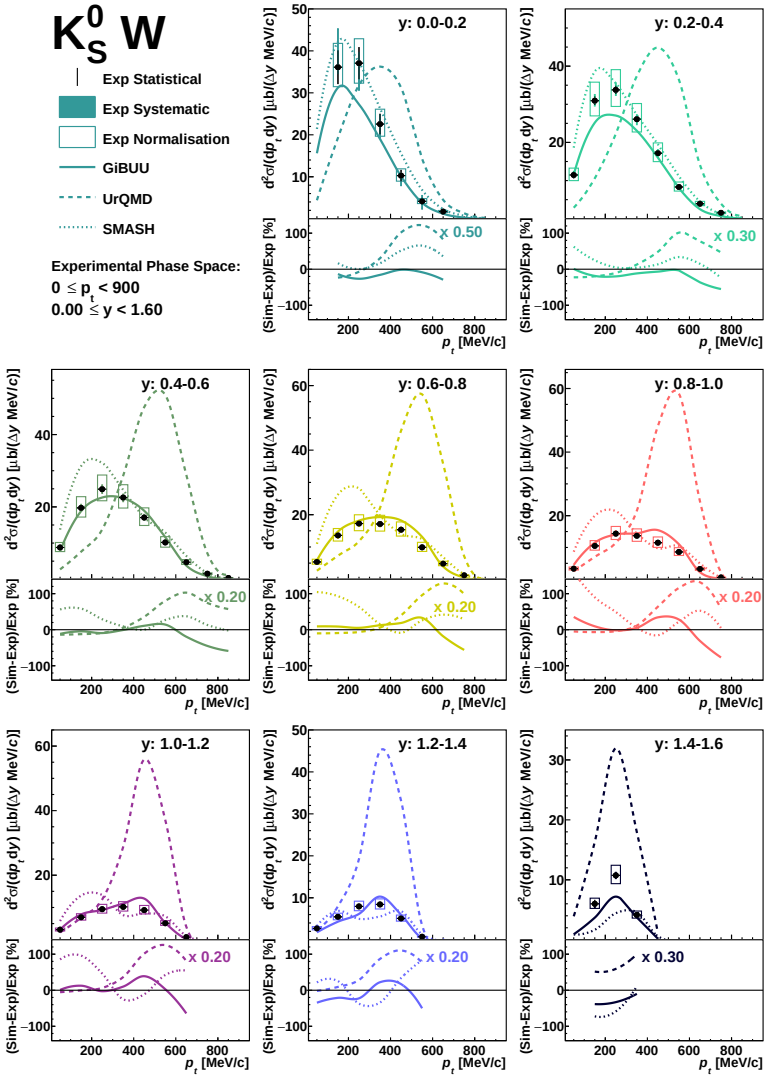

Figure 5.17: Comparison of absolute normalised transport codes GiBUU (solid curve), UrQMD (dashed curve) and SMASH (dotted curve) to the experimental K^0_S cross-section in tungsten. Experimental errors are indicated in black for the statistical, filled boxes for the systematic and open boxes for the normalisation error. In the upper panels the comparison of the transport models to the experimental data is shown, while the lower panel indicates the difference in percents. See text for details.

The trend of the shifted peak to higher transverse momentum in GiBUU and SMASH up to mid-rapidity and to lower transverse momenta for higher rapidities can also be seen for carbon depicted in Fig. 5.18. In addition the growing overprediction towards higher rapidities is also observed while for $1.4 < y < 1.6$ the difference seems

to reduce.

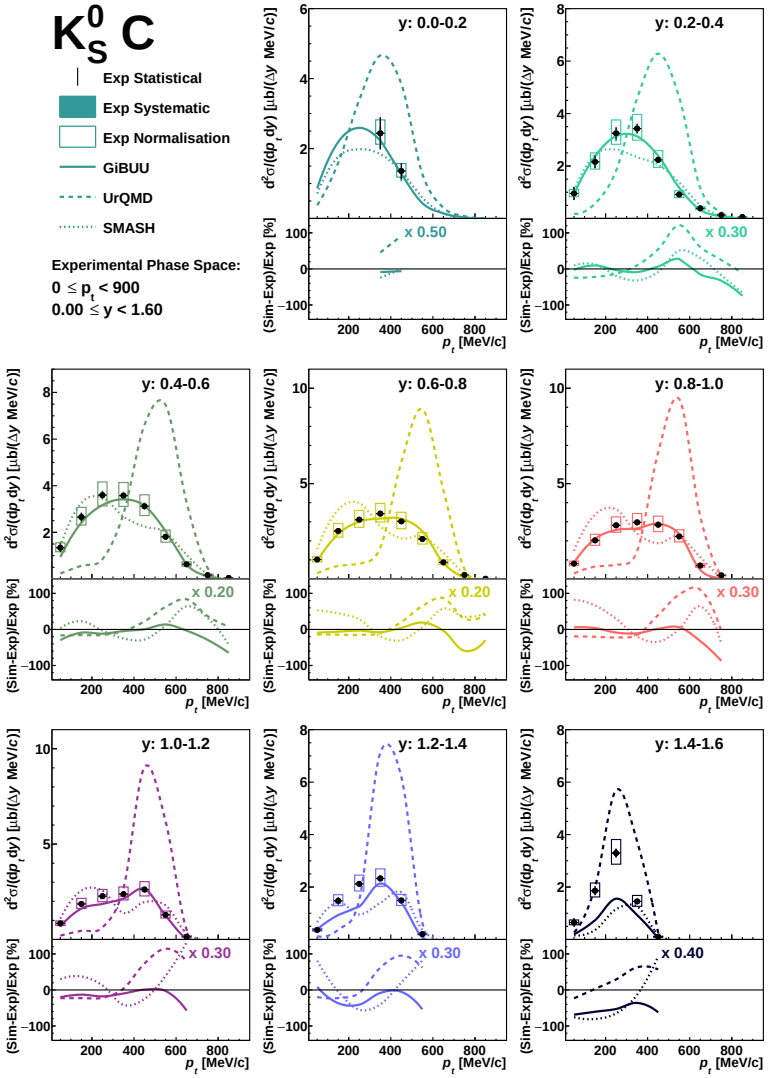

Figure 5.18: Comparison of absolute normalised transport codes GiBUU (solid line), UrQMD (large boxes) and SMASH (small boxes) to the experimental K^0_S cross-section in carbon. The error representation is analogous to Fig. 5.17. See text for details.

Also here GiBUU and SMASH show equity by the predicted shape and cross-section. While SMASH begins to show a growing double peak structure for rapidities $0.4 < y < 1.4$, the earlier dominant peak at lower rapidities vanishes in the region $1.4 < y < 1.6$.
In summary GiBUU shows a remarkable precise prediction for K^0_S in carbon and tungsten. For Λ a general underestimation of the yield at lower rapidities can be

observed ($0 < y < 0.75$) in both systems which decreases up to the measured rapidity of y = 1.05.
SMASH shows a similar behaviour as GiBUU with an additional double-peak structure at mid-rapidity, more pronounced for K^0_S. This is most likely due to the decay of heavy resonances. This effect is even more pronounced for the UrQMD model.
Here a general hardening of the p_t spectra can be observed up to $y \approx 0.7-0.9$ for both particles in both system. For higher rapidities a slight softened spectra is seen. In terms of the predicted cross-section UrQMD show increasing deviations for more forward rapidities.
These effects which are present for the UrQMD model in the present version 3.4 are known and a improved version coping with the hardening of the p_t spectra is already under development.

5.2.2.2 Rapidity

By the integration of the presented transverse momentum spectra in Section 5.2.2 absolute normalised rapidity spectra were extracted, which are presented in this section. All figures share the same convention of statistical errors indicated in black, systematic uncertainties shaded in green and normalisation errors in shaded red. The transport code GiBUU is represented by the solid red line, UrQMD by the dashed blue line and SMASH by the dotted green line. Again the upper panel shows the comparison of the transport model with the experimental data, while the lower plot presents the difference in percent.
The absolute normalised rapidity distribution of Λ in tungsten is illustrated in Fig. 5.19. As in the section before, SMASH and GiBUU show very similar results. They predict a rather flat distribution in the range of $0.4 < y < 1.05$ with a slight inclination to higher values for higher rapidities. In the backward rapidity of $0 < y < 0.4$ a steep rise of the cross-section can be seen. Here UrQMD predicts a similar shape like SMASH and GiBUU with a larger offset to higher cross-section for lower rapidities and a steeper angle in the range of $0.4 < y < 1.05$.
In contrast to the prediction of the simulation, the experimental deduced show a constant rise of the cross section for forward to backward rapidity with a maximum at $0.15 < y < 0.3$ and a drop to backward rapidity. This shift to backward rapidities can be attributed to scattering of the Λ inside the tungsten nucleus. As similar shapes were predicted by the transport models, also in the simulation these scattering effects are considered.

For the lighter target (C) UrQMD can predict the rapidity distribution in the range of $0.3 < y < 0.9$ very well with an overestimation towards edges, as depicted in Fig. 5.20. Both, GiBUU and SMASH, predict a rather flat distribution and therefore underestimate the cross-section. Moreover both fail to reproduce the experimental shape.

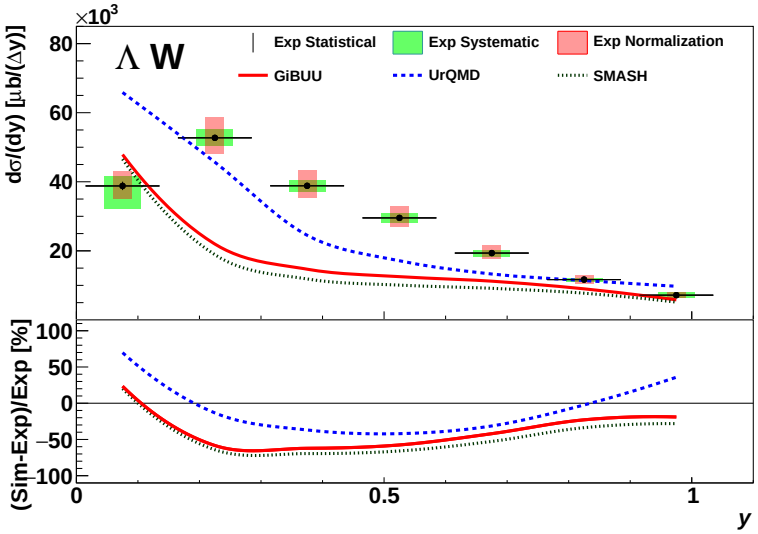

Figure 5.19: Absolute normalised rapidity spectra for GiBUU (solid red), UrQMD (dashed blue), SMASH (dotted green) and experiment in black for Λ in tungsten. Statistical errors are indicated in black, systematic errors by the green shaded boxed and normalisation errors by the orange shaded boxes. For details see text.

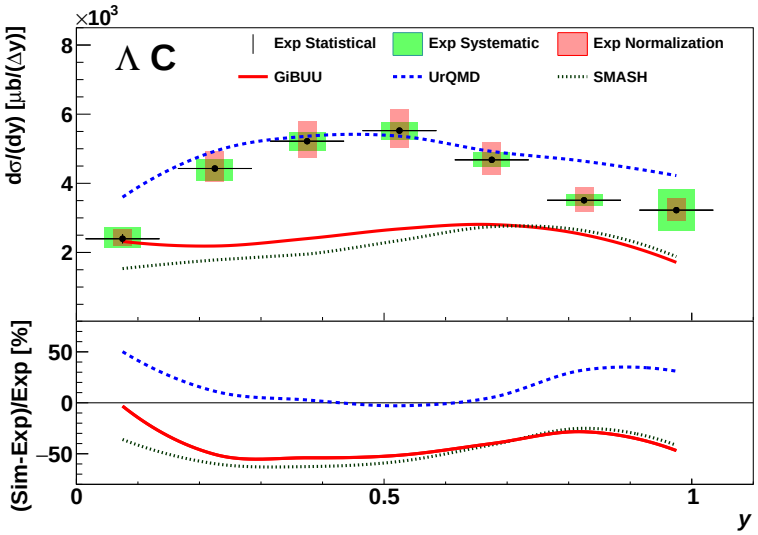

Figure 5.20: Absolute normalised rapidity spectra for GiBUU (solid red), UrQMD (dashed blue), SMASH (dotted green) and experiment in black for Λ in carbon. Statistical errors are indicated in black, systematic errors by the green shaded boxed and normalisation errors by the orange shaded boxes. For details see text.

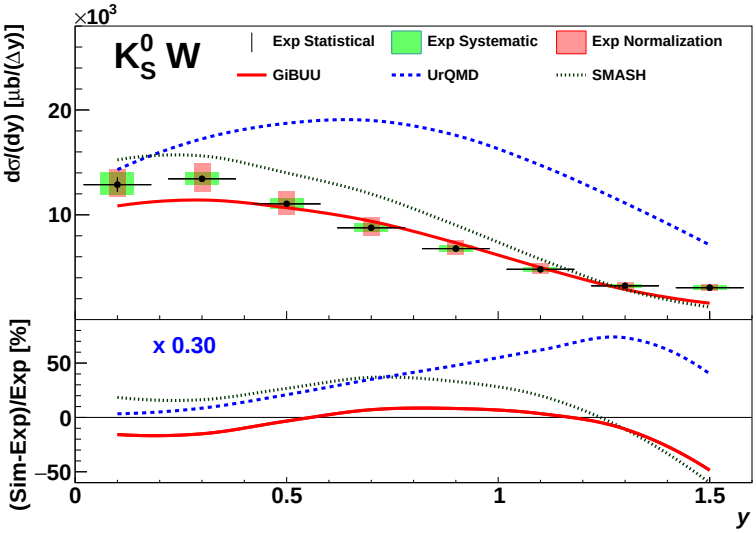

Figure 5.21: Absolute normalised rapidity spectra for GiBUU (solid red), UrQMD (dashed blue), SMASH (dotted green) and experiment in black for K^0_S in tungsten. Statistical errors are indicated in black, systematic errors by the green shaded boxed and normalisation errors by the orange shaded boxes. For details see text.

If we also consider the K^0_S in the heavy system the experimental distribution shows clear backward scattering as already discussed in Section 5.2.1.2, which is reproduced by SMASH and GiBUU. However GiBUU underestimates the cross-section at backward rapidity in contrast to SMASH, which overestimates it. The agreement between GiBUU is very well between $0.4 < y < 1.4$, while SMASH shows a slight offset.
UrQMD predicts are rather symmetric distribution for the K^0_S and overestimates the cross-section nearly over the entire range.

For the lighter target carbon all three transport model predict a symmetric shape, also seen in the experimental data. Again UrQMD overestimates the yield with growing difference to forward rapidity.
SMASH and GiBUU predict nearly the same cross-section as a function of the rapidity with a well agreement between $0.2 < y < 1.2$ and a slight underestimation in the lower and higher rapidity.

In summary, no transport model is able to reproduce the shape of Λ in tungsten, while UrQMD showed a better agreement. For carbon only UrQMD could correctly predict the shape at mid-rapidity with an overestimation at the lower and higher rapidity. SMASH and GiBUU predict a rather flat distribution with an underestimated cross-section.
For the K^0_S both SMASH and GiBUU show a good agreement for both targets with

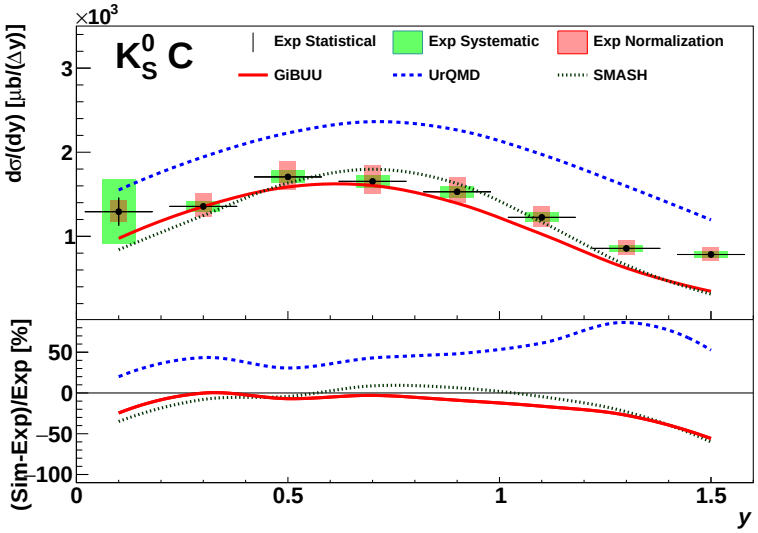

Figure 5.22: Absolute normalised rapidity spectra for GiBUU (solid red), UrQMD (dashed blue), SMASH (dotted green) and experiment in black for K^0_S in carbon. Statistical errors are indicated in black, systematic errors by the green shaded boxed and normalisation errors by the orange shaded boxes. For details see text.

deviations at lower and upper rapidities.
UrQMD overestimates the K^0_S cross-section for both systems and predicts for carbon and tungsten a symmetric rapidity distribution. But as already mentioned before, the model is under development to cope with these effects.

5.3 $P - \Theta$

The corrected yield distributions for Λ is illustrated in Fig. 5.23 for tungsten panel (a) and carbon panel (b).
For the heavy target most of the yield was measured at the lower edged of the accessible momenta range and the upper edged of the angle Θ. If we compare this to (b), where the $\pi^- C$ reactions are illustrated, the yield is shifted to lower angles and higher momenta. Due to the lower angle and higher momenta in the lighter target, scattering inside the nucleus is dominant.

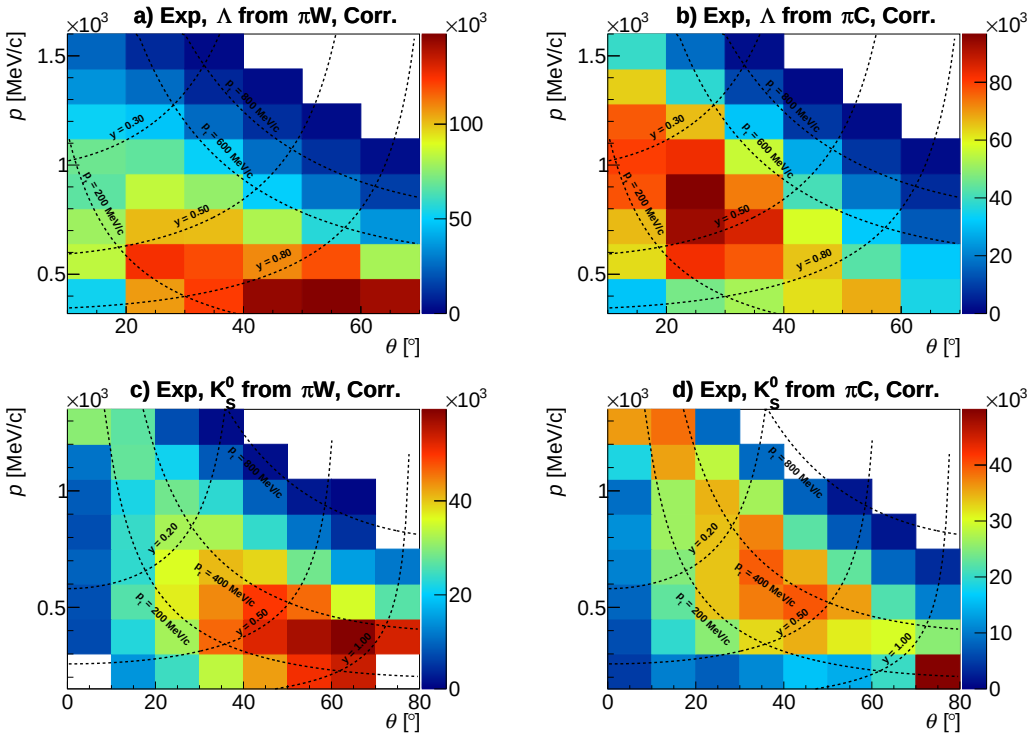

Figure 5.23: Corrected experimental $p-\Theta$ yield for Λ and K^0_S in tungsten (a,c) and carbon (b,d), respectively. The dashed lines represent constant values for $y = 0.3, 0.5, 0.8$ (Λ) $y = 0.2, 0.5, 1.0$ (K^0_S) and $p_t = 200, 600, 800$ MeV/c. Most of the yield is at low p_t and backward rapidity.

The $p-\Theta$ of the K^0_S distribution are illustrated for C and W in Fig. 5.23 panel (c) and Fig. 5.23 panel (d), respectively. Also here a similar behaviour can be observed. In case of tungsten the yield is shifted towards smaller angles and smaller momenta compared to carbon. Thus also here, scattering is dominant.

5.3.1 Kaon Nuclear Modification Factor

In order to gain an insight into the KN interaction, the phase space distribution can be compared from the heavy to the lighter target. In general, the ratio $R(\sigma^K_A/\sigma^K_C)$ is derived as a function of the momentum, in which A is the mass number of the heavy nucleus. Since the average nucleon density also increases with increasing nucleus size, the modifications within nuclear matter should be more pronounced in the heavy [35]. The nucleus in-medium KN interaction is predicted to be repulsive, leading to an acceleration of the kaons as they traverse the nucleus, and hence

leading to suppression in the low momentum region in respect to lighter nucleus (C). However, the strength of the potential is expected to increase with increasing momentum of the kaon. This is confirmed by a detailed study of K^0 production in p+Nb reactions measured with HADES [37].
The ratio of the production cross-section R(σ^K_A/σ^K_C) for K^+ and K^0 as a function of the momentum is shown in Fig. 5.24. The left panel compares the ratio of this work (black circles) to the one of FOPI (blue triangles) [34]. For the HADES data the systematic uncertainties are indicated by the green shaded area, the normalisation errors in red and the statistical errors by the black bars. The presented normalisation uncertainty is a conservative estimate as most contributions to the error are expected to cancel [59]. The ratio was extracted in the overlap area of the $p-\Theta$ spectra for both collision systems.
A depletion of the ratio can be observed for kaons with momenta $p_{K^0} < 0.2$ GeV/c, which is not covered by the presented ratio whereas the high momentum range is covered in contrast to FOPI. In the overlap area, both experiments are well in agreement and follow the same trend.

The extracted ratio is also compared to the K^+ results in proton-induced reaction from ANKE at 1.5 GeV (open triangles) and 2.3 GeV (full triangles) [80] in the right panel of Fig. 5.24. A similar trend of a depletion at low momenta as well as a suppression at high momenta is seen by ANKE. However, the ratio by ANKE is slightly lower. But, a one-to-one comparison is not possible, since K^+ also are affected by Coulomb interaction.
Nevertheless, the deduced ratio can be compared to the GiBUU transport model, with and without the repulsive KN interaction. The ratio in comparison to GiBUU calculations is depicted in Fig. 5.25, in which the blue dotted curve depicts the ratio without the KN potential and green dashed with the potential. The upper panel shows the comparison, while the lower plot illustrated the difference (Sim-Exp)/(Exp) in percent.
For the simulation, the ratio was extracted in the overlap region of the experimental $p-\Theta$ region in the momentum range of $225 < p_{K^0_S} < 1275$ MeV/c, whereas for lower momenta the full phase space was considered. It can be seen that for the GiBUU predictions including the repulsive χ-EFT potential, the depletion for low momenta is reproduced.

The experimental ratio shows a better agreement with the prediction including a repulsive KN potential. However both predictions are very similar for in the momentum region of $375 < p_{K^0_S} < 825$, deviations are observed for higher momenta. This effect can be attributed to the fact that the strength of the repulsive χ-EFT KN potential is increasing with increasing kaon momenta. Hence, a similar observation to the results presented in [37] is made. Even though within errors no conclusive statement can be drawn, the experimental data seem to favour a repulsive KN interaction.

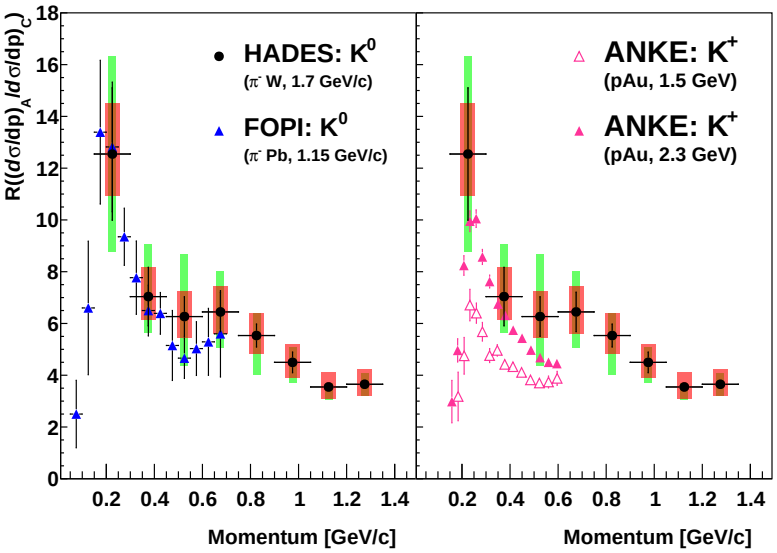

Figure 5.24: Ratio of the inclusive cross-section of K^0 (K^+) produced in π/proton reactions off heavy nuclei normalised to carbon. The black full circles represent the ratio of this work, with statistical error bars in black, systematic uncertainties in green, and normalisation errors in red. The filled blue triangle present the K^0_S ratio πPb/C measured by FOPI at an incident momentum of 1.15 GeV/c [34]. The open triangles (1.5 GeV) and filled triangles (2.3 GeV) represent the ratio of K^+ measured by ANKE of protons impinging on Au/C [80].

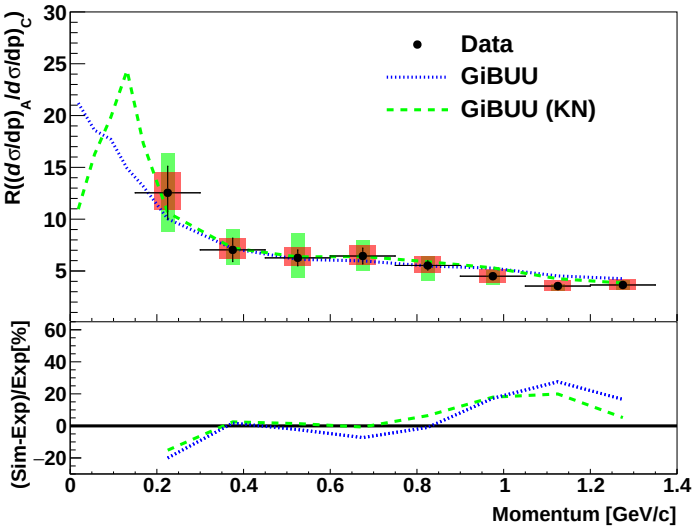

Figure 5.25: Ratio of the inclusive K^0_S ratio produce by pions impinging on tungsten and carbon. The black circles depict the experimental data, where the black full circles represent the ratio of this experiment, with statistical error bars in black, systematic uncertainties in green and normalisation error in red. The solid lines depict the predictions of GiBUU without (blue dotted) and with (green dashed) a KN potential. The lower panel illustrated the difference between experiment and simulation in percent.

5.4 Summary of the Inclusive Analysis

In this section the inclusive analysis of Λ and K_S^0 for a $\pi^- + C$ and $\pi^- + W$ was presented.
In the beginning, the reconstruction procedure was outlined and the acceptance and efficiency correction were explained including also the self-consistency check. To estimate the uncertainties introduced by the different analysis steps, the systematic error estimation was outlined, where the topological cuts have been identified as the main source of the error.
The corrected and absolute normalised experimental p_t distributions have been extrapolated to the full phase-space by applying a Boltzmann fit.
These spectra then could be compared to three state-of-the-art transport models: GiBUU, UrQMD and SMASH. Here very distinct behaviour depending in the particle and nuclear environment could be deduced in p_t and rapidity.
For the kaon modification inside nuclear matter a trend towards a KN-potential was observed.
Thus the results obtained in the inclusive analysis can be used to improve the particle yields and moreover the kinematics which reflect the underlying physics.

6

Exclusive Λ and K_S^0 production in $\pi^- + A$ @ 1.7 GeV/c

The sub-threshold production of K_S^0 mesons and Λ hyperons in AuAu collision, at $\sqrt{s} = 2.4$ GeV has been measured by the HADES collaboration [81]. Of great interest is the study of the in-medium modification of K_S^0 and Λ, which are expected to be significant in heavy ion collisions (HIC) where baryonic densities ρ_B exceed the normal nuclear density. Therefore a detailed investigation of the $\langle A_{part} \rangle$ dependence and the shapes of the transverse momentum as well as rapidity distribution of Λ and K_S^0 were investigated separately. In this context state-of-the-art hadronic transport models were used for comparison, employing the Isospin Quantum Molecular Dynamics model (IQMDv.c8 [82]), the Hadron String Dynamics(HSDv.711n [36]) model and the Ultrarelativistic Quantum Molecular Dynamics model (UrQMDv3.4 [2, 3]). The latter UrQMD model was also compared to the inclusive spectra of Λ and K_S^0 presented in Section 5.2.2. Concerning the sub-threshold production as well as the in-medium modification no consistent picture could be extracted, as none of the models was able to reproduce all kinematic variables of Λ and K_S^0 at the same time.
Contrary, to the widely-used individual investigation of the hadron properties, a simultaneous study of the in-medium effects was carried out in this work, due to the associated production of the Λ (Σ^0) and K_S^0. In the following the (semi-)exclusive channel of $\pi^- + A \rightarrow \Lambda + K_S^0 + X$ was selected in order to test the in-medium modification of both particles simultaneously. For this purpose the GiBUU transport model was employed.

Due to the dominant decay channel of Σ^0 ($\Sigma^0 \rightarrow \Lambda + \gamma$, BR $\approx 100\%$ [1]) into Λ, both hyperons can not be distinguished in the final state. Hence, the Λ properties can not be studied without assumptions on the Σ^0 properties.

The first part gives an overview of the predictions from χ-EFT and the implementation of these potentials in the GiBUU code.
This is followed by a systematic study on the involved production processes predicted by GiBUU. The last part will present and discuss the comparison of the different in-medium scenarios to the experimental data based on various kinematic observables.

6.1 GiBUU In-Medium Modification

Hyperons and kaons are modified within nuclear matter already at normal nuclear saturation density. Depending on the type of particle and the strength of the coupling these are known to some extend as discussed in (Section 1.4.1, Section 1.4.2). For the KN interaction a repulsive behaviour has already been conformed by various experiments [80, 34, 83], while the absolute strength differs between $U^{KN} = 20 - 40$ MeV. The in-medium χ-EFT KN potential implemented in GiBUU features in contrast to other transport models not only a density dependence but also a explicit momentum dependence [37]. For the hyperons, in particular Λ and Σ^0, no explicit YN potential is implemented in GiBUU. Here the simulation of the YN potential is modelled by the nucleon-nucleon relativistic mean-field potential, multiplied by a factor of 2/3 [71] (positive implies attractive). Hence Λ and Σ are treated in the same way. However by employing next-to-leading-order (NLO) χ-EFT, prediction for the in-medium modification for different densities as a function of the momentum for the Λ and Σ^0 were deduced [54]. Within χ-EFT the Λ single particle potential is predicted to be predominantly attractive with a repulsive core at higher momenta, as introduced in Section 1.4.2. The difference in density leads to a change of the absolute depth of the potential and the momentum where the interaction changes from attractive to repulsive.
In contrast, the Σ^0 is predicted to be predominantly repulsive. Only for the lowest considered densities and momenta a shallow attractive interaction is predicted.

These calculations were compared to the implemented potentials of the GiBUU model. As pion-nucleus reactions probe the interaction up to nuclear saturation densities, the comparison was done for the prediction of $k_F = 1.35$ fm. The real part of the already discussed Λ single particle potential is illustrated in panel (a) in Fig. 6.1 as a function of the momentum, indicated by the dotted red line. The shaded area corresponds to the uncertainties of the theoretical calculation. Indicated in black is the modified NN potential implemented in GiBUU, which is used to model the Λ

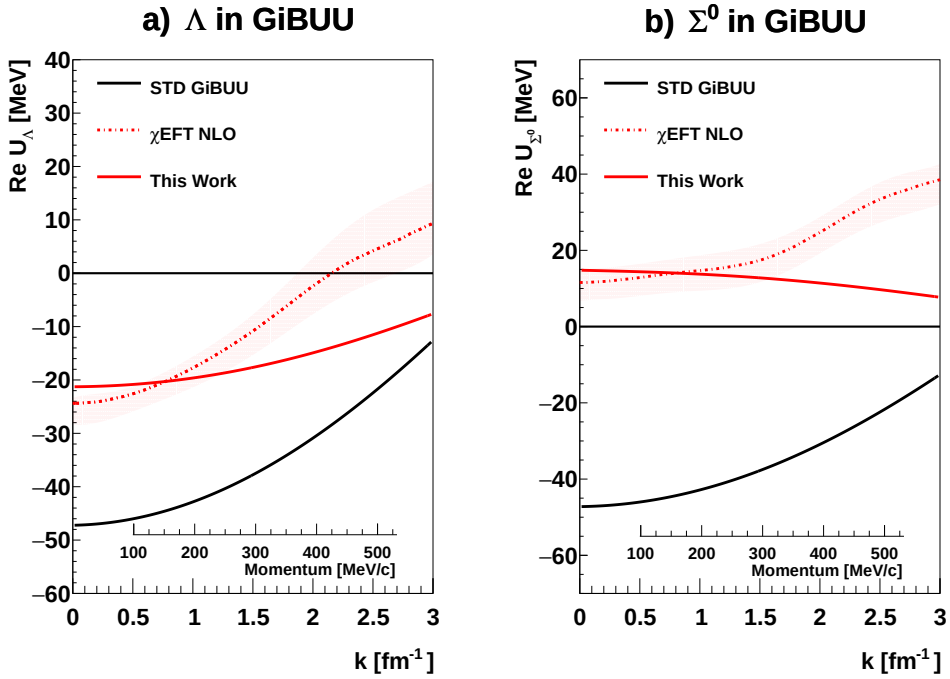

Figure 6.1: Real part of the χ-EFT single particle potential taken from [54] for Λ in panel (a) and Σ^0 in panel (b) indicated by the red dotted curves. The red shaded area corresponds to the systematic uncertainty of the calculations. The black solid line resembles the standard potential implemented in GiBUU. The red solid line indicates the implemented potential of this thesis, which is more in agreement with the χ-EFT single particle potential. See text for details.

in-medium behaviour. The trend of the χ-EFT prediction and the GiBUU potential are very similar, but the absolute scale deviates by $\Delta U^{YN} \approx 25$ MeV. Indeed GiBUU favours a stronger attractive interaction and besides that, χ-EFT predicts an earlier onset of the repulsive part.
Similar to the Λ, also the Σ^0 is presented in panel (b) of Fig. 6.1 with the same colouring scheme. Here the differences are tremendous. The χ-EFT approach predicts and overall repulsive interaction, while the implementation of GiBUU assumes a highly attractive interaction.

In order to mimic the predictions of the χ-EFT single particle potentials, a separate treatment of Σ^0 and Λ was implemented into the GiBUU code, which is still based on the modified nucleon-nucleon relativistic mean-field potential.
In this approach, for the first time, it is possible to assign separately the scaling parameters to the NN potential for Λ and Σ^0. The red dotted line in panel (a) of Fig. 6.1 depicts the modified NN potential for the Λ with a scaling factor of $NN_\Lambda = 0.3$

Scenario	K^0 ES	K^0 Pot.	Λ ES	Λ Pot.	Σ^0 ES	Σ^0 Pot.
Elastic Scattering (ES(Y,K))	✓	✗	✓	✗	✓	✗
ES Hyperons (ES(Y))	✓	χ-EFT	✓	✗	✓	✗
GiBUU Standard (STD)	✓	χ-EFT	✓	2/3	✓	2/3
Repulsive Σ^0 (RS)	✓	χ-EFT	✓	0.3	✓	-0.2

Table 6.1: Overview of the different simulated scenarios.

and in panel (b) same figure for the Σ^0 with a modification factor of $NN_{\Sigma^0} = -0.2$. In both cases, especially for the Σ^0, the difference between the χ-EFT prediction and the GiBUU implementation is reduced. As [54] points out, the charged Σ^+ and Σ^- have similar potentials inside symmetric nuclear matter as the Σ^0. Only smaller deviations are expected of the order 0.5-1 MeV, due to the mass difference of the Σs. Therefore also the Σ^+ and Σ^- are treated with the modification factor of $NN_{\Sigma} = -0.2$. Therefore, according to theoretical predictions, a more realistic treatment of the hyperon inside a dense medium could be implemented in the GiBUU transport code. To compare this model and test the sensitivity to different in-medium interaction, different scenarios were simulated and compared to experimental kinematic distribution. As no efficiency correction can be applied, as this would cause a model dependence, the GiBUU output is folded with the acceptance and efficiency of the HADES detector and therefore a one to one comparison to experimental data can be performed. The first scenario (ES(Y,K)) is a simplified approach, in which only elastic scattering for the K^0, Λ and Σ^0 is considered . For the second scenario (ES(Y)) the χ-EFT treatment of the KN interaction is accounted for, while for the hyperons still only elastic scattering is considered. In the third one (STD), the GiBUU standard implementation of the Λ and Σ^0 is employed. There both hyperons are treated in the same way with an attractive potential correspond to $NN_{\Sigma^0} = NN_{\Lambda} = 2/3$. The last scenario (RS) features the new approach of the implementation of the approximated χ-EFT predictions, with an attractive ΛN together with a repulsive Σ^0N interaction. All scenarios are summarised in Table 6.1.

6.2 GiBUU Event Evolution

To get an insight in the involved reaction dynamics from the first collisions to the final state, transport codes are commonly employed. Here, every single step is known and can be studied. The following subsection deals with the analysis procedure to obtain these reaction dynamics predicted by the GiBUU model.
For this purpose snapshots are produced at every given time-step, where the position and momentum of each particle is stored. With this, the evolution of a single particle

or the whole nucleus, predicted by GiBUU, can be accessed.
Therefore, the contributions of the exclusive channel $\pi^- + A \rightarrow \Lambda(\Sigma^0) + K_S^0 + X$ can be analysed, meaning that the role of secondary hyperon production or their creation position can be investigated in detail. The entire procedure is only shown for carbon, while all presented distributions for tungsten can be found in Appendix D.1.

6.2.1 Nucleus Radius

To extract all necessary information, the first step is to define the origin of a cartesian coordinate system in every time step. For this purpose the assumption was made, that all protons and neutrons are constituents of the nucleus and the origin $\vec{O}$ is defined as the geometrical centre. From now on every distance was calculated with respect to this origin $\vec{O}$, indicated by the blue point in the centre of Fig. 6.2, illustrating the procedure.
To estimate the size of the nucleus, the radius is calculated as an average over all nucleons as well as all three dimensions with:

$$R = \frac{1}{6} \sum_{i=x,y,z} |Max(r_i)| + |Min(r_i)| \tag{6.1}$$

where

R: radius of nucleus
$Max(r_i)$: largest positive distance to origin
$Min(r_i)$: largest negative distance to origin

The maximal and minimal distance in space are indicated in Fig. 6.2.
As all protons and neutrons are considered for the determination of the radius, this procedure is only valid in an early stage of the reaction, before the pion interacted with the nucleus. During the time evolution the nucleons diffuse as they get transported outwards by inelastic or elastic reactions which indeed leads to an artificially increase of the nucleus radius.

The reconstructed nucleus radius for carbon and tungsten is depicted in Fig. 6.3 . The graphs are scaled according to their maximum.

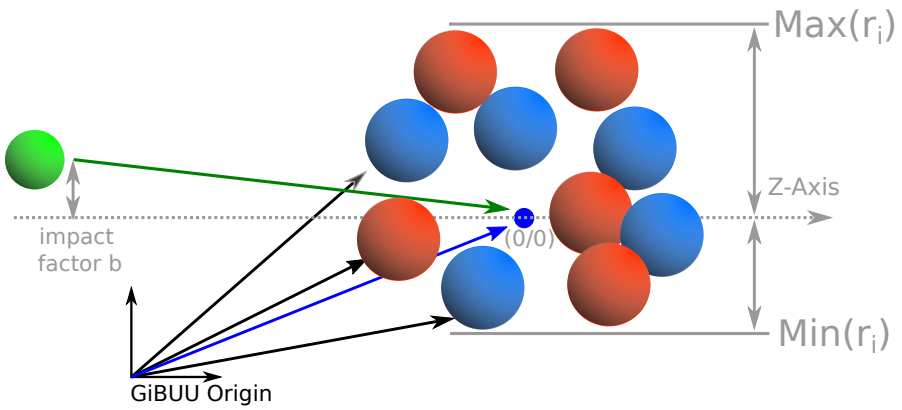

Figure 6.2: Illustration of the GiBUU event topology. The calculated origin is depicted in blue, with the nucleus constituents drawn in light blue and red circles. The green circle represents the incident pion. See text for details.

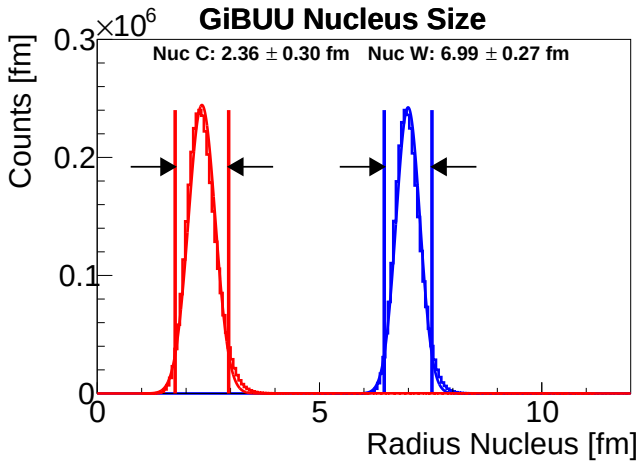

Figure 6.3: Nuclear radius for carbon and tungsten extracted from GiBUU.

Both distributions are fitted with a Gaussian to extract the radius of the nucleus given by the the mean μ and the width defined within 2σ. On the left of Fig. 6.3 the distribution of the carbon radius is depicted with an radius of $R_C = 2.36 \pm 0.30$ fm. For tungsten a radius of $R_W = 6.99 \pm 0.27$ fm was extracted, shown on the right, same figure. As the initial distribution of the nucleons inside the GiBUU code taking into account the Fermi-motion, the radius for carbon and tungsten is not a simple delta function.
These numbers can be compared to the well known equation of $R = r_0 (A)^{1/3}$ taken from [84], with a radius of $r_0 = 1.2$ fm, which gives the approximate radius of a nucleus on the basis of the mass number A. Here we find for carbon $R_C = 2.18$ fm and for

tungsten $R_W = 6.82$ fm . Both values are very close to the one extracted from GiBUU, confirming the method for the extraction of the nucleus radius.
In simulation, the assumption that the pion interacts close to the upstream surface of the nucleus can be tested.
The interaction point of the incident pion with the carbon nucleus as a function of the impact parameter b vs. the z-coordinate calculated relative to the origin $\vec{O}$, is illustrated in Fig. 6.4 To guide the eye, the thick black line represent the mean value of the nucleus radius while the two thinner lines show the extracted width of 2σ.
It is perfectly evident from this figure that due to their large inelastic cross-section the negative pions have a very short mean free path and therefore interact very close to the upstream surface.

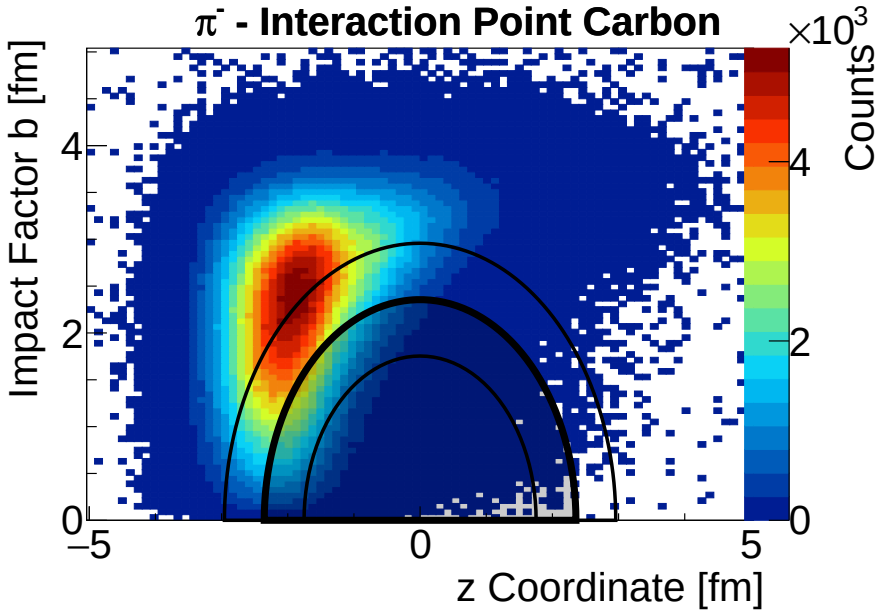

Figure 6.4: Interaction point of the negative pions with the carbon nucleus. The thick line represents the mean value of the carbon nucleus radius, while the thinner lines show the width of 2σ. The assumption of the interaction close to the upstream surface is evident in GiBUU.

6.2.2 Contributing Channels

To determine the contributing production channels as well as the complete history of each selected particle in the (semi-)exclusive analysis, a dedicated reconstruction procedure was developed. This procedure is outline in the following and was applied

to GiBUU simulation in the standard configuration (STD, see Table 6.1).

The snapshot output of GiBUU provides the position, momentum and PID of each particle at every given time step. All information are stored in a so called particle vector.
Changes were only stored if the type or amount of a particle species changes in this particle vector between subsequent steps. Therefore, elastic scattering events like $\pi^- + p \rightarrow \pi^- + p$ were not considered in the presented procedure, as neither the number of particles nor their species changes. In Fig. 6.5 the extraction procedure for an example of a secondary production with a final state of ΛK_S^0 is illustrated. Step I represent the initial state of the simulation, in which so far no interaction took place as the simulation is in an early stage. The first important information can be extracted at step II. This is the last point in time before the π^- reacted inelastically. Therefore, the reaction point of the π^- as well as the radius of the nucleus can be extracted at this time stage as depicted in Fig. 6.4. In this example the reaction $\pi^- + n \rightarrow \Sigma^- + K_S^0$ took place at step III. To extract every single channel a so called reaction vector (RV) was constructed. If particles in the particle vector occurred or disappeared, they were tracked within the RV. As GiBUU only provides the snapshots and not the exact binary collision information, the exact nucleon which was part of the interaction is unknown as all nucleons are indistinguishable, like illustrated in Fig. 6.5. This means also that all produced protons/neutrons cannot be distinguished from the nucleus constituents.
Hence, charge conservation reveals that the missing nucleon was a neutron going from step II to step III for the RV of $\pi^- \rightarrow \Sigma^- + K_S^0$.

At step IV a secondary reaction $\Sigma^- + p \rightarrow \Lambda + n$ takes place . Since the nucleons are not traced, the full RV looks like $\pi^- + n \rightarrow \Sigma^- + K_S^0 \rightarrow \Lambda + K_S^0$.

For every single reaction this vector can be compared to the set of already existing ones. If the RV is already known, the corresponding channel is incremented by one. Otherwise it is added to the pool. Therefore, the final state of $\Lambda + K_S^0$ can be categorised into primary reactions (e.g. RV: $\pi^- + p \rightarrow \Lambda + K_S^0$) and secondary contributions (e.g. RV: $\pi^- + n \rightarrow \Sigma^- + K_S^0 \rightarrow \Lambda + K_S^0$). In this way the procedure takes into account an arbitrary number of production channels as well as multi-step production and allow not only to trace particles but also to extract their abundance. To validate the procedure, the most abundant primary reaction channels, equivalent to the fist $\pi^- + A$ reaction, were investigated. Only channels with a hyperon together with a kaon in the final state were considered. By comparing the extracted abundance to the implemented elementary reaction cross-section listed in Table 5.7, similar ratios should be extracted. Therefore, relevant reactions are compared to the most abundant $\Sigma^- K^0$ channel and listed in Table 6.2.

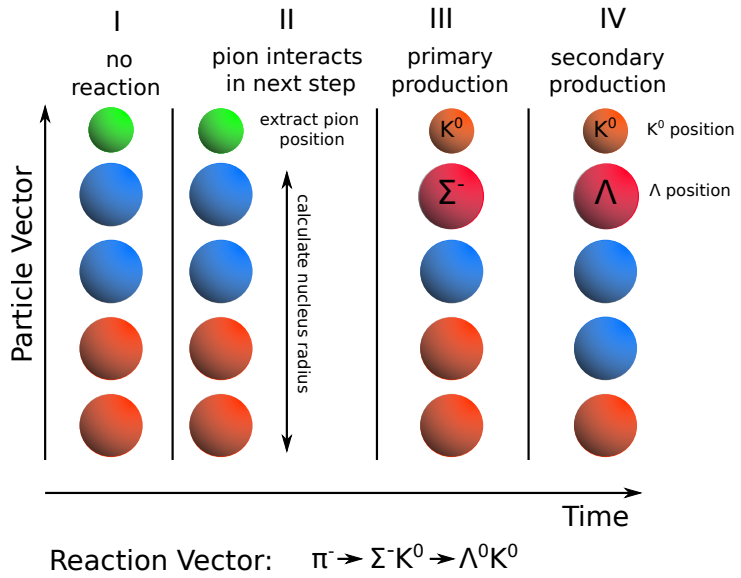

Figure 6.5: Illustration of the GiBUU production history extraction. Blue and orange circles represent nucleons, green circles pions, red circles hyperons and the small orange circle kaons. The reaction vector summarises the transition from the initial to the final state. See text for details.

By comparing the relative abundance extracted with the present procedure, listed in the third column of Table 6.2, to the one calculated on the basis of the elementary cross-section, listed in the fifth column, one finds a good agreement. The difference between the cross-section calculated ratio and the one based on the present procedure is listed in the last column. As expected deviations are observed, as pion nucleus reaction ($\pi^- + C$) were compared to the implemented cross-section parametrisation of elementary reactions. Since the first case also includes Fermi-motion, which can slightly change the relative abundance of channels, as a change of the available energy can result in a change of the cross-section. In addition, in-medium potential are included in the $\pi^- + C$ simulations . All in all the procedure show promising results and gives the possibility to provide access to the creation mechanism implemented in GiBUU.
The procedure was applied to the (semi-)exclusive channel $\pi^- + C \rightarrow \Lambda + K^0_S + X$. In the following only contributions were further considered with a relative fraction larger then 1%. Therefore $\pi^- + C$ and $\pi^- + W$ reactions were simulated and their corresponding creation history was recorded were in the final state a pair of Λ (Σ^0) and K^0_S was found. In Table 6.3 the creation history is summarised for the lighter target nucleus (C).

Quite remarkably, the dominant contribution originates from secondary produc-

Channel	Abs.	Relative	σ_{GiBUU} [mb]	Ratio	Δ
$\rightarrow \pi^- + n \rightarrow \Sigma^- K^0$	266243	100.0	0.458	100.0	0
$\rightarrow \pi^- + p \rightarrow \Sigma^- K^+$	92269	34.3	0.156	34.0	0.3
$\rightarrow \pi^- + p \rightarrow \Sigma^0 K^0$	80325	30.0	0.132	28.8	1.2
$\rightarrow \pi^- + n \rightarrow \Lambda^0 K^0 \pi^-$	65325	24.7	0.140	32.7	8.0
$\rightarrow \pi^- + p \rightarrow \Lambda^0 K^0$	51924	19.5	0.067	14.6	4.9
$\rightarrow \pi^- + p \rightarrow \Lambda^0 K^0 \pi^0$	48612	18.4	0.110	24.0	5.6

Table 6.2: Comparison of elementary cross section to the primary collision of $\pi^- + C$. All channels have been normalised to the production channel of $\Sigma^- K^0$. The last column reads the difference of the relative abundance between the implemented cross-section and the here employed procedure.

Channel	Occurrence [%]	Abs.	Relative
$\rightarrow \pi^- + n \rightarrow \Sigma^- K^0 \rightarrow \Lambda^0 K^0$	12.5	88117	100.0
$\rightarrow \pi^- + p \rightarrow \Lambda^0 K^0$	10.5	74509	84.6
$\rightarrow \pi^- + p \rightarrow \Sigma^0 K^0$	10.5	74268	84.3
$\rightarrow \pi^- + n \rightarrow \Sigma^- K^0 \rightarrow \Sigma^0 K^0$	7.8	55458	62.9
$\rightarrow \pi^- + n \rightarrow \Lambda^0 K^0 \pi^-$	6.6	46548	52.8
$\rightarrow \pi^- + p \rightarrow \Lambda^0 K^0 \pi^0$	4.8	34049	38.6
$\rightarrow \pi^- + p \rightarrow \Sigma^0 K^0 \rightarrow \Lambda^0 K^0$	2.5	17548	19.9
$\rightarrow \pi^- + n \rightarrow \Lambda^0 K^0 \pi^- \rightarrow \Lambda^0 \Delta^- K^0 \rightarrow \Lambda^0 \pi^- K^0$	2.1	15176	17.2
$\rightarrow \pi^- + p \rightarrow \Sigma^0 K^0 \pi^0$	1.1	7487	8.5

Table 6.3: Production channel in $\pi^- + C$ reaction in the final exclusive channel of $\pi^- + A \rightarrow \Lambda + K^0_S + X$

tion of primary $\Sigma^- + K^0$ reaction for the lighter target, while the abundance of nearly all other channels are primary processes with relative abundances according to their implemented elementary cross-section. Also other multi-step processes can occur, although their abundance are quite low. As expected, the final state of $\Lambda + K^0_S$ and $\Sigma^0 + K^0_S$ without an additional pion dominate the admixture of the (semi-)exclusive channel.
The same procedure was applied for the heavier tungsten target and the obtained results are listed in Table 6.4. Similar to the light nucleus, the primary $\Sigma^- + K^0$ channel is dominant. Besides, due to the much larger path length in nuclear medium, the chances of multi-step processes is increased, which is reflected in the much higher fraction of multi-step processes.

This large inelastic $\Sigma^- + p$ cross-section implemented in GiBUU, has already been measured to some extend and is predicted by theory. The theoretical predictions of

Channel	Occurrence [%]	Abs.	Relative
$\rightarrow \pi^- + n \rightarrow \Sigma^- K^0 \rightarrow \Lambda^0 K^0$	18.7	105476	100.0
$\rightarrow \pi^- + n \rightarrow \Sigma^- K^0 \rightarrow \Sigma^0 K^0$	4.6	26008	24.7
$\rightarrow \pi^- + p \rightarrow \Lambda^0 K^0$	4.3	23977	22.7
$\rightarrow \pi^- + p \rightarrow \Lambda^0 K^0 \pi^-$	2.9	16136	15.3
$\rightarrow \pi^- + n \rightarrow \Sigma^- K^0 \rightarrow \Sigma^0 K^0 \rightarrow \Lambda^0 K^0$	2.7	15334	14.5
$\rightarrow \pi^- + n \rightarrow \Sigma^- K^0 \rightarrow \Sigma^0 K^0 \rightarrow \Sigma^- K^0 \rightarrow \Lambda^0 K^0$	2.7	15179	14.4
$\rightarrow \pi^- + p \rightarrow \Sigma^0 K^0 \rightarrow \Lambda^0 K^0$	1.9	10759	10.2
$\rightarrow \pi^- + p \rightarrow \Sigma^0 K^0$	1.8	10018	9.5
$\rightarrow \pi^- + n \rightarrow \Sigma^- K^0 \rightarrow \Sigma^0 K^0 \rightarrow \Sigma^+ K^0 \rightarrow \Lambda^0 K^0$	1.7	9350	8.9
$\rightarrow \pi^- + n \rightarrow \Lambda^0 K^0 \pi^- \rightarrow \Delta^- \Lambda^0 K^0 \rightarrow \pi^- \Lambda^0 K^0$	1.4	7980	7.6
$\rightarrow \pi^- + p \rightarrow \Sigma^0 K^0 \rightarrow \Sigma^- K^0 \rightarrow \Lambda^0 K^0$	1.4	7598	7.2
$\rightarrow \pi^- + p \rightarrow \Lambda^0 K^0 \pi^0$	1.0	5692	5.4

Table 6.4: Production channels in $\pi^- + W$ reactions in the final exclusive channel of $\pi^- + A \rightarrow \Lambda + K_S^0 + X$

the inelastic cross section are depicted together with the experimental data in Fig. 6.6, taken from [40]. The left panel shows the reaction $\Sigma^- + p \rightarrow \Lambda + n$ while the right panel shows $\Sigma^- + p \rightarrow \Sigma^0 + n$. Assuming that the Σ^- would have the largest predicted momentum ($p \approx 600$ MeV/c), corresponding to the lowest inelastic cross-sections, the cross-section are in the order of $\sigma \approx 20$ mb for both reaction channels.
Any other exclusive elementary reaction cross-sections for $\pi^- + A$ listed in Table 5.7 has a cross-section of $\sigma < 0.5$ mb. Here, similar to the theoretical predictions as well as experimental observations, GiBUU predicts a large contribution of secondary processes from Σ^-.

Panel (a) of Fig. 6.7 shows the cross-sections of $\Lambda + N \rightarrow \Sigma^0 + N$ (yellow), $\Sigma^0 + N \rightarrow \Lambda + N$ (red), $\Sigma^- + p \rightarrow \Lambda + n$ (blue) and $\Sigma^- + p \rightarrow \Sigma^0 + n$ (green) as a function of momentum, which are implemented in GiBUU.

The comparison between the experimentally measured cross-sections together with the theoretical predictions (Fig. 6.6) and cross-section parametrisations implemented in GiBUU (Fig. 6.7, panel (a)) proves that the dominant Σ^--channel is considered correctly in GiBUU. To emphasis the multi-step production via the Σ^- channel, the mean free path of the above mentioned inelastic channels as a function of the hyperon momentum is depicted in Fig. 6.7 panel (b). The dashed horizontal lines illustrate the diameter of the target nuclei , as illustrated in Fig. 6.3, for carbon ($d_C = 4.72$ fm) and tungsten ($d_W = 13.98$ fm).

One can see that the Σ^- the mean free path is in the order of the carbon nucleus diameter. Therefore, secondary Λ/Σ^0 production is expected to be large. By comparing the mean free path of the Λ and Σ channels, also here, depending on the

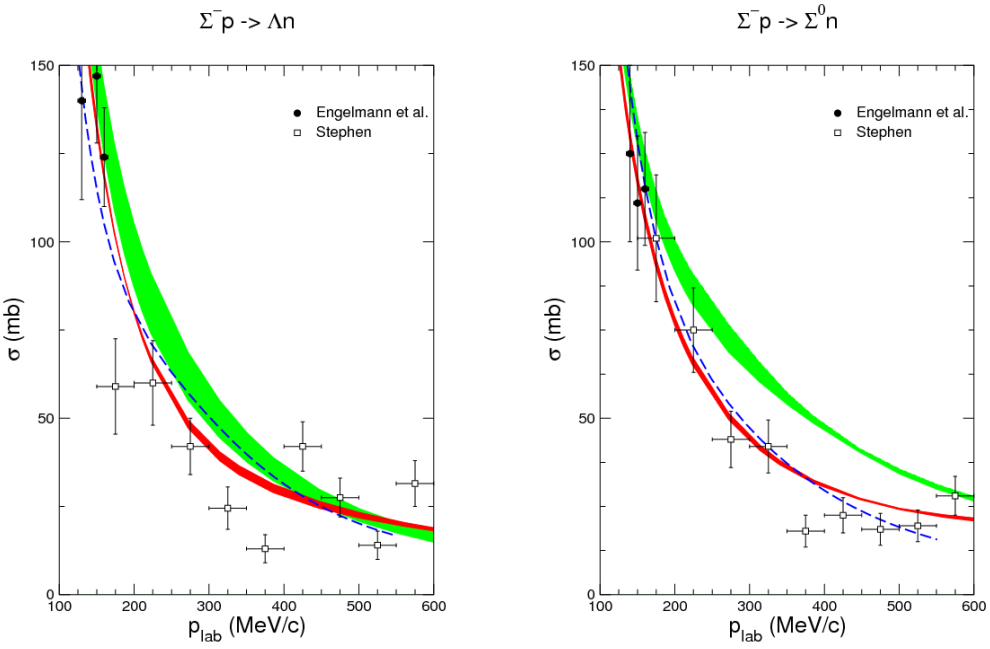

Figure 6.6: Theoretical prediction with experimental data for the cross section of $\Sigma^- + p \rightarrow \Lambda + n$ (left) and $\Sigma^- + p \rightarrow \Sigma^0 + n$ (right) taken from [40]. Green corresponds to leading and red to next to leading order calculations.

momentum, the mean free path becomes smaller than the nucleus diameter and hence multi-step production can occur.
Not only the production, but also the effective path inside the nuclear medium was studied. For this, similar to the extraction of the π^- interaction point in Fig. 6.4, the creation position of the final-state particles was studied. This corresponds to the IV step illustrated in the schematic of the presented procedure (Fig. 6.2), at the point in time where no inelastic interaction takes place any more. For this we distinguish between primary and secondary contributions as well as the particle species Λ and Σ^0. Depicted in Fig. 6.8 panel (a) is the creation point in space for Λ in primary reactions, while in panel (b) the secondary Λ position is illustrated for $\pi^- + C$ collisions. In the lower panel the same for the Σ^0 can be seen in panel (c) for primary and panel (d) for secondary reactions.

As expected for primary Λ in panel (a) and primary Σ^0 in panel (c) the creation point is upstream the surface, close to the reaction point of the π^-.
For the secondary contributions a rather symmetric distribution around the z-origin is observed in panel (b) for the Λ and Σ^0 in panel (d). While for the latter particle

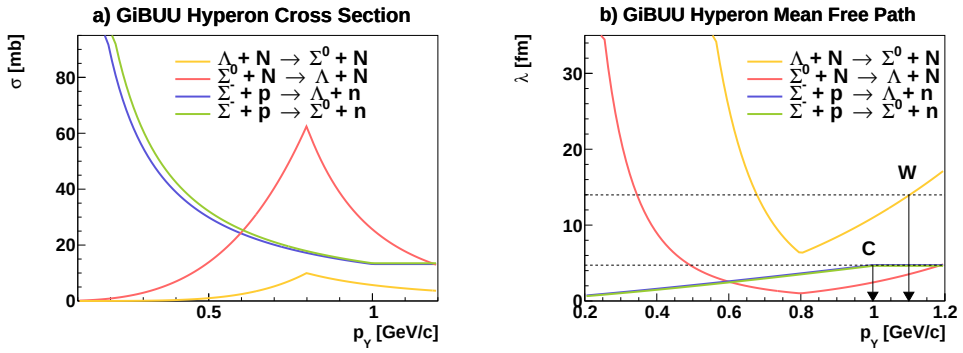

Figure 6.7: Inelastic cross-section (left) with corresponding mean free path (right) for $\Lambda + N \rightarrow \Sigma^0 + N$ (yellow), $\Sigma^0 + N \rightarrow \Lambda + N$ (red), $\Sigma^- + p \rightarrow \Lambda + n$ (blue) and $\Sigma^- + p \rightarrow \Sigma^0 + n$ (green) as a function of momentum. The dashed horizontal line indicates the diameter of carbon and tungsten.

species a slightly shifted distributions to higher z is visible.
In the next step it was investigated how large is the fraction of Λ and Σ^0 that have a rather large path length inside the nucleus, at least half of the nucleus diameter at $b = 0$, meaning that they were produced before the nucleus origin indicated by $z = 0$. Therefore, all Λ and Σ^0 located in front of $z = 0$ were integrated and compared to the total number of produced Λ and Σ^0. It is found that 53.7% in carbon and 61.94% in tungsten of the hyperons have a rather large path within the nucleus depending on the impact parameter b. Hence, πA reactions are especially suited to study in-medium effects of hyperons since the effective path within the nucleus is rather large.
All in all, it can be stated that GiBUU shows a remarkable prediction power by comparing the implemented cross-section to the available experimental data and theoretical predictions. Moreover, it is understood how GiBUU populates the exclusive channel and so that one can state that the production mechanism is under control.
In addition, also for the inclusive spectra of the K^0_S, GiBUU proved the remarkable good prediction power, supporting the statement that all production mechanism are under control. Hence GiBUU should provide reliable predictions for the (semi-)exclusive $K^0_S\Lambda$ channel. Moreover, the transport code GiBUU was already successfully employed for the prediction and extraction of the KN interaction [37].

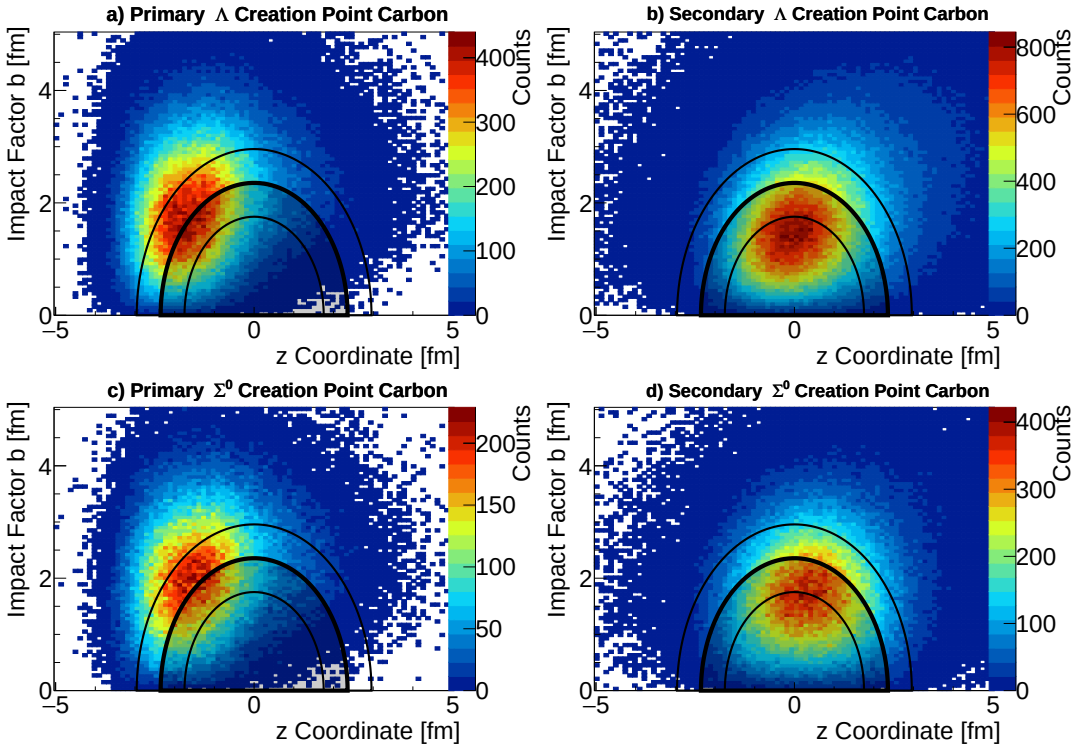

Figure 6.8: Creation point of Λ in primary reaction (a) and secondary (b) and Σ^0 in primary (c) and secondary (d) production in carbon.

6.3 Analysis Procedure

In this section the analysis procedure to extract the (semi-)exclusive $K^0_S\Lambda$ channel is presented. In the first part of the section the selection the (semi-)exclusive channel is outlined, followed by the background determination and subtraction. The end of this section deals with the fitting procedure in order to compare the results of GiBUU with the experimental data and the determination of the systematic uncertainties.

6.3.1 Event and Track Selection

For the (semi-)exclusive $K^0_S\Lambda$ channel the reaction $\pi^- + A \rightarrow \Lambda + K^0_S + X$ is selected in the final state. Both Λ and K^0_S were reconstructed via their dominant weak charged decay channels. Also the Σ^0 is contributing to the selected channel, due to the decay of $\Sigma^0 \rightarrow \Lambda + \gamma$ (BR ≈ 100% [1]). Hence the following channels are mainly contributing to the final state: ΛK^0_S, $\Lambda K^0_S \pi^0$, $\Sigma^0 K^0_S$ and $\Sigma^0 K^0_S \pi$.
The minimal criteria each event had to fulfil was the final state pattern of a minimum

of two positive and two negative charged particles ($\Lambda \rightarrow p + \pi^-, K^0_S \rightarrow \pi^+ + \pi^-$) within the HADES acceptance. As this criteria reduces the available experimental statistics tremendously, the particle identification of the daughter particles was based on a likelihood method, which does not introduce a hard cut. For details see Section 3.2.2. The ambiguities introduced by the two π^- in the final state was solved by means of a simultaneous invariant mass decision. In this procedure both possible combinations were formed, $\Lambda_{(1)}(p\pi^-_{1,})$, $K^0_{S(1)}(\pi^+\pi^-_2)$ and $\Lambda_{(2)}(p\pi^-_{2,})$, $K^0_{S(2)}(\pi^+\pi^-_1)$ on the basis of the invariant mass technique, while assuming the respective nominal mass of the daughter particles. For both combinations of ΛK^0_S the simultaneous difference of the invariant masses was calculated corresponding to

$$\Delta_i = \left| \frac{M_{\Lambda_i} - M_{\Lambda_{PDG}}}{\sigma_\Lambda} \right| + \left| \frac{M_{K^0_{S,i}} - M_{K^0_{S,PDG}}}{\sigma_{K^0_S}} \right| \tag{6.2}$$

where i donates the combinations and σ_{Λ,K^0_S} the width of the invariant mass distributions. The latter was extracted in a two step procedure. The invariant mass of the K^0_S candidates as a function of the invariant mass of the Λ candidates is illustrated in Fig. 6.9. For the extraction of σ_Λ a 4σ pre-cut was performed on the K^0_S invariant mass as shown by the area between the dotted black line in Fig. 6.9, where the width and mean were taken from the averaged values of the inclusive analysis (Table 5.3).

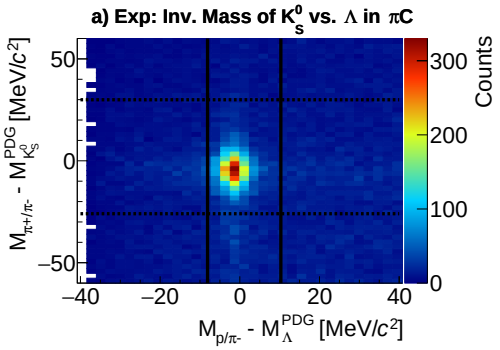

Figure 6.9: Invariant mass distribution of K^0_S candidates vs. invariant mass distribution of Λ candidates. The area between the dotted line indicates the invariant mass region with $4\sigma_{incl}$ around μ, while the σ_{incl} is the averaged resolution obtained in the inclusive K^0_S analysis. The same is indicated for the Λ by the solid lines.

In the next step the area between the dotted lines, corresponding to the preselected Λ invariant mass, was projected onto the x-axis depicted in Fig. 6.10 panel (a) to extract in an iterative procedure the mean μ_Λ and sigma σ_Λ of the Λ on the basis of the invariant mass distributions. Therefore, the invariant mass distribution

was fitted with a Gaussian for the signal (red curve) together with a parabola for the background (blue curve). A similar approach is applied for the K_S^0. In the next step the such obtained means (μ_Λ, $\mu_{K_S^0}$) and sigmas (σ_Λ, $\sigma_{K_S^0}$) were used again for the pre-selection of the Λ and K_S^0. Hence, the dotted lines in Fig. 6.9 were evaluated a second time on the basis of the mean and sigma of the actual invariant mass distribution and not on the basis of the averaged values of the inclusive analysis. Meaning that more reliable means μ and sigma σ could be extracted by repeating the fitting process. Also for the K_S^0 the procedure was redone. In this way also the yield of the Λ and K_S^0 were obtained, respectively.

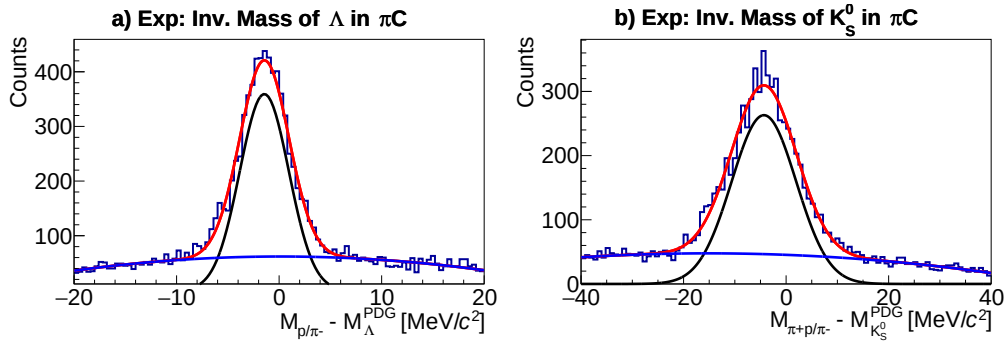

Figure 6.10: Invariant mass distribution of Λ in panel (a) and K_S^0 in panel (b). These distributions corresponds to the shaded areas of Fig. 6.9. Red depicts the combined fit, while blue illustrated the background modelled with a parabola and the signal modelled with a Gaussian in black.

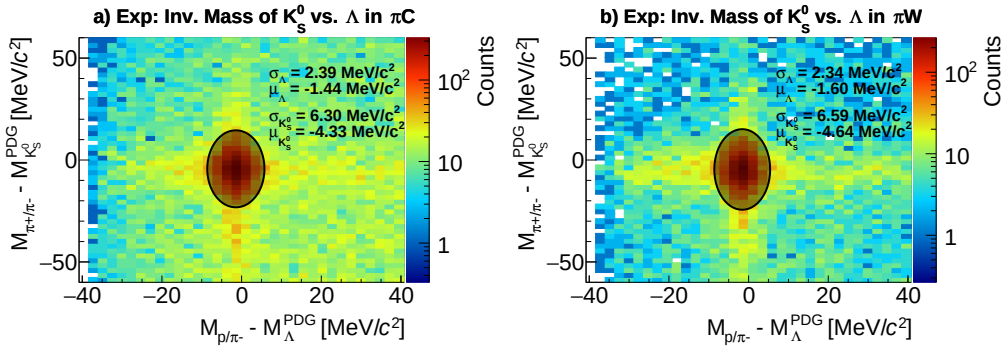

Figure 6.11: Invariant mass distribution of K_S^0 candidates vs. invariant mass of Λ candidates. The shaded area corresponds to the applied 3σ two dimensional elliptical cut. See text for details.

Based on the extracted information the combinations with the smallest Δ (Eq. (6.2)), and therefore the best simultaneous agreement of the invariant mass

distribution was selected for further analysis.
This does not introduce any bias as systematic checks showed that no substantial number of events lie within the expected area if the worse combination was selected. For the final event selection, a simultaneous 3σ cut on both invariant mass distributions was performed to select the (semi-)exclusive channel. As the widths of the Λ and K^0_S distributions are different a **t**wo **d**imensional **e**lliptic (TDE) cut was performed:

$$\sqrt{\left(\frac{\Delta M_\Lambda - \mu_\Lambda}{3 * \sigma_\Lambda}\right)^2 + \left(\frac{\Delta M_{K^0_S} - \mu_{K^0_S}}{3 * \sigma_{K^0_S}}\right)^2} \leq 1 \tag{6.3}$$

where

ΔM: difference of the invariant mass to the nominal one
μ: mean of the distribution
σ: width of the invariant mass distributions

The experimental invariant mass distribution for the K^0_S candidates vs. the invariant mass distribution for the Λ candidates is illustrated in Fig. 6.11, where $\pi^- + C$ is depicted in panel (a) and $\pi^- + W$ in panel (b). The black shaded areas indicates the 3σ TDE. The width σ and mean μ for both particles, in both nuclear system for simulation and experiment are listed in Table 6.5.

Scenario	σ_Λ [MeV/c^2]	μ_Λ [MeV/c^2]	$\sigma_{K^0_S}$ [MeV/c^2]	$\mu_{K^0_S}$ [MeV/c^2]
W Exp	2.34	-1.60	6.59	-4.64
W ES (Y,K)	2.51	-1.29	6.51	-3.56
W ES (Y)	2.52	-1.31	6.50	-3.51
W STD	2.41	-1.14	6.56	-3.26
W RS	2.53	-1.22	6.49	-3.43
C Exp	2.39	-1.44	6.30	-4.33
C ES (Y,K)	2.33	-1.12	6.24	-3.23
C ES (Y)	2.31	-1.12	6.28	-3.19
C STD	2.29	-1.05	6.36	-2.84
C RS	2.31	-1.10	6.34	-3.14

Table 6.5: Summary of the width σ and μ of the invariant mass distributions for the exclusive analysis.

Independently of the system, particle or employed scenario, all agree very well. All events, that passed this stage were considered further for the analysis.

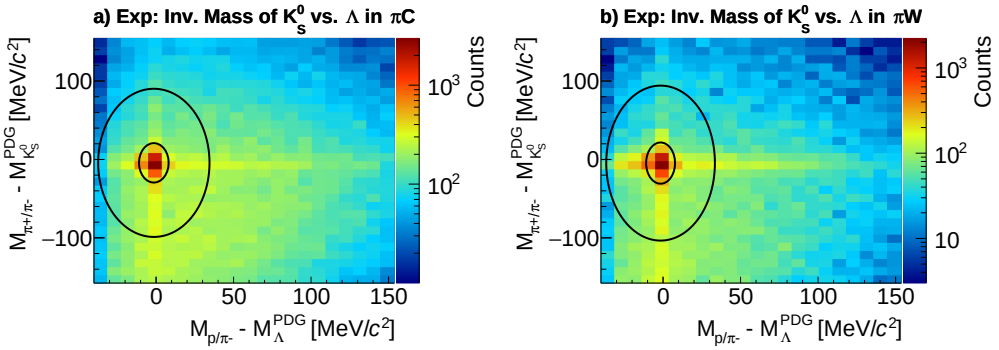

Figure 6.12: Invariant mass distribution of K^0_S candidates vs. invariant mass distribution of Λ candidates. The area between the two ellipses correspond to the selected sideband sample of $4 < \sigma < 15$ for carbon in panel (a) and tungsten in panel (b).

6.3.2 Background Determination

Although, the selection procedure introduced in Section 6.3.1 provides a clean sample, small background contributions were still remaining.
Therefore, a suitable sideband technique had to be applied in order to subtract the remaining background.
Due to the two dimensional invariant mass selection a commonly used one dimensional sideband technique which needs to be applied for each particle separately, was not applicable. To select a suitable sibeband with enough statistics to describe the remaining background, a TDE selection of $4 < \sigma < 15$ was performed in the two dimensional invariant mass plane. The experimental invariant mass distributions together with the TDE selection are shown in Fig. 6.12 for $\pi^- + C$ (a) and $\pi^- + W$ (b) collisions, respectively.

However due to this two dimensional selection, the sideband sample cannot be simply scaled to background contribution of Fig. 6.10. But to determine the background contribution, one can make use of the fact that the $\Lambda(K^0_S)$ signal stays the same after the two dimensional cut was applied. For illustration purposes one can assume an extracted yield of S = 100 in the one dimensional projection. Due to the TDE cut this yield of S = 100 will stay the same, but the background will be reduced to an unknown number. However, the background contribution can be estimated by the difference between the total number of events passing the TDE (e.g N = 105) and the number of the extracted yield (S = 100). In this example a background contribution of B = N-S = 5 is extracted. In this way, the sideband sample can be scaled to correct for the background contribution.
As the yield was extracted for the kaon and Λ independently, the resulting scaling

factor was calculated by:

$$\alpha = \frac{N_{cut} - \frac{1}{2}\left(S_\Lambda + S_{K_S^0}\right)}{N_{side}} = \frac{N_{cut} - \varnothing S}{N_{side}} = \frac{B}{N_{side}} \tag{6.4}$$

where

N_{cut}: entries after the TDE cut
$\varnothing S$: average yield extracted by the fit to the 1D inv. mass distribution
N_{side}: entries of the sideband sample

In a last step the sideband sample is scaled with α and subtracted to extract a background free data sample.

6.3.3 Fitting Procedure

In order to compare the Λ and K_S^0 kinematic distributions of experimental and simulated data after the TDE has been applied a fitting procedure was employed that scales the simulated distribution to the experimental one on the basis of a reducing χ^2/NDF. The definition of the χ^2/NDF, which was used for this analysis is as follows:

$$\frac{\chi^2}{NDF} = \frac{1}{N-1}\sum_{i=0}^{N}\frac{(E_i - \alpha \cdot S_i)^2}{\sigma} \tag{6.5}$$

where

$\frac{\chi^2}{NDF}$: reduced χ^2
N: number of entries
E_i: experimental entry
S_i: simulated entry
$\alpha = \frac{\sum_{i=0}^{N}(E_i \cdot S_i)}{\sum_{i=0}^{N}\left(S_i^2\right)}$: simulation scaling factor, for details see Appendix D.3
σ: combined error ($\sqrt{\sigma_{exp}^2 + \sigma_{sim}^2}$)
σ_{exp}: combined experimental error ($\sqrt{\sigma_{stat}^2 + \sigma_{sys}^2}$)
σ_{sim}: combined simulation error ($\sqrt{\sigma_{stat}^2 + \sigma_{sys}^2}$)

The following kinematic distributions have been investigated: the momentum p, polar angle Θ, transverse momentum p_t and rapidity y distributions for Λ and K^0_S, respectively. To determined a global χ^2/NDF a global fit was performed taking into account all kinematic distributions simultaneously. In this way also a global scaling factor was obtained.

6.3.4 Systematic Uncertainties

To estimate the systematic error introduced by the selection procedure and applied selections, all cuts were varied.
As the exclusive channel is not efficiency corrected and the experimental data is compared to the simulation on the basis of shapes, the systematic variations tests the impact on the shapes and not on the yield.
To evaluate the systematic uncertainties, first a nominal reference spectrum of the kinematic distributions was produced employing the nominal selections listed in Table 6.6.

Type	Nominal Value	Explanation
Signal Extraction	$\sigma_{signal} = 4 \cdot \sigma_{\Lambda,K^0_S}$	Cut for 1D-Proj.
Range Sideband	$\sigma_{side} = 4 < \sigma_{\Lambda,K^0_S} < 15$	Cut for Sideband Sample
TDE Cut	$\sigma_{TDE} = 3 \cdot \sigma_{\Lambda,K^0_S}$	Cut of TDE
Yield	$\varnothing S = \frac{1}{2}\left(S_\Lambda + S_{K^0_S}\right)$	Yield for Scaling/Det. of Background

Table 6.6: Nominal cuts applied for the exclusive analysis.

All selections were varied with the 8 different selection sets listed in Table 6.7. The full analysis chain of the exclusive analysis was then carried based on these different selection sets. The resulting spectra were then scaled to the reference spectrum by means of the effective total yield.

The systematic error for each cut set was then calculated bin wise as the relative difference $\left(\frac{R-V}{R}\right)$ of the variation entry V to the reference spectrum entry R.
All these errors were then combined quadratically to extract the total systematic error bin-by-bin.
The average errors corresponding to the cut variations for simulation and experiment in both system are listed in 6.7. The resulting total error is summarised in the last row.

Cut Set	Cut Variation	Exp [%]	ES(Y,K) [%]	ES(Y) [%]	STD [%]	RS [%]
W						
1	$\sigma_{signal} - 1\sigma$	4.29	3.53	3.62	4.07	3.35
2	$\sigma_{signal} + 1\sigma$	1.46	1.69	1.70	2.04	1.63
3	$\sigma_{TDE} - \frac{1}{2}\sigma$	3.60	2.99	3.21	3.67	3.14
4	$\sigma_{TDE} + \frac{1}{2}\sigma$	2.33	1.22	1.32	1.42	1.29
5	$5 < \sigma_{side} < 15$	2.40	1.26	1.33	1.41	1.26
6	$4 < \sigma_{side} < 10$	1.92	1.94	1.89	2.30	1.86
7	$\varnothing S = S_{K^0_S}$	0.38	1.13	1.19	1.65	0.66
8	$\varnothing S = S_{\Lambda}$	0.61	1.23	1.31	1.82	0.69
Sum	σ_{sys}	6.99	5.82	6.04	7.04	5.60
C						
1	$\sigma_{signal} - 1\sigma$	6.14	3.75	3.59	3.68	3.85
2	$\sigma_{signal} + 1\sigma$	2.45	1.65	1.66	1.66	1.66
3	$\sigma_{TDE} - \frac{1}{2}\sigma$	5.50	3.43	3.37	3.54	3.48
4	$\sigma_{TDE} + \frac{1}{2}\sigma$	2.44	0.75	0.84	0.76	0.82
5	$5 < \sigma_{side} < 15$	2.43	0.68	0.75	0.68	0.73
6	$4 < \sigma_{side} < 10$	3.49	2.01	2.03	2.02	2.04
7	$\varnothing S = S_{K^0_S}$	1.73	1.11	1.13	0.76	1.02
8	$\varnothing S = S_{\Lambda}$	1.18	1.35	1.20	0.79	1.07
Sum	σ_{sys}	10.11	6.05	5.93	5.93	6.10

Table 6.7: Cut variation for the systematic error evaluation.

6.4 Results and Discussion

After the reliability of GiBUU was studied and verified it can be used to provide predictions, which then can be confronted with experimental data.
As a short reminder, four different scenarios were considered (Table 6.1). The first one is a simple assumption, in which only elastic scattering for KN and YN (ES(Y.K)) was considered. Followed by the second, where the χ-EFT potential of KN was considered (ES(Y)). The third scenario deals with the standard implementation of GiBUU, where the Λ and Σ interaction was considered to be attractive with 2/3 of the NN potential (STD). The last one took into account the predicted repulsive interaction of the Σ^0, where an approximation of the χ-EFT prediction was implemented (RS). For details see Section 6.1. The systematic errors are indicated by the width of the band represented in the colours of the different scenarios.

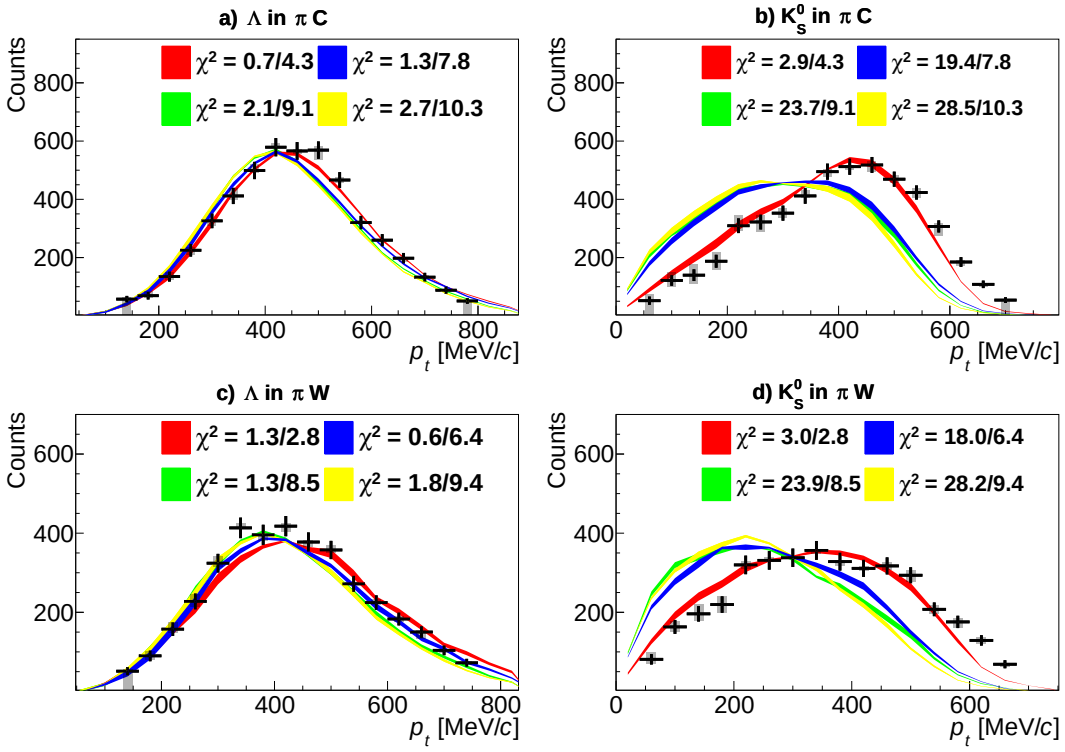

Figure 6.13: Transverse momentum of Λ in carbon (a), tungsten (c) and of K^0_S in carbon (b) and tungsten (d). Coloured in black are the experimental data with the systematic uncertainty shaded in grey. For the different scenarios the following colour code is employed: ES(Y,K) in yellow, ES(Y) in green, STD in red, RS in blue. The first number of χ^2/NDF reads the χ^2/NDF of the current kinematic variable while the second number reads the global value.

The upper panel illustrates the kinetic variable for the lighter system carbon for Λ in panel (a) and K_S^0 in panel (b). The lower one illustrates the same variable in tungsten for Λ in panel (c) and K_S^0 in panel (d).
In the upper area of each panel next to the colour codes of the different scenarios the χ^2/NDF values are shown, where the first one is the χ^2/NDF of the single kinematic distribution and the second one the global χ^2/NDF. For convenience χ^2/NDF will be abbreviated in the text by χ^2. A summary of all extracted χ^2 is listed in Table 6.8.
First we focus on the transverse momentum distribution of the Λ in Fig. 6.13 carbon in panel (a) and tungsten in panel (b). For both nuclei a rather symmetric distribution can bee seen. By eye all four scenarios look very similar, although the χ^2 are quite different. For the light nucleus, ES(Y,K) shows the least agreement with $\chi^2_{ES(Y,K)} = 2.74$ followed by ES(Y) with $\chi^2_{ES(Y,K)} = 2.13$. If we now consider the in-medium modification of the hyperons, the standard version of GiBUU fits much better with $\chi^2_{STD} = 0.66$ with respect to $\chi^2_{RS} = 1.35$. For tungsten STD, ES(Y) and ES(Y,K) show comparable results, whereas RS is favoured the most.
For the K_S^0 the differences are more pronounced in both nuclear system as depicted in panel (b) for carbon and panel (c) for tungsten of Fig. 6.13. While ES(Y,K), ES(Y) and RS show comparable results, STD deviates largely. However the latter is very well in agreement with the experimental data.
This proves that the K_S^0 is not only sensitive to the Y potential but also even more sensitive compared to the Λ, due to its lower rest mass.

If we focus on the rapidity distribution in Fig. 6.14, in all cases the distributions of the different scenarios are very similar for both particles in both collision systems. Nevertheless, a shallow trend towards STD is observed.
By comparing the Θ distributions of Λ in panel (a) for carbon and panel (c) for tungsten of Fig. 6.16 a similar trend as for the transverse momentum (Fig. 6.13) can be observed. Again ES(Y,K), ES(Y) and RS predict very similar results, while the standard implementation STD show small variation, and hence agrees best with the experimental data. In addition, this trend towards STD is also favoured by the K_S^0 in panel (b) for carbon and panel (d) for tungsten.
For the momentum in Fig. 6.17 for the Λ, similar to the rapidity, no clear separation is visible. In case of the K_S^0 again the standard implementation is favoured, while the agreement for the heavier system in panel (d) is better then for the lighter system in panel (b). Here, the shape is well produced with a small offset to lower values.
As a realistic implementation of a combination of the KN and the YN potentials should be able to describe all here presented kinematic distributions simultaneously, a global fit was applied to all distributions at once to extract a global χ^2 is extracted. For tungsten the global χ^2 read: $\chi^2_{ES(Y,K)} = 9.38$, $\chi^2_{ES(Y,K)} = 8.50$, $\chi^2_{STD} = 2.84$ and $\chi^2_{STD} = 6.39$. For carbon: χ^2: $\chi^2_{ES(Y,K)} = 10.26$, $\chi^2_{ES(Y,K)} = 9.09$, $\chi^2_{STD} = 4.26$ and $\chi^2_{STD} = 7.77$ was extracted. A clear hierarchy is apparent for both nuclear systems.

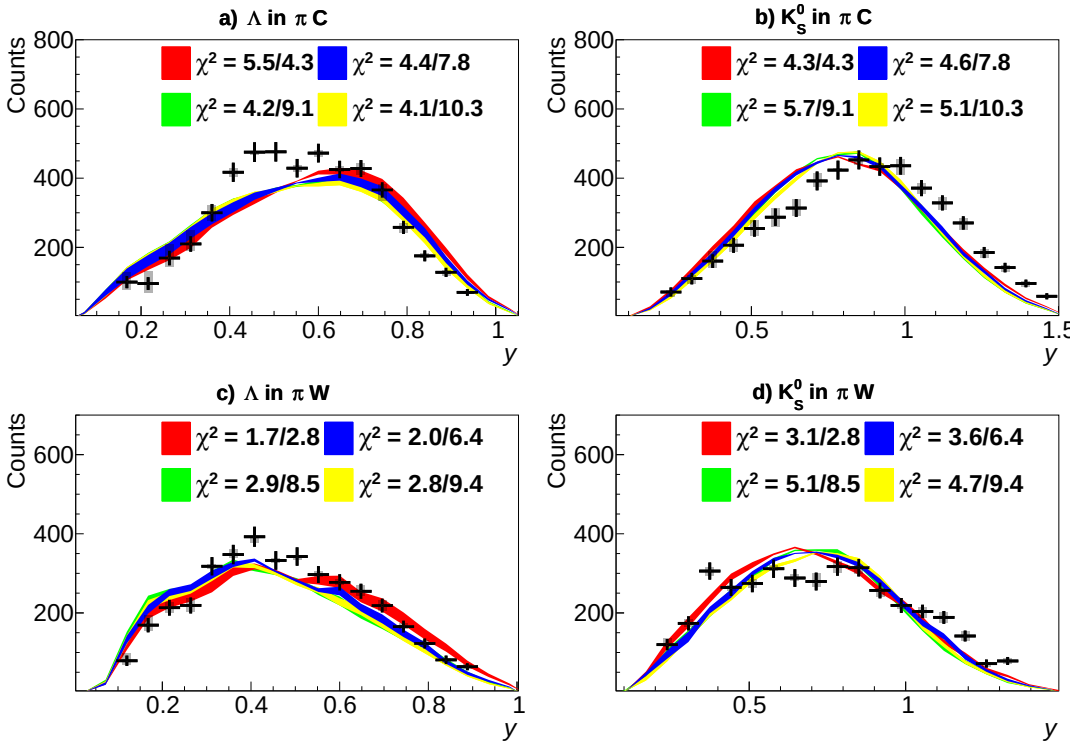

Figure 6.14: Rapidity of Λ in carbon (a), tungsten (c) and K^0_S in carbon (b) and tungsten (d). Coloured in black are the experimental data with the systematic uncertainty shaded in grey. For the different scenarios the following colour code is employed: ES(Y,K) in yellow, ES(Y) in green, STD in red, RS in blue. The first number of χ^2/NDF reads the χ^2/NDF of the current kinematic variable while the second number reads the global value.

The least fitting scenario is ES(Y,K), where beside elastic scattering no in-medium potentials was considered. Taken into account the implemented χ-effective KN potential of [37], an improvement in the description of the data could be achieved. For the hyperon interaction the standard version is clearly favoured, in which the Λ and Σ^0 was considered to be attractive with a modified NN potential. The implementation of the repulsive Σ^0 is largely disfavoured in both nuclear systems.

	ES(Y,K)	ES(Y)	STD	RS
W Λ P_t	1.78	1.27	1.30	0.64
W Λ Y	2.81	2.93	1.70	1.98
W Λ P	2.58	2.31	1.85	1.01
W Λ Θ	3.25	3.30	1.49	3.48
W K_S^0 P_t	28.19	23.86	2.96	17.98
W K_S^0 Y	4.73	5.06	3.07	3.60
W K_S^0 P	20.21	18.01	6.04	13.55
W K_S^0 Θ	8.42	6.75	1.17	5.13
C Λ P_t	2.74	2.13	0.66	1.35
C Λ Y	4.13	4.20	5.55	4.44
C Λ P	1.14	1.01	2.72	1.02
C Λ Θ	8.72	7.96	5.50	8.12
C K_S^0 P_t	28.49	23.67	2.85	19.44
C K_S^0 Y	5.06	5.72	4.27	4.64
C K_S^0 P	20.27	18.70	5.87	15.35
C K_S^0 Θ	7.91	5.43	2.03	3.94
W Global χ^2/NDF	9.38	8.50	**2.84**	6.39
C Global χ^2/NDF	10.26	9.09	**4.26**	7.77

Table 6.8: Summary of all χ^2/NDF. At the end the global values are listed.

The in-medium potential of hyperons and kaons can lead to a shift of their corresponding production threshold. Therefore, the ratio of Λ/Σ^0 predicted by each of the scenarios can be compared to world data. The Λ/Σ^0 ratio as a function of the excess energy ϵ taken from [85] is depicted in Fig. 6.15. In this work the ratio measured in elementary reactions with COSY [86, 87] has been compared to that in p+Nb of HADES as well as elementary cross-sections taken from Landolt-Bornstein [78]. In addition, simulations with UrQMD have been carried out for elementary and p+Nb reactions over the entire range of excess energy.
The Λ/Σ^0 ratio predicted by each presented scenario is also depicted in Fig. 6.15. The same colouring scheme as for the comparison of the kinematic distributions is applied. The filled markers correspond to Λ/Σ^0 ratios in tungsten, while the open markers depicts the ratios in carbon. All Λ/Σ^0 ratios are listed in Table 6.9.

For the lighter target all predict a ratio of around $\Lambda/\Sigma^0 \approx 2$, while ES(Y,K), ES(Y) and STD are slightly lower and RS is slightly higher. If we compare the ratio in the heavier system tungsten, the difference increases. Here ES(Y,K) and ES(Y) predict a ratio of $\Lambda/\Sigma^0 \approx 4$, STD $\Lambda/\Sigma^0 = 3.6$ and RS a much higher ratio of $\Lambda/\Sigma^0 = 6.06$.
By comparing the extracted Λ/Σ^0 ratios to the world data in Fig. 6.15, the Λ/Σ^0 ratio of the RS scenario in tungsten overshoots all measured data point and the UrQMD

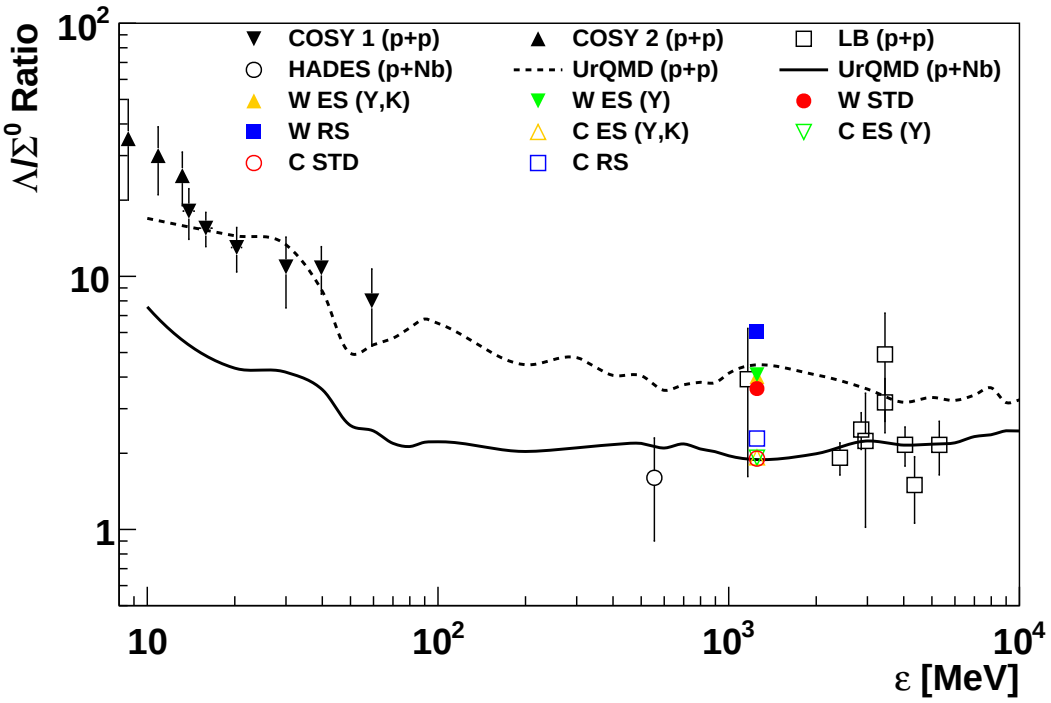

Figure 6.15: Λ/Σ^0 ratio as a function of the excess energy ϵ for p+Nb in HADES, elementary reaction from Landolt Bornstein [78] and UrQMD simulations taken from [85]. In this work also COSY [86, 87] has been included. Filled markes correspond to predictions of the different scenarios in tungsten and open markers for carbon. See text for details.

prediction, although still agrees within errors.
All other ratios are in the range of the measured experimental data and the prediction by UrQMD. While within errors no conclusive results can be extracted, the scenario of the repulsive interaction of the Σ^0 is disfavoured in terms of the Λ/Σ^0 ratio.

Scenario	W $\frac{\Lambda}{\Sigma^0}$	C $\frac{\Lambda}{\Sigma^0}$
ES(Y,K)	4.02	1.93
ES(Y)	4.08	1.92
STD	3.60	1.90
RS	6.06	2.29

Table 6.9: Λ/Σ^0 ratio for the different scenarios in tungsten (left) and carbon (right).

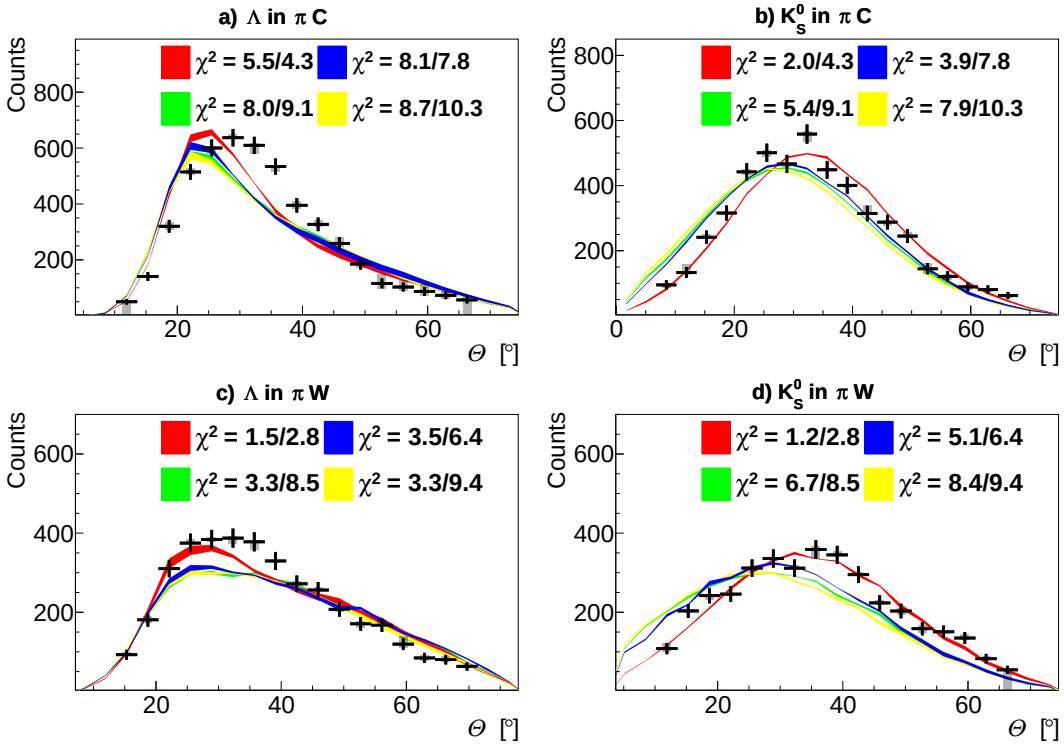

Figure 6.16: Θ of Λ in carbon (a), tungsten (c) and K^0_S in carbon (b) and tungsten (d). Coloured in black are the experimental data with the systematic uncertainty shaded in grey. For the different scenarios the following colour code is employed: ES(Y,K) in yellow, ES(Y) in green, STD in red, RS in blue. The first number of χ^2/NDF reads the χ^2/NDF of the current kinematic variable while the second number reads the global value.

6.5 Summary of the Exclusive Analysis

In this section the analysis of the (semi-)exclusive channel $\pi^- + A \rightarrow \Lambda + K^0_S + X$ was presented. Special attention was payed on the production processes and cross-section implemented in GiBUU.
It was shown, how GiBUU was modified to include a parametrisation of the YN interaction similar to the χ-effective single particle potentials taken from [54]. In this way it was possible to simulate for the first time a repulsive Σ^0 and attractive Λ at the same time. This gives the possibility to test different assumption and compare the prediction to experimental data in a heavy (tungsten) and light (carbon) nuclei. It was found that the scenario of the repulsive interaction of the Σ^0 is disfavoured by consideration of the kinematic distributions of Λ and K^0_S. Moreover, a comparison of the Λ/Σ^0 ratio confirms this observation.
The best matching results is extracted by employing a KN potential and a modified NN potential with a scaling of 2/3, which features an attractive Λ and attractive Σ^0 interaction.

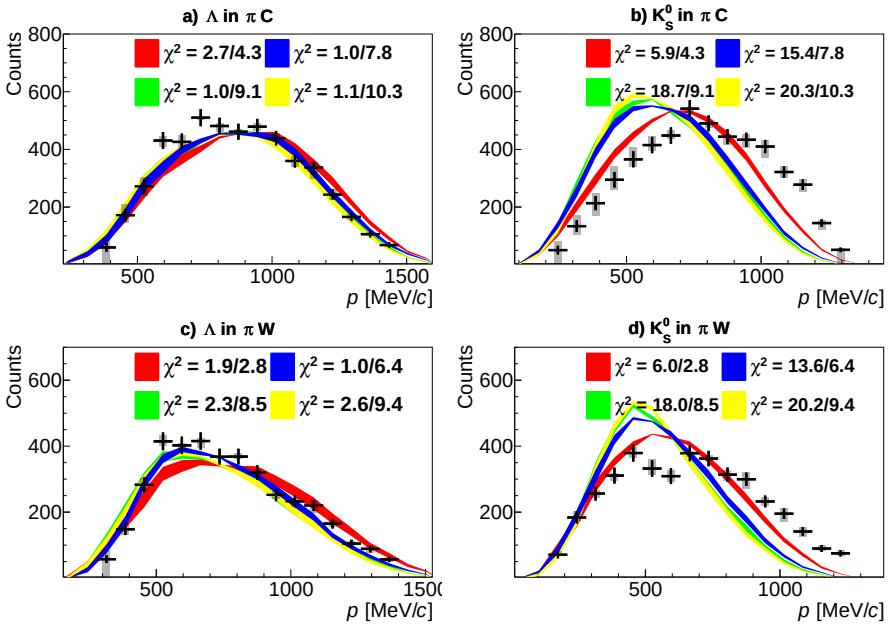

Figure 6.17: Momentum of Λ in carbon (a), tungsten (c) and K^0_S in carbon (b) and tungsten (d). Coloured in black are the experimental data with the systematic uncertainty shaded in grey. For the different scenarios the following colour code is employed: ES(Y,K) in yellow, ES(Y) in green, STD in red, RS in blue. The first number of χ^2/NDF reads the χ^2/NDF of the current kinematic variable while the second number reads the global value.

7
Summary and Outlook

The precision measurement of two solar mass neutron stars (NS) [17, 18] and recent observations of the neutron star merger [88] provide stringent constrains on the equation of state (EoS) of models describing such dense objects. All these observations reduce the allowed phase space, while the hyperon puzzle, that questions the presence of hyperons within NS, is still unsolved. The precise knowledge of the hyperon interaction with (normal) nuclear matter is crucial to derive reliable predictions of the EoS describing dense stellar objects with hyperon content. As the Λ is the lightest hyperon among all others, it is expected to appear first. Whereby, the exact onset of the Λ appearance is strongly dependent on its interaction within (dense) nuclear matter. So far, the ΛN interaction have been constrained by scattering experiments and the spectroscopy of hypernuclei. However, a differential study of the Λ propagation within (normal) nuclear matter is still missing.
First, the reconstruction efficiency correction of HADES was investigated in detail. Hence, differences in the detector response in the experiment and simulation were deduced. For this purpose, the elastic scattering in a subsequent experimental campaign with negatively charged pions at an incident pion beam momentum of $p_{\pi^-} = 690$ MeV/c impinging on a polyethylene (C_2H_4) target was studied. Exploiting the characteristic kinematical constraints of elastic scattering events, the background from inelastic reactions was significantly reduced. Whereby, full-scale Pluto simulations containing only elastic-scattering events ($\pi^- + p \rightarrow \pi^- + p$) were used. By measuring one of the two elastic scattered particles (π^- or p), the second one could be predicted based on the stringent kinematic constraints. Therefore, with the search for the predicted particle in the corresponding detector segment

a efficiency matrix could be retrieved. This procedure was performed separately for the MDC chambers (Fig. 4.3) and the META (Fig. 4.9) system (RPC/TOF). In this way, a systematic offset between experimental data and simulation of $\Delta\epsilon = 3\%$ is observed. This deduced difference was considered as systematic uncertainty in the analysis.
In this work also the inclusive production of Λ and K_S^0 were discussed. Both hadrons were reconstructed via their dominant weak charged decay channels, $\Lambda \rightarrow p + \pi^-$ (BR $= 63.9 \pm 0.5\%$ [1]) and $K_S^0 \rightarrow \pi^+ + \pi^-$ (BR $= 69.2 \pm 0.05\%$ [1]). Due to the dominant Σ^0 decay channel of $\Sigma^0 \rightarrow \Lambda + \gamma$ (BR $\approx 100\%$ [1]), the Σ^0 contributes to the observed Λ yield. The absolute normalised (double-differential) distributions for both particles were extracted in $\pi^- +$C and $\pi^- +$W reactions at an incident beam momentum of $p_{\pi^-} = 1.7$ GeV/c for both sets of kinematic variables, $p_t - y$ and $p - \Theta$. A Boltzmann fit was applied to the measured p_t spectra in order to extrapolate the yield in the uncovered regions. Hence, the rapidity density distributions dN/dy were extracted, which show strong scattering effects for both hadrons in the heavier target (W) as the distributions are shifted to backward rapidity with respect to the ones in the lighter target (C). The integrated production cross-section within the HADES acceptance for Λ ($0 \leq y < 1.05$) and K_S^0 ($0 \leq y < 1.6$) in $\pi^- +$C reactions are found to be equal to $\Delta\sigma_{\mathrm{C}}^{\Lambda} = 4347 \pm 19(\mathrm{stat}) \pm^{+129}_{-131} (\mathrm{sys})^{+188}_{-154}(\mathrm{norm})\mu$b and $\Delta\sigma_{\mathrm{C}}^{K_S^0} = 2080 \pm 14(\mathrm{stat})^{+83}_{-83}(\mathrm{sys}) \pm^{+84}_{-68} (\mathrm{norm})\mu$b and in $\pi^- +$W reactions equal to $\Delta\sigma_{\mathrm{W}}^{\Lambda} = 29712 \pm 127(\mathrm{stat}) \pm^{+677}_{-1114} (\mathrm{sys})^{+1416}_{-1159}(\mathrm{norm})\mu$b and $\Delta\sigma_{\mathrm{W}}^{K_S^0} = 12797 \pm 68(\mathrm{stat}) \pm^{+302}_{-277}$ $(\mathrm{sys})^{+559}_{-457}(\mathrm{norm})\mu$b.

In comparisons to three state-of-the-art transport models (GiBUU, UrQMD and SMASH) (Section 5.2.2), the absolute normalised (double-)differential spectra are found to be best described by the GiBUU model. The in-medium modification of K_S^0 was evaluated on the basis of the cross-section ratio of $R(\sigma_W^K/\sigma_C^K)$ as a function of the momentum in comparison to GiBUU predictions with and without χ-EFT KN potential (Section 5.3). Here a trend towards the in-medium χ-EFT KN potential is observed, however, not significant within the statistical errors and systematic uncertainties.
The K_S^0 together with Λ (Σ^0) interaction was investigated in more detail on the basis of the (semi-)exclusive channel $\pi^- + A \rightarrow \Lambda + K_S^0 + X$. Contrary, to the widely-used individual investigation of the hadron properties, a simultaneous study of the in-medium effects was conducted, due to the associated production of the Λ and K_S^0. To test different assumptions of the hyperon and kaon interaction within nuclear matter the GiBUU model was employed. Hence, to verify the validity of the model systematic checks were carried out (Section 6.2). To examine the predictions of χ-EFT [54], the hyperon potentials implemented in GiBUU were modified to mimic the theoretical YN interaction (Section 6.1). The sensitivity of the presented (semi-)exclusive channel to the in-medium potentials was demonstrated in this work. Indeed, different

scenarios/assumptions of the hyperon and kaon interaction implemented in GiBUU, result in different kinematic distributions within the HADES acceptance (Section 6.4). In total four different scenarios were considered. The first scenario only comprised the elastic scattering of the hyperons and kaons (ES(Y,K)). In the second one also the repulsive χ-EFT in-medium KN potential was considered, whereby the hyperons still could only scatter elastically (ES(Y)). The third scenario was the widely-used (standard) assumption, in which the ΛN and ΣN interaction were considered to be attractive with 2/3 of the NN potential (STD). To mimic the repulsive $\Sigma^0 N$ interaction predicted by the χ-EFT theory, the potential implemented in GiBUU was modified (RS). In this way, a realistic model of an attractive ΛN, repulsive $\Sigma^0 N$ and repulsive KN interaction in accordance to theoretical predictions was tested. The so simulated kinematic distributions on the basis of the four different scenarios were fitted globally to the experimental data and hence χ^2/NDF in light (C) and heavy (W) nucleus were extracted:

	ES(Y,K)	ES(Y)	STD	RS
W Global χ^2/NDF	9.38	8.50	**2.84**	6.39
C Global χ^2/NDF	10.26	9.09	**4.26**	7.77

The same scenario is favoured in both systems: repulsive χ-EFT KN interaction together with an attractive ΛN and an attractive $\Sigma^0 N$ interaction. The attractive $\Sigma^0 N$ interaction is in contradiction to χ-EFT calculations, in which the $\Sigma^0 N$ interaction is predicted to be repulsive. In addition, the scenario with the repulsive $\Sigma^0 N$ predicts a large Λ/Σ^0 ratio, which disagrees to the world data (Fig. 6.15).
This result has a huge influence on the underlying EoS, which describes objects like neutron stars. Due to the predicted repulsive ΣN interaction, it is expected that the Σ^0 will not appear in the core of a neutron star with hyperon content, based on calculations from [89]. However, they demonstrated that if the interaction would be attractive, they should appear at densities around 5 ρ_0.
As these are very promising results and the analysis itself including the predictions of GiBUU demonstrated to be well under control, further steps can be taken in the future. First, similar to the χ-EFT repulsive in-medium KN interaction, the full single particle potential for the hyperons predicted by χ-EFT could be implemented in the GiBUU transport model.
On the experimental side, HADES was quite recently equipped with a new RICH detector and an **e**lectromagnetic **cal**orimeter (ECAl) [90]. First measurements demonstrated the ECAl to be within the expected performance. It will be fully operational in near future. With the ECAl a dedicated Σ^0 sample could be selected as the γ of the decay $\Sigma^0 \rightarrow \Lambda + \gamma$ can be reconstructed and studied in the same manner as presented in this work. Another π^--beam campaign is proposed by the HADES collaboration

in 2021. An increased statistic, would allow to perform the (semi-)exclusive analysis in a (double-)differential way. Hence, the results and presented analyses of this work will be used in the future. The inclusive cross-sections serve as an input for transport models to constraint the branching ratios of the resonance decays and can improve the implemented cross-section parametrisations. In this way, the prediction power of transport models can be improved, which is of particular importance for the interpretation of heavy ion collisions, as the latter undergo a large density and temperature evolution. The (semi-)exclusive analysis showed, that a simultaneous investigation of the hadron properties is crucial to draw conclusions about (possible) in-medium modification of hadrons. The disfavour of the repulsive $\Sigma^0 N$ interaction constraints theoretical calculations. Moreover, this observation has direct consequences for an improved description of the in-medium hyperon interaction and hence is relevant to provide more realistic EoS of dense nuclear matter with hyperon content, in heavy ion collisions, but possibly also in neutron stars.

A

Data and Even Selection

A.1 Exclusive PID - Carbon

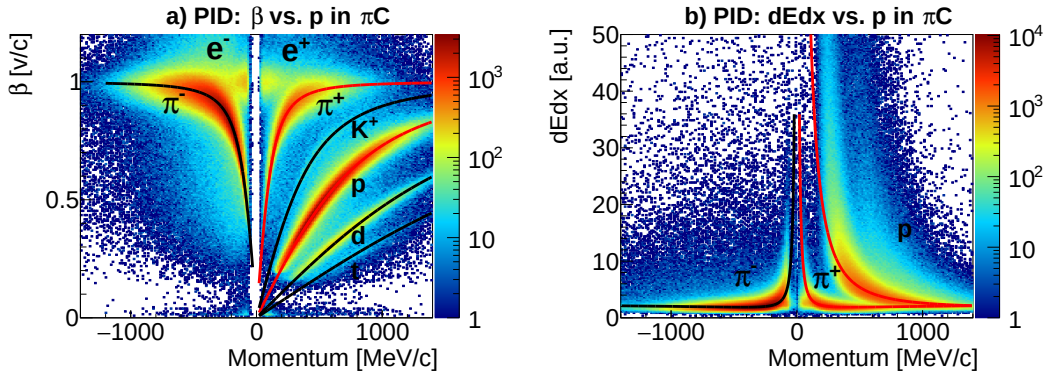

Figure A.1: Energy loss and β as a function of momentum in panel (a) and (b) πC, respectively. In the β momentum-plane a visible separation between the particles species can be seen while the dEdx is more entangled. The lines represent the theoretical curves. Indicated in red for p and π^+.

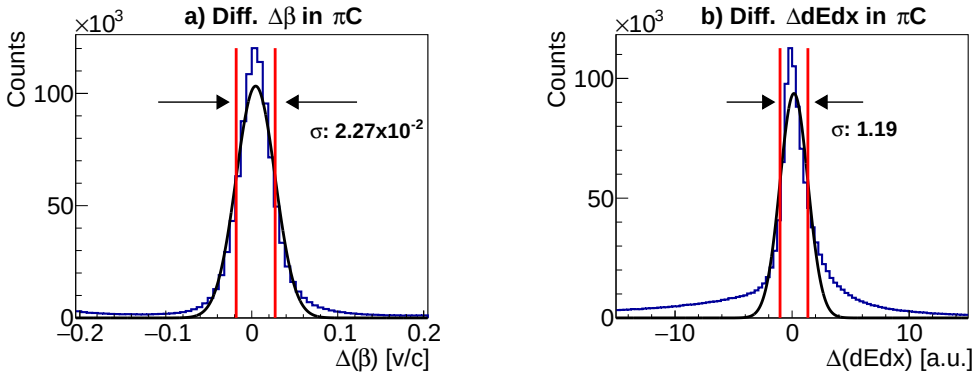

Figure A.2: Difference spectra for the particle identification, for β in panel (a) and dEdx in panel (b) assuming theoretical values for a proton for carbon. The peak is fitted with a single Gaussian and the fits are indicated by the two lines with their corresponding value.

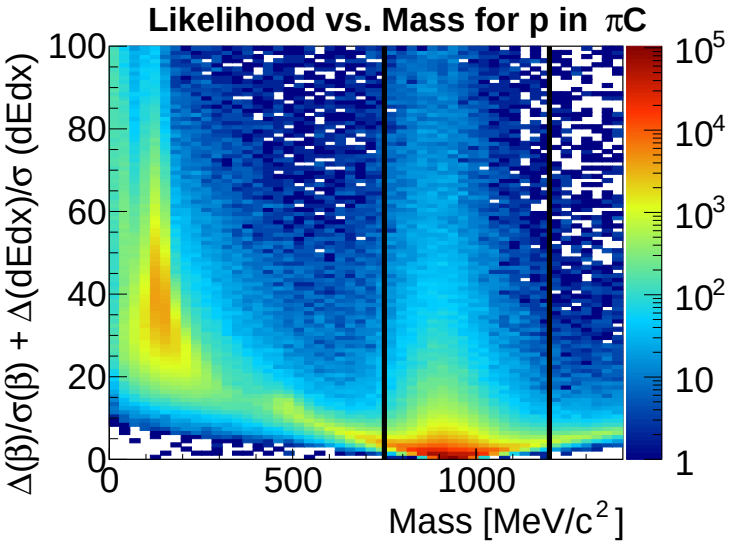

Figure A.3: Likelihood value for a proton as a function of the momentum for carbon. All protons have very low values of p_{like} with an anti-correlation of the π^+, illustrating the separation power of the technique.

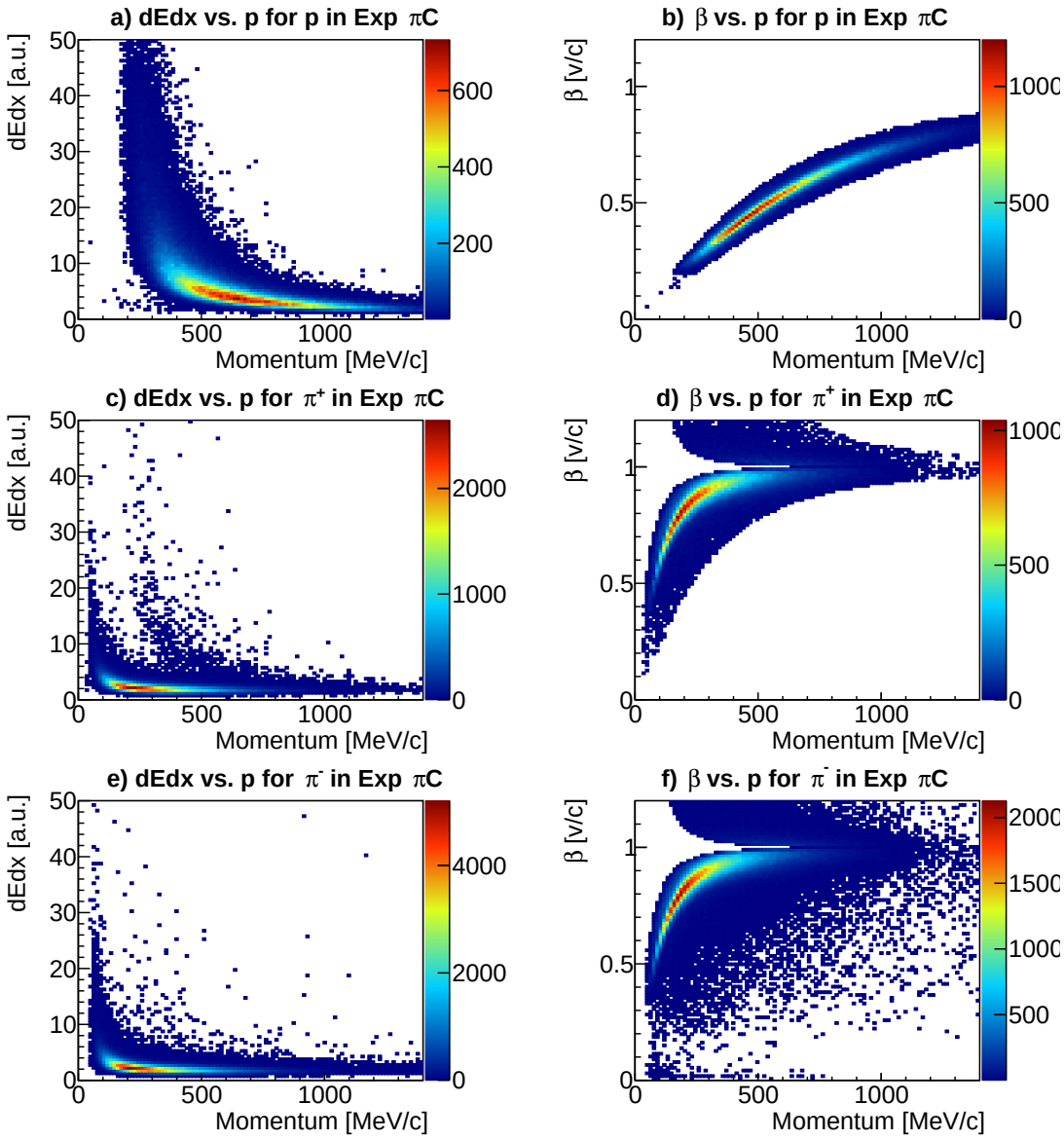

Figure A.4: Particle distributions for carbon after the liklihood selection for dEdx/β vs. momentum for p in panel (a)/(b), π^+ in panel (c)/(d) and π^- in panel (e)/(f).

A.2 Topological Cuts

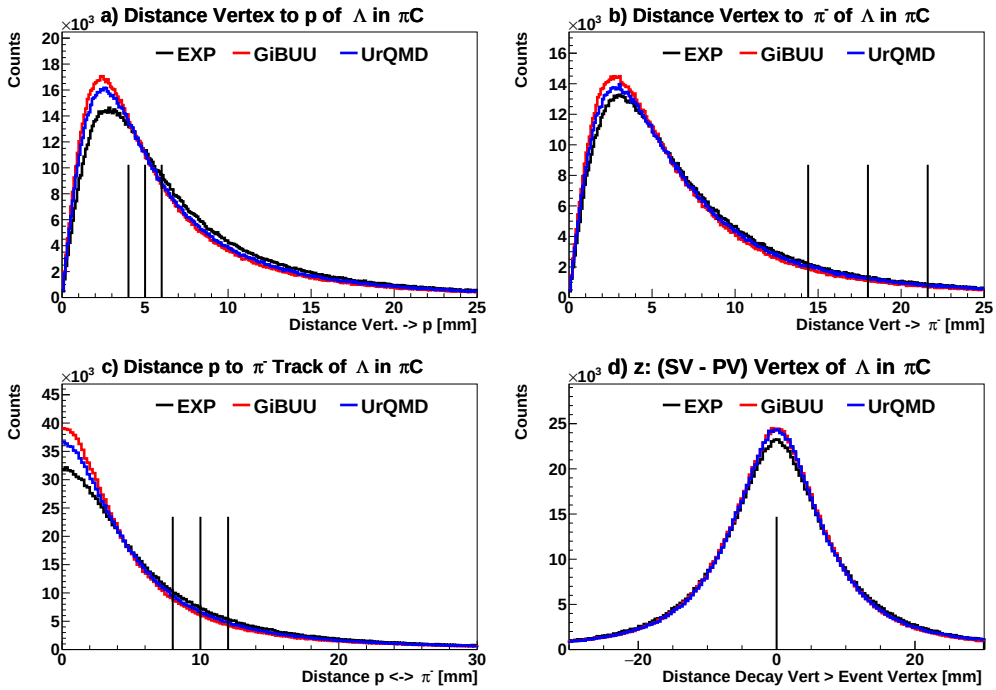

Figure A.5: Topological distributions for Λ in $\pi^- C$ for experiment (black), GiBUU (red) and UrQMD (blue). The black lines represent the applied topological cuts, where the line in the middle represents the nomial cut and the outer lines the systematic variation.

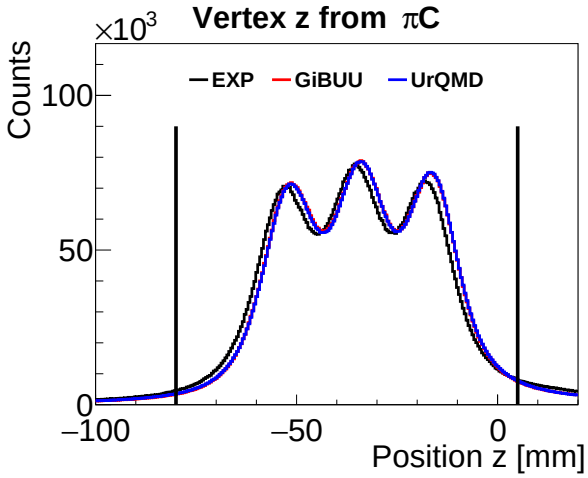

Figure A.6: Z component of the primary vertex for experiment (black), GiBUU(red) and UrQMD (blue) for carbon. The black lines indicated the applied cuts, while the three peaks correspond to the single segment of the target.

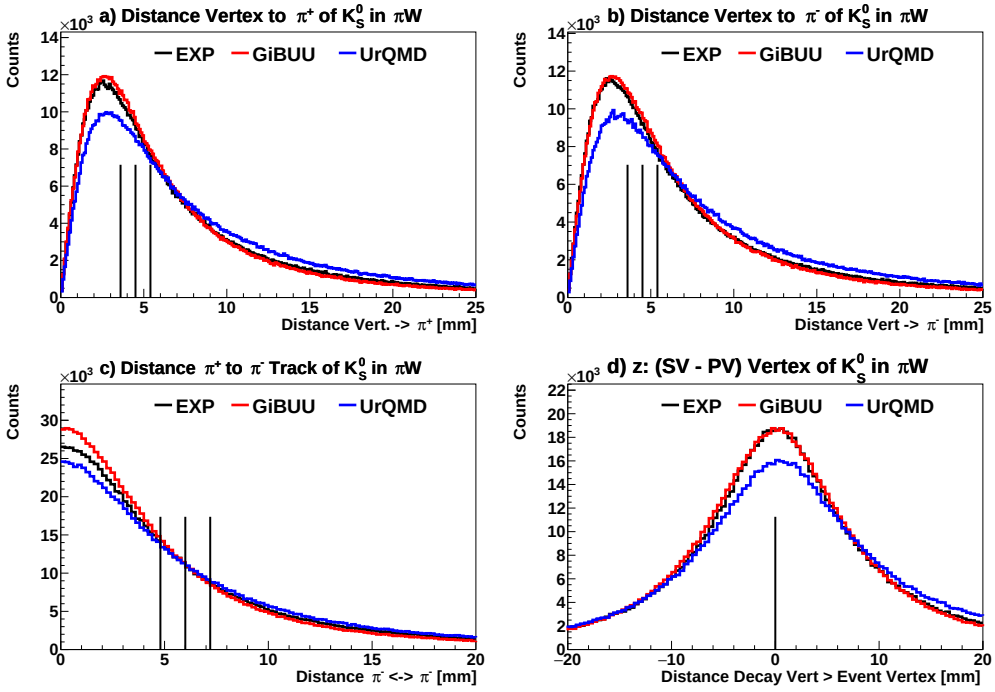

Figure A.7: Topological distributions for K_S^0 in $\pi^- W$ for experiment (black), GiBUU (red) and UrQMD (blue). The black lines represent the applied topological cuts, where the line in the middle represents the nomial cut and the outer lines the systematic variation.

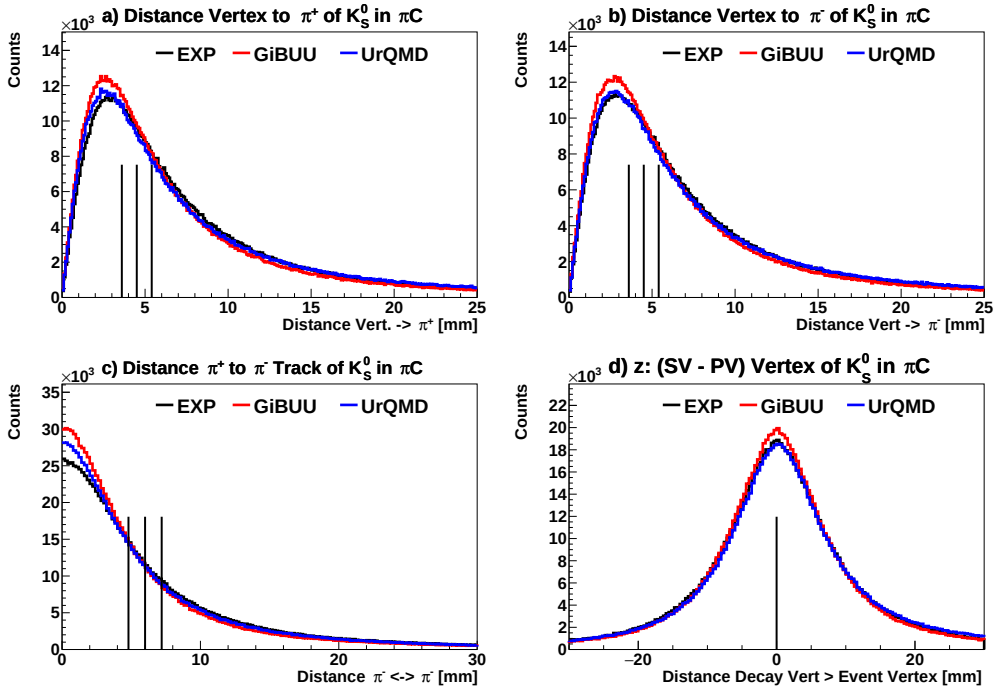

Figure A.8: Topological distributions for K^0_S in $\pi^- C$ for experiment (black), GiBUU (red) and UrQMD (blue). The black lines represent the applied topological cuts, where the line in the middle represents the nomial cut and the outer lines the systematic variation.

B

Experimental Efficiency Calculations

B.1 MDC Efficiency - Cuts

Pion - MDC

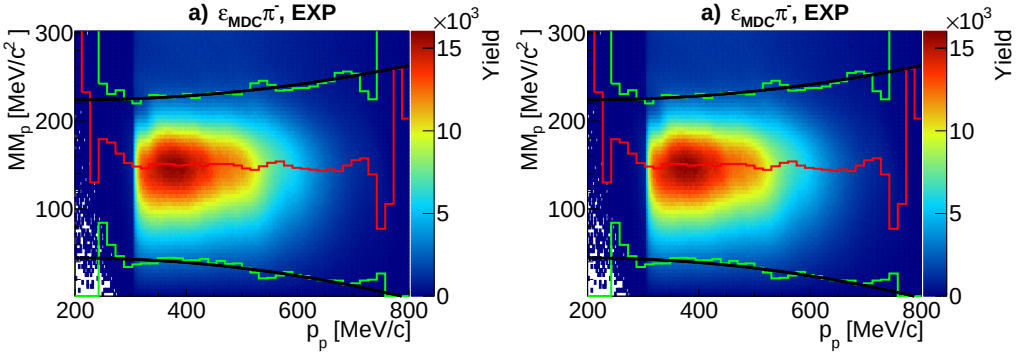

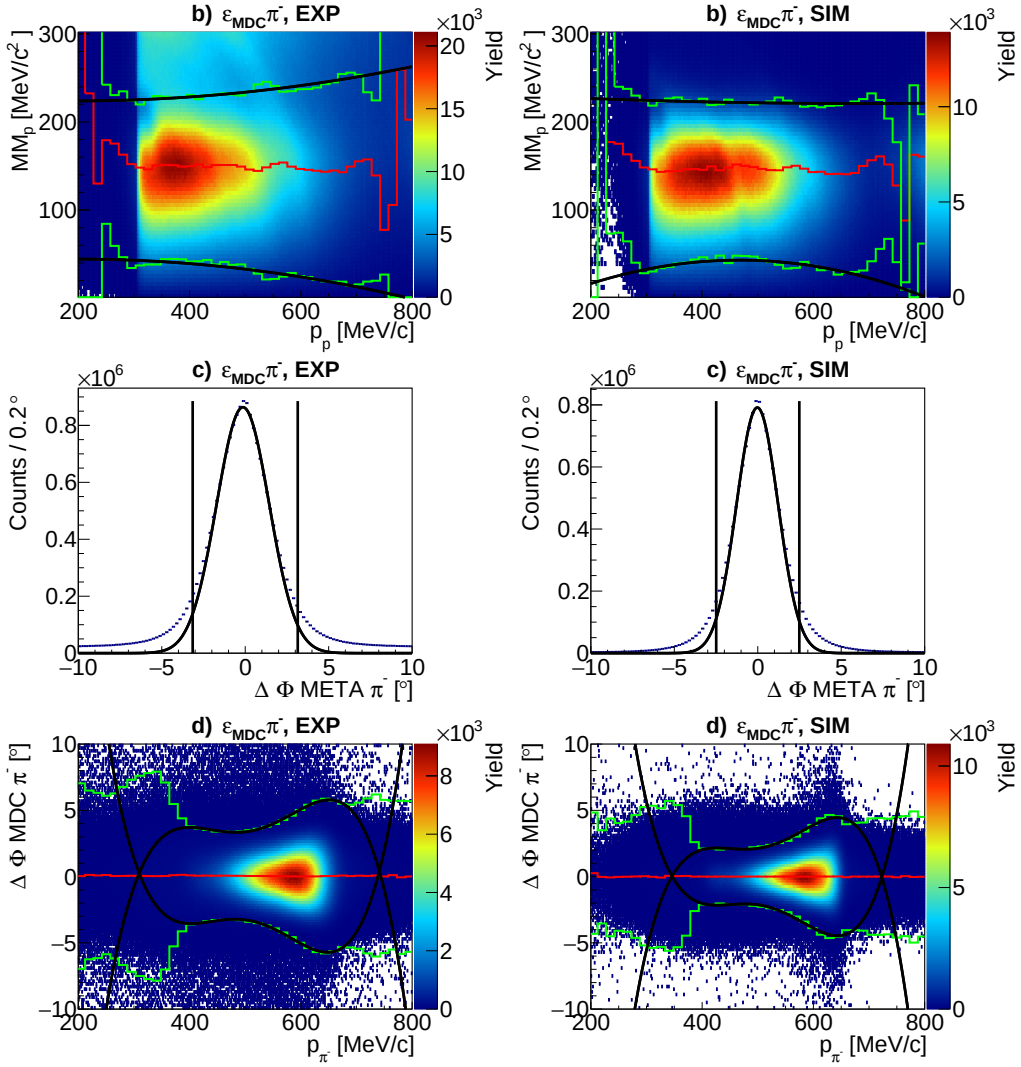

Figure B.1: Cuts for the efficiency calculation of MDC for π^-. Left experimental cuts, right for the simulation.

Proton - MDC

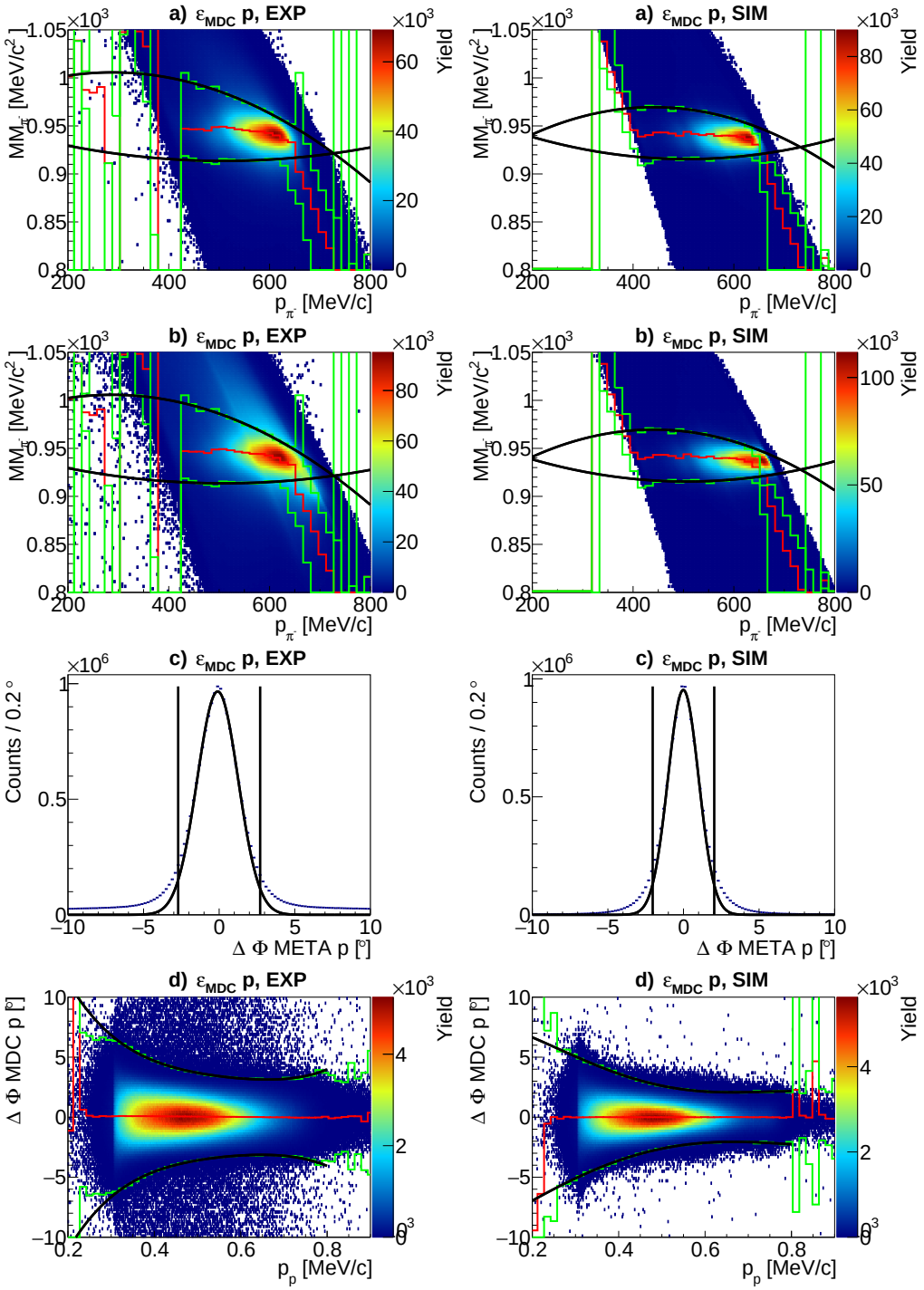

Figure B.2: Cuts for the efficiency calculation of MDC for proton. Left experimental cuts, right for the simulation.

B.2 META Efficiency - Cuts

Pion - META

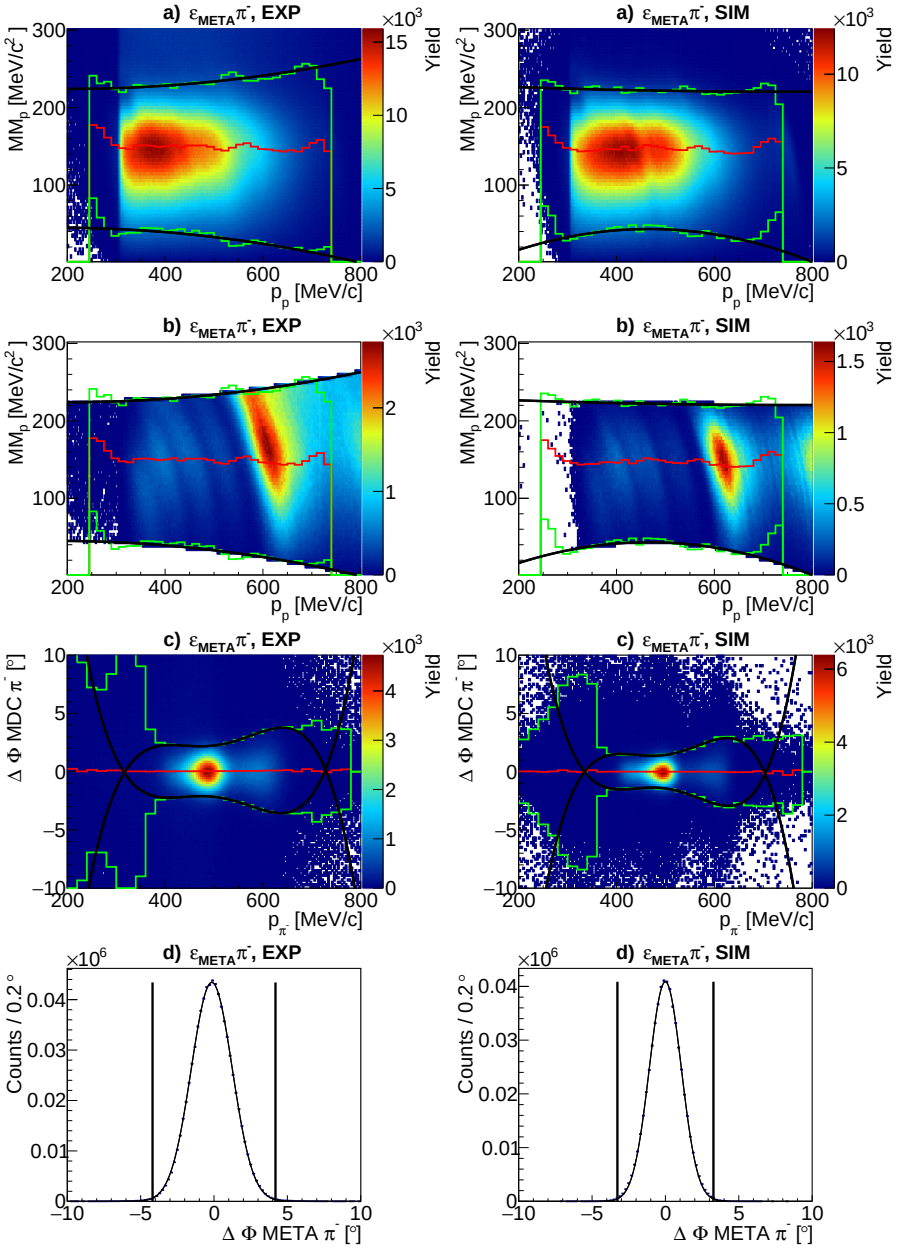

Figure B.3: Cuts for the efficiency calculation of META for π^-. Left experimental cuts, right for the simulation.

Proton - META

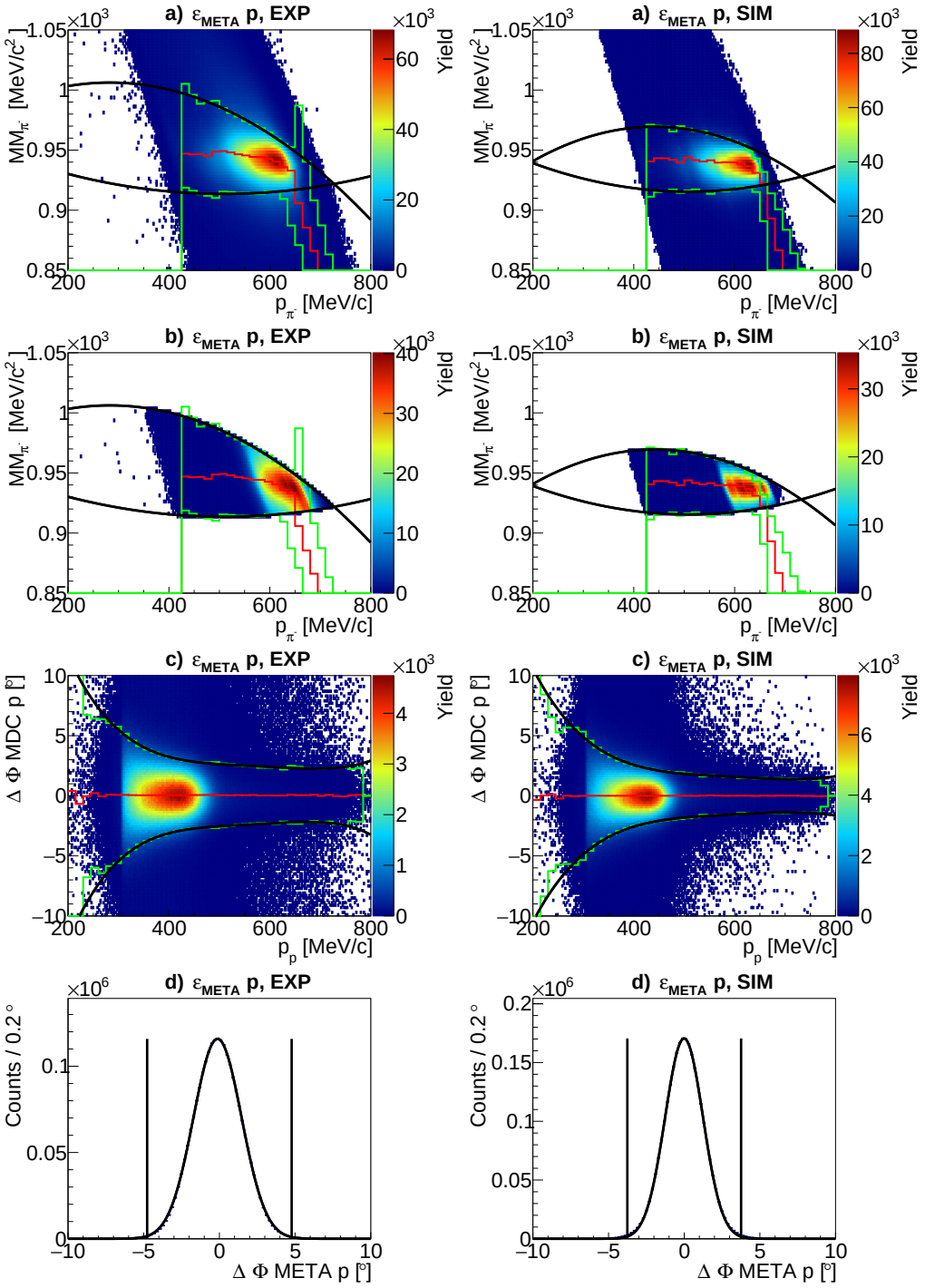

Figure B.4: Cuts for the efficiency calculation of META for proton. Left experimental cuts, right for the simulation.

C

Inclusive Analysis

C.1 K^0_S and Λ (C) Fit Parameters

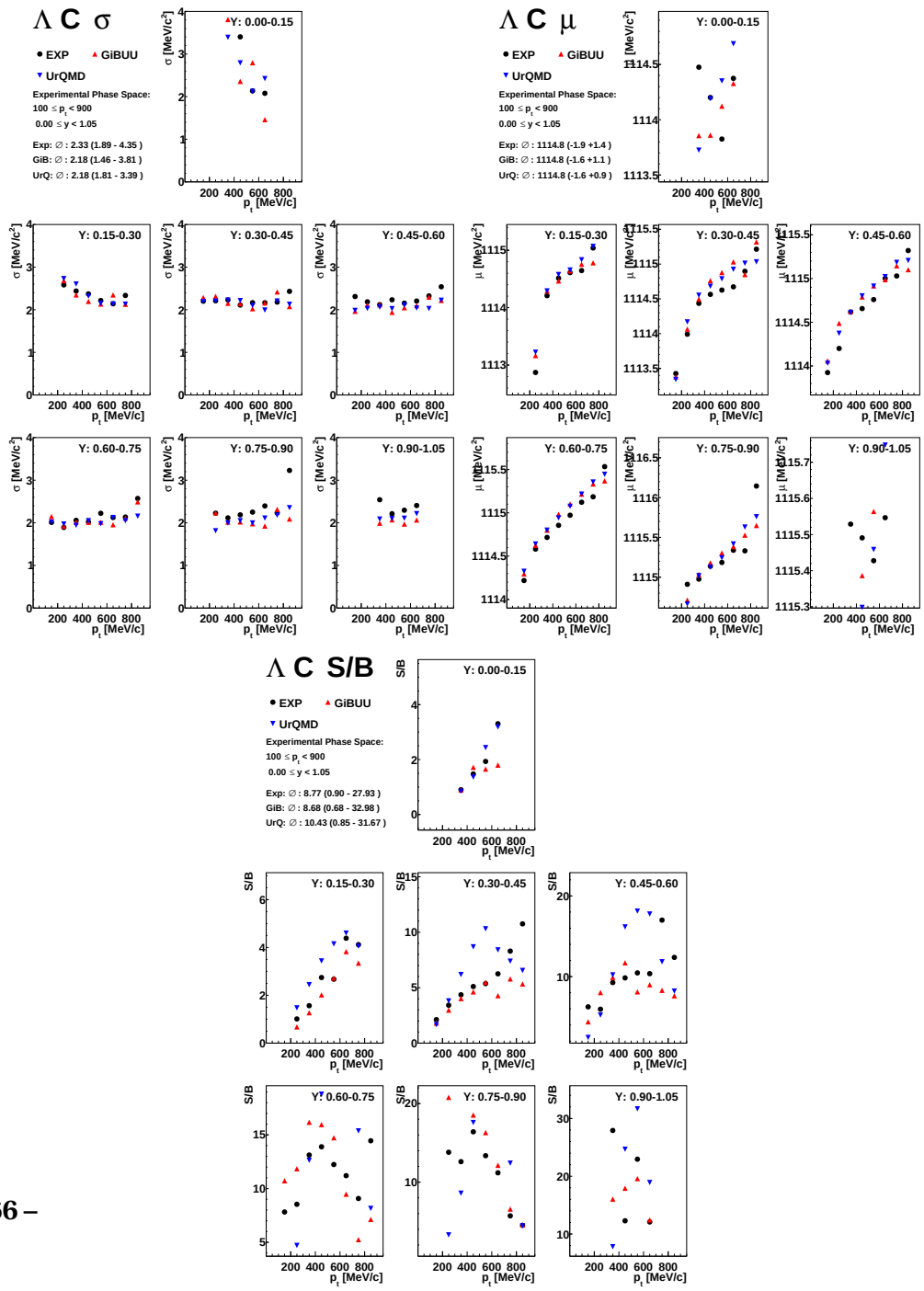

Figure C.1: Fit parameter for Λ in carbon.

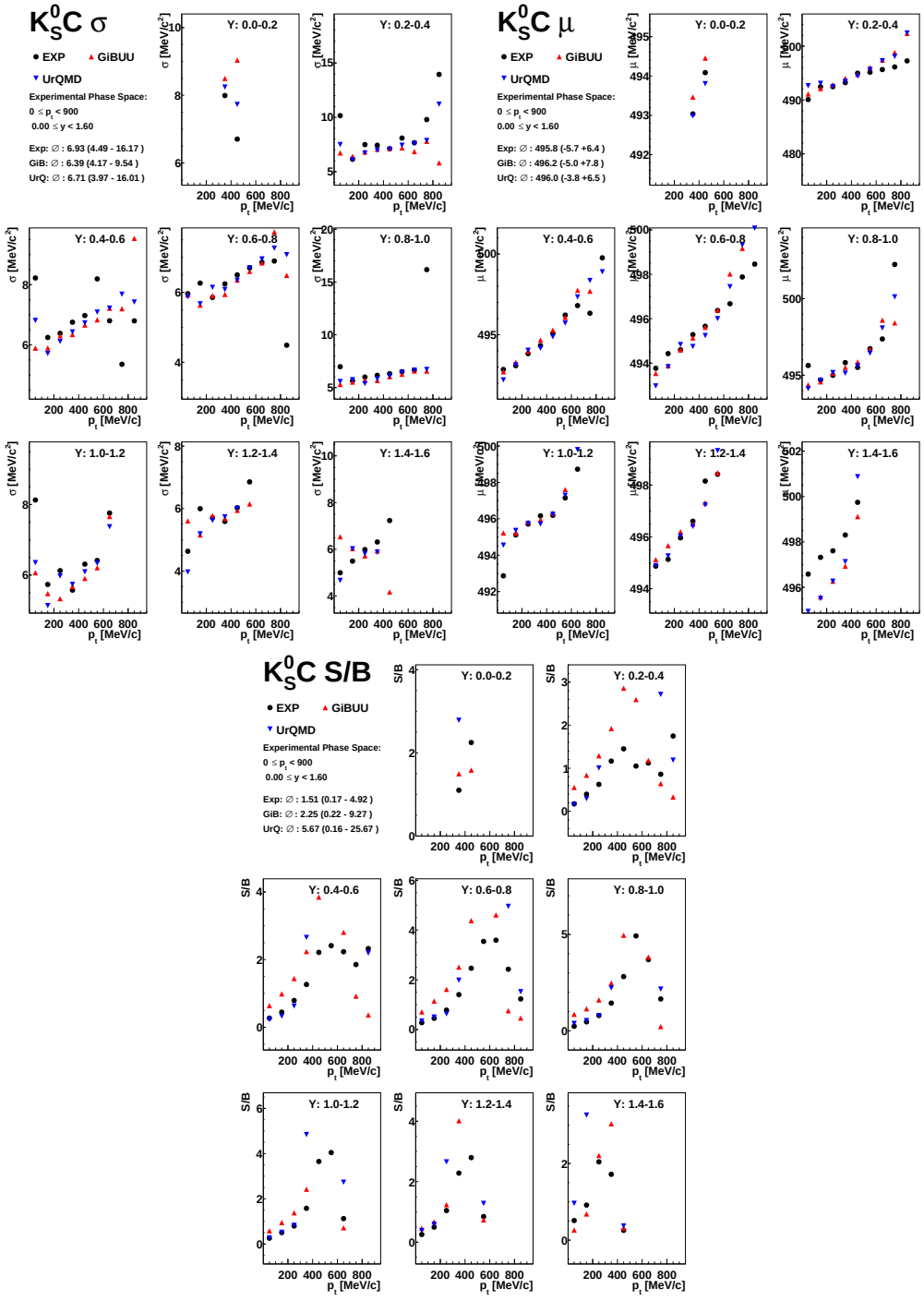

Figure C.2: Fit parameter for K^0_S in carbon.

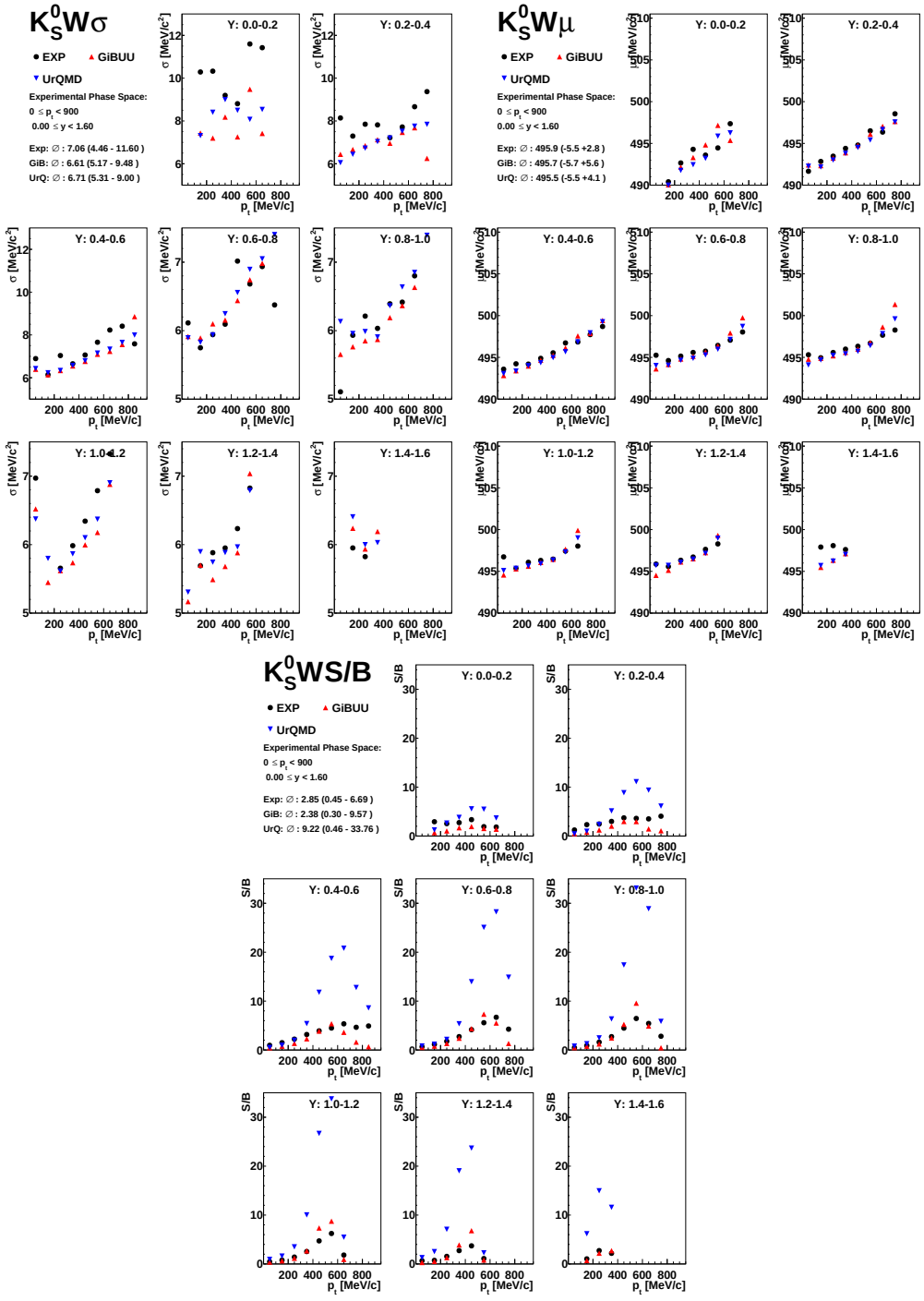

Figure C.3: Fit parameter for K^0_S in tungsten.

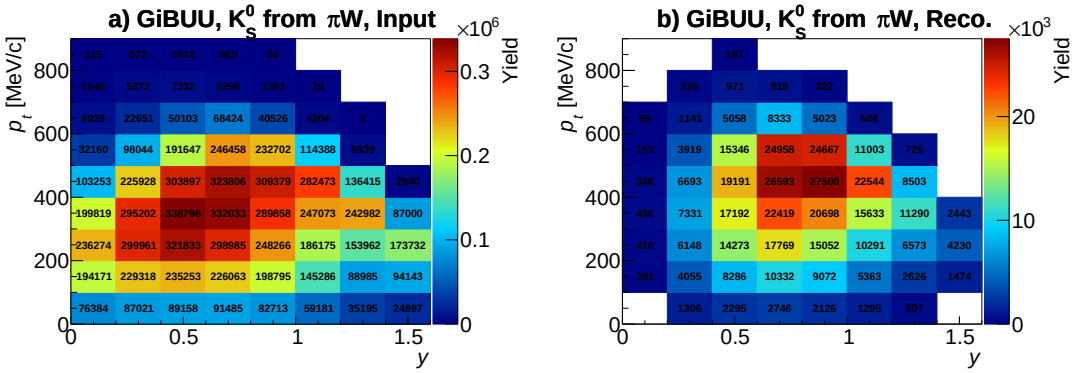

Figure C.5: GiBUU input panel (a) and panel (b) the reconstructed yield inside the HADES acceptance for K^0_S in tungsten.

C.2 Input - Reconstruction

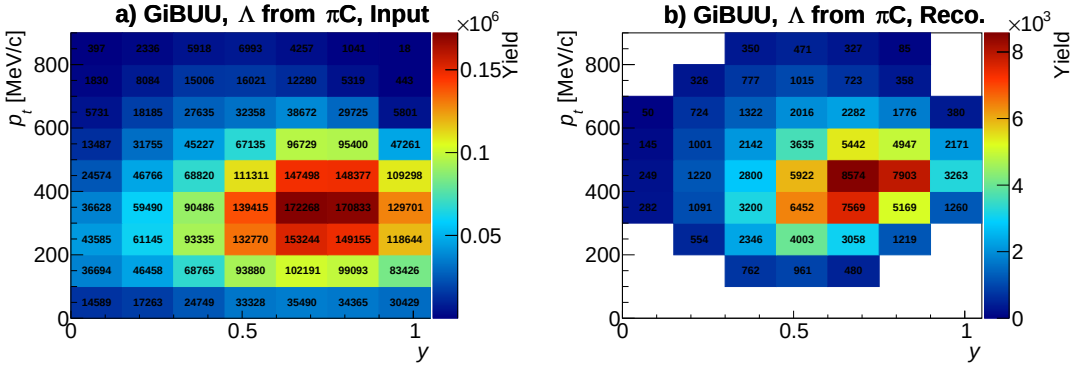

Figure C.4: GiBUU input panel (a) and panel (b) the reconstructed yield inside the HADES acceptance for Λ in carbon.

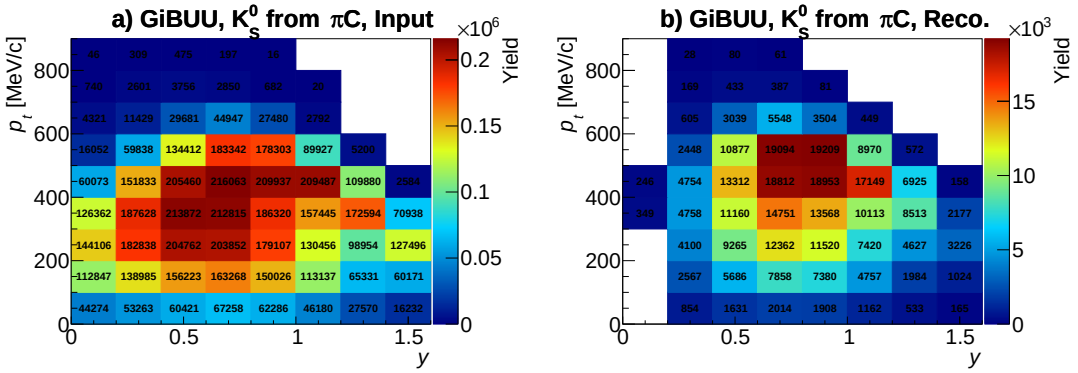

Figure C.6: GiBUU input panel (a) and panel (b) the reconstructed yield inside the HADES acceptance for K^0_S in carbon.

C.3 Self Consistency Check

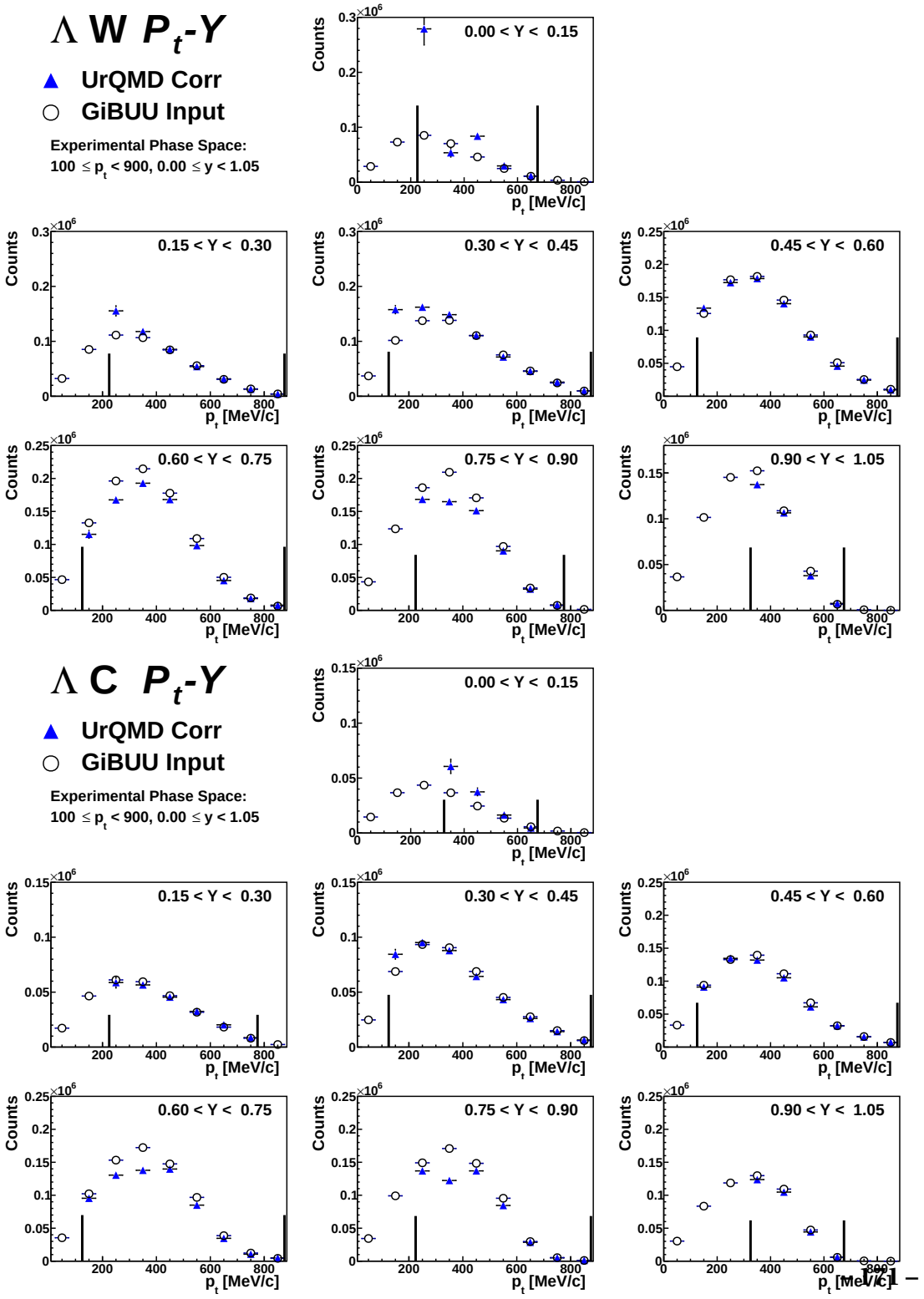

Figure C.7: Self-consistency for Λ in tungsten and carbon.

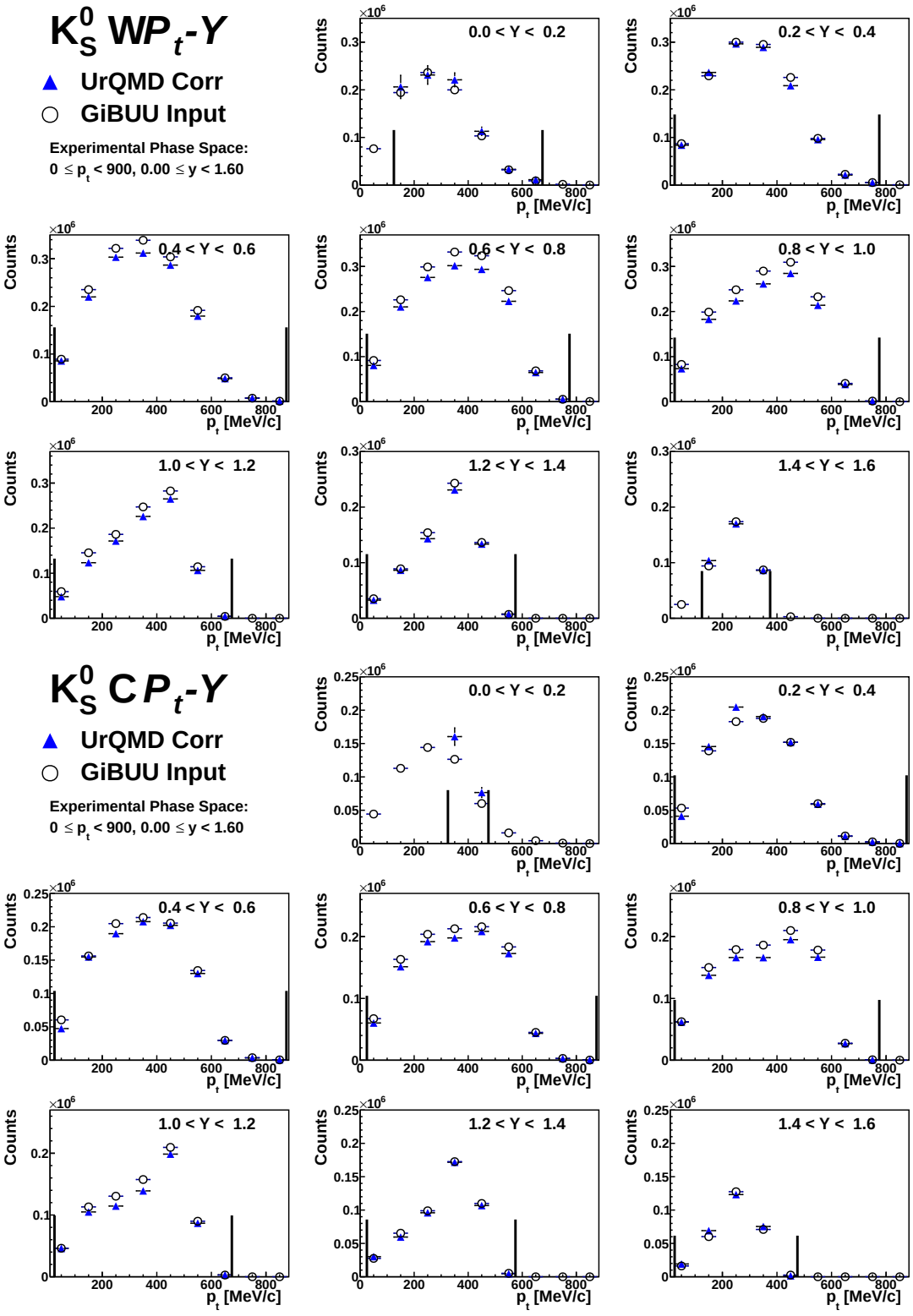

Figure C.8: Self-consistency for K^0_S in tungsten and carbon.

C.4 Boltzmann Extrapolation K_S^0

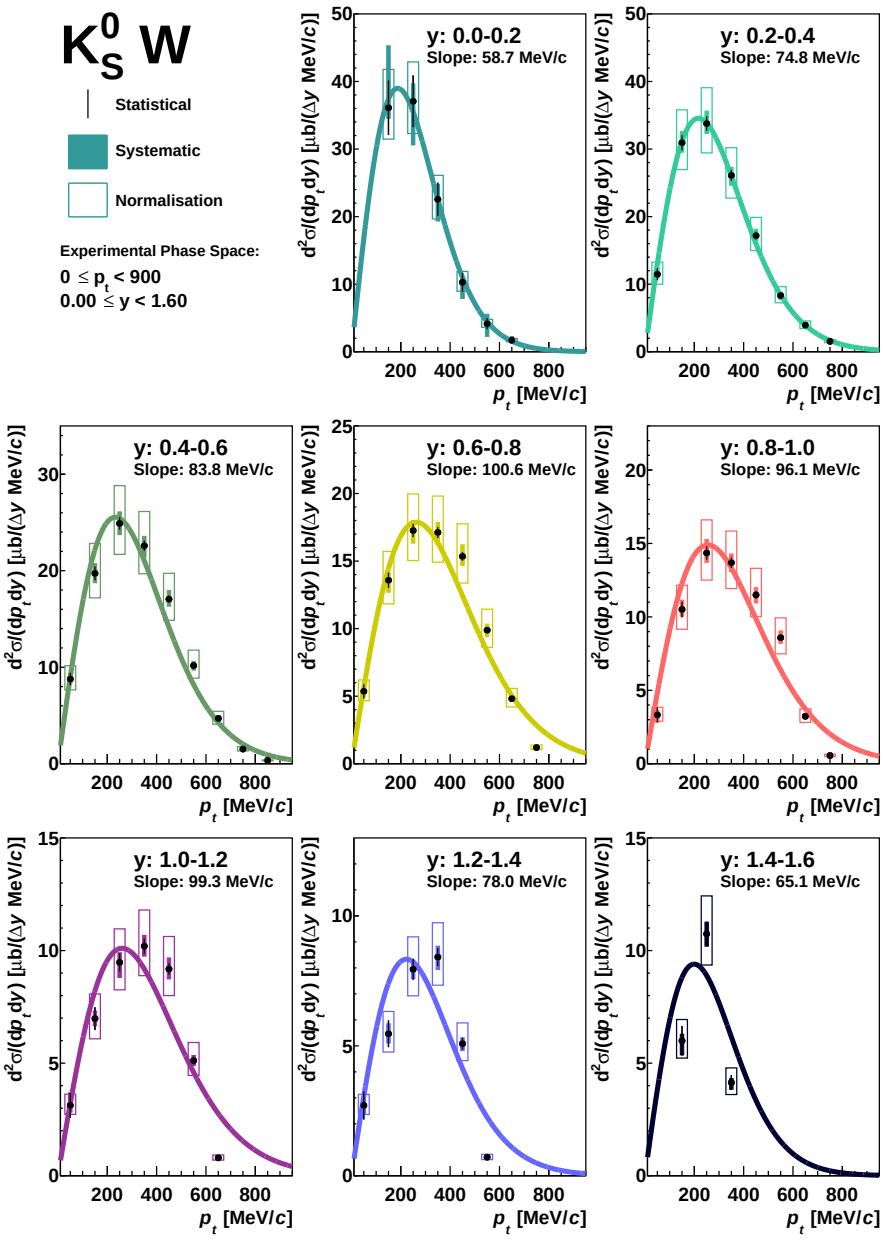

Figure C.9: Boltzmann extrapolation of K_S^0 in tungsten.

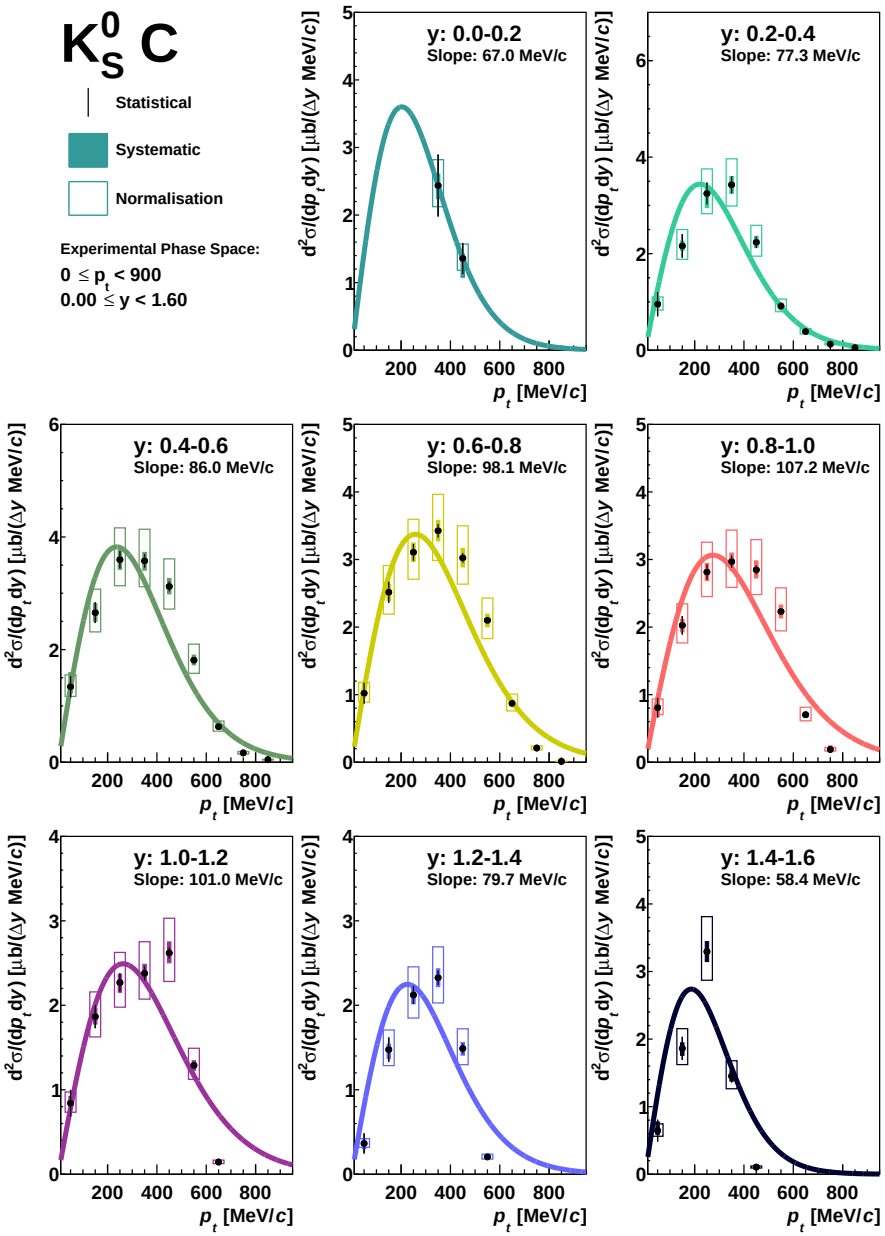

Figure C.10: Boltzmann extrapolation of K^0_S in carbon.

C.5 Resonance Contribution - UrQMD

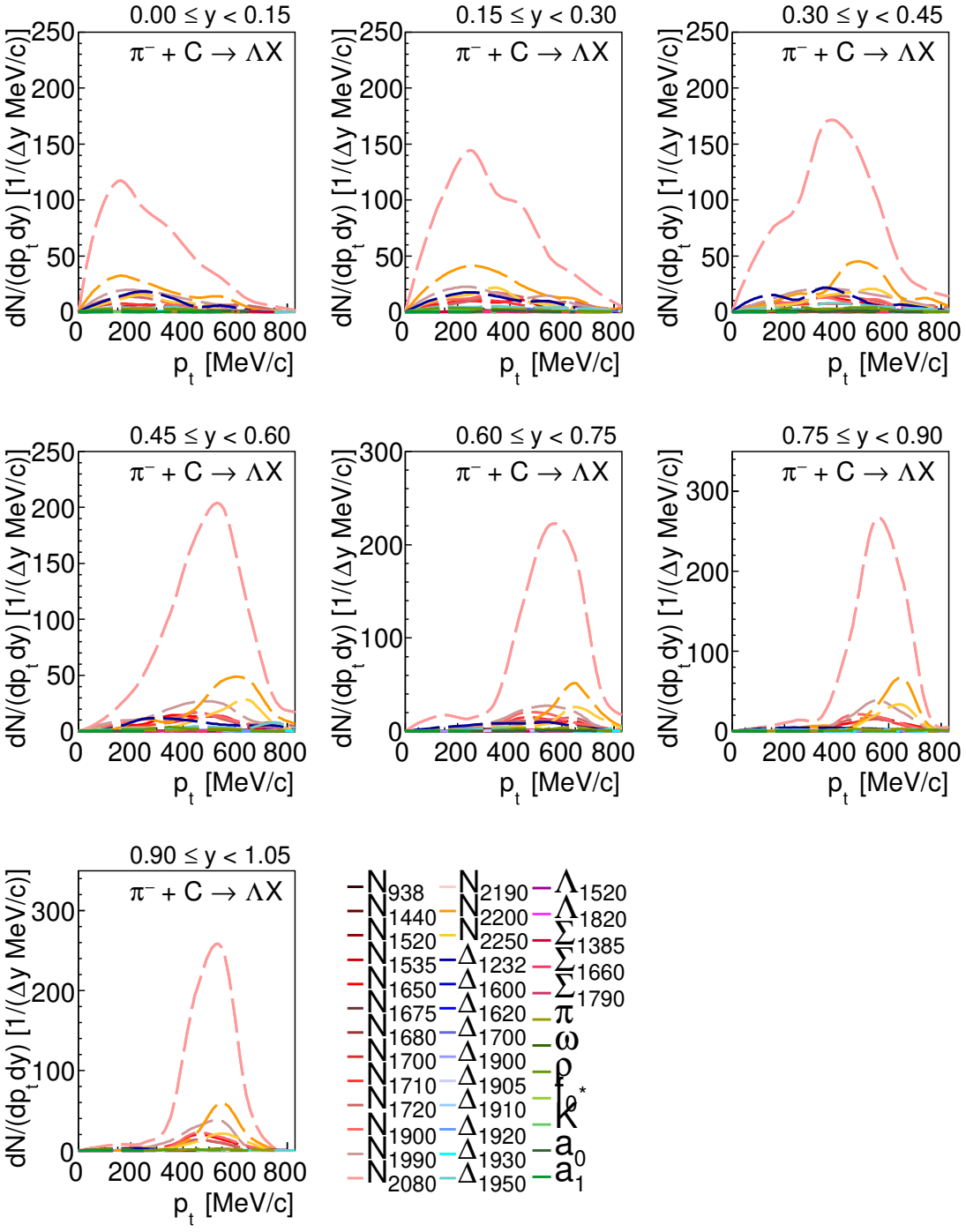

Figure C.11: Resonances contribution to the Λ yield of UrQMD in carbon.

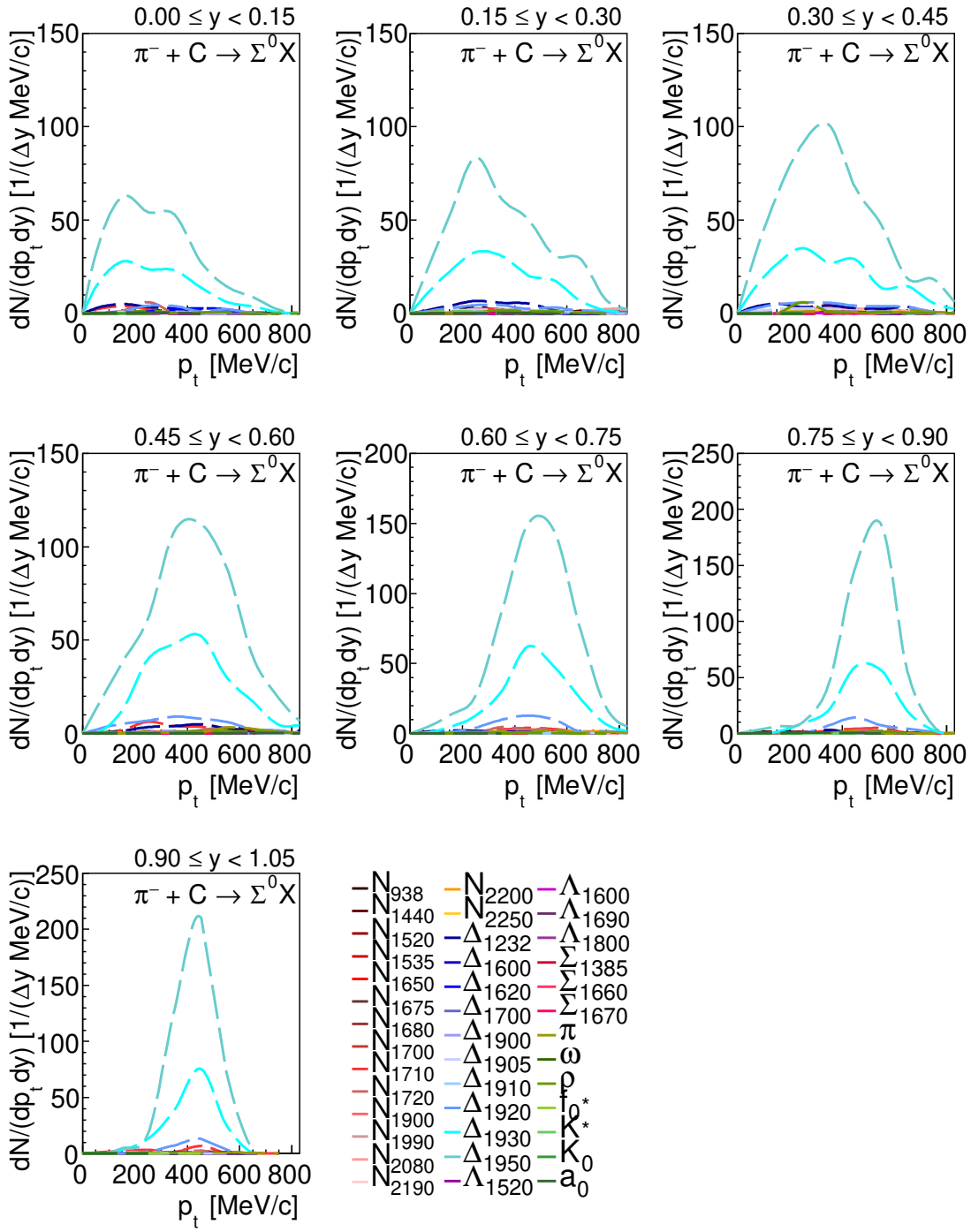

Figure C.12: Resonances contribution to the Σ^0 yield of UrQMD in carbon.

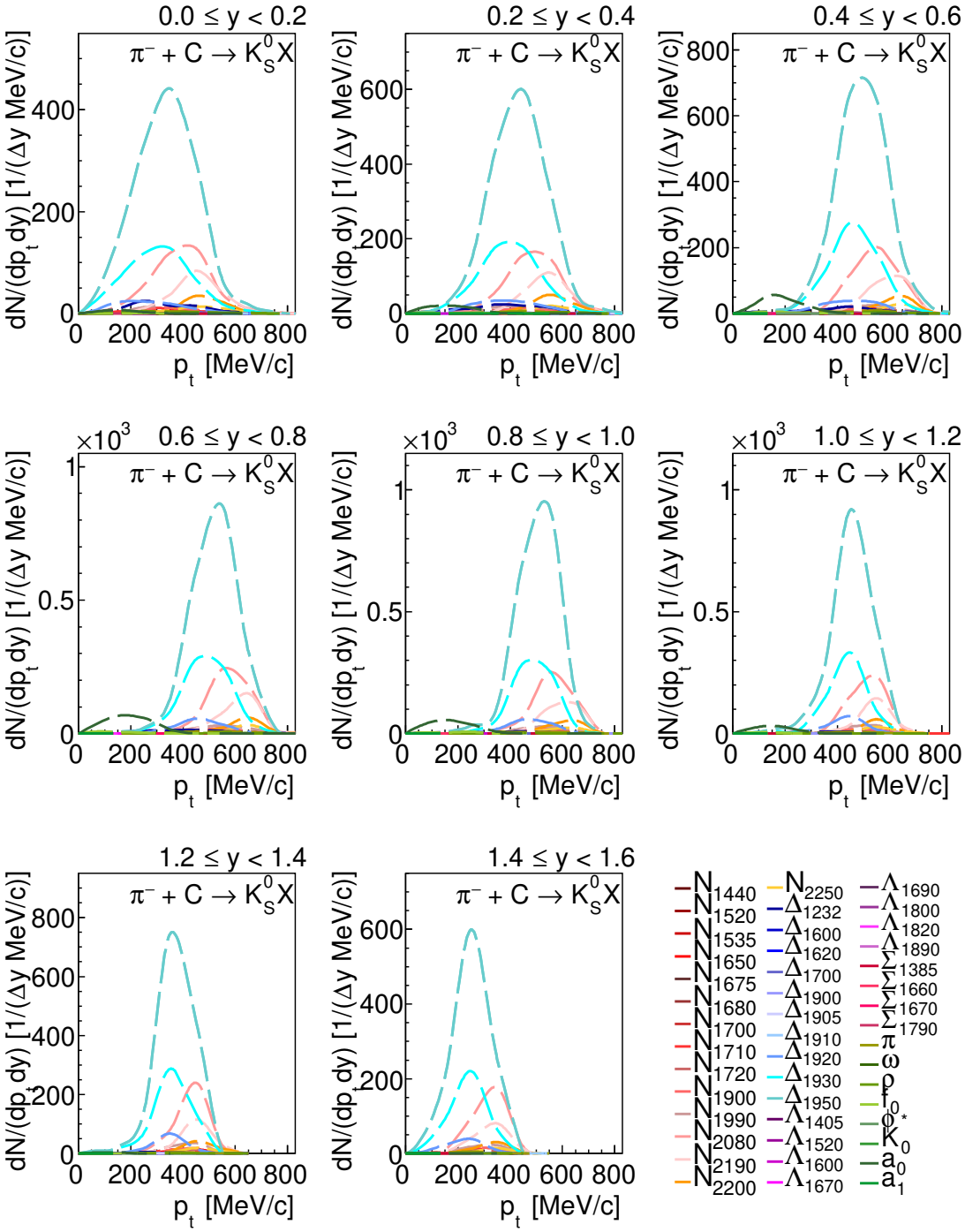

Figure C.13: Resonances contribution to the K^0_S yield of UrQMD in carbon.

D

Exclusive Analysis

D.1 Hyperon Creation

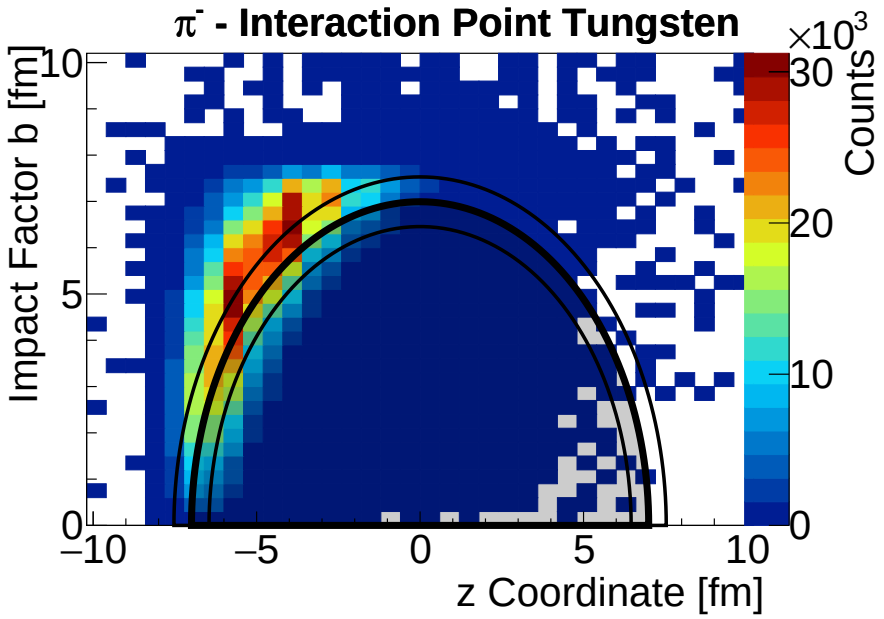

Figure D.1: Pion interaction point with the tungsten nucleus.

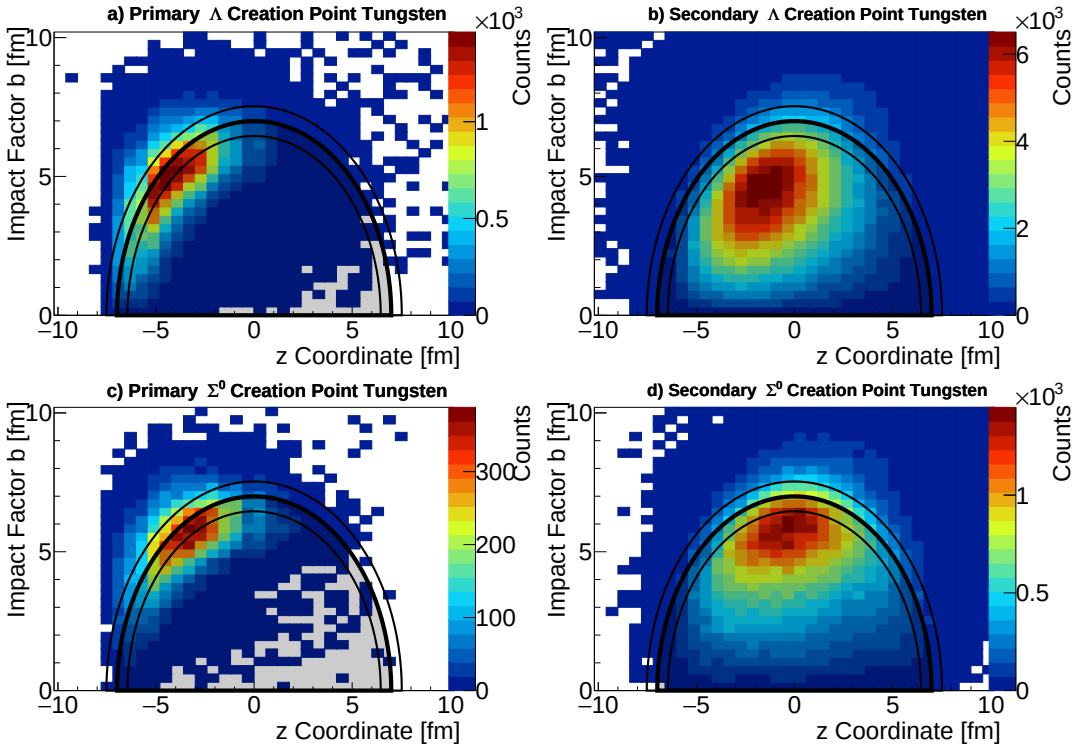

Figure D.2: Upper row: primary (a) and secondary (b) creation point of Λ in tungsten. Lower row: primary (a) and secondary (b) creation point of Σ^0 in tungsten.

D.2 Invariant Mass Cut

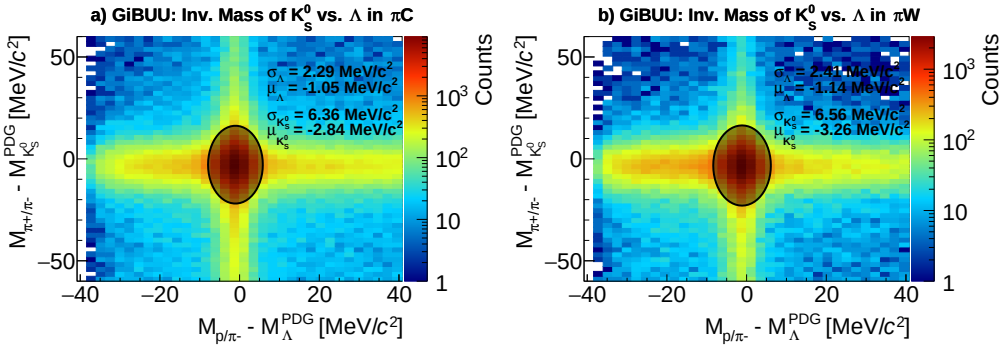

Figure D.3: Invariant mass of K_S^0 candidates vs. invariant mass of Λ candidates in GiBUU, on the left for carbon and on the right for tungsten.

D.3 χ^2 Scaling Factor

General form of χ^2:

$$\frac{\chi^2}{NDF} = \frac{1}{N-1}\sum_{i=0}^{N}\frac{\left(E_i - f(i,\alpha)\right)^2}{\sigma_E^2} \tag{D.1}$$

where

$\frac{\chi^2}{NDF}$: reduced χ^2
N: number of data points
E_i: experimental value
σ_E^2: combined experimental error
$f(i,\alpha)$: general function for reduction

General minimisation of χ^2 :

$$\frac{\partial}{\partial\alpha}\left(\frac{\chi^2}{NDF}\right) = \frac{1}{N-1}\sum_{i=0}^{N}\frac{\left(E_i - f(i,\alpha)\right)\cdot\frac{\partial}{\partial\alpha}f(i,\alpha)}{\sigma_E^2} = 0 = \sum_{i=0}^{N}\left(E_i - f(i,\alpha)\right)\cdot\frac{\partial}{\partial\alpha}f(i,\alpha)$$

assuming a simple scaling factor α of simulation data S_i:

$$f(i,\alpha) = \alpha\cdot S_i$$
$$\frac{\partial}{\partial\alpha}f(i,\alpha) = S_i$$
$$\rightarrow \alpha = \frac{\sum_{i=0}^{N}(E_i\cdot S_i)}{\sum_{i=0}^{N}\left(S_i^2\right)}$$

List of Figures

List of Tables

Bibliography

[1] C. Patrignani et al. Review of Particle Physics. *Chin. Phys. C*, 40(10):100001, 2016.

[2] S. A. Bass et al. Microscopic models for ultrarelativistic heavy ion collisions. *Prog. Part. Nucl. Phys.*, 41:255–369, 1998. [Prog. Part. Nucl. Phys.41,225(1998)].

[3] M Bleicher, E Zabrodin, C Spieles, S A Bass, C Ernst, S Soff, L Bravina, M Belkacem, H Weber, H Stöcker, and W Greiner. Relativistic hadron-hadron collisions in the ultra-relativistic quantum molecular dynamics model. *Journal of Physics G: Nuclear and Particle Physics*, 25(9):1859–1896, Sep 1999.

[4] O. Buss, T. Gaitanos, K. Gallmeister, H. van Hees, M. Kaskulov, O. Lalakulich, A. B. Larionov, T. Leitner, J. Weil, and U. Mosel. Transport-theoretical Description of Nuclear Reactions. *Phys. Rept.*, 512:1–124, 2012.

[5] J. Weil, V. Steinberg, J. Staudenmaier, L. G. Pang, D. Oliinychenko, J. Mohs, M. Kretz, T. Kehrenberg, A. Goldschmidt, B. Bäuchle, J. Auvinen, M. Attems, and H. Petersen. Particle production and equilibrium properties within a new hadron transport approach for heavy-ion collisions. *Phys. Rev. C*, 94:054905, Nov 2016.

[6] Roel Aaij et al. Observation of $J/\psi p$ Resonances Consistent with Pentaquark States in $\Lambda_b^0 \to J/\psi K^- p$ Decays. *Phys. Rev. Lett.*, 115:072001, 2015.

[7] G. Aad et al. Observation of a new particle in the search for the Standard Model Higgs boson with the ATLAS detector at the LHC. *Physics Letters B*, 716(1):1 – 29, 2012.

[8] S. Chatrchyan et al. Observation of a new boson at a mass of 125 GeV with the CMS experiment at the LHC. *Physics Letters B*, 716(1):30 – 61, 2012.

[9] Peter W. Higgs. Broken symmetries and the masses of gauge bosons. *Phys. Rev. Lett.*, 13:508–509, Oct 1964.

[10] Alexandre Deur, Stanley J. Brodsky, and Guy F. de Teramond. The QCD Running Coupling. *Prog. Part. Nucl. Phys.*, 90:1–74, 2016.

[11] Stefan Scherer. Introduction to chiral perturbation theory. *Adv. Nucl. Phys.*, 27:277, 2003. [,277(2002)].

[12] Kenji Fukushima and Tetsuo Hatsuda. The phase diagram of dense QCD. *Rept. Prog. Phys.*, 74:014001, 2011.

[13] Y. Aoki, G. Endrodi, Z. Fodor, S. D. Katz, and K. K. Szabo. The Order of the quantum chromodynamics transition predicted by the standard model of particle physics. *Nature*, 443:675–678, 2006.

[14] J. R. Oppenheimer and G. M. Volkoff. On massive neutron cores. *Phys. Rev.*, 55:374–381, Feb 1939.

[15] Richard C. Tolman. Static solutions of einstein's field equations for spheres of fluid. *Phys. Rev.*, 55:364–373, Feb 1939.

[16] Feryal Özel and Paulo Freire. Masses, Radii, and the Equation of State of Neutron Stars. *Ann. Rev. Astron. Astrophys.*, 54:401–440, 2016.

[17] Antoniadis et al. A massive pulsar in a compact relativistic binary. *Science*, 340(6131), 2013.

[18] P. B. Demorest, T. Pennucci, S. M. Ransom, M. S. E. Roberts, and J. W. T. Hessels. A two-solar-mass neutron star measured using shapiro delay. *Nature*, 467:1081 EP –, Oct 2010.

[19] V. A. Ambartsumyan and G. S. Saakyan. The Degenerate Superdense Gas of Elementary Particles. *Soviet Astronomy*, 4:187, October 1960.

[20] Diego Lonardoni, Alessandro Lovato, Stefano Gandolfi, and Francesco Pederiva. Hyperon puzzle: Hints from quantum monte carlo calculations. *Phys. Rev. Lett.*, 114:092301, Mar 2015.

[21] Thomas Hell and Wolfram Weise. Dense baryonic matter: Constraints from recent neutron star observations. *Phys. Rev. C*, 90:045801, Oct 2014.

[22] Wolfram Weise. Topics in low-energy QCD with strange quarks. *Hyperfine Interactions*, 233(1):131–140, Aug 2015.

[23] Volker Koch. Introduction to chiral symmetry. In *3rd TAPS Workshop on Electromagnetic and Mesonic Probes of Nuclear Matter Bosen, Germany, September 10-15, 1995*, 1995.

[24] M. Gell-Mann, R. J. Oakes, and B. Renner. Behavior of Current Divergences under $SU_3 \times SU_3$. *Phys. Rev.*, 175:2195–2199, 1968.

[25] S. Klimt, M. Lutz, and W. Weise. Chiral phase transition in the su(3) nambu and jona-lasinio model. *Physics Letters B*, 249(3):386 – 390, 1990.

[26] Torsten Dahms. *Dilepton spectra in p+p and Au+Au collisions at RHIC*. PhD thesis, SUNY, Stony Brook, 2008.

[27] Agakishiev et al. Dielectron production in Ar + KCl collisions at 1.76*A* GeV. *Phys. Rev. C*, 84:014902, Jul 2011.

[28] G. Agakishiev et al. First measurement of proton-induced low-momentum dielectron radiation off cold nuclear matter. *Phys. Lett.*, B715:304–309, 2012.

[29] G. E. Brown, Guo-Qiang Li, R. Rapp, Mannque Rho, and J. Wambach. Medium dependence of the vector meson mass: Dynamical and/or Brown-Rho scaling? *Acta Phys. Polon.*, B29:2309–2321, 1998.

[30] Christian Fuchs. Kaon production in heavy ion reactions at intermediate energies. *Prog. Part. Nucl. Phys.*, 56:1–103, 2006.

[31] D. B. Kaplan and A. E. Nelson. Strange Goings on in Dense Nucleonic Matter. *Phys. Lett.*, B175:57–63, 1986.

[32] Ann E. Nelson and David B. Kaplan. Strange condensate realignment in relativistic heavy ion collisions. *Physics Letters B*, 192(1):193 – 197, 1987.

[33] V. Metag, M. Nanova, and E. Ya. Paryev. Meson–nucleus potentials and the search for meson–nucleus bound states. *Prog. Part. Nucl. Phys.*, 97:199–260, 2017.

[34] M. L. Benabderrahmane et al. Measurement of the in-medium K^0 inclusive cross section in π^--induced reactions at 1.15 GeV/c. *Phys. Rev. Lett.*, 102:182501, May 2009.

[35] Markus Buescher et al. Inclusive K^+ meson production in proton nucleus interactions. *Eur. Phys. J.*, A22:301–317, 2004.

[36] W. Cassing and E. L. Bratkovskaya. Hadronic and electromagnetic probes of hot and dense nuclear matter. *Phys. Rept.*, 308:65–233, 1999.

[37] G. Agakishiev et al. Medium effects in proton-induced K^0 production at 3.5 GeV. *Phys. Rev.*, C90:054906, 2014.

[38] B. Sechi-Zorn, B. Kehoe, J. Twitty, and R. A. Burnstein. Low-energy Λ-proton elastic scattering. *Phys. Rev.*, 175:1735–1740, Nov 1968.

[39] G. Alexander, U. Karshon, A. Shapira, G. Yekutieli, R. Engelmann, H. Filthuth, and W. Lughofer. Study of the $\Lambda-n$ system in low-energy $\Lambda-p$ elastic scattering. *Phys. Rev.*, 173:1452–1460, Sep 1968.

[40] J. Haidenbauer, S. Petschauer, N. Kaiser, U.-G. Meißner, A. Nogga, and W. Weise. Hyperon–nucleon interaction at next-to-leading order in chiral effective field theory. *Nuclear Physics A*, 915:24 – 58, 2013.

[41] J.A. Kadyk, G. Alexander, J.H. Chan, P. Gaposchkin, and G.H. Trilling. Λp interactions in momentum range 300 to 1500 mev/c. *Nuclear Physics B*, 27(1):13 – 22, 1971.

[42] Oliver Werner Arnold. *Study of the hyperon-nucleon interaction via femtoscopy in elementary systems with HADES and ALICE*. PhD thesis, Munich, Tech. U., 2017.

[43] Avraham Gal. Old and New in Strangeness Nuclear Physics. *AIP Conf. Proc.*, 2130(1):020001, 2019.

[44] A. Gal, E. V. Hungerford, and D. J. Millener. Strangeness in nuclear physics. *Rev. Mod. Phys.*, 88:035004, Aug 2016.

[45] D. J. Millener, C. B. Dover, and A. Gal. Λ-nucleus single-particle potentials. *Phys. Rev. C*, 38:2700–2708, Dec 1988.

[46] D. J. Prowse. ${}_{\Lambda\Lambda}\mathrm{He}^{6}$ double hyperfragment. *Phys. Rev. Lett.*, 17:782–785, Oct 1966.

[47] The identification of a double hyperfragment. *Nuclear Physics*, 49:121 – 132, 1963.

[48] Aoki et al. Direct observation of sequential weak decay of a double hypernucleus. *Progress of Theoretical Physics*, 85(6):1287–1298, 06 1991.

[49] Evidence for a bound state of the Σ4 He hypernucleus. *Physics Letters B*, 231(4):355 – 358, 1989.

[50] P. Khaustov et al. Evidence of Ξ hypernuclear production in the ${}^{12}\mathrm{C}(K^-, K^+)^{12}_{\Xi}\mathrm{Be}$ reaction. *Phys. Rev. C*, 61:054603, Mar 2000.

[51] S. Aoki et al. Production of Two Single- Hypernuclei by - Capture. *Progress of Theoretical Physics*, 89(2):493–500, 02 1993.

[52] K. Nakazawa et al. The first evidence of a deeply bound state of Xi–14N system. *Progress of Theoretical and Experimental Physics*, 2015(3), 03 2015.

[53] O. Hashimoto and H. Tamura. Spectroscopy of Lambda hypernuclei. *Prog. Part. Nucl. Phys.*, 57:564–653, 2006.

[54] S. Petschauer, J. Haidenbauer, N. Kaiser, Ulf-G. Meißner, and W. Weise. Hyperons in nuclear matter from su(3) chiral effective field theory. *The European Physical Journal A*, 52(1):15, Jan 2016.

[55] H. Geissel et al. The gsi projectile fragment separator (frs): a versatile magnetic system for relativistic heavy ions. *Nuclear Instruments and Methods in Physics Research Section B: Beam Interactions with Materials and Atoms*, 70(1):286 – 297, 1992.

[56] J Dıaz et al. Design and commissioning of the GSI pion beam. *Nucl. Instrum. Meth.*, A478:511–526, 2002.

[57] HADES Collaboration. A facility for pion-induced nuclear reaction studies with HADES. *The European Physical Journal A*, 53(9):188, Sep 2017.

[58] G. Agakishiev et al. The High-Acceptance Dielectron Spectrometer HADES. A41:243–277, 2009.

[59] J. Wirth. (Strange) Meson Production in Pion-Nucleus Collisions at 1.7 GeV/c - Strong Absorption of Hadrons with Hidden and Open Strangeness.

[60] K. Zeitelhack et al. The HADES RICH detector. *Nucl. Instrum. Meth.*, A433:201–206, 1999.

[61] J Michel, M Böhmer, M Kajetanowicz, G Korcyl, L Maier, M Palka, J Stroth, A Tarantola, M Traxler, C Ugur, and S Yurevich. The upgraded HADES trigger and data acquisition system. *Journal of Instrumentation*, 6(12):C12056–C12056, dec 2011.

[62] A Neiser, J Adamczewski-Musch, M Hoek, W Koenig, G Korcyl, S Linev, L Maier, J Michel, M Palka, M Penschuck, M Traxler, C Uğur, and A Zink. TRB3: a 264 channel high precision TDC platform and its applications. *Journal of Instrumentation*, 8(12):C12043–C12043, dec 2013.

[63] J. Adamczewski-Musch et al. Inclusive Λ production in proton-proton collisions at 3.5 GeV. *Phys. Rev.*, C95(1):015207, 2017.

[64] J. Adamczewski-Musch et al. Σ^0 production in proton nucleus collisions near threshold. *Phys. Lett.*, B781:735–740, 2018.

[65] H. Schuldes. Strangeness production in Au(1.23 AGeV)+Au collisions. *Nuclear Physics A*, 967:804 – 807, 2017. The 26th International Conference on Ultra-relativistic Nucleus-Nucleus Collisions: Quark Matter 2017.

[66] S. Wheaton, J. Cleymans, and M. Hauer. THERMUS A thermal model package for ROOT. *Computer Physics Communications*, 180:84–106, January 2009.

[67] I. Fröhlich et al. Pluto: A Monte Carlo Simulation Tool for Hadronic Physics. *PoS*, ACAT:076, 2007.

[68] K. Tsushima, S.W. Huang, and Amand Faessler. The role of the Δ (1920) resonance for kaon production in heavy ion collisions. *Physics Letters B*, 337(3):245 – 253, 1994.

[69] K. Tsushima, S. W. Huang, and Amand Faessler. A Study of the π B —> Y K reactions for kaon production in heavy ion collisions. *Austral. J. Phys.*, 50:35–43, 1997.

[70] K. Tsushima, A. Sibirtsev, A. W. Thomas, and G. Q. Li. Resonance model study of kaon production in baryon-baryon reactions for heavy-ion collisions. *Phys. Rev. C*, 59:369–387, Jan 1999.

[71] Christoph Hartnack, Helmut Oeschler, Yvonne Leifels, Elena L. Bratkovskaya, and Jorg Aichelin. Strangeness Production close to Threshold in Proton-Nucleus and Heavy-Ion Collisions. *Phys. Rept.*, 510:119–200, 2012.

[72] Torbjörn Sjöstrand, Stephen Mrenna, and Peter Skands. PYTHIA 6.4 physics and manual. *Journal of High Energy Physics*, 2006(05):026–026, may 2006.

[73] Torbjörn Sjöstrand, Stephen Mrenna, and Peter Skands. A brief introduction to pythia 8.1. *Computer Physics Communications*, 178(11):852 – 867, 2008.

[74] R. Brun, F. Bruyant, M. Maire, A. C. McPherson, and P. Zanarini. GEANT3. 1987.

[75] P. Salabura. Private communication.

[76] A. A. Sibirtsev, W. Cassing, and C. M. Ko. Anti-Kaon production in nucleon-nucleon reactions near threshold. *Z. Phys.*, A358:101–106, 1997.

[77] W. Cassing, E. L. Bratkovskaya, U. Mosel, S. Teis, and A. Sibirtsev. Kaon versus anti-kaon production at SIS energies. *Nucl. Phys.*, A614:415–432, 1997.

[78] A. Baldini, V. Flaminio, W. G. Moorhead, and D. R. O. Morrison. Vii.2 cross section data: Datasheet from landolt-börnstein - group i elementary particles, nuclei and atoms · volume 12b: "subvolume b" in springermaterials

(https://dx.doi.org/10.1007/10367917_29). Copyright 1988 Springer-Verlag Berlin Heidelberg.

[79] Jan Steinheimer and Marcus Bleicher. Sub-threshold ϕ and Ξ^- production by high mass resonances with UrQMD. *J. Phys.*, G43(1):015104, 2016.

[80] M. Büscher et al. Inclusive K^+-meson production in proton-nucleus interactions. *The European Physical Journal A - Hadrons and Nuclei*, 22(2):301–317, Nov 2004.

[81] J. Adamczewski-Musch et al. Sub-threshold production of K^0_s mesons and Λ hyperons in Au+Au collisions at $\sqrt{s_{NN}} = 2.4$ GeV. *Phys. Lett.*, B793:457–463, 2019.

[82] C. Hartnack, Rajeev K. Puri, J. Aichelin, J. Konopka, S. A. Bass, Horst Stoecker, and W. Greiner. Modeling the many body dynamics of heavy ion collisions: Present status and future perspective. *Eur. Phys. J.*, A1:151–169, 1998.

[83] G. Agakishiev et al. In-medium effects on K^0 mesons in relativistic heavy-ion collisions. *Phys. Rev. C*, 82:044907, Oct 2010.

[84] Bozena Nerlo-Pomorska and Krzysztof Pomorski. Simple formula for nuclear charge radius. *Zeitschrift für Physik A Hadrons and Nuclei*, 348(3):169–172, Sep 1994.

[85] Adamczewski-Musch et al. Σ^0 production in proton nucleus collisions near threshold. *Physics Letters B*, 781, 11 2017.

[86] P. Kowina et al. Energy dependence of the Λ/Σ production cross-section ratio in p-p interactions. *The European Physical Journal A - Hadrons and Nuclei*, 22(2):293–299, Nov 2004.

[87] S. Sewerin et al. Comparison of Λ and Σ^0 production near threshold in proton-proton collisions. *Phys. Rev. Lett.*, 83:682–685, Jul 1999.

[88] B. P. Abbott et al. Gw170817: Observation of gravitational waves from a binary neutron star inspiral. *Phys. Rev. Lett.*, 119:161101, Oct 2017.

[89] Haris Djapo, Bernd-Jochen Schaefer, and J Wambach. Appearance of hyperons in neutron stars. *Phys. Rev. C*, 81, 11 2008.

[90] W. Czyzycki et al. Electromagnetic Calorimeter for HADES. 2011.

Danksagungen

An diesem Punkt möchte ich mich bei all denen bedanken die mich Unterstützt haben und diese Arbeit erst möglich gemacht haben.
Allen voran gilt mein Dank Laura, die mich in Ihre Gruppe aufgenommen hat. Durch sie habe ich viel über physikalische Zusammenhänge und wissenschaftliches Arbeiten gelernt und wie man diese vor einem internationalem Publikum verteidigt. Allgemein hat sie immer grossen Wert darauf gelegt das sich ihre Studenten und Doktoranden weiterbilden, sei es durch organisieren von Meetings mit Fachleuten, das finanzieren von internationalen Konferenzen, einem Journal Club, eine Vorlesung passend zum Promotionsthema um nur einige zu nennen.
Des weiteren ermöglichte sie mir mein Wissen über Informatik weiter zu bilden in dem ich die System-Administration übernehmen durfte.
Sie war auch an vorderster Front als es darum ging diese Thesis Korrektur zu lesen und zu verbessern, was sicher nicht immer ein Vergnügen war. Auch mein Verkaufsgeschick für Möbel hat sich deutlich verbessert, da sie immer grossen Wert auf "sell the couch" gelegt hat, sei es bei Vorträgen oder wissenschaftlichen Arbeiten.
Danke!
Bei Chii und Oliver möchte ich mich bedanken, da sie mir am Anfang geholfen haben mich durch den HADES-Software-Wald zu kämpfen. Auch möchte ich mich bei meinen alten Zimmer-Kollegen Rafal, Sverre und Martin (technisch nicht direkt Zimmer-Kollege) bedanken die mich mit Rat und Tat Unterstützt haben. Ein besonderer Dank geht an Tobias, der die Geduld aufbrach mich in die Geheimnisses des KTAs Computer-Clusters einzuweihen und als treuer Hotelzimmer-Genosse (das mit dem "warmen" Wasser verzeih ich dir nie!). Ausserdem möchte ich mich noch bei Ralf und Lukas bedanken, die immer ein offenes Ohr hatten und Hilfsbereit waren. Vielen lieben dank auch an Petra und Sigrid die sich mit abertausenden Anträgen und Verwaltungsfragen auseinander setzen musste, dass der Laden läuft. Ein grosses Dankeschön geht auch an Benjamin, Josef und Stefan die mir immer weiterhelfen konnten wenn nicht mal sudo oder die google Seite 2 die Lösung brachte. Danke auch an Andi, Ante, Bernie, Dimitar, Jürgen und Vale für die Unterstützung wenn die Physik nicht so wie ich wollte. Besonders möchte ich auch noch Sissi danken für die Unterstützung, die vielen Gespräche und die tollen Abende im Isartor. Explizit möchte ich mich noch bei Joana bedanken, dass sie das alles so lange aushält mit

mir. Versteh ich selber nicht.
Auch der gesamten HADES Collaboration möchte ich für ihre Unterstützung danken. Besonderen dank gilt hier Jochen, Manuel, Pavel, Piotr und Romain. Von der theoretischen Seite möchte ich mich herzlich bei Hannah, Marcus, Theodoros, Vincent und Jan für die Hilfe bedanken. Ohne euch hätte ich das nie transportiert bekommen.
Letztlich möchte ich mich noch bei meiner Mutter bedanken, auf die ich im Studium immer zählen konnte oder die finanziell ausgeholfen hat wenn am Ende des Monats nur noch Yam-Yam Suppe auf dem Menü stand.
Allgemein möchte mich bei allen bedanken die meinen Weg während der Doktorarbeit gekreuzt haben und mich Unterstützt haben.
Es war eine tolle Zeit.